HIGH INTENSITY BEAM ISSUES IN THE CERN PROTON SYNCHROTRON

THIS IS A TEMPORARY TITLE PAGE
It will be replaced for the final print by a version
provided by the service academique.

Thèse n. 1234 2011
présenté le 15 Mai 2012
à la Faculté des Sciences de Base
Laboratoire de physique des accelerateurs de particules
Programme doctoral en physique
École Polytechnique Fédérale de Lausanne

pour l'obtention du grade de Docteur ès Sciences
par

Sandra Aumon

acceptée sur proposition du jury:

Prof. Olivier Schneider, président du jury
Prof. Leonid Rivkin, directeur de thèse
Dr. Simone Gilardoni, rapporteur
Prof Mauro Migliorati, rapporteur
Prof Aurelio Bay, rapporteur

Lausanne, EPFL, 2012

Pour Maman and somehow to Nicolas . . .

Acknowledgements

The first time I heard about the CERN Organization was during a second year course of Newtonian Mechanics in High School. At that time, LEP was in its last year of operation before the shut down. Of course, I had no idea about Accelerator Physics and I was from the idea to do a PhD in this field. In fact, I did not imagine in High School that, one day, I would work in the largest lab in Physics of the world. And I must say that I was very lucky to have as teacher Mr Castor during my Master in Clermont-Ferrand. He told us about some possibilities of doing an internship at CERN in Radiation Protection but also in the Accelerator Physics Group. Again, I did not have a clear idea about how an accelerator is working, and after a short one day visit at CERN with Stephane Maury, I thought that it would be worth to try the experience. I was not thinking to do research afterwards, then I convince myself to take the chance before the end of my study and in particular, before going back in the industry after my diploma thesis. This chance might never happen again in my life!

When I was a child, I read several times all the Tintin comics books, in particular, I appreciated those in which Tintin is going to to the Moon. When I arrived at CERN, I really felt like I was in this laboratory in Syldavia: the control room, everybody working for this huge project, a few people working in a white coat and the 50-60's old style buildings. Except that I did not find yet the Pr. Tournesol. For my Master thesis, my supervisors were Michel Martini and ... a certain Simone Gilardoni and my first task was to perform MAD simulations at a certain energy so-called transition energy with the gamma transition jump in the CERN PS. I was far to imagine that transition energy would follow me during my PhD.

Here I come to the first person that I want to thank, Simone Gilardoni. He has been my mentor, supervisor and confidant during these 6 years at CERN and it is rather difficult to find a better supervisor. I would like to profit of these acknowledgements to thank him. He has been very patient with me and he always helped me in the hardest (and the easiest) moments of the thesis but also outside work. I am very grateful for all the knowledges that he gave me about this beautiful machine, the PS. It is difficult to write here my admiration for him and I just hope that we can continue to collaborate in the future.

I would like to thank my EPFL supervisor, Leonid Rivkin, for having accepted me as a doctoral student and for all the support that he provided during my PhD.

I am very grateful to Oliver Bruening and Gianluigi Arduini for the opportunity they gave me to work in the Accelerator Physics Group but also for the advices and supports they provided during my stay at CERN.

My acknowledgements are also for Elias Metral. I would like to thank him for his help and

for all the advices, the long discussions we had about this instability and collective effects in general. I am very grateful also to Giovanni Rumolo and Benoit Salvant, Elena Benedetto for their support all along my PhD.
If there is a team at CERN which had a large impact on my thesis, it is obviously the PS-PSBooster Operation group. I want to thank all of them for the fantastic help and support that they provided to me during my MDs but also for their friendship. In particular, thanks to Pierre Freyermuth, Oliver Hans, Marc Delrieux, Fabrice Chapuis, Rodolphe Maillet and Herve Genoud for their precious help during my measurements. Of course, I am very grateful to Rende Steerenberg for all the large support and discussions. I hope that we can continue to collaborate in the future. Thank you all for your friendship and for having accepted me in your team!
I want thank the RF Group and in particular Heiko Damerau and Alan Findlay for their help. I am very grateful to Jan Borburgh, Wolfgang Bartmann and Brennan Goddard for interesting discussions. Also, many thanks to Alexey Burov, Nicolas Mounet, Riccardo De Maria, Hannes Bartosik, Yannis Papaphilippou, Vladimir Kornilov for ideas, advices.
I want to particularly thank Roderik Bruce. Beside the fact that he is my confidant and my best friend, he is for me still now the example to follow. I would like to write here all my admiration for him, for all the help he gave me even when he was still in his PhD, all the time that he spent with me for moral support and for the work. I am very grateful for the advices and idea that he gave me. And I want to thank him for his friendship. Tack så mycket!
Beside the work, there is a life and I must say that the time I had in Geneva was absolutely great. I would to thank all my friends in France in all around the world:Roderik, Erik, Elena, Riccardo, Sandro, Tapas, Alexander, Tanja, Jean Charles, Steffen, Daniel, Guillermo and my dear officemate Glenn.
What about Rodolphe ? Thanks to him ! Without Rodolphe, nothing would have been possible and I would have never finished my PhD, New Super Mario Bros Wii and Rayman! I hope we can continue to track the Star Coins in the next Mario! Thank you Luigi!
The least but not the last. *D'abord, je ne saurais écrire toute la gratitude, l'admiration que je dois à Maman. Bien sur, il est facile d'écrire que, sans elle, je ne serais jamais allée si haut. Mais c'est tellement vrai... Cette thèse, c'est aussi le resultat de tout les sacrifices que tu as fait le long de ta vie pour moi, pour qu'on ait une vie meilleure et pour mes études. Merci, cette thèse, c'est pour toi.*
The life would be very boring alone... Pierre, tu m'as supporté pendant ces années difficiles de thèse, matin et soir. Tu m'as aidé pour mes mesures, dans ma vie, tu as été et tu es le parfait compagnon et ami qu'on puisse avoir. J'espere qu'on continuera cette aventure ensemble encore longtemps ...

Geneva, the 15 of May 2012 S. A.

Abstract

This PhD work is about limitations of high intensity proton beams observed in the CERN Proton Synchrotron (PS) and, in particular, about issues at injection and transition energies. With its 53 years, the CERN PS would have to operate beyond the limit of its performance to match the future requirements. Beam instabilities driven by transverse impedance and aperture restrictions are important issues for the operation and for the High-Luminosity LHC upgrade which foresees an intensity increase delivered by the injectors.

The main subject of the thesis concerns the study of a fast transverse instability occurring at transition energy. The proton beams crossing this energy range are particularly sensitive to wake forces because of the slow synchrotron motion. This instability can cause a strong vertical emittance blow-up and severe losses in less than a synchrotron period. Experimental observations show that the particles at the peak density of the beam longitudinal distribution oscillate in the vertical plane due to a short range wake field and following a travelling wave of about 700 MHz. In order to perform measurements, a dedicated single bunch beam was set up with a zero chromaticity plateau around transition energy. Extensive measurements were performed of the dynamics of instability in order to compute rise times and intensity thresholds. These measurements were done for several peak densities and the results show that the longer the bunch length, the higher is the threshold in intensity. Other measurements performed with a small negative chromaticity and another working point show that the intensity threshold can be pushed at higher values—in this case, the threshold was increased by 20%. The particularity of this work is that the instability is triggered during the acceleration. At transition energy, the momentum compaction factor is zero and the exchange of particles between the head and the tail of the beam from synchrotron motion, which is a natural way to damp instabilities, vanishes for few turns. Therefore the measurements at which η the instability is triggered are fundamental to know in which longitudinal regime the instability develops. Macro particle simulations were performed in order reproduce the dynamics of the instability with the *HEADTAIL* code, that simulates the beam interaction with the impedance of the machine. In the case of the PS, a very detailed impedance model does not exist, therefore a very simple resonator impedance was considered. The parameters of the code were adapted in order to simulate the beam as close as possible to the experimental conditions. The simulations showed that the travelling wave is well reproduced and therefore rise times were extracted for different beam intensities and compared to the measurements. A good agreement is found for a such simple impedance model. The intensity thresholds are reproduced for zero chromaticity within 30% and it is clear that some damping mechanisms occurring in

the measurements are not reproduced by the code. In particular, octupolar components of the field, non-linear coupling and transverse space charge are not taken into account. These limitations could cause some discrepancies between model and measurements. This study allows to establish a broadband impedance model which can be use to predict the dynamics of the instability. A few experiments were done also with the use a gamma transition jump. In this case, the instability appears in the adiabatic regime and the rising of the instability is following the peak density of the beam. Both the intensity threshold measurements and the simulations show that the gamma jump is by far the most efficient way to increase significantly the intensity threshold. The choice of adequate working point appears also to be a cure of the instability. This study with the support of measurements provides a rough impedance model confirmed by simulations and an understanding of the different mechanisms triggering the instability.

The last part of the thesis is dedicated to proton beam losses studies at injection energy. An eventual upgrade of the high intensity beam is limited by large beam losses at injection in the PS. Losses were measured with the current beam loss monitor system of the PS that they occur while the incoming beam enters in the machine and then during several hundred turns while the beam is circulating. Optics measurements were performed to check the mismatch of the transfer line between the PSBooster and the PS. A significant horizontal dispersion mismatch was found and in particular a difference in optics between the four injection lines of the PS. Aperture bottlenecks were found at the injection septum in both transverse planes and at the maximum of the injection bump. With the help of Monte Carlo simulations, the high radiation outside the ring induced by the losses was understood. However, the mismatch does not explain the continuous losses after the beam is injected. A possible explanation is that the space charge forces contribute to make particles cross resonances and are lost while they are oscillating at high amplitudes. The transverse phase space is refilled due to the combination of the synchrotron motion and space charge. Several solutions were proposed to improve the situation. A new optics of the transfer line and at injection could make the beam size smaller. Some special quadrupoles already installed in the PS could be used to adapt the optics of the incoming beam. Increase the injection energy from 1.4 GeV to 2 GeV kinetic would cause a gain of 65% in space charge forces, and these studies are currently ongoing for the upgrade of the PS in the framework of high-intensity LHC upgrade project. High intensity beams are also perturbed by space charge forces and transverse instabilities. Coherent tune shift measurements were performed at injection and extraction in order to evaluate the transverse imaginary part of the impedance and the contribution of the space charge to betatron frequency shift with the beam intensity.

keyword: accelerator, high intensity beams, impedance, transition energy, injection, wake field, gamma jump, fast vertical instability, beam dynamics, Pole Face Winding (PFW), working point, chromaticity, beam breakup, space charge, fast head-tail, mismatch, PS upgrade

Résumé

Ce travail de thèse traite des limitations des faisceaux haute intensité de proton actuellement observées dans le PS du CERN, et en particulier, à l'injection et l'énergie de transition. Après 53 ans d'activité, le PS devra fonctionner au-delà de la limite de ces performances pour répondre aux exigences futures des expériences. Les instabilités générées par l'impédance transverse et les restrictions d'ouverture sont des problèmes importants pour l'opération et la ligne directrice de l'expérience des Neutrinos du Gran Sasso (CNGS) et la mise à jour du LHC pour la haute luminosité qui prévoit une augmentation de l'intensité fournie par les injecteurs.

Le sujet principal de cette thèse concerne l'étude d'une instabilité rapide qui se développe autour de l'énergie de transition. Le faisceau de proton qui traverse cette énergie est particulièrement sensible aux forces de sillage à cause du mouvement synchrotronique qui devient très lent. Cette instabilité peut provoquer des gonflements d'emittance verticale et de grandes pertes de faisceaux qui se produisent en moins d'une periode synchrotronique. Des observations expérimentales montrent que les particules situées au pic de densité oscillent dans le plan vertical à cause d'un champs électrique de sillage à courte portée et selon une oscillation à 700 MHz. Un faisceau contenant un seul paquet a été reglé pour effectuer les mesures avec un plateau avec zero chromaticité. Des mesures approfondies ont été faites de la dynamique de l'instabilité afin de calculer les temps de montée et les intensités seuil. Ces mesures ont été effectuées pour plusieurs intensités pic et les résultats montrent que plus la longueur du paquet est longue, plus haute sera l'intensité seuil. D'autres mesures ont été effectuées avec une petite et négative chromaticité et cet autre point de fonctionnement montre que l'intensité seuil peut être montée à des valeurs plus grandes - dans ce cas l'intensité seuil a été montée de 20%. La particularité de ce travail est que l'instabilité est declanchée pendant l'accélération. À l'énergie de transition, l'échange des particules entre la tête et la queue du faisceau disparait pour plusieurs tours. Donc les mesures de seuil de η sont fondamentales pour connaitre le regime longitudinale dans lequel l'instabilité se developpe, ici dans la region non adiabatique. Des simulations *HEADTAIL* ont été effectuées afin de reproduire la dynamique l'instabilité avec l'impédance de la machine. Dans le cas du PS, il n'existe pas de modèle complet d'impédance donc un simple modèle resonateur large bande a été consideré. Les paramètres du code ont été adaptés afin de simuler les conditions sous lesquels le faisceau a été mesuré, aussi proche que possible. Les simulations montrent que l'onde se déplaçant sur le paquet est bien reproduite. Les temps de montée ont été extrait pour plusieurs intensités de faisceau et comparées aux mesures. Un bon accord est trouvé avec ce simple modèle d'impédance. Les intensités seuil peuvent être reproduite à 30% près. Certains mecanismes de d'amortissement

dans les mesures ne sont pas dans le code. En particulier, les composantes octupolaires de champs, les couplages non-linéaires et la charge d'espace transverse ne sont pas pris en compte dans les simulations. Ces limitations pourraient causer certaines divergences entre le modèle et les mesures. Cette étude permet d'établir un modèle d'impédance large bande qui peut être predictif. Quelques mesures ont été faites aussi avec un saut en gamma transition pour lesquelles les intensités seuil sont plus grands. Le developpement l'instabilité suit la variation du pic de densité et on peut appliquer le formalisme des faisceaux "coasting". Les simulations et les mesures montrent que le gamma jump est de loin le moyen le plus efficace pour augmenter de façon significative les seuils en intensité. Un choix adequate d'un point de fonctionnement semble aussi un moyen de supprimer l'instabilité.
La dernière partie de la thèse est dediée aux pertes de faisceau de proton à l'énergie d'injection. L'augmentation de l'intensité du faisceau CNGS est limitée par ces pertes. À l'aide moniteurs de perte actuellement installés dans le PS, il a été mesuré que les pertes proviennent lors l'entrée du faisceau dans la machine et pendant plusieurs centaines de tours après. Des mesures d'optique ont été effectués afin de vérifier le mismatch entre la ligne de transfert du Booster au PS. Un mismatch en dispersion horizontale a été mesurée ainsi qu'une difference en optique entre les quatres lignes d'injection du PS. Des restrictions d'ouverture ont été trouvées au septum dans les deux plans et au maximum et au minimum de la perturbation de la trajectoire. À l'aide de simulations Monte Carlo, la haute radiation en dehors de l'anneau induites par les pertes ont été comprises. Des explications possibles concernant les pertes tour par tour pourraient être attribué à la charge d'espace qui pourraient faire traverser des resonances aux particules. Oscillant à haute amplitude, elles sont perdues pendant la perturbation de trajectoire. Plusieurs solutions ont été proposées afin d'ameliorer la situation. Une nouvelle optique de la ligne de transfert et de l'injection pourraient réduire la taille du faisceau. Des quadripoles installés dans l'anneau pourraient être utilisés pour adopter l'optique d'injection au faisceau entrant. Augmenter l'energie d'injection de 1.4GeV à 2GeV permetrait un gain de 65% de charge d'espace et des études sont actuellement en cours pour le projet PS-Upgrade. Les faisceaux hautes intensités sont perturbés par la charge d'espace et par des instabilités transverses. Des mesures de déviation du nombre d'onde ont été effectuées en variant l'intensité aux énergies d'injection et d'extraction, ceci afin d'évaluer la partie imaginaire de l'impédance transverse et la contribution de la charge d'espace.
mots-clés : accélérateur, faisceau haute intensité, impédance, énergie de transition, injection, champs de sillage, instabilité transverse rapide, gamma jump, dynamique faisceau, Pole Face Windings, point de fonctionnement, chromaticité, beam breakup, charge d'espace, mismatch, PS upgrade

Contents

List of Figures

List of Tables

Introduction

When the design of the CERN PS was proposed early in the 50's, none imagined at that time that the first Proton Synchrotron would run 53 years after its commissioning in 1959. Today, the PS is the most versatile machine of the CERN accelerator complex. During its long life, the PS accelerated different kind of particles. Even if only protons and ions are currently in operation, the beam characteristic provided by the PS to the users and to LHC are various in terms of beam current, bunch length and transverse emittance. The beam intensity delivered by the PS has continuously increased over the years and future CERN projects are planning to increase the number of protons per bunch. Limitations are already visible on high intensity beams in normal operation, however substantial efforts are currently ongoing to push forward the performances of the accelerator.

In the case of the PS, aperture restrictions along the ring are often the consequence of large transverse beam size. The halo of the beam hits the vacuum chamber and the particles are lost in the accelerator. It can induce some important problems such as irradiation and premature damage of equipments.

During the design of an accelerator, the first step is to study the dynamics of a single particle, i.e. the interactions between particles with the environment are neglected. These types of interaction are called Collective effects. However, while the beam intensity is increasing, these effects become more important and undesirable consequences on the beam can be observed such as emittance blow up, losses and instabilities. When the beam current is increased, the electromagnetic fields generated by itself, in particular those generated by its direct interaction with its surroundings, will perturb the external guiding field. When the perturbation is strong enough, the beam becomes unstable. The fields act back on the particles and they are called wake fields. Collective effects can limit the performances of an accelerator and the next step is to study these possible effects on the beam operation or on an intensity increase and find adapted cures.

In the CERN PS, the beam has to cross a range in energy in which the beam can be easily perturbed by such forces. This is called the transition energy and the PS was the first machine to go through successfully to this energy range. The work of this thesis is first dedicated to the study of a fast instability developing in the vertical plane at transition energy. After having presented briefly the PS and its particularities, Chapter 4 is presented the studies

carried out for this instability mainly visible on high intensity single bunch beams. Extensive measurements were performed to understand the mechanism of the fast vertical instability under different optics and beam conditions. This instability occurs due to the interaction of the beam with the impedance of the machine and at transition, the slowing down synchrotron motion makes wake fields easily excite particle oscillations along the bunch. The first goal of this study is to measure intensity thresholds and growth rate of the instability for different beam parameters such longitudinal emittance and chromaticity in order to identify possible cures. This studies aims also to compare measurements to a theoretical model based on macro-particle simulations with the HEADTAIL code: it computes the beam interaction with an impedance. This allows to deduce an effective impedance model from a simple broadband resonator which are able to predict intensity thresholds without chromaticity within a factor 2.

In Chapter 4.10, measurements were performed with a special optics, the gamma transition jump, used since the 70's in the PS in order to increase the speed of the transition crossing and to cure longitudinal instabilities. The use of such optics scheme naturally increases the intensity thresholds of the instability and in addition the measurements shows that an adequate working point such a chromaticity-jump is proposed as possible additional cure. Finally, the study shows that this instability is rather close to the coasting beam formalism and to the Beam Breakup in the Linacs.

Chapter 5 is dedicated to the understanding of high beam losses at injection energy, which provoke irradiation of the equipments. It corresponds to 3-4% of the beam. Measurements with beam loss monitors were performed as well as matching measurements in order to understand the cause of the losses. Aperture restrictions were identified at the injection septum and in the ring. Propositions were done to reduce these losses and they are part now of the PS Upgrade for the High Luminosity LHC Injector Upgrade. This project consists of identifying the limitations in the different injectors in the chain and adapting them for the future High Luminosity LHC beam. For the PS, the injection energy will be increased from 1.4 GeV to 2 GeV.

This thesis shows that the studies of collective effects in the PS are important and have to be carried out since the intensity will continue to increase. The operation of the machine shows already that it is working beyond its limit, therefore the studies are important to continue the PS operation for the next 25 years. In particular, this thesis pointed out that a complete impedance model is needed and this is the reason why efforts were carried out during this phD work to establish a rough model of impedance from beam based measurements. With an accurate model of impedance, the results of the fast instability measurements presented in this thesis could be used as a support to validate this model, which would help to identify future limitations and push them forward.

1 Basic concepts of Beam Dynamics

1.1 Transverse beam dynamics

The guiding and the focusing of charged particles in a circular accelerator is performed by a repetitive pattern of magnetic elements separated by straight sections: they constitute the lattice of the accelerator. The basic structure is composed by dipoles which curve the particles trajectory and by quadrupoles focusing the beam. They form the linear elements of the lattice. This chapter introduces the basic concepts of transverse dynamics of charged particles in the machine. Many comprehensive texts on accelerator physics exist. Sands [14] gives an introduction to the subject, although focused on electron storage rings, and Martini [1] gives a detailed account of transverse dynamics. Textbooks covering everything from introductory matters to advanced topics include the books by Wiedemann [2] and Lee [15].

Many types of devices constructed for particle acceleration exist but in this thesis I am concerned only with synchrotrons and give here an overview of their mode of operation. A summary of other types of accelerators can be found in Ref. [2].

1.1.1 Coordinate system

A synchrotron is a circular accelerator where charged particles are travelling on a fixed orbit. Magnetic fields are used to keep them on the wanted trajectory and, at every machine revolution, they go though an accelerating longitudinal electric field provided by radio frequency (RF) cavities. As the particles gain energy, the magnetic fields are adjusted synchronously so that the orbit remains unchanged. The maximum achievable energy in a synchrotron is limited by the capacity of the bending fields and the radius of curvature of the ring and, in the case of particles with large energy losses from radiation, by the power of the RF system.

Synchrotrons include normally some straight sections. The accelerating elements and beam diagnostics devices are usually placed in a straight section, as well as injection and extraction systems. The physics of the particle beam motion in an accelerator is treated in the following

sections.

The transverse motion of charged particles though a beam transport or in a circular accelerator is governed by the Lorentz force equation

$$\vec{F} = q(\vec{E} + \vec{v} \times \vec{B}) \tag{1.1}$$

with q the charge of the particle, $\vec{E}$ the electric field in general coming from the radio frequency cavities, $\vec{B}$ the magnetic field and $\vec{v}$ the velocity of the particles $|\vec{v}| = \beta c$ where β is the relativistic parameter and c the speed of light. The Lorentz force is applied as bending force in the magnets to guide the particle on a design orbit which ideally all the particle should follow. Fig. 1.1 shows a particle travelling on the ideal orbit, called also design orbit. In order to describe the motion of the particles, a coordinate system is needed. Instead of choosing a fixed Cartesian reference system, a right-hand orthogonal system $(\vec{u}_x, \vec{u}_y, \vec{u}_s)$ is used to describe the motion of a particle following the ideal orbit. Therefore the s-coordinate measures the travelled distance along the design path and the coordinates (x, y) show the transverse deviation of a real particle from the design path at a certain s. Hence the individual particle trajectory is from Fig 1.1

$$\vec{r}(x, y, s) = r_0(s) + x\vec{u}_x(s) + y\vec{u}_y(s) \tag{1.2}$$

r_0 is the design orbit radius,s is used as independent variable instead of time to express the Lorentz force [1],

$$\frac{d}{dt} = \frac{ds}{dt}\frac{d}{ds} = v\frac{d}{ds} \tag{1.3}$$

and,

$$\frac{df}{dt} = v\frac{df}{ds} \tag{1.4}$$

And in a similar way for the second s-derivative of f

$$\frac{d^2f}{dt^2} = v^2\frac{d^2f}{ds^2} + v\frac{df}{ds}\frac{dv}{ds} \tag{1.5}$$

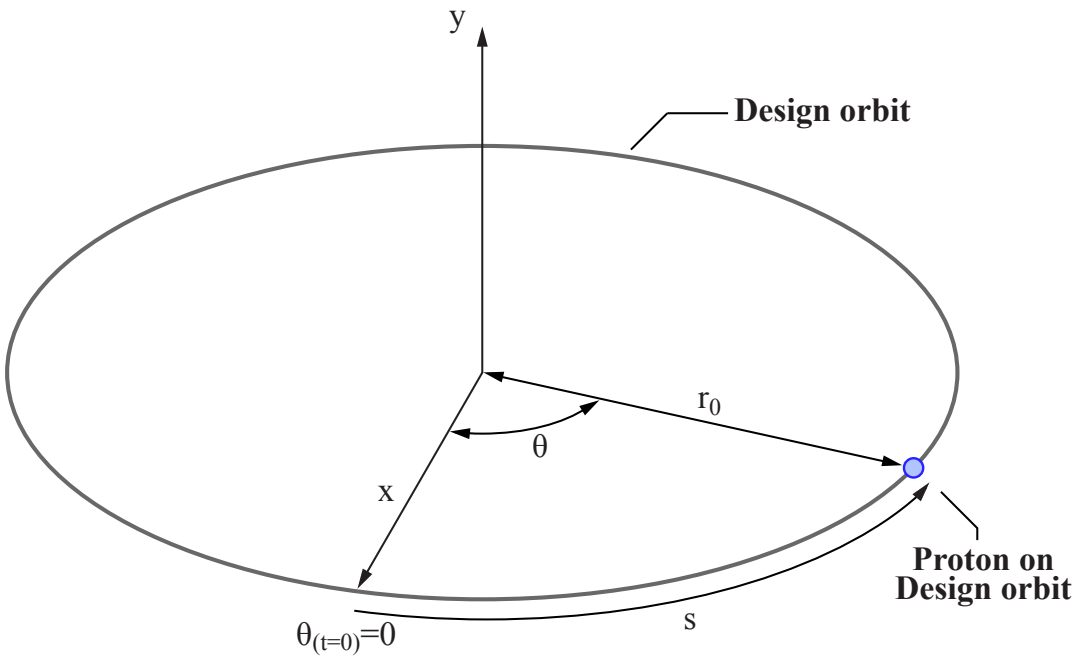

(a)

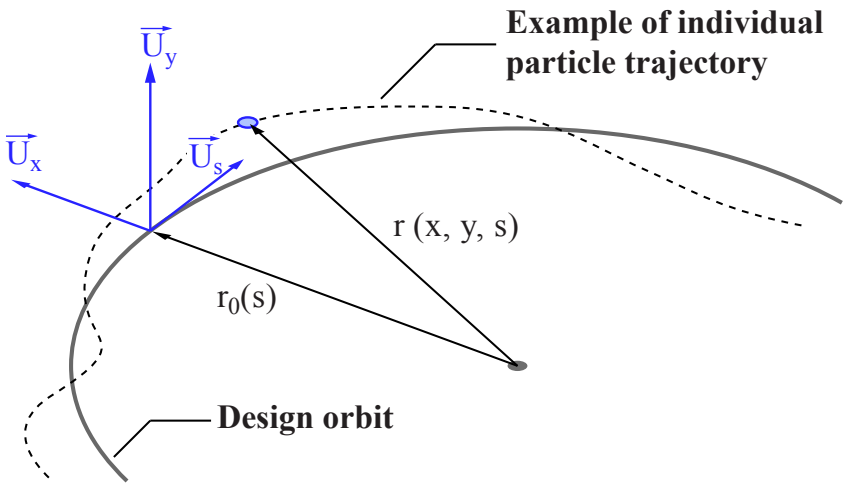

(b)

Figure 1.1: Coordinate system.

1.1.2 Equation of motion

One can derive with respect to the s-variable the individual particle trajectory $\vec{r}(x,y,s)$ of Eq. 1.2 from 1.3 and 1.4 using the Frenet-Serret theorem for the differentiation with respect to s of the vectors $(\vec{u}_x, \vec{u}_y, \vec{u}_s)$ [16]

$$\frac{d\vec{u}_x}{ds} = k_x\vec{u}_s \qquad \frac{d\vec{u}_y}{ds} = k_y\vec{u}_s \qquad \frac{d\vec{u}_s}{ds} = -k_x\vec{u}_x - k_y\vec{u}_y \tag{1.6}$$

Then, setting $h = 1 + k_x x + k_y y$, with k_x, k_y are the curvatures in the x-direction and the y-direction,

$$\begin{aligned} r'(x,y,s) &= h\vec{u}_s + x'\vec{u}_x + y'\vec{u}_y & (1.7)\\ r''(x,y,s) &= (k_x'x + k_y'y + 2k_x x' + 2k_x y')\vec{s} + \left[x'' - k_x(1+k_x x)\right]\vec{u}_x & (1.8)\\ &\quad + \left[y'' - k_y(1+k_y y)\right]\vec{u}_y \end{aligned}$$

Using the classic Newton theorem of the momentum change due to the Lorentz force and assuming that γ, v are constant, i.e. no particle acceleration, so no electric field (we are interested of the motion in the different magnets of the lattice)

$$\vec{F} = m\gamma\frac{d^2\vec{r}}{dt^2} = q(\vec{v}\times\vec{B}) = qv(\vec{r'}\times\vec{B}) \tag{1.9}$$

The Lorentz force and the magnetic field can also be expressed in the (x,y,s) reference system as follow

$$B(x,y,s) = B_s(x,y,s)\vec{u}_s + B_x(x,y,s)\vec{u}_x + B_y(x,y,s)\vec{u}_y \tag{1.10}$$

We suppose there is no solenoid magnetic field, so $B_s = 0$. Using the expressions of r' of Eq. 1.9, the term $r'\times\vec{B}$ can be developed as done in Ref. [1]. The motion in (x,y) planes of a particle travelling around the reference orbit (i.e. for $x=0, y=0$) and in the vicinity of the ideal momentum, can be expanded, with the particle momentum expression yielding to

$$\frac{1}{p} = \frac{1}{(1+\delta)p_0} \quad \text{with} \quad \delta = \frac{p-p_0}{p_0} = \frac{\Delta p}{p_0} \tag{1.11}$$

Then the equation of motion is linearized keeping the terms in (x,y) and (x',y') yielding to

$$\begin{aligned} x'' &= k_x h - (1-\delta)h^2\frac{e}{p_0}B_y(x,y,s)\\ y'' &= k_y h - (1-\delta)h^2\frac{e}{p_0}B_x(x,y,s) \end{aligned} \tag{1.12}$$

For small deviations from the design orbit in (x,y), the magnetic field components can expanded in series to the first order keeping only the dipolar and the quadrupolar fields, which

provide focusing. Using the Maxwell equations $\vec{\nabla} \times \vec{B} = 0$ and $\vec{\nabla} \cdot \vec{B} = 0$, one finds

$$\frac{\partial B_x}{\partial x} = \frac{\partial B_y}{\partial y} \qquad \text{and} \qquad \frac{\partial B_y}{\partial x} = \frac{\partial B_x}{\partial y} \tag{1.13}$$

the normalized gradient k_0 is then introduced as well as the skew gradient $\underline{k_0}$

$$k_0 = \frac{e}{p_0}\left(\frac{\partial B_y}{\partial x}\right)_{x=y=0} \quad \text{and} \quad \underline{k_0} = \frac{e}{p_0}\left(\frac{\partial B_x}{\partial x}\right)_{x=y=0} \tag{1.14}$$

However, we are not interested by magnetic fields which introduce coupling between the (x, y)-planes therefore $\underline{k_0} = 0$. We supposed that the deflections of the particles occur in the horizontal plane only as it is the case in general in a synchrotron (no vertical dipole) and the equations of motion, namely the Hill equation, read [1, 17]

$$\begin{aligned} &x''(s) + \left(k_0(s) + \frac{1}{\rho_0^2(s)}\right) x(s) = \frac{\delta}{\rho_0(s)} \\ &y''(s) - k_0(s)\, y(s) = 0 \end{aligned} \tag{1.15}$$

with ρ_0 the bending radius, $\rho_0 = \rho_x = 1/k_x(s)$ since the ideal orbit lies in the $(x - s)$ plane. Within a magnetic element, k_0 and ρ_0 are constant and the solution of Eq. 1.15 gives either a harmonic oscillation or an exponential function depending on the sign of k_0. We note that there has to be different types of solutions in the horizontal and the vertical planes.

The general solution for x can be expressed by means of two linearly independent solutions $C_x(s), S_x(s)$ to the homogeneous problem, which are determined by the initial conditions $C_x(0) = 1, C_x'(0) = 0$ and $S_x(0) = 0, S_x'(0) = 1$, and a particular solution $\delta d_x(s)$ with $d_x(0) = d_x'(0) = 0$. These functions are (with $K = K_0 + 1/\rho_0^2$):

$$\begin{aligned} C_x(s) &= \frac{1}{2}\left(e^{i\sqrt{K}s} + e^{-i\sqrt{K}s}\right) \\ S_x(s) &= \frac{1}{2i\sqrt{K}}\left(e^{i\sqrt{K}s} - e^{-i\sqrt{K}s}\right) \\ d_x(s) &= \frac{1}{\rho_0 K}\left[1 - C_x(s)\right] \end{aligned} \tag{1.16}$$

A solution with arbitrary initial conditions can then be expressed as a linear superposition of C_x, S_x, d_x in form of a transfer matrix, propagating the initial conditions along s:

$$\begin{bmatrix} x(s) \\ x'(s) \\ \delta \end{bmatrix} = \begin{bmatrix} C_x(s) & S_x(s) & d_x(s) \\ C_x'(s) & S_x'(s) & d_x'(s) \\ 0 & 0 & 1 \end{bmatrix} \begin{bmatrix} x(0) \\ x'(0) \\ \delta \end{bmatrix} \tag{1.17}$$

Here d_x gives the δ-dependence of the trajectory and is called dispersion. In this thesis I discuss only circular accelerators and, if Eq. (1.15) is solved in every element of the lattice, the coordinates of a particle can be propagated around the ring by means of matrix multiplications. An analogous solution exists for y.

A common simplification to Eq. (1.17) is done by assuming short magnets with high strengths. Writing the length of a given magnet as l, this assumption gives $|\sqrt{K}l| \ll 1$ and $l \to 0$ while Kl remains constant if end-field of the magnets effects are neglected. The transfer matrix can then be expanded in a power series. Keeping only first order terms in $\sqrt{K}l$, the matrix becomes particularly simple. As an example, the transformation of a quadrupole becomes

$$\begin{bmatrix} x(s) \\ x'(s) \\ \delta \end{bmatrix} = \begin{bmatrix} 1 & 0 & 0 \\ -K_0 l & 1 & 0 \\ 0 & 0 & 1 \end{bmatrix} \begin{bmatrix} x(0) \\ x'(0) \\ \delta \end{bmatrix}. \tag{1.18}$$

This is called the thin-lens approximation because of its similarity with the transformation of an optical lens with focal length $f = K_0 l$.

Equation. (1.15) can also be solved globally in the whole accelerator. Then $K_0(s), \rho_0(s)$ are piecewise constant functions with the same periodicity as the lattice. The general solution can be written as [1]

$$x(s) = \sqrt{2J_x \beta_x(s)} \cos[\mu_x(s) - \phi_x] + \delta D_x(s). \tag{1.19}$$

The betatron function $\beta_x(s)$ is periodic and positive and its square shows the variation of the beam envelope along s, while J_x is an integration constant representing the oscillation amplitude of a single particle.

Furthermore, $\mu_x(s) = \int_0^s \beta_x^{-1}(\varsigma) d\varsigma$ is called the betatron phase and $D_x(s)$ is a particular solution to Hill's equation but with periodic boundary conditions. I call $D_x(s)$ the periodic dispersion and $d_x(s)$ the locally generated dispersion, that is, the dispersion generated in a certain part of the ring.

From Eq. (1.19), it can be seen that the particles perform pseudo-harmonic oscillations, called betatron oscillations. Their amplitude is modulated along s by $\sqrt{\beta_x}$ and the phase varies with $\mu_x(s)$. For off-energy particles, the oscillation takes place around a different closed orbit, given by $D_x \delta$.

The fundamental solutions of the Hill equation can also be expressed in terms of β_x:

$$\begin{aligned} C_x(s) &= \sqrt{\frac{\beta_x(s)}{\beta_x(0)}} \left(\cos[\mu_x(s) - \mu_x(0)] - \alpha_x(0) \sin[\mu_x(s) - \mu_x(0)] \right) \\ S_x(s) &= \sqrt{\beta_x(s)\beta_x(0)} \sin[\mu_x(s) - \mu_x(0)] \end{aligned} \tag{1.20}$$

Here I have introduced $\alpha_x(s) = -\beta_x'(s)/2$ and I will refer to $(\beta_x, \alpha_x, \gamma_x, D_x)$, where $\gamma_x = (1 + \alpha_x^2)/\beta_x$, as the optical functions of an accelerator. $(\beta_x, \alpha_x, \gamma_x)$ are called Twiss parameters. By inserting Eq. (1.20) in Eq. (1.17) one can construct the transfer matrix for an arbitrary distance in the ring or for a complete revolution. Transfer matrices for the optical functions themselves can also be constructed from the fundamental solutions.

All information about the linear focusing of a lattice can be obtained from β_x. A differential equation in β_x can be obtained by inserting Eq. (1.19) in Eq. (1.15):

$$\frac{1}{2}\beta_x\beta_x'' - \frac{1}{4}{\beta_x'}^2 + K(s)\beta_x^2 = 1 \tag{1.21}$$

However, Eq. (1.21) is analytically solvable only in special cases.

Analogous definitions exist for the vertical plane. However, since dispersion is generated by dipoles [see Eq. (1.16)], which in flat accelerators bend only in the $(x-s)$ plane, the vertical dispersion typically vanishes in rings.

1.1.3 Beam Emittance

Starting from the solution of Hill equation and its derivative, an invariant can be defined [1]:

$$\begin{aligned} x(s) &= a\sqrt{\beta(s)}\cos(\mu(s)+b) \\ x'(s) &= \frac{1}{2}a\frac{\beta'}{\sqrt{\beta}}\cos(\mu+b) - a\mu'\sqrt{\beta}\sin(\mu+b) \end{aligned}$$

The (a,b) coefficients are determined with $\alpha = -\frac{1}{2}\frac{d\beta}{ds} = -\frac{1}{2}\beta'$ and $\mu' = \frac{1}{\beta}$ and the phase is eliminated by writing

$$\begin{aligned} a\cos(\mu+b) &= \frac{x}{\beta} \\ a\sin(\mu+b) &= -(x'\sqrt{\beta} + \alpha\frac{x}{\sqrt{\beta}}) \end{aligned}$$

Squaring and summing the above equations and using $\gamma(s) = \frac{1+\alpha^2(s)}{\beta(s)}$,

$$a^2 = \gamma x^2 + 2\alpha x x' + \beta x'^2 = constant = \epsilon \tag{1.22}$$

This is the equation of an ellipse and its surface is a constant of motion $\forall x, x'$ with the area πa^2 as illustrated in Fig. 1.2. This is defined as the Courant-Snyder invariant and the parameter ϵ is called the physical beam emittance. Without non-linear fields, the particles describe an invariant ellipse with parameters $a \leq \epsilon$ determined by the optical properties of the lattice. The physical beam emittance is conserved in the absence of acceleration, radiation or collective

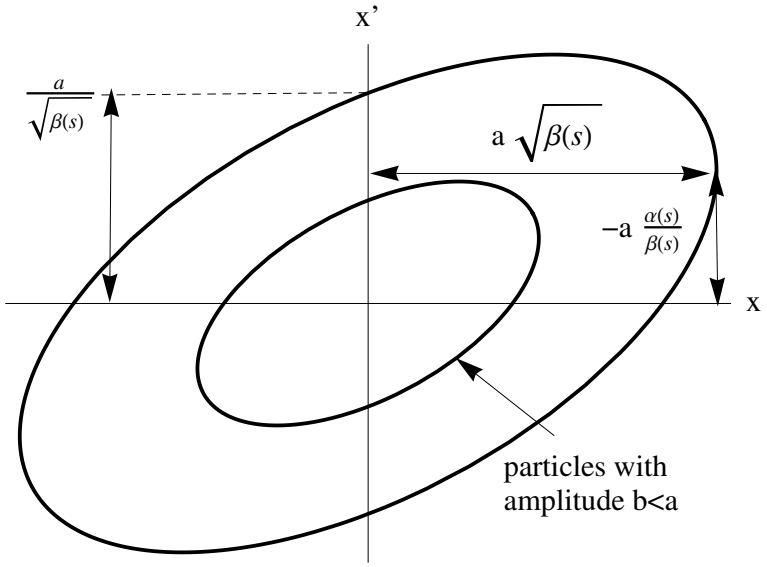

Figure 1.2: Phase plane $(x(s), x'(s))$ ellipses for particles with different amplitudes.

effects. A normalized beam emittance can be defined which does not depend on the energy

$$\epsilon^* = \epsilon(\beta\gamma) \tag{1.23}$$

with β, γ the Lorentz parameters, ϵ the physical emittance and ϵ^* the normalized emittance which remains constant with the energy, while the physical emittance is shrinking during the acceleration [1].

The Twiss parameters $\alpha(s), \beta(s), \gamma(s)$ determine the shape and the orientation of the ellipse at an azimuthal location s along the lattice. As a particle trajectory evolves along the ring, the ellipse continuously changes its form but not its area. Every time the trajectory covers one cell of length L along s, the ellipse is the same, since the Twiss parameters are periodic with period L. Consequently, on every machine revolution the particle coordinates (x, x') will appear on the same ellipse [1]

$$x(s+kC) = a\sqrt{\beta(s)}\left(\cos[\mu(s)+b]\cos 2\pi kQ - \sin[\mu(s)+b]\sin 2\pi kQ\right)$$

since $\mu(s+kC) - \mu(s) = 2\pi kQ$. Thus the particle will appear cyclically at certain points on the ellipse. If Q, called tune, is a irrational number, the particle trajectory will cover the ellipse whereas it will appear at only n points on the ellipse if the tune is a rational number.

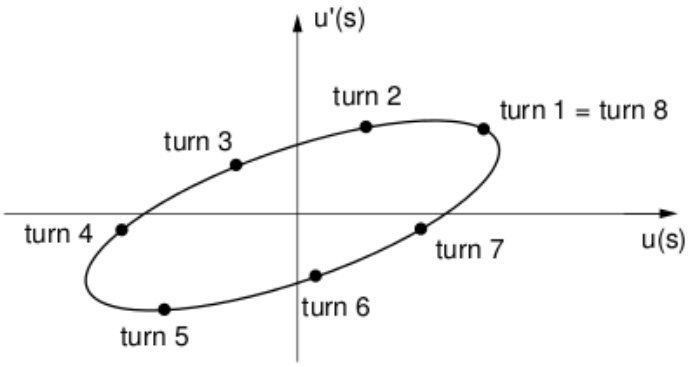

Figure 1.3: Phase plane motion for one particle after many turns [1].

1.1.4 Number of betatron oscillations Q

The number of betatron oscillations $Q_{x,y}$ per machine turn is called tune and depends mainly on the quadrupoles. It is given by

$$Q_{x,y} = \frac{1}{2\pi} \oint \frac{ds}{\beta_{x,y(s)}}. \tag{1.24}$$

Normally accelerators are operated so that Q_x and Q_y are far from certain values called resonances, mainly due to magnetic errors [1]. The simplest of them can be understood by considering the x-position of a particles at some fixed value s_0 over several consecutive turns. Since $\beta_x(s)$ is periodic, it is clear that the amplitude in Eq. 1.19 is constant $\sqrt{2J_x\beta_x(s_0)}$. The only variable changing is the phase μ_x, which increases by $2\pi Q_x$ on every turn. Therefore, the motion in x at s_0 is indistinguishable from a sampled harmonic oscillation. If Q_x is an integer, the motion in Eq. (1.19) would be periodic and $x(s_0)$ would have the same value on every revolution. In that case, any imperfections in the magnetic field around the ring act as perturbations, which are synchronous with the oscillation frequency. This will excite resonances, causing an increasing amplitude and unstable motion.

Therefore, integer values of Q_x have to be avoided. As it turns out [2] other resonances are excited by higher order multipole errors if the horizontal and vertical tunes satisfy

$$kQ_x + lQ_y = m, \tag{1.25}$$

where (k,l,m) are integers. Each resonance is connected with a certain order of a magnetic multipole. Normally the resonances at small values of (k,l,m) are the strongest and most destructive ones. Eq. 1.25 describes a set of lines in the $Q_x - Q_y$ plane, which should be avoided and the tunes are normally chosen far from the lowest order resonances. This position in the plane is called working point.

The Hill equation (1.15) takes only linear magnetic fields into account, which are normally

the dominating ones. However, higher-order multipoles are present in all real accelerators. Examples of sources of such non-linearities include imperfections in the magnet construction, effects at the ends of magnets or from non-linear elements put in the ring on purpose, in particular sextupole magnets. They are deployed for chromaticity correction. The spread in δ among the particles within the beam causes each particle to be focused differently in the quadrupoles and therefore to have different values of Q_x. The ratio $\Delta Q_x/\delta$ is called chromaticity [2]. This is a second-order effect and therefore not present in Eq. (1.15). To properly account for non-linearities, one needs to include higher order terms in Eq. (1.15). If small, they can be treated as perturbations. A mathematical treatment of this can be found in literature [2, 15].

1.1.5 Chromaticity

The focal property of lattice elements depend upon the momentum deviation, since the equations of motion of an off-momentum particle are [1]

$$\begin{aligned} x'' + k_0(1-\delta)x &= 0 \\ y'' - k_0(1-\delta)y &= 0 \end{aligned}$$

where δ is the relative momentum deviation from the design momentum p_0. This momentum dependence of the focalisation causing tune changes, is called chromatic effect. The tune variation with the momentum is called chromaticity and is defined as

$$Q' = \frac{\Delta Q}{\Delta p/p_0} \tag{1.26}$$

the relative chromaticity is defined as

$$\xi = \frac{\Delta Q/Q}{\Delta p/p_0} \tag{1.27}$$

Particles with different momenta are spread where there is dispersion. Higher momentum particles are focused less than particles with the design momentum p_0, lower momentum particles are focused more as shown in Fig. 1.4. Indeed if $f(\delta)$ and $K(\delta)$ are the focal length and the normalized gradient, at momentum $p = p_0(1+\delta)$, of a quadrupole of length l, with

$$K(\delta) = \frac{e}{p}\frac{\partial B_y}{\partial x} \qquad \frac{1}{f(\delta)} = \frac{K_0 l}{1+\delta}$$

Therefore, once the particles are spread by momentum in a region with dispersion, we can apply focusing corrections depending on the momentum using a sextupole magnet: they focuse higher-momentum particles and defocus lower-momentum particles. Hence, it can be used to correct the chromatic focusing errors in a region with non-zero dispersion. The contribution to chromaticity arising from pure quadrupole elements (also pure dipoles) is

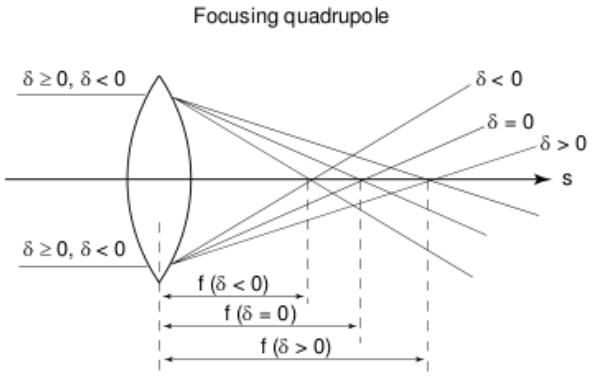

Figure 1.4: Schematic representation of chromatic effect a quadrupole in a dispersion-free region. [1].

called the natural chromaticity. Thus, the natural chromaticity of a lattice is given by [1]

$$\begin{aligned} \xi_{x0} &= -\frac{1}{4\pi Q_x}\int_s^{s+C}\beta_x(s)K_0(t)dt \\ \xi_{y0} &= -\frac{1}{4\pi Q_y}\int_s^{s+C}\beta_y(s)K_0(t)dt \end{aligned} \tag{1.28}$$

The control of the chromaticity is important in order to avoid shifting the beam into resonance due magnetic imperfections. Particles with different momenta have a different tune with respect to the on-momentum particle. It is important to control chromaticities to prevent the beam from transverse instabilities [10].

1.2 Longitudinal beam dynamics

In the previous section, we concentrated the discussion on the interaction of charged particles with magnetic fields for their guiding through the system of beam transport. These fields act on the transverse motion of the particles but do not change to their energy. For the acceleration of the beam, electric forces are generated in the s-direction. Such fields are called longitudinal or accelerating fields and they make the charged particles gain or lose energy. They also provide a focusing in energy to keep the particles in a same bunch. In this section, we describe the longitudinal dynamics in a synchrotron and its stability limits. Again, many textbooks and courses are focused on this subject [2, 18].

1.2.1 Energy gain per turn

The application of radio frequency fields is frequently used for the acceleration and energy focusing of charged particles in a synchrotron. Both, fields and particle motion are synchronized in such a way to allow the acceleration of the beam by the generation of a longitudinal electric field $E(s,t)$ in the s-direction with the form

$$E(s,t) = E_0(s)e^{i\omega t+\phi} \tag{1.29}$$

with ω the angular frequency of the electric field, E_0 is its amplitude and ϕ the phase at the moment the particle enters in the accelerating section. Therefore a proton going through a RF structure feels an oscillating longitudinal electric field that can be written as

$$E_s(t) = \frac{V}{g}\sin(\phi_{rf}(t)+\phi) \tag{1.30}$$

with V the voltage amplitude of the cavity assumed to constant along the gap g, $\phi_{rf}(t)$ the phase of the RF cavity voltage and $\phi_{rf}(t) = \omega_{rf}t$ with $\omega_{rf}t$ the angular frequency of the RF voltage. The particle gain energy and the RF phase ϕ_{rf} is tuned in a such a way to give a positive kick to the particle each turn and therefore ϕ_{rf} is synchronized with the revolution frequency. For systematic acceleration, the phase of the RF fields in each of the accelerating sections must reach specific values in voltage at the moment the particles arrive. If the phase of the field of N accelerating sections is adjusted to be the same at the time of arrival of the beam, the total acceleration is N times the acceleration in each individual section. In a similar way as the ideal particle travelling on the design orbit in the transverse dynamics, it exists also in longitudinal dynamics a reference particle called the synchronous particle going through the RF cavity with the same phase ϕ with respect to the RF phase every turn. This phase is called the synchronous phase and the angular RF frequency has to be adjusted as a integer multiple of the revolution frequency

$$\omega_{rf} = \omega_0 h \tag{1.31}$$

with h the harmonic number indicating also the maximum number of bunches the machine can accept in a given longitudinal configuration. In a synchrotron such as the PS, the beam is divided in bunches. As example, we cite the nominal LHC beam in the CERN PS which $h = 7$ at injection meaning the accelerator can contain up to 7 bunches.

The RF cavities normally use a sinusoidal voltage $V(t)$ with an angular frequency $\omega_{RF} = h\omega_0$ allowing to accelerate by ΔE a particle every turn or compensate the energy loss per turn. While the particle is passing in a RF gap g, the amplitude of the accelerating field is changing according to

$$E = E_{RF}\sin(\omega_{rf}t + \phi(t)) \tag{1.32}$$

The effective electric field seen by the particle over the RF gap assuming that the velocity increase per turn is small compared to the longitudinal particle velocity.

$$\overline{E} = \frac{E_{RF}}{T}\int_{T/2}^{T/2}\sin(\omega_{rf} + \phi)dt = E_{RF}\mathbf{T}\sin\phi \tag{1.33}$$

with T the time needed for the particle to pass the gap,**T** the transit time

$$\mathbf{T} = \frac{\sin\left(\frac{h\omega_0}{2\beta c}\right)}{\frac{h\omega_0}{2\beta c}} \tag{1.34}$$

Finally, the energy gain per turn for the synchronous particle, a particle arriving in the middle of the RF cavity gap at the time $t = 0$

$$\Delta E = e\overline{V}\sin\phi \tag{1.35}$$

with $\overline{V}$ is the effective voltage. In the absence of other sources of energy change, the energy rate dE/dt is related to the energy gained per turn

$$\frac{dE}{dt} = \frac{\omega_0}{2\pi}e\overline{V}\sin\phi \tag{1.36}$$

In the case of non-relativistic machines, the revolution frequency is changing according to $1/f = \beta c/C_0$ where C_0 is the design path length. In order to maintain the RF resonance condition, the frequency of the RF cavities must be also changed.

1.2.2 Dispersion Effects due to Guide Fields

From the previous, one can write the total change in δ of a particle during one turn as the difference between gain and loss, so

$$\dot{\delta} \approx \frac{eV(\tau) - U_{\text{loss}}(\delta)}{TE_0}, \tag{1.37}$$

where dots designate time derivatives, T is the revolution time, U_{loss} is the energy loss during one revolution and τ is the arrival time with respect to the ideal particle at the cavity. It is defined so that $\tau > 0$ for particles ahead. A bunch of charged particles has a spread in energy for many reasons as example Coulomb scattering which convert transverse momentum into longitudinal. In an accelerator or storage ring, particles with different energies have different closed orbits and their length are given by

$$C = C_0(1 + \alpha_c\delta + \mathcal{O}(\delta^2)) \tag{1.38}$$

as defined in the previous paragraph C_0 is the orbit length of a so called on-momentum particle. The coefficient α_c is the momentum compaction of the accelerator ring. The relation between an energy offset δ and the path length during one revolution is given by α_c

$$\alpha_c = (\Delta C/C_0)/\delta \tag{1.39}$$

with C_0 is the path length of the ideal particle. The momentum compaction α_c is the average of $D_x(s)/\rho_0(s)$ over the ring and is therefore an intrinsic property of the lattice. More details will be given in Sec. 1.3.1. The fraction of momentum spread is related to the fractional energy spread $\Delta E/E_0$ by

$$\delta = \frac{\Delta p}{p_0} \approx \frac{1}{\beta_0^2}\frac{\Delta E}{E_0} \tag{1.40}$$

The momentum compaction of most accelerators is positive ($\alpha_c > 0$). It implies that particles with larger energy will travel along longer closed orbit with more radial excursions. A longer closed orbit may imply relatively longer revolution period T. On the other hand, a higher energy particle travels with higher velocity and the period of revolution will be relatively shorter. The result is a slip in revolution time every turn and therefore in arrival time τ with respect to the synchronous particle such as $\Delta\tau = -\delta T$ since τ is defined as positive for particles arriving at the cavity before the ideal one. Since $T = C/\beta_{rel}c$, a slip factor is defined as

$$\frac{\Delta\tau}{T} = -\frac{\Delta T}{T} \approx \frac{\Delta C}{C_0} - \frac{\Delta\beta_{rel}}{\beta_{rel}} \tag{1.41}$$

Only the lowest order of the fractional momentum spread is kept

$$\dot{\tau} \approx -(\frac{1}{\gamma_{rel0}^2} - \alpha_c)\delta = \eta\delta \tag{1.42}$$

where γ_{rel0}^2 is the relativistic mass factor of the ideal particle and η is called the momentum compaction factor.

From Eq. (1.42) it is clear that two regimes are possible. Defining $\gamma_t = \sqrt{\alpha_c^{-1}}$, we see that if $\gamma_{rel0}^2 > \gamma_t$, a particle with higher momentum than the reference particle has a longer revolution time, while it is the opposite if $\gamma_{rel0}^2 < \gamma_t$. At $\gamma_{rel0}^2 = \gamma_t$ all particles have the same revolution

time, regardless of energy. The energy $mc^2\gamma_t$ is usually referred to as the transition energy. Section 1.3.1 will be entirely dedicated to the transition energy.

1.2.3 Longitudinal Equation of Motion

Many textbooks treat in detail the longitudinal dynamics of single particle in accelerator, in particular Ref. [18] [2]. In this paragraph, we will derive the longitudinal motion of a non synchronous particle with a momentum $p = p_0 + \Delta p$, a phase $\phi = \phi_0 + \Delta\phi$, an angular frequency $\omega = \omega_0 + \Delta\omega$, $E = E_0 + \Delta E$ for its energy and their deviations are assumed to be small. Let consider a particle lagging behind the synchronous particle P_s, the arrival time change in the RF cavity $\delta\tau$ with respect to P_s is obtained from $\Delta T/T = \eta\delta$

$$\delta\tau = -\eta T_0 \delta \tag{1.43}$$

The negative sign comes from the period of a higher-momentum particle is larger above transition ($\eta > 0$) and therefore its time of arrival slips. The deviation of the phase with respect to the synchronous one ϕ_s is written as $\Delta\phi = h\omega_0\delta\tau$ and the deviation in angular frequency $\Delta\omega$

$$\Delta\omega = -\frac{1}{h}\frac{d\phi}{dt} \tag{1.44}$$

then the deviation in momentum Δp is obtained using the definition of the momentum compaction factor η

$$\Delta p = -\frac{p_0}{\eta\omega_0}\Delta\omega = \frac{p_0}{\eta h\omega_0}\frac{d\phi}{dt} \tag{1.45}$$

and

$$\frac{d\Delta p}{dt} = \frac{dp}{dt} - \frac{dp_0}{dt} \simeq \frac{e\widehat{V}}{C_0}(\sin(\phi_s + \Delta\phi) - \sin\phi_s) \tag{1.46}$$

Using Eq. 1.45 and Eq. 1.46, a second order non-linear equation of the phase is obtained, which is the basic phase equation valid for all amplitude, assuming that the parameters are slowly changing, i.e. in adiabatic conditions,

$$\frac{d}{dt}\left(\frac{R_0 p_0}{\eta h\omega_0}\frac{d\phi}{dt}\right) - \frac{e\hat{V}}{2\pi}\left(\sin\phi - \sin\phi_s\right) = 0 \tag{1.47}$$

Small amplitude oscillations - Phase Stability

Let's consider the case where the parameters R_0, η, ω_0 and $\hat{V}$ are constant or at least change very slowly with time compared to the variable $\Delta\phi = \phi - \phi_s$. Eq. 1.47 is frequently approximated

for small deviation of the phase, hence one can write

$$\ddot{\phi} - \frac{e\hat{V}\eta\cos\phi_s h\omega_0}{2\pi R_0 p_0}\left(\sin\phi - \sin\phi_s\right) = 0 \tag{1.48}$$

then by using $\Delta\phi = \phi - \phi_s$ and by keeping only the first order, and assuming small amplitude oscillation and slow change of the phase, the equation of motion of the phase can be linearized

$$\frac{d^2\Delta\phi}{dt^2} - \frac{e\hat{V}\cos\phi_s\eta h\omega_0}{2\pi R_0 p_0}\Delta\phi = 0 \tag{1.49}$$

From Eq. 1.49, the longitudinal motion of a particle around the synchrotron particle is stable if $\eta\cos\phi_s < 0$ and we can define the synchrotron angular frequency ω_s and the synchrotron tune $Q_s = \omega_s/\omega_0$

$$\omega_s = \sqrt{\frac{e\hat{V}h\omega_0|\eta\cos\phi_s|}{2\pi R_0 p_0}} \tag{1.50}$$

$$Q_s = \sqrt{\frac{e\hat{V}h|\eta\cos\phi_s|}{2\pi\omega_0 R_0 p_0}} \tag{1.51}$$

Q_s is the number of synchrotron oscillations a particle makes in one revolution turn. The synchrotron motion is very slow and Q_s is usually of the order of 0.001 to 0.01. ω_s must be real in order to get a stable motion which means that $\eta\cos\phi_s$ has to be positive. Stable synchrotron phase motion needs the following conditions to be satisfied:

$$\gamma < \gamma_{tr} \quad \eta < 0 \quad 0 < \phi_s < \frac{\pi}{2} \quad \sin\phi_s > 0 \tag{1.52}$$

$$\gamma > \gamma_{tr} \quad \eta > 0 \quad \frac{\pi}{2} < \phi_s < \pi \quad \sin\phi_s > 0 \tag{1.53}$$

$\sin\phi_s < 0$ are not considered since it corresponds to a deceleration. At $\eta = 0$, ω_s goes to zero, there is no more phase stability and the longitudinal motion is frozen, at least in first approximation. The momentum compaction factor - or called also slip factor -η can be expanded in a Taylor series as

$$\eta = \frac{1}{T_0}\frac{T - T_0}{\delta} = \eta_0 + \eta_1\delta + \mathcal{O}(\delta^2) \tag{1.54}$$

and higher order of momentum compaction, if non negligible, has to be taken into account at transition energy, since $\eta_0 = 0, \eta_1 \neq 0$, the longitudinal motion becomes nonlinear with δ. From the stability condition Eq. 1.53, the RF phase ϕ_s must be switched rapidly from ϕ_s to $\pi - \phi_s$ in order to maintain stability above transition. Outside transition energy, the synchrotron motion is adiabatic, meaning that a change of the longitudinal phase space

$\Delta p, \Delta\phi$ is followed by a change of the longitudinal motion. At transition neighbourhood, this not true any more and the synchrotron motion is called nonadiabatic. Sec. 1.3.1 will be entirely devoted to the longitudinal dynamics around transition energy. Finally, if $\Delta\phi << 1$, the longitudinal equation of motion for small oscillation amplitude is written as

$$\ddot{\phi} + \omega_s^2 \Delta\phi = 0 \tag{1.55}$$

Around the stable synchronous phase ϕ_s, small amplitude motions are pure harmonic oscilla-

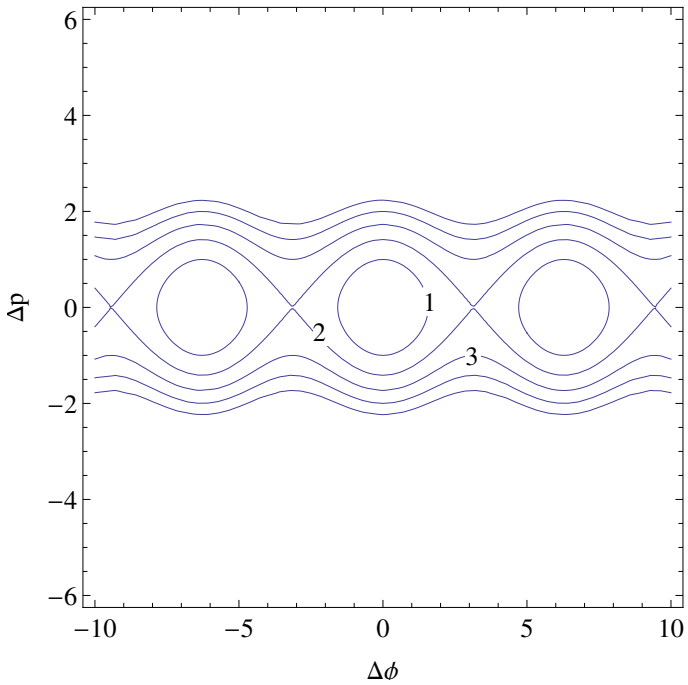

Figure 1.5: Particle trajectory in the longitudinal phase space deduced from Eq. 1.55. 1. is for small oscillation around the synchrotron phase, the motion is stable. 2 describes the motion at the limit of the stability. This limit is called separatrix. 3 shows an unstable motion.

tions which correspond to ellipse in the frame ($\Delta\phi$,Δp), as described in Fig. 1.5. The Eq. 1.49 is multiplied by $d(\Delta\phi)/dt$ and then integrated with respect to time. The resulting expression by substituting Eq. 1.45 gives, as in the transverse betatron motion, an ellipse in the phase space $(\Delta\phi, \Delta p)$ centred on $(\phi_s, 0)$. The area of the ellipse is a constant for small deviation of the momentum and the phase,

$$(\Delta p)^2 + \left(\frac{e\hat{V} p_0 \cos\phi_s}{2\pi R_0 \eta h \omega_0}\right)(\Delta\phi)^2 = \text{constant} \tag{1.56}$$

Synchrotron oscillations performed by particles in the longitudinal phase space for small amplitude around the stable phase ϕ_s and for a stable motion is described by Eq. 1.55 and illustrated in Fig. 1.6. In a similar way as in transverse dynamics, particles describe in the longitudinal phase space elliptical trajectories which are invariant for small amplitude and if

the force, acting on the particles such as mechanical pendulum, is linear with the phase. In the case of unstable motion the trajectories quickly lead to unbound amplitudes in energy and phase.

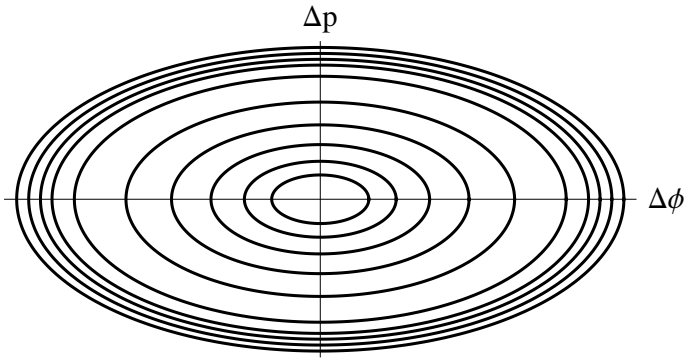

Figure 1.6: Synchrotron oscillations in phase space for stable motion $\omega_s^2 > 0$ and small amplitude.

Large amplitude oscillations - RF acceptance

For larger oscillation amplitudes we cannot anymore approximate the trigonometric function $\sin\phi \simeq \phi$ by its argument. Considering again the equation of motion,

$$\ddot{\phi} - \frac{\omega_s^2}{\cos\phi_s}\left(\sin\phi - \sin\phi_s\right) = 0$$

multiplying by $\dot{\phi}$ and integrating leads to the invariant of the motion:

$$\frac{1}{2}\dot{\phi}^2 - \frac{\omega_s^2}{\cos\phi_s}\left(\cos\phi - \phi\sin\phi_s\right) = \text{constant} \tag{1.57}$$

The synchrotron motion is still identical to a mechanical pendulum, the motion is then conservative and an invariant of the motion can be found. The same result has been used in transverse phase space and the area occupied by this beam in phase space has been called the beam emittance. Similarly, we define an emittance for the longitudinal phase space.

When ϕ reaches the value $\pi - \phi_s$ the factor $(\sin\phi - \sin\phi_s)$ in the equation of motion becomes zero and for higher values of ϕ the force is no more attractive in such a way that the motion becomes unstable. Hence $\pi - \phi_s$ is an extreme elongation corresponding to a stable motion. The corresponding curve is called the separatrix and the area delimited by this curve is called the RF bucket. The equation of the separatrix is written as following,

$$\frac{\dot{\phi}}{2} - \frac{\omega_s^2}{\cos\phi_s}\left(\cos\phi + \phi\sin\phi_s\right) = -\frac{\omega_s^2}{\cos\phi_s}\left(\cos(\pi - \phi_s) + (\pi - \phi_s)\sin\phi_s\right) \tag{1.58}$$

Figure 1.7 presents an example of RF bucket with the limit of the synchrotron motion stability,

the separatrix. In this case, the bucket is stationary, i.e. the synchrotron phase $\phi_s = \pi$ meaning there is no acceleration, since

$$\phi_s = \arccos\left(\mathrm{Sign}(\eta)\sqrt{1-\left(\frac{\mathrm{prate}\quad 2\pi R_s}{eV}\right)^2}\right) \tag{1.59}$$

with prate is the gain in momentum in GeV/c/s. In a stationary bucket - no acceleration - prate= 0. From Eq. 1.58, the maximum stable value of $\Delta\phi$ is

$$(\hat{\phi^2}_{max}) = 2\omega_s^2\left(2-(\pi 2\phi_s)\tan\phi_s\right) \tag{1.60}$$

For any invariant of the motion there exists a relation between the maximum energy and the maximum phase deviations,

$$(\Delta\phi_{max}) = \frac{|\eta|h}{Q_s p_0 R_0}(\Delta p_{max}) \tag{1.61}$$

and the expression of the RF acceptance is then [18]

$$\left(\frac{\Delta E}{E_0}\right)_{max} = \beta\sqrt{\frac{e\hat{V}}{\pi h\eta E_0}\left(2-\cos\phi_s-(\pi-2\phi_s)\sin\phi_s\right)} \tag{1.62}$$

The maximum phase deviation is also related to the RF acceptance. In the case of acceleration, $\phi_s \neq \pi$ and the shape of the RF bucket has a fish-like shape as presented in Fig. 1.8

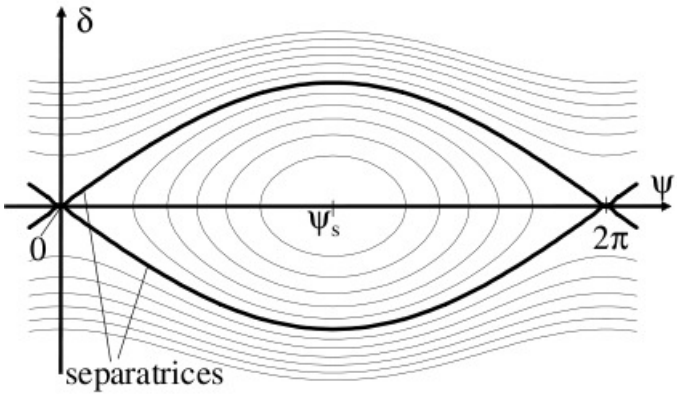

Figure 1.7: RF stationnary bucket ($\phi_s = \pi$) and the limit of the synchrotron motion, the separatrix [2].

The longitudinal emittance ϵ_l of a Gaussian bunch distribution is defined with the r.m.s bunch length $\sigma_{\Delta\phi}$ and momentum spread $\sigma_{\Delta p}$ and describes an elliptical area in the $(\Delta\phi, \Delta p)$ phase space,

$$\epsilon_l = \frac{4\pi}{h}\sigma_{\Delta\phi}\sigma_{\Delta p} \tag{1.63}$$

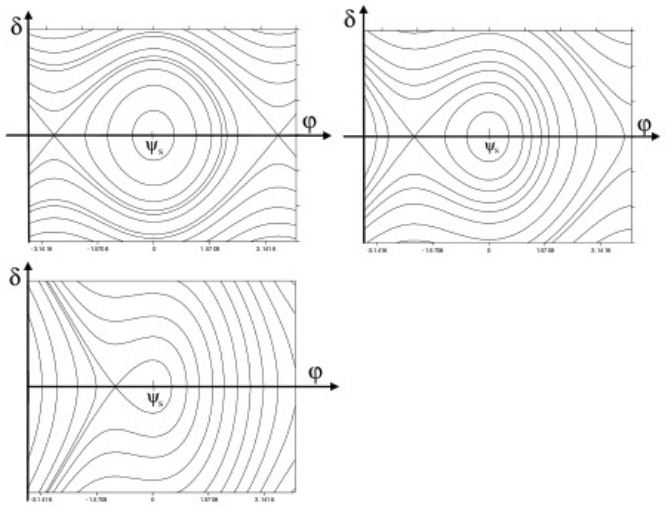

Figure 1.8: Longitudinal phase space for particles above transition energy for synchrotron phases $\phi_s = 170$ (top left), $5\pi/6$ top right, $2\pi/3$ bottom [2].

where the r.m.s bunch length and momentum spread are defined as

$$\begin{aligned} \sigma_{\Delta\phi} &= \Delta\phi_{max}/2 \\ \sigma_{\Delta p} &= \Delta p_{max}/2 \end{aligned}$$

In order to use Eq. 1.63, the bunch should be longitudinally matched to the bunch, meaning that the following matching condition is satisfy

$$\frac{R_0 \eta \sigma_{\Delta p}}{Q_s \sigma_{\Delta\phi}} = 1 \tag{1.64}$$

If the bunch is not matched to the bucket, the beam will filament in the phase space as shown in Fig. 1.9 and the longitudinal emittance might not be conserved.

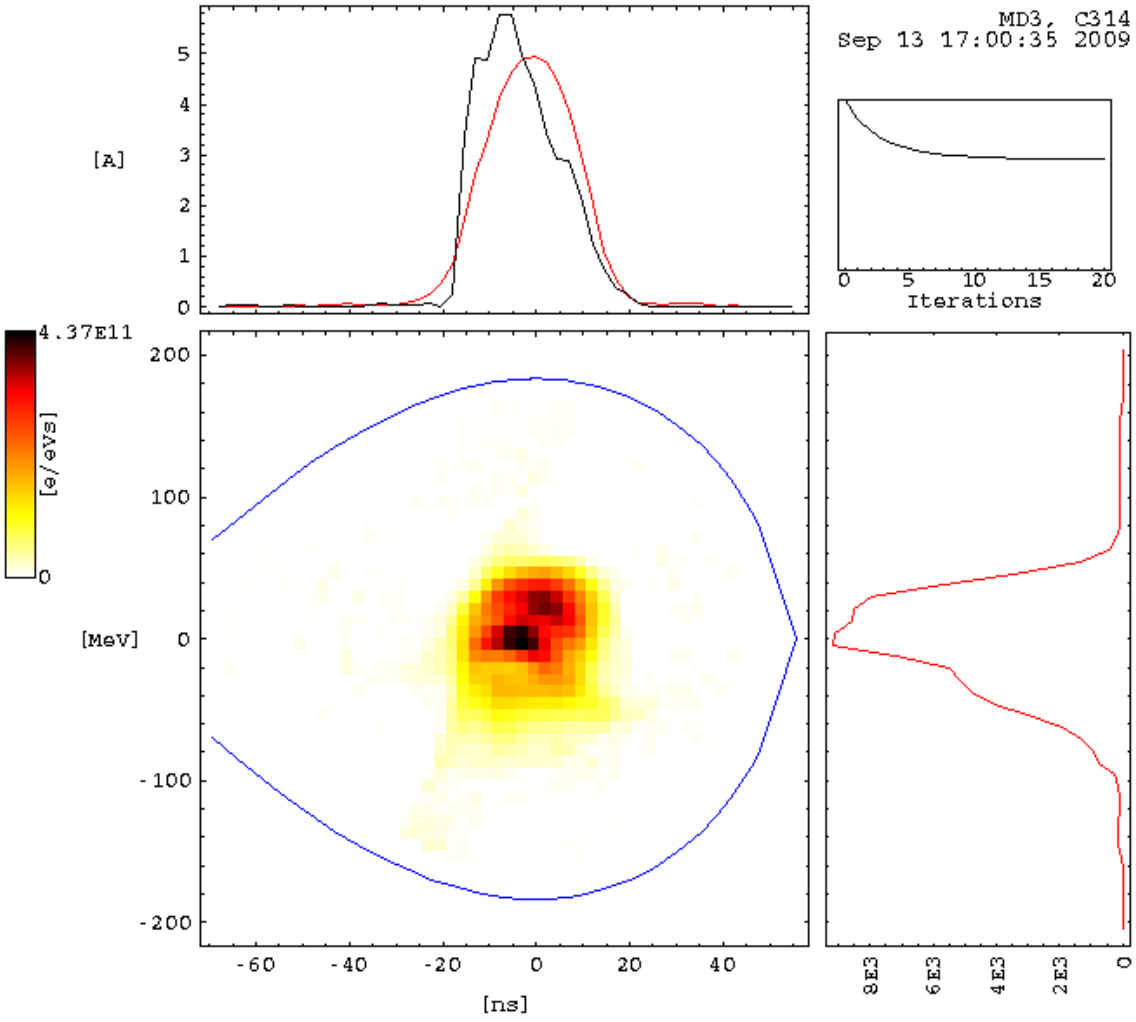

Figure 1.9: Longitudinal phase space measurement after transition energy in the PS showing a mismatch of the beam particle in the RF bucket. A filamentation is observed.This measurements was performed with tomographic reconstruction of the longitudinal phase space [3]

1.3 Transition Crossing

The CERN Proton Synchrotron is the first accelerator to have crossed transition energy. Two months after the first turn of the beam in the PS, the 16 of september 1959, a bunch with an intensity of about 10^{10} protons per pulse was accelerated through this critical energy [19]. The sign of the RF stable phase had to be reversed at transition energy. This chapter is focused on the description of the longitudinal particle motion around transition. In this energy range, the synchrotron motion is no longer adiabatic and the usual equations of Chap. 1.2 cannot be used.

1.3.1 Transition Energy

In a synchrotron, a relative energy error can be related to a relative change in revolution frequency. Many medium and high energy synchrotrons have to cross an energy at which the derivative of the revolution frequency $\Delta f/f$ with respect to the momentum error $\Delta p/p$ changes sign and has to cross zero. This energy is called transition energy noted E_{tr}.

Crossing transition energy corresponds to a change of sign of the slip factor η which relates the frequency spread in the beam to its momentum spread given by,

$$\frac{\Delta f}{f} = \eta \frac{\Delta p}{p} \qquad \text{with} \qquad \eta = \frac{1}{\gamma^2} - \frac{1}{\gamma_{tr}^2} \tag{1.65}$$

with γ_{tr} is the relativistic mass α_c at transition energy $\gamma_{tr} = E_{tr}/E_0$. Let remind the definition of the momentum compaction factor which determines γ_{tr},

$$\frac{1}{\gamma_{tr}^2} = \alpha_c = \frac{dC/C}{dp/p} = \frac{1}{C_0} \oint \frac{D(s)}{\rho(s)} ds \tag{1.66}$$

where α_c is the momentum compaction , C_0 is the path length in meter of a particle with a nominal momentum p_0 on the reference orbit, $D(s)$ is the dispersion function in meter at the longitudinal position s, $\rho(s)$ is the bending radius in meter in the magnet at the location s. α_p depends on the machine optics and a rough estimation of the relativistic transition energy mass factor γ_{tr} is given by,

$$\alpha_c = \frac{1}{C_0 \rho_0} \oint D(s) ds \qquad \begin{cases} \rho = \rho_0 & \text{in dipoles} \\ \rho = \infty & \text{anywhere else} \end{cases} \tag{1.67}$$

then

$$\begin{aligned} \alpha_c &= \frac{1}{C_0 \rho_0} < D > \cdot C_{magn} \quad \text{with } C_{magn} = 2\pi\rho_0 \\ \alpha_c &\simeq \frac{< D >}{R} \end{aligned}$$

Since the dispersion function is approximately,

$$\begin{aligned} D &\simeq \frac{R}{Q_x^2} \\ \alpha_c &= \frac{1}{\gamma_{tr}^2} \simeq \frac{1}{Q_x^2} \end{aligned} \tag{1.68}$$

In a regular lattice, $\gamma_{tr} \simeq Q_x$, the relativistic mass factor at transition energy γ_{tr} is close to the bare horizontal tune. In the case of the PS, $Q_x = 6.25$ and $\gamma_{tr} \simeq 6.1$. Therefore the transition energy is determined by the choice of the lattice and can be modified by a change in optics as explained in Sec. 1.3.6 for the case of the PS and in Ref. [20, 21] for the SPS. During the design of an accelerator, the decision can be made to avoid transition crossing either by making the injection energy above E_{tr} or by designing the lattice to obtain an imaginary gamma transition γ_{tr} as it is the case for the CERN LEIR.

Previously we have shown how to roughly determine γ_{tr}. Let consider in more detail the transition energy crossing. An energy deviation in medium energy synchrotron such as the CERN PS has two opposite effects which can be seen from Eq. 1.66.

- Below transition, an increase in energy means that the velocity of the particles evolves more rapidly than the path length. The revolution frequency increases with the particle energy.
- Above transition, an increase in energy results mainly in an increase of the path length than a revolution frequency.
- At transition, the variation of velocity is compensated by a variation in path length, i.e. a variation in energy does not modify the revolution frequency: this is the isochronous condition.

The acceleration through transition energy affects thereby widely the longitudinal dynamics of the beam and special precautions are needed in order to avoid unfavourable effects caused by this singularity over a fairly large energy range on both sides of γ_{tr}.

1.3.2 Phase stability

The longitudinal phase stability of the beam is the first caution in an accelerator in which the transition energy has to be crossed. In this section, the RF stable phase to apply on the cavities on both sides of γ_{tr} will be studied with the longitudinal linearised phase equation for small amplitude $\Delta\phi$ defined as [22],

$$\frac{d}{dt}\left(\frac{m_0\gamma C_0}{2\pi h\eta}\frac{d}{dt}\Delta\phi\right) + \frac{eV_{rf}}{C_0}\sin\phi_s\Delta\phi = 0 \tag{1.69}$$

where m_0 is the particle mass, e the electron charge, γ the relativistic mass factor, C_0 is the circumference defined as $C_0 = 2\pi\rho_0$ with ρ_0 the bending radius in the magnets, h is the

harmonic number, V_{rf} is the voltage applied on the RF cavities, η is slippage factor as defined in Eq. 1.65 and $\Delta\phi$ the particle phase deviation with respect to the synchronous phase ϕ_s.

Eq. 1.69 shows that the solution of the differential equation is oscillatory if the two terms have the same sign. However the slippage factor η changes sign at transtion, i.e. when $\gamma = \gamma_{tr}$. Therefore the sign of the synchronous phase ϕ_s has to be change also in order to keep the phase stability condition. If the sign of the ϕ_s is not changed, the solution becomes exponential making the longitudinal motion of the particles going out of the RF bucket and thus unstable. In order to keep the longitudinal focusing, the solution of the Eq. 1.69 has to be oscillatory on both sides of the transition energy and the stability condition is obtained if:

$$\begin{aligned} 0 < \phi_s < \pi/2 \quad & \text{for } \gamma < \gamma_{tr} \\ 0 > \phi_s > -\pi/2 \quad & \text{for } \gamma > \gamma_{tr} \end{aligned}$$

Let now consider the Eq. 1.66. An increase in beam energy below transition leads to an increase of the revolution frequency. Consider also a particle P_1 lagging in energy with respect to the synchronous particle P_s. The particle P_1 will travel slower than P_0 and if the phase is such that P_1 is receiving more energy, the particle will catch up the equilibrium one. Above transition, the situation is reserved and the particle P_1 with a lag has to much energy. If the RF phase is kept as below transition, the particle P_1 will be lost. However by changing the phase by $(\pi - \phi_s)$, P_1 will receive less energy. In this way, the particles stay focused around the equilibrium one. In order to maintain the longitudinal stability in either side of the transition energy, the phase of the RF cavities has to jump when $\gamma = \gamma_{tr}$. This is called the phase jump or phase shift. The concept is illustrated in Fig 1.10. If this is done at the right moment, the longitudinal phase equation can be written in a form valid below and above transition as Eq. 1.69.

The transition energy in the PS is about $\gamma_{tr} \simeq 6.1$. Fig. 1.11 shows the relativistic mass factor γ as a function of the particle momentum, the γ_{tr} and the evolution of the slip factor η which goes to zero when $\gamma = \gamma_{tr}$. One can measure around this energy range the longitudinal distribution at a given location in the machine over few hundred turns through transition as shown in Fig. 1.12. The beam profiles are acquired over several turns with a special device called wallcurrent monitor, that the principle is explained in Sec.4.1.3. The trigger of the turn by turn acquisition is synchronised with the RF train, i.e. with the RF phase. At transition ϕ_s changes and Fig. 1.12 gives the impression that the beam is jumping whereas this is due to the phase shift of the RF cavities.

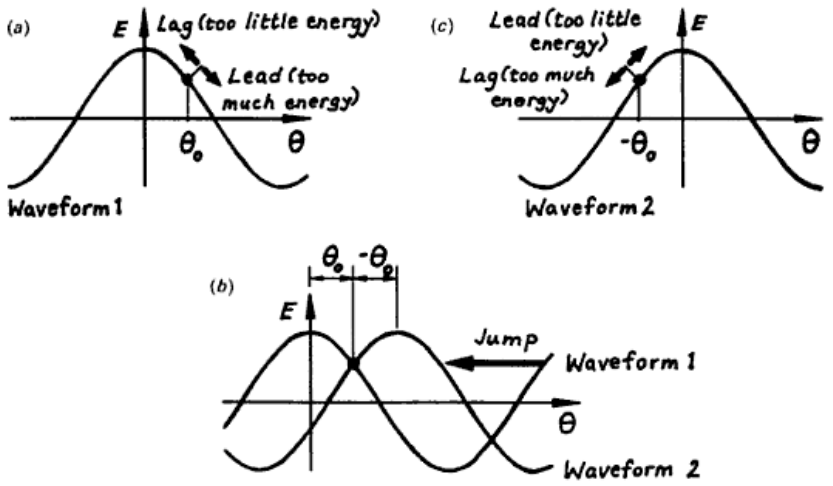

Figure 1.10: Phase stability and the phase jump at transition.(a) Below transition,(b) at transition, (c) above transition

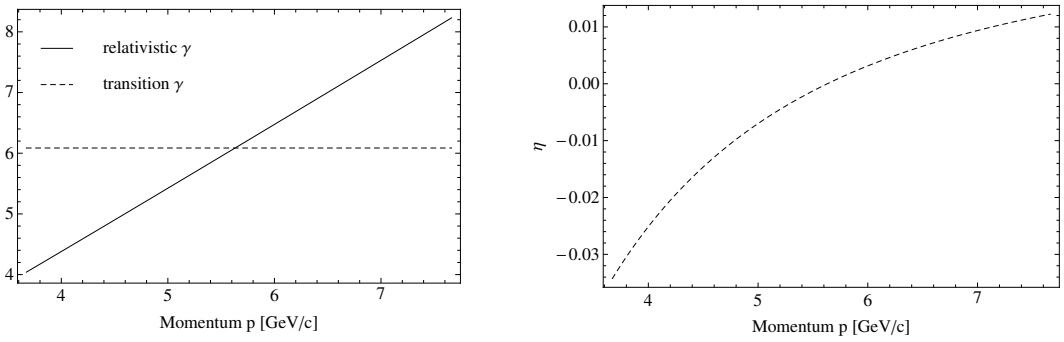

Figure 1.11: On the top, relativistic mass factor as a function of beam momentum p in the CERN PS through transition. When $\gamma = \gamma_{tr}$, i.e. when the dashed curve meets the plain curve, the beam is at transition energy. On the right, the slippage factor of the PS through transition as a function of the beam momentum. η changes sign when $\gamma = \gamma_{tr}$.

1.3.3 Synchrotron oscillation frequency through transition

In the previous section, it was explained that the longitudinal linear equation 1.69 for small particle amplitude is valid on both sides of the transition energy if the phase jump of the RF cavities is done at the right moment, i.e. at $\gamma = \gamma_{tr}$. With this assumption, an adiabatic solution is applied over the whole range of γ from injection to top energy with the exception of a fairly narrow band on either side of transition. The criterion for the validity of this solution is that the coefficients do not vary so much over one synchrotron oscillation [23]. This breaks down in the neighbourhood of transition and new solutions of the Eq. 1.69 should be found. Outside this energy range, the solutions are considered adiabatic and the particles are following a

change of bucket. The adiabatic solution of Eq. 1.69 can be written in the following form [4],

$$\Delta\phi = A\left(\frac{2\pi h\eta}{\gamma m_0 e V_{rf}\sin|\phi_s|}\right)^{1/4}\sin\int\omega_s dt \tag{1.70}$$

with ω_s is the synchrotron oscillation frequency defined in Eq. 1.50, with A the amplitude which is varying slowly with time, ω_0 is the revolution angular frequency. One can note that the phase shift of ϕ_s is needed at transition in order to keep ω_s real. From the Chap. 1.2, we have shown that the particles are moving on an elliptical trajectory with an angular frequency ω_s in the $(\Delta\phi, \Delta p)$ phase space and the area of the ellipse for a given particle remained an invariant as γ increases. While ω_s goes to zero at transition energy, i.e. when $\eta = 0$, the particle motion in the $(\Delta\phi, \Delta p)$ phase space is frozen which makes the whole system very stiff. In order to visualize the evolution of ω_s though transition, the literature [4] introduces a variable $\omega_{s\infty}$ which is the angular synchrotron frequency if $\gamma_{tr} = \infty$, i.e.

$$\omega_{s\infty} = \sqrt{\frac{2\pi e V_{rf}\sin|\phi_s|}{C_0^2\gamma m_0}\gamma^{-2}} \tag{1.71}$$

then ω_s is normalised by $\omega_{s\infty}$,

$$\frac{\omega_s}{\omega_{s\infty}} = \sqrt{|\eta|}\gamma = \begin{cases} \sqrt{1-(\gamma/\gamma_{tr})^2} & \text{below transition} \\ \sqrt{(\gamma/\gamma_{tr})^2-1} & \text{above transition} \end{cases} \tag{1.72}$$

which provides a convenient way to plot an universal curve for synchrotron oscillation frequency as a function of γ/γ_{tr} and illustrates very clearly ω_s at the transition point as shown in Fig. 1.13.

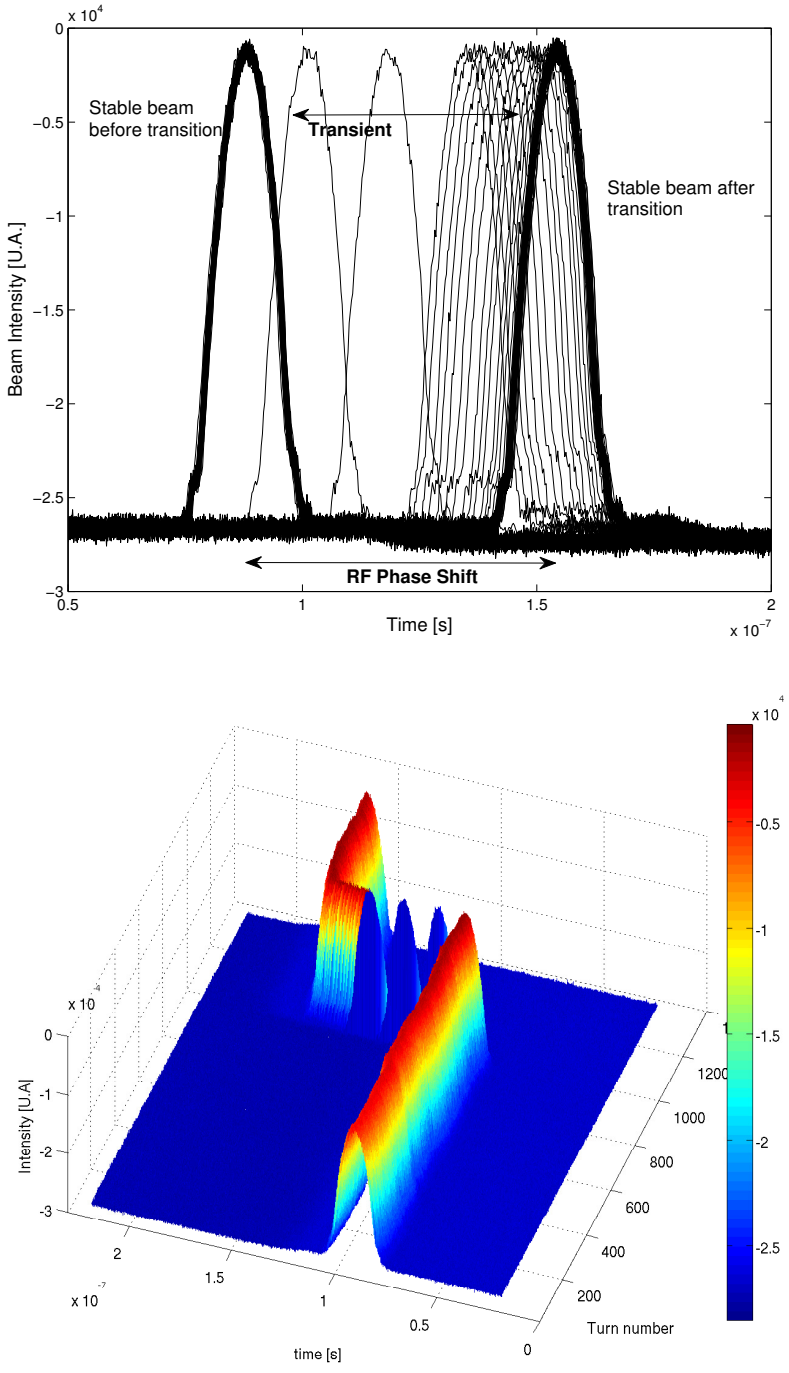

Figure 1.12: On the top, the figure represents several superposed longitudinal distribution, i.e. the particle distribution as a function of time. The profile can be fitted by a Gaussian or a parabolic distribution and the 4σ of the distribution represents the bunch length. Several measured longitudinal beam profile are plotted in the figure before and after transition in the CERN PS. We can see that the phase shift takes several turns in reality. On the bottom, the figure presents the time evolution of the beam distribution through transition in 3D.

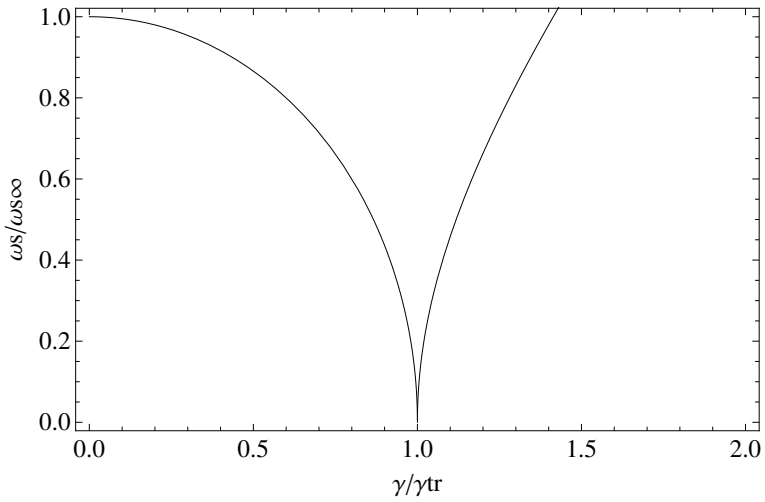

Figure 1.13: Universal curve for the normalised synchrotron frequency.

1.3.4 Equation of motion through transition

This section aims to describe briefly the longitudinal dynamics at transition. The most complete textbook which derives in the details the equations of motion in this regions is the Ng [23]. Up to this point, only the solutions of the Eq. 1.69 in the adiabatic zone were mentioned. The nonadiabatic solution covers the energies in which the synchrotron motion is very slow, i.e. the rate change of bucket height is changing faster than the rate change of executing synchrotron oscillations. In the next paragraph, the longitudinal solution of the Eq. 1.69 will be explained for energies not too far from transition. It will allow to delimit the nonadiabatic zone by introducing the notion of nonadiabatic time T_c. Then we will show the appropriate solution when the adiabatic assumption breaks. For the rest of the thesis, the following convention for the slippage factor η will be used,

$$\begin{cases} \eta < 0 & \text{if} \quad \gamma < \gamma_{tr} \\ \eta > 0 & \text{if} \quad \gamma > \gamma_{tr} \\ \eta = 0 & \text{if} \quad \gamma = \gamma_{tr} \end{cases}$$

The differential longitudinal phase equation for small $\Delta\phi$ governing the motion of the particle is written as following with the assumption that we can neglect the slow variations of all the parameters except η/E_{tot}, where E_{tot} is the total energy of the particles [23],

$$\frac{d}{dt}\left(\frac{E_{tot}}{\eta}\frac{d\Delta\phi}{dt}\right) - \left(\frac{eV_{rf}h\cos\phi_s\omega_0^2}{2\pi\beta^2}\right)\Delta\phi = 0 \tag{1.73}$$

The second bracket term is considered time independent and the variation of η/E_{tot} is linear in time near transition by writing,

$$\gamma = \gamma_{tr} + \dot{\gamma}t \quad \begin{cases} t < 0 \text{ below transition} \\ t > 0 \text{ above transition} \end{cases} \tag{1.74}$$

By combining the definition of the slippage factor definition with the equation above, one can find the linear time dependance of the ratio η/E_{tot}

$$\frac{\eta}{E_{tot}} \approx \frac{2\dot{\gamma}t}{\gamma_{tr}^4 E_0} \tag{1.75}$$

where E_0 is the rest energy of the particle, $\dot{\gamma}$ is the derivative with time of γ which is a constant since the function $\gamma(t)$ is linear with the time t. The expression above is only valid if t is not too far from transition. Then the Eq. 1.73 can be transformed in order to express it as a function of the synchrotron oscillation frequency ω_s,

$$\frac{d}{dt}\left(\frac{1}{\omega_s^2}\frac{d\Delta\phi}{dt}\right) + \Delta\phi = 0 \tag{1.76}$$

However, the expression of ω_s loses its meaning close to transition and the Eq. 1.50 is be considered as a definition only. The Eq. 1.76 is a fundamental expression.

Nonadiabatic time

We used the assumption of a linear variation of η/E_{tot} while all the other parameters such as the rf voltage V_{rf} are held fixed. However if η is not varying rapidly, the bucket height is proportional to $\sqrt{E_{tot}/|\eta|}$ [22]. Therefore the bucket height increases to infinity while transition approches and the particle will not be able to catch up a rapid change of the bucket shape. This time period is defined as the nonadiabatic region which goes from $t = -T_c$ to $t = T_c$ with T_c the nonadiabatic time. This region is determined by [23]

$$\omega_s \leq \frac{2}{(\Delta E)_{bucket}} \frac{d(\Delta E)_{bucket}}{dt} \tag{1.77}$$

Inside the adiabatic region, the rate at which the bucket height is changing is faster than the rate of executing synchrotron oscillations. The expression of the synchrotron angular frequency become with the Eq. 1.75

$$\omega_s = \omega_0 \left(-\frac{eV_{rf} h \cos\phi_s \dot{\gamma} t}{\gamma_{tr}^4 \beta^2 E_0} \right)^2 \tag{1.78}$$

Then, evaluating at $t = -T_c$,

$$\omega_s|_{t=-T_c} = \frac{\omega_0}{\beta} \left(\frac{eV_{rf} h \cos\phi T_c \dot{\gamma}}{\gamma_{tr}^4 E_0} \right)^{\frac{1}{2}} \tag{1.79}$$

The expression of the nonadiabatic time is obtained from Eq. 1.77

$$T_c = \left(\frac{\beta^2 \gamma_{tr}^4 E_0}{eV_{rf} h \cos\phi_s \dot{\gamma} \omega_0^2} \right)^{\frac{1}{3}} \tag{1.80}$$

The literature gives also [23]

$$T_c = \left[\left(\frac{\beta^2 \gamma_{tr}^4}{2\omega_0 h} \right) \left(\frac{|\tan\phi_s|}{\dot{\gamma}^2} \right) \right]^{\frac{1}{3}} \tag{1.81}$$

If $-T_c \leq t \leq T_c$ the time is close enough to transition in such a way that the particle does not catch up with a rapid changing of the bucket shape. In the following paragraphs, the equation of motion will be solved in the cases:

- $t > |T_c|$, the adiabatic region which is not too far away from transition.
- $t \leq |T_c|$, the nonadiabatic zone in which the synchrotron motion is frozen.

Equation of motion in the adiabatic region close to transition

Let remind the general equation Eq. 1.76 of the longitudinal motion for small phase offset:

$$\frac{d}{dt}\left(\frac{1}{\omega_s^2}\frac{d\Delta\phi}{dt}\right)+\Delta\phi=0$$

The following idea is to not to solve exactly the differential equation but look into approximations [23]. The adiabatic region in which the longitudinal equation of motion will be solved is not too far from transition. The particle is still performing synchrotron oscillations with a slowly frequency $\omega_s/2\pi$. A general solution of the Eq. 1.76 can be written in the form in the adiabatic region

$$\Delta\phi = B\sqrt{\omega_s}e^{i\int\omega_s dt} \tag{1.82}$$

Again with the assumption of a constant RF voltage, constant synchrotron phase ϕ_s and a linear time variation of η/E_{tot}, we can find again the nonadiabatic time from

$$\omega_s^2 = b|t| \qquad \text{with} \qquad b=\frac{\dot{\gamma}heV_{rf}|\cos\phi_s|\omega_0^2}{\beta\pi\gamma^4E_0}$$

$$T_c=\left(\frac{1}{b}\right)^{1/3} \qquad \omega_s^2=\frac{|t|}{T_c^3} \qquad \text{as defined in the section 1.3.4}$$

The energy offset expression is found as

$$\Delta E = i\omega_s\Delta\phi\frac{\beta^2\gamma E_0}{|\eta|h\omega_0}\left[1+\frac{1}{16}\left(\frac{T_c}{|t|}\right)^3\right]e^{-i\varphi} \tag{1.83}$$

with

$$\varphi=\tan^{-1}\frac{1}{4}\left(\frac{T_c}{|t|}\right)^{3/2} \tag{1.84}$$

From the Eq. 1.82, we can see the width of the bucket is shrinking due to the factor $\sqrt{\omega_s}$. In the other hand the height ΔE is increasing while $|t|$ is approaching zero in the denominator. Then there is also a phase advance of the energy offset defined also as a tild in the ellipse of the bunch phase space. These equations show that the longitudinal motion is slowing down in the adiabatic region. There is no clearcut boundaries between the adiabatic and nonadiabatic region. We would like to relate the constant B to the tilted bunch area, the longitudinal emittance in eV.s defined as [23]

$$S=\pi\frac{\Delta\phi}{h\omega_0}\widehat{\Delta E}\cos\varphi \tag{1.85}$$

the definition of the half bunch length and half energy spread in the adiabatic region [23]

$$\widehat{\Delta\phi} = h\omega_0 \left(\frac{2ST_c^2\dot{\gamma}}{\pi\beta_t^2\gamma_t^4 E_0} \right)^{1/2} \left(\frac{|t|}{T_c} \right)^{1/4} \tag{1.86}$$

$$\widehat{\Delta E} = \left(\frac{S\beta_t^2\gamma_t^4 E_0}{2\pi T_c^2\dot{\gamma}} \right)^{1/2} \left(\frac{T_c}{|t|} \right)^{1/4} \left[1 + \frac{1}{16} \left(\frac{T_c}{|t|} \right)^3 \right]^{1/2} \tag{1.87}$$

Equation of motion in the nonadiabatic region

In order to study the bunch shape through transition, i.e. in the nonadiabatic region the general Eq. 1.76 is derived in the following form by setting

$$x = \frac{|t|}{T_c} \qquad \text{and} \qquad dx = \frac{1}{T_c} dt \tag{1.88}$$

by substituting 1.88 in Eq. 1.76

$$\frac{d}{dx}\left(\frac{1}{x}\frac{d\phi}{dx} \right) + \Delta\phi = 0 \tag{1.89}$$

In the nonadiabatic region, $|x| < 1$. The important fact of the derivation is that the half bunch length and energy offset should be the same as the one in the adiabatic regime while the beam enters and goes out of the nonadiabatic region, therefore the half bunch length and half energy spread coming out will be correct and matched to adiabatic solution when the synchrotron motion will start again, i.e. when $t > T_c$.From Eq.1.89. A way to find the exact solution for the phase offset and energy offset is to derive the Eq 1.89 in a form that it can be solved with Bessel function. This method is valid for every x. Let set $y = \frac{2}{3}x^{3/2}$ and $\Delta\phi = \varphi y^{2/3}$ [24] which gives by substitution in Eq. 1.89

$$\frac{d^2\varphi}{dy^2} + \frac{1}{y}\frac{d\varphi}{dy} + \left(1 - \frac{(2/3)^2}{y^2} \right)\varphi = 0 \tag{1.90}$$

The exact solution for the phase offset and energy offset

$$\begin{aligned} \Delta p(x) &= A y^{1/3} (\cos\psi_1 J_{-1/3}(y) + \sin\psi_1 N_{-1/3}(y)) \\ \Delta\phi(x) &= A y^{2/3} (\cos\psi_1 J_{2/3}(y) + \sin\psi_1 N_{2/3}(y)) \end{aligned} \tag{1.91}$$

with A, ψ_1 are constant to be determined from the initial conditions, J_n is the Bessel function of the first kind and N_n is the Bessel function of the first kind. If the phase shift is done at the right moment, the equation of $\Delta\phi$ is symmetric with respect to the transition $x = 0$. This leads to an important conclusion [4]: when entering in the transition region with a elliptical bunch

phase space which given by the adiabatic solution, the bunch comes out in the other side with the same shape.

1.3.5 Unfavourable effects during transition crossing

The previous paragraph was dedicated to the longitudinal equation of motion of the beam around transition energy. It has been demonstrated that particles evolve in a nonadiabatic regime at which means that any change in the RF bucket will weakly affect the longitudinal beam distribution. It has been shown also that the distribution in the longitudinal phase space has a symmetric behaviour with respect to the energy $\gamma = \gamma_{tr}$. In the opposite of the adiabatic theory which predicts that the bunch length is going to zero for $\eta = 0$, it reaches instead a minimum at transition and evolve with a mirror symmetry with respect to $\gamma = \gamma_{tr}$. In order to prevent any blow up of the longitudinal emittance, it is fundamental to preserve this symmetry. However, some effects might occur at transition energy which break the symmetry. It happens whether the stable phase jump is not performed at the right moment or with the presence of longitudinal space charge forces [25]. Some of these effects will be developed in this paragraph in particular the consequence of the longitudinal space charge force on the bunch length at transition energy. This effect was a serious limitation in the CERN PS during the 60's and the solution proposed is the so-called *gamma transition jump* [25], still in use in the PS. It consists of changing the periodic optics with the help of fast pulsed quadrupoles in order to modify dynamically the momentum compaction factor η. It allows the beam to cross faster the nonadiabatic regime. The gamma jump is a way to cure longitudinal instabilities and is today an important process in order to cross efficiently the transition energy, still particularly critical for high intensity beams[25–28].

Mistiming in the RF phase shift

Let consider that the RF phase shift is not performed at the right moment, i.e. not at $x = 0$. In the previous section, it has been demonstrated it exists a symmetry in the longitudinal behaviour of the beam - the bunch length for example - with respect to the transition time. If the phase jump is done too early or too late, this symmetry is broken and the phase space will emerge from the nonadiabatic region with a wrong ellipse orientation and therefore will not match the adiabatic solution after transition as illustrated in Fig. 1.14. It results in a mismatch in phase $\Delta\phi$ and a filamentation of the beam in the phase ellipse and in order to give finally a blow-up of the longitudinal emittance. In the CERN PS, the tolerance on the transition timing is about 1 ms [26]. Up to this value, very large bunch length oscillations are observed.

Bunch length oscillation excitation

So far, only the dynamics of a single particle have been considered, i.e. collective effects have been neglected. When beam intensities increase, this assumption is no longer valid. The self space charge forces - the Colombian interaction between charged particles - in a beam act in all directions, but only the longitudinal force inside a bunch will be considered. Fig. 1.15 shows the equilibrium bunch length with and without space charge forces as transition is crossed. In order to the beam remains stable after transition, the longitudinal focusing properties of the

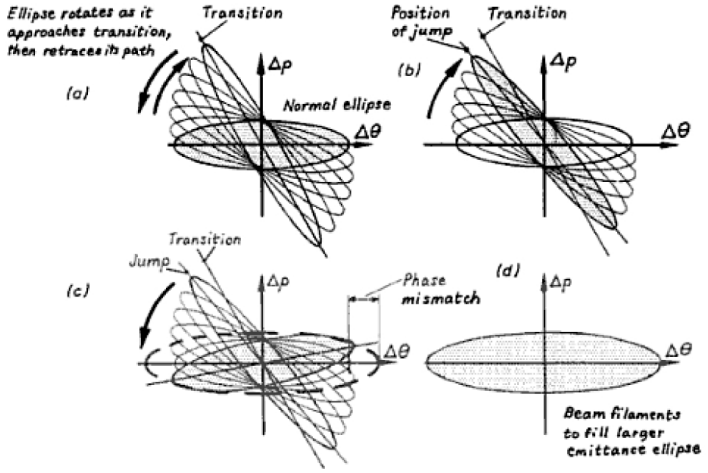

Figure 1.14: Mistiming transition.(a) Correct timing, (b) Jump is made too early, (c) Ellipse retraces its but overshoots,(d) subsequent filamentation [4].

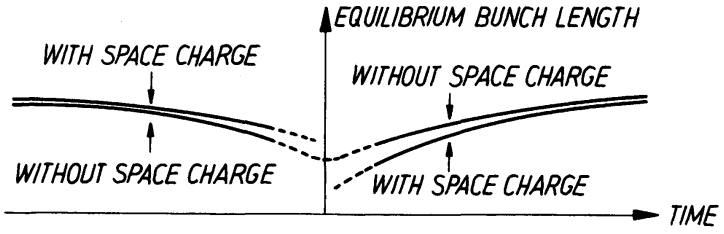

Figure 1.15: Equilibrium bunch length as a function of time assuming space charge forces [4].

RF system have to be changed. Particles of the same charge always repel each other. Therefore, they counteract the RF forces before transition and help the RF forces above transition [27]. Due to space charge forces, the equilibrium bunch length is larger below transition than if there were no charge charge. Outside the region around transition, the conditions changes slowly in the machine compared to the period of the synchrotron oscillations and the bunch is able to adjust itself adiabatically to changing conditions thus maintaining itself in equilibrium. At transition the synchrotron frequency goes to zero and all motion is frozen. Above transition the bunch will emerge with a larger bunch length left over from the influence of the space charges below transition. The true equilibrium bunch length is now shorter than without space charge and the bunch will start to oscillate, see Fig. 1.16. The symmetry that was so important for a clean passage transition has been broken. Several remedies have been proposed and studies, the most successful method is the so-called γ_{tr}-jump [25].

1.3.6 Gamma Transition Jump

Crossing transition energy can be an intensity limitation. High intensity beams are concerned by unfavourable effects such as longitudinal emittance blow-up and stability issues. In past,

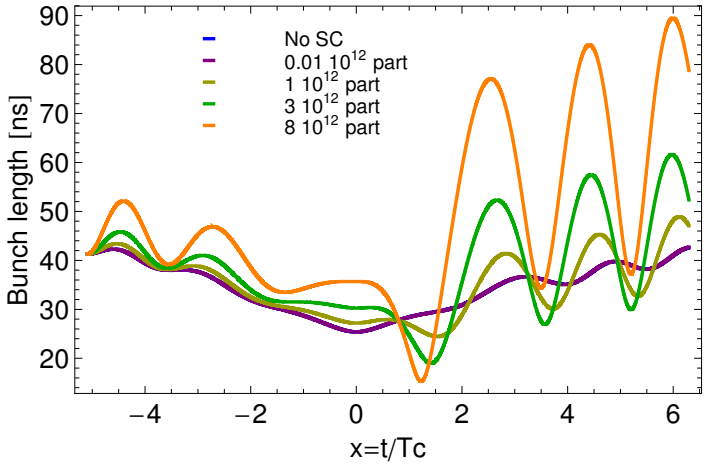

Figure 1.16: Bunch length oscillations as a function of time assuming longitudinal space charge forces for different beam intensity. These are the results of *HEADTAIL* of bunch length simulations through transition energy [5].

the intensity was limited at transition crossing due to a longitudinal microwave instability which can induce severe losses and large blow up of the longitudinal distribution [28]. However, the major issue was the mismatch in bunch length that we mentioned in the previous paragraph [25]. A possible solution is to catch up the bunch length after transition energy by changing dynamically the momentum compaction α_c and η, i.e. the optics, and increase as much as possible the speed of the transition crossing. This remedy used in the CERN PS since the 60's is called *gamma transition jump* and is noted γ_{tr}-jump. The first remark is that the gamma transition jump is a perturbation of the optics. In the PS, the γ_{tr}-jump is performed with quadrupoles spread around the ring in doublet in triplet, that a layout is presented in Ref. [29, 30]. The quadrupoles change the unperturbed optics and hence the local dispersion function, allowing to modify the momentum compaction α_c [28]

$$\alpha_c = \frac{1}{\gamma_{tr}^2} = \oint \frac{D(s)}{\rho(s)} ds$$

The dispersion function is modified by the gradient of the quadrupoles according to

$$\vec{D}^* = \left(\vec{I} + \vec{M}\vec{K}\right)^{-1} \vec{D} \tag{1.92}$$

with $\vec{D}^*$, the perturbed dispersion function, is defined as $\vec{D}^* = (D_1^*, D_2^*, ..., D_j^*, ..., D_n^*)$ the modified dispersion at the jth quadrupole, $\vec{D}$ the nominal dispersion function, $\vec{K}$ is the vector containing the gradient of the quadrupoles, I is the identity vector and $\vec{M}$ is the perturbation $m_{i,j}$ between a location i and the place of the quadrupole j defined as

$$m_{i,j} = \frac{\beta_i \beta_j}{2 \sin \pi Q} \cos\left(|\mu_j - \mu_i| - \pi Q\right) \tag{1.93}$$

The expression of the change in γ_{tr} is calculated as follow, assuming here that there is only two families of quadrupoles with the gradients k_1, k_2 and that the tune shift is zero (zero tune shift condition)

$$\Delta(\gamma_{tr}^{-2}) = a(m_{i,j}D_i)k_1^2 + b(m_{i,j}D_i)k_1k_2 + c(m_{i,j}D_i)k_2^2 \tag{1.94}$$

where a, b, c depend on the nominal optics. The sign of $\Delta(\gamma_{tr}^{-2})$ changes when $b >> a$ (and c) and k_1 or k_2 inverts its sign: it results a γ_{tr}-jump. Its principle is then to increase artificially the speed of the transition crossing by changing the γ_{tr} of the machine with help of quadrupoles placed at non zero dispersion location. The unperturbed γ_{tr} and the γ_{tr}-jump as nominally implemented in the CERN PS are compared in Fig. 1.17 and Fig. 1.18 shows the resulting momentum compaction factor η as well. One can remember that when $\gamma = \gamma_{tr}$, this is

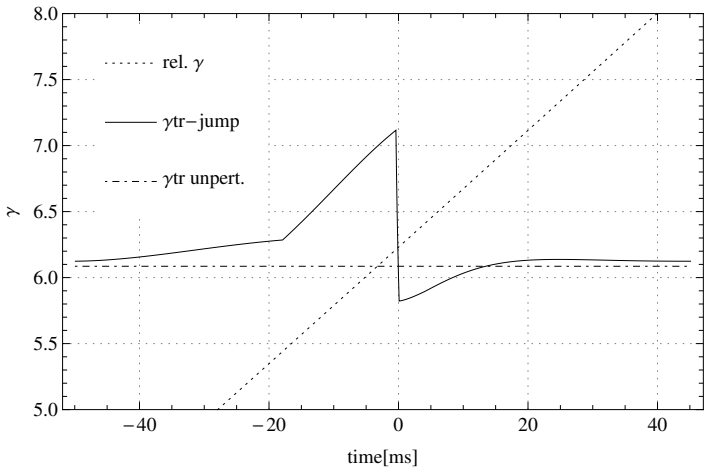

Figure 1.17: Gamma transition jump in the CERN PS. The dotted curve represents the relativistic gamma as a function of time, the dotdashed one is the unperturbed gamma transition, and the plain curve reminds the γ_{tr} with gamma transition jump.

transition energy. Instead of keeping γ_{tr} constant with the energy, Fig. 1.17 shows that γ_{tr} stays at a safe distance from the curve of the Lorentz factor γ. Then a jump in γ_{tr} is performed by $\Delta\gamma_{tr} \simeq -1.24$ in 500 μs, the transition crossing speed is 50 $\dot{\gamma}$, where $\dot{\gamma}$ is the time derivative of the Lorentz factor γ with $\dot{\gamma}$=49.9 s^{-1}. The transition energy is also making higher from 6.085 to about 6.2 with the γ_{tr}-jump method. As a consequence, the momentum compaction factor η is also changing during the γ_{tr}-jump. Outside the range in energy in which the gamma transition jump, η is unchanged and is the same as the unperturbed η from the bare optics. The doublet and triplet of quadrupoles are powered by currents which are presented in Fig. 1.19 as a function of time. The jump of the optics function η and γ_{tr} are then triggered mainly by the doublets whereas the triplets are used to give the general shape of η, γ_{tr}. The gamma transition jump is also a method to alleviate a longitudinal microwave instability at transition energy in the PS, in such a way to cross the nonadiabatic region faster than the time needed by the instability to grow [29].

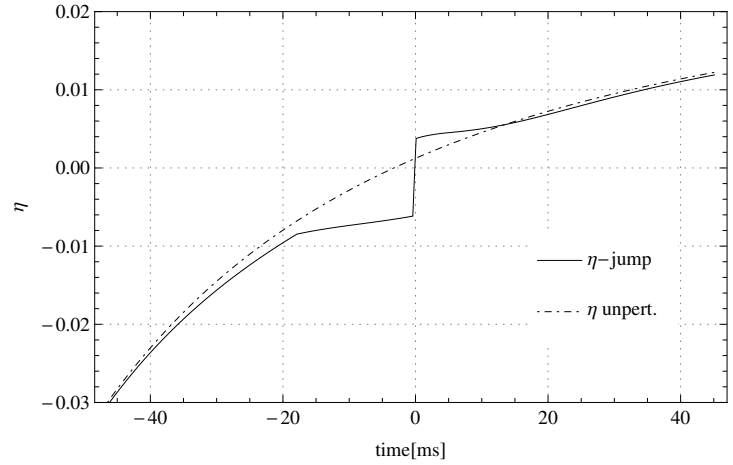

Figure 1.18: Resulting of the momentum compaction η with the gamma transition jump in the CERN PS. The dotdashed curve represents the unperturbed η as a function of time, and the plain curve reminds the one with gamma transition jump.

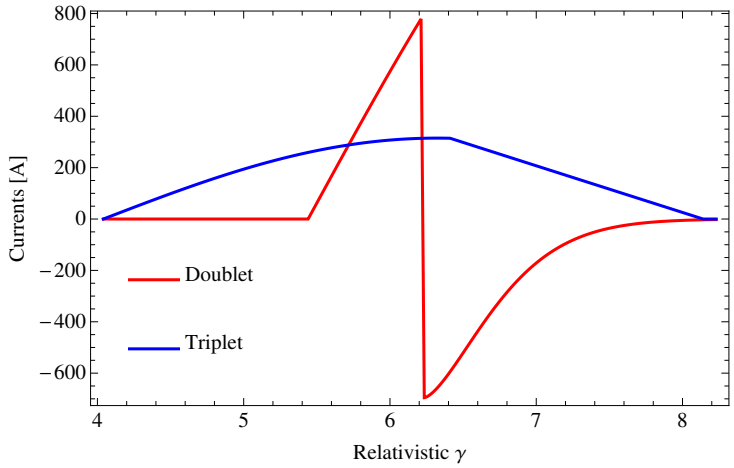

Figure 1.19: Current powering the gamma transition jump quadrupoles as a function of time. The γ_{tr}-jump is triggered while the currents of doublets are changing sign.

The gamma transition jump is used in the CERN PS since the 60's and is a method to cure instabilities [28]: the beam stays a shorter time with a frozen longitudinal motion, which makes the beam less sensitive wake forces, this will be developed in the next section. The disadvantage of the γ_{tr}-jump is the increase of the transverse beam size since the beta function can become very large - up to 80 m at certain locations - resulting in severe aperture limitation. In the PS, the quadrupoles of the γ_{tr}-jump are spread out the ring and are powered in the same way. Studies were carried out in 2006-2007 in order to study the optics whether the machine is splitted in two parts [30] and powered differently. The results show that it is possible to reduce the beam size at locations where the beam envelop is too large and increase it where the machine aperture is larger. The other disadvantage is that the γ_{tr}-jump was designed for a

horizontal tune of $Q_x = 6.25$ in order to obtain a zero tune shift condition. However, the tunes are not necessary at 6.25 and a clear tune shift can be observed while γ_{tr}-jump is performed.

1.4 Collective effects in Synchrotrons

Up to now, only single particle dynamics has been considered and the interaction with the other particles and the beam surrounding was neglected. However instabilities such as the fast transverse turbulence at transition studied in the Chap. 4 are driven by the multi-particle effect and by the interaction of the beam with its environment. This chapter is meant to help the reader to understand the basis which leads to the multi-particle dynamics. Many particles in a beam may represent a sizable charge and current which act as a source of electromagnetic fields (self fields). They are modified by boundary conditions imposed by the beam surroundings (vacuum chambers, cavities, etc.) and act back on the beam. Image currents created by the beam itself due to its environment will travel with the beam particle and if the the vacuum chamber is not perfectly conducting or contains discontinuities, electromagnetic fields are left behind and influence the motion of the particles that follow. These fields are called wake fields and they induce beam trajectory deflections and perturb the beam distribution. The strength of the interaction of the bunch with its environment is described in frequency domain by a coupling impedance $Z(\omega)$. This allows to describe the beam-impedance interaction which can lead to instabilities driven by the intensity. The colombian interaction between particles, so called space charge, will be also described as well as its effect on the coherent and incoherent motion of the beam. Many textbooks are dedicated to the Collective Effect subject such as Chao [31], Ng [32] and the courses from E. Metral and G. Rumolo [24].

1.4.1 Wake field and Impedance

Charged particles travelling with a velocity close to the speed of light generate electromagnetic fields, the Lienard-Wiechert field. Let assume here that the vacuum chamber is completely smooth and infinitely conducting. Then the force of the beam particle from the beam comes from only sources: electromagnetic interaction of the beam with all other beam particles in the beam, which we call self-forces, reflection of electromagnetic fields from the walls of the vacuum chamber, which we call image forces. Image currents are also then created and follow the beam. In the case of not perfectly conducting wall or if there are discontinuities, the images charges will slow down and electromagnetic fields, the wake fields, are left behind the particles and they might influence the motion of the particles which follow. They can lead to energy loss and instabilities. These wake fields are treated as a perturbation and they should be added to the external fields seen by particles coming from RF cavities, magnets,

$$\vec{F}_{total} = \vec{F}_{ext} + \vec{F}_{wake} \tag{1.95}$$

with $\vec{F}_{ext}$ is the external force, $\vec{F}_{wake}$ the force from the wake field

$$\begin{aligned} \vec{F}_{ext} &= q(\vec{E}_{ext} + \vec{v} \wedge \vec{B}_{ext}) \\ \vec{F}_{wake} &= q(\vec{E}_{wake} + \vec{v} \wedge \vec{B}_{wake}) \end{aligned}$$

The computation of the wake fileds is not trivial and approximations are usually required. A charged test particle sees a wake force and is travelling behind a source particle at a distance z. One note the longitudinal s-axis, the axis of symmetry of the vacuum chamber for a circular accelerator ring. For the moment, the transverse coordinates x, y formed the right-handed Cartesian coordinate system. The electromagnetic fields ($\vec{E}$,$\vec{B}$) and the wake fields are function of x, y, s, t, with t the time. The longitudinal location of the test particle is s related to the time t by $s = z + \beta c t$ with β the relativistic parameter, c the speed of light. The longitudinal postion of the source particle is s_s. The distance z is time independante regardless one machine revolution. Let start from the single particle motion formalism, let x_1, y_1 the test particle displacement and x_0, y_0 the one of a source particle in a asymmetric structure

$$\ddot{x_i} + Q_{x0}\omega_0^2 x_i = \frac{F_{pert}(x_1, y_1, x_0, y_0, t = \frac{s_s - z}{v})}{m_0 \gamma} \tag{1.96}$$

where $\ddot{x_i}$ is the double of time derivative x_i, ω_0 is the angular revolution frequency, γ the relativistic energy factor and the perturbative force can be expanded to the first order in term of x_1 and x_0, considering the horizontal plane only for the moment and neglecting any coupling

$$F_{pert} = \left(\frac{\partial F_{pert}}{\partial x_1}\right) x_1 + \left(\frac{\partial F_{pert}}{\partial x_0}\right) x_0 \tag{1.97}$$

If the displacement of the source particle x_0 is zero, the test particle undergoes a force proportional to its own displacement x_1 which might remind a quadrupolar force in a magnet. On the other hand, if $x_1 = 0$, the test particle experiments a force independent of its position which reminds a dipolar component of a magnetic field. Therefore the perturbative force F_{pert} can be written with a dipolar part, which depends only of the position of the source particle and with a quadripolar part, which depends on the displacement of the test particle. In the case of ultra-relativistic beams, the source point charge does not feel the electromagnetic fields it generates. However, it is not true for non-relativistic particles.

The effect of the wake force affecting a test particle induces a change in momentum Δp such as a kick and in general we are interested by the integrated wake field seen by a trailing particle following the source distribution over a path length L.

$$v\Delta p_x = \int_0^L F_\perp ds = \int_0^L (F_{dip} + F_{quad}) ds \tag{1.98}$$

with $F_{dip} = \left(\frac{\partial F_{pert}}{\partial x_0}\right) x_0$, with $F_{quad} = \left(\frac{\partial F_{pert}}{\partial x_1}\right) x_1$. The notion of wake potential $\vec{W}(x_0, y_0, x_1, y_1, t)$ is then introduced as the integrated Lorentz force generated by a source distribution with a total charge q_0 and velocity $\beta_0 c$ at a location $(x_0, y_0, s_0 = \beta_0 c)$. This perturbative force is felt by the trailing particle behind the source at a distance z with a total charge q_1 and velocity $\beta_1 c$ at

a location $(x_1, y_1, s_1 = s_0 - z)$

$$\vec{W^{pot}}(x_0, y_0, x_1, y_1, t) = -\frac{1}{q_0 q_1}\int_{s_1=0}^{L} \vec{F}(x_0, y_0, x_1, y_1, t)_{t=(s_1+z)/\beta_1 c} ds_1 \tag{1.99}$$

Hence longitudinal wake potential $W_{\parallel}^{pot}$ and transverse wake potentials $\vec{W^{pot}}_x$ and $\vec{W^{pot}}_y$ can be then written

$$\begin{aligned}
W_{\parallel}^{pot}(x_0, y_0, x_1, y_1, t) &= -\frac{1}{q_1}\int_{s_1=0}^{L} E_s(x_0, y_0, x_1, y_1, t)_{t=(s_1+z)/\beta_1 c} dz_1 && (1.100)\\
W_x^{pot}(x_0, y_0, x_1, y_1, t) &= -\frac{1}{q_1}\int_{s_1=0}^{L} (E_x - \beta c B_y)(x_0, y_0, x_1, y_1, t)_{t=(s_1+z)/\beta_1 c} ds_1 && (1.101)\\
W_y^{pot}(x_0, y_0, x_1, y_1, t) &= -\frac{1}{q_1}\int_{s_1=0}^{L} (E_y - \beta c B_x)(x_0, y_0, x_1, y_1, t)_{t=(s_1+z)/\beta_1 c} ds_1 && (1.102)
\end{aligned}$$

We might introduce the wake function $\vec{W}(x_0, y_0, x_1, y_1, z)$ which is convoluted with a beam distribution $\lambda(z)$ gives the wake potential

$$\vec{W^{pot}}(x_0, y_0, x_1, y_1, t) = \int_{z'=-\infty}^{\infty} \vec{W}(x_0, y_0, x_1, y_1, z - z')\lambda(z') dz' \tag{1.103}$$

The wake functions are considered as Green functions they are wake potentials generated by a travelling point-like charge $\delta(s - \beta c t)$. Therefore and from the Eq. 1.98 the transverse forces are written as a function of a driven term of the wake function (dipolar part) and of a detuning term of the wake function (quadrupolar part)

$$\begin{aligned}
\int_L F_x ds &= -q_1 q_2 (x_0 W_x^{dip}(z) + x_1 W_x^{quad}(z)) && (1.104)\\
\int_L F_y ds &= -q_1 q_2 (y_0 W_y^{dip}(z) + y_1 W_y^{quad}(z)) && (1.105)
\end{aligned}$$

Beam coupling impedance

The electromagnetic fields are generally computed in frequency domain than in time domain [33]. The longitudinal and transverse beam coupling impedance $Z_{\parallel}, Z_x, Z_y$ are the

Fourier transforms of the wake functions

$$Z_{\parallel} = -\int_{-\infty}^{+\infty} W_{\parallel}(z)\frac{e^{jkz}}{\beta c}dz \tag{1.106}$$

$$Z_x = j\int_{-\infty}^{+\infty} W_x(z)\frac{e^{jkz}}{\beta c}dz \tag{1.107}$$

$$Z_y = j\int_{-\infty}^{+\infty} W_y(z)\frac{e^{jkz}}{\beta c}dz \tag{1.108}$$

The other way around, the wake functions can be obtained by the inverse Fourier transforms of the impedances. The notion of the dipolar and quadrupolar wake functions is then extended to the impedance and the term of generalized impedance is introduced [34]

$$Z_x = x_1 Z_x^{driving} + x_2 Z_x^{detuning} \tag{1.109}$$

$$Z_y = y_1 Z_y^{driving} + y_2 Z_y^{detuning} \tag{1.110}$$

1.4.2 Space Charge

The space charge effect is one of the most fundamental collective effect. The Coulomb forces and current of the beam create self-fields and image fields which alter its dynamic behaviour and influence the single-particle motion as well as coherent oscillations of the beam as a whole. They can act like a distributed lens, defocusing the beam in both transverse planes. The effect of the direct space charge is evaluated for transport lines and synchrotrons where the number of betatron oscillations per machine turn, Q, is reduced by ΔQ . In a real accelerator, the beam is also influenced by the environment (beam pipe, magnets, etc.) which generates indirect space charge effects, which can be easily understood by introducing images charges and current in the wall. At the opposite of the direct space charge, the indirect effect does not cancel while the velocity v is approaching c, therefore they might become a limitation for high energy synchrotron. For the case of the CERN PS which belongs to medium energy machines, the direct and indirect effect has to evaluated. Several textbooks and courses are dedicated to the space charge effect such as the book of A. Chao [31] and the Refs. [24] [35] [6]. Ref. [36], mainly devoted to the impedance model of the SPS, contains also a comprehensive explanation of the space charge and the impedance resulting from space charge effect.

Direct Space Charge - Self Field

Consider two particles of equal charge $+e$. A rest, they experiment a repulsion due to Coulomb force. When travelling with velocity $v = \beta c$, they are then two parallel currents $I = ve$ which attract each other. The Lorentz force on the particle 2 with velocity $\vec{v}_2$

$$\vec{F} = e(\vec{E} + \vec{v}_2 \times \vec{B}) \tag{1.111}$$

considering that the the beam 1 produces only an electric field in its rest frame

$$F_{x,y} = eE_{x,y}(1 - \beta_1\beta_2) \tag{1.112}$$

if $\beta_1 = \beta_2$

$$F_{x,y} = eE_{x,y}(1 - \beta^2) = e\frac{E_{x,y}}{\gamma^2} \tag{1.113}$$

the force decreases then rapidly with the beam energy, proportional to $1/\gamma^2$. $eE_{x,y}$ is the electric part of the force whereas the $-eE_{x,y}\beta^2$ is the magnetic part which is attractive when $\beta \to 1$ while the electric part stays constant, hence the total force becomes attractive for ultra relativistic beams particle [6].

We consider now a coasting beam, i.e. unbunched with a circular cross section of radius $r = a$ and line charge density $\lambda = \pi a^2 \eta_c$ moving at constant velocity v, the current $I = \beta c\lambda$, with η_c the uniform charge density [Cb/m^3]. In the following, the fields are described in polar coordinates r, ϕ. Due to symmetry, the electric field has a radial component (E_r) while the

magnetic field lines are circles around the cylinder shape beam, hence it has a azimuthal component (B_ϕ). The electric field and the magnetic field components are calculated from the Maxwell equations using the its integral forms, the Gauss law, div $\vec{E} = \eta_c/\epsilon_0$ and the Stroke law, curl $\vec{B}$

$$E_r = \frac{I}{2\pi\epsilon_0\beta c}\frac{r}{a^2} \qquad B_\phi = \frac{I}{2\pi\epsilon_0 c^2}\frac{r}{a^2} \quad r < a \tag{1.114}$$

both electric and magnetic fields vanish at $r = 0$ and increase linearly with r up to the edge of the cylinder ($r < a$). The space charge force $\vec{F^{sc}}$ acting on a particle of charge q within a beam

$$F^{sc} = q(E_r - v_s B_\phi)\vec{r} = \frac{q\lambda}{2\pi\epsilon_0\gamma^2}\frac{r}{a^2}\vec{r} \tag{1.115}$$

Then by replacing r by the transverse coordinates x, y, on might write the forces F_x and F_y

$$F_x = \frac{qI}{2\pi\epsilon_0 c\beta c\gamma^2 a^2}x \qquad F_y = \frac{qI}{2\pi\epsilon_0 c\beta c\gamma^2 a^2}y \tag{1.116}$$

and Ref. [24] describes approximatively the space charge force for a bunched beam with Gaussian densities in r and in s with respectively the rms σ_z for the Gaussian longitudinal density and the rms σ_r for the transverse Gaussian distribution, the radius of the uniform distribution a is replaced by $a = \sqrt{2}\sigma_r$

$$F_r = \frac{e\lambda(s)}{2\pi\epsilon_0\gamma^2}\left(\frac{1 - e^{\frac{r^2}{2\sigma_r^2}}}{r}\right) \quad \text{with} \quad \lambda_s = \frac{q}{\sqrt{2\pi}\sigma_s}e^{-\frac{s^2}{2\sigma_s^2}} \tag{1.117}$$

for particles with $r << \sigma_r$, the space charge force is written as approximatively

$$F_r = \frac{e\lambda(s)}{2\pi\epsilon_0\gamma_0^2}\frac{r}{2\sigma_r^2} \tag{1.118}$$

and for simplicity, one can compute the maximum transverse space charge force,

$$F_{x,y} = \frac{e^2 N_b}{4\pi\sqrt{2\pi}\epsilon_0\gamma^2\sigma_s\sigma_{x,y}^2}(x, y) \tag{1.119}$$

From Eq. 1.116, the force produced by space charge is linear with the transverse coordinates (x, y), comparable to the focusing force from a quadrupole in linear optics. Fig. 1.20 shows the force F_x with respect to x and compares the focusing effect of quadrupole magnet with a uniform and a Gaussian distribution. While the quadrupole is focusing in one plane and defocusing in the other one, the space charge force is defocusing in both planes. From Eq. 1.116 and Eq. 1.119, the space charge force is always defocusing and is directly proportional to the number of particle, hence more intense is the beam, stronger is the direct space charge. This force vanishes for ultra-relativistic beams while $\gamma \to \infty$. The motion of the particle in absence of space charge is the Hill equation and is determined by the linear focusing provided by the

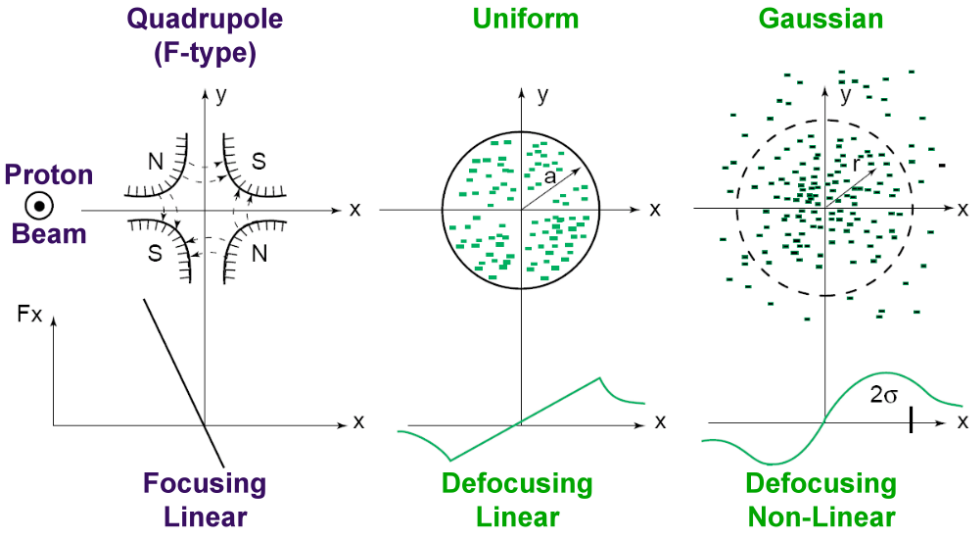

Figure 1.20: Focusing and defocusing force F_x with respect x of a quadrupole (left) and space charge dominated beam: uniform (centre), and Gaussian (right) [6].

quadrupoles. In presence of external forces such as space charge

$$y'' + Q_{y0}^2 \omega_0^3 y = \frac{F^{sc}}{\gamma m_0} \tag{1.120}$$

with F^{sc} computed in Eq. 1.119, m_0 the particle mass, y the vertical position of a single particle, Q_0 the unperturbed tune, ω_0 the revolution frequency. The expression of the space charge force Eq. 1.119 is insert in the equation of motion

$$y'' + \left(Q_{y0}^2 \omega_0^2 - \frac{e^2 N_b}{4\pi\sqrt{2\pi}\epsilon_0 \gamma^2 \sigma_s \sigma_{x,y}^2} \right) y = 0 \tag{1.121}$$

The term is brackets represents the squared of the new betatron frequency with includes the space charge force. We call the corresponding tune Q_y which is related to the unperturbed tune Q_{y0} by

$$Q_y^2 = Q_{y0}^2 \left(1 - \frac{1}{\gamma m_0 \omega_0^2} \frac{e^2 N_b}{4\pi\sqrt{2\pi}\epsilon_0 \gamma^2 \sigma_s \sigma_{x,y}^2} \right) \tag{1.122}$$

The space charge force leads to change in tune ΔQ of the individual particle. The change is assume to be small with $\Delta Q_y << Q_{y0}$, such as the quadratic term can be neglected

$$Q_y^2 = (Q_{y0} + \Delta Q)^2 \simeq Q_{y0}^2 + 2 Q_{y0} \Delta Q \tag{1.123}$$

The change in betatron frequency ΔQ depends of the position of each individual particle,

leading to a incoherent tune shift

$$\Delta Q_{y,inc} = \frac{1}{2Q_{y0}\omega_0^2\gamma m_0} F^{sc} \tag{1.124}$$

Incoherent Tune Shift due to the Beam Pipe Walls

In the last paragraph, the impact of the self-field created by the beam alone results in the direct space charge and in space charge tune spread, incoherent. In real accelerator, a high intensity beam is surrounds by magnets, RF cavities, vacuum pipe, accelerator gaps. The beam induces surface charges or currents into the environment that act back on the beam, resulting in a indirect space charge tune shift.

At the opposite of the direct space charge (direct Colombian repulsion force between protons), the forces acting on a single particle due to the electromagnetic interactions of the beam with its surrounding will depends on the incoherent motion and also on the global position of the bunch particle with respect to the beam pipe walls. Let consider a source particle 1 acting on a trailing particle 2 following at a distance z_1. The positions, here vertical, are considered small enough to be able to linearise the force F_y acting on the test particle. Coupling terms between horizontal and vertical planes are neglected. As already mentioned in Sec. 1.4.1,The resulting wake force is composed into a dipolar contribution F_y^{dip} that depends on the vertical position $y_1$of the source and a quadrupolar contribution F_y^{quad} that depends on the test particle position y_2 [24][36]. This linearization is a first order Taylor expansion of the wake field and was applied to several beam pipe geometries in Ref. The term of dipolar and quadrupolar wake function were chosen to make a parallel with dipole magnet, which gives the same angle independent of the particle position, and quadrupolar since the angle increase linearly with the transverse offset of the test particle. These assumption might be incorrect if the beam are far from center of the element that nonlinear and coupling terms can be significant. The symmetry of the element is also a very important point because it modifies the different contributions - particularly for asymmetric chamber - to the wake force and considering a system of many particle, several contributions to the total force $< F_y >$ due to all the particles acting on the test particle of a vertical position y_2 with a longitudinal distance z to beam center [36]

$$\begin{aligned} \langle F_y(y_2,z)\rangle &= \sum_{i\neq 2} y_i F_y^{dip}(z_i) + \sum_{i\neq 2} y_2 F_y^{quad}(z_i) && (1.125)\\ &= \bar{y}\left(\langle F_y^{dip}(z)\rangle + \langle F_y^{quad}(z)\rangle\right) + \Delta y \langle F_y^{quad}(z)\rangle && (1.126) \end{aligned}$$

where $\langle F_y^{dip}(z)\rangle$ and $\langle F_y^{quad}(z)\rangle$ are the total and quadrupolar forces created by the beam on the trailing particle, $\bar{y}$ is the vertical location of the center of mass of the bunch, $\Delta y = y_2 - \bar{y}$ is the incoherent motion of the trailing particle. We have hence separated the wake force into a

coherent force $\langle F_y^{coh} \rangle$

$$\langle F_y^{coh} \rangle = \bar{y} \left(\langle F_y^{dip} \rangle + \langle F_y^{quad} \rangle \right) \tag{1.127}$$

that depends only on the coherent position of the bunch $\bar{y}(t)$ and an incoherent force $\langle F_y^{quad} \rangle$

$$\langle F_y^{incoh} \rangle = \Delta \langle y F_y^{coh} \rangle \tag{1.128}$$

that depends only on the incoherent position $\Delta y(t)$ of the test particle. From these equation, one can write the motion of any particle from the general equation of motion

$$y_2''(t) + \left(\omega_0^2 Q_y^2 - \frac{\langle F_y^{quad} \rangle}{m_0 \gamma} \right) y_2(t) = \bar{y}(t) \frac{\langle F_y^{dip} \rangle}{m_0 \gamma} \tag{1.129}$$

In the absence of coherent motion, $\bar{y}(t) = 0$ and the quadrupolar force creates then an incoherent vertical tune shift ΔQ_y^{incoh}, which assumes that the wake force is a small perturbation of the particle motion. This leads to an incoherent vertical tune shift

$$\Delta Q_y^{incoh} = -\frac{\langle F_y^{quad} \rangle}{2 m_0 \gamma \omega_0^2 Q_y} \tag{1.130}$$

The perturbed solution can be written as the form [36]

$$y(t) = Re \left[A e^{j(Q_y + \Delta Q_y^{incoh}) \omega_0 t} \right] \tag{1.131}$$

Coherent Tune Shift

The same analysis can be made for the coherent motion for the beam centroid of the particle distribution

$$\bar{y}''(t) + \left(\omega_0^2 Q_y^2 - \frac{\langle F_y^{quad} \rangle}{m_0 \gamma} \right) \bar{y}(t) = \frac{\langle F_y^{dip} \rangle}{m_0 \gamma} \tag{1.132}$$

which leads to the coherent vertical tune shift

$$\Delta Q_y^{coh} = \Delta Q_y^{incoh} - \frac{\langle F_y^{dip} \rangle}{2 m_0 \gamma \omega_0^2 Q_y} \tag{1.133}$$

Eq. 1.129 for the single test particle takes the form [36]

$$y_2''(t) + \omega_0^2 Q_y^2 y_2(t) + 2\omega_0^2 Q_y \left(\Delta Q_y^{incoh} (y_2(t) - \bar{y}) + \Delta Q_y^{coh} \bar{y} \right) = 0 \tag{1.134}$$

The perturbed solution for coherent motion is then of the form

$$y(t) = Re\left[Ae^{j(Q_y+\Delta Q_y^{coh})\omega_0 t}\right] \tag{1.135}$$

From this form, a non zero imaginary part of the coherent tune shift leads

- damping of coherent oscillation for $Im[\Delta Q_y^{coh}] > 0$
- exponential growth of the oscillations for $Im[\Delta Q_y^{coh}] < 0$

The coherent tune shift can be related to the dipolar part of the impedance [36], the beam is assumed coasting,

$$\Delta Q_y^{coh} = \Delta Q_y^{incoh} + j\frac{q_2 I Z_y^{dip}}{2Lm_0\gamma\omega_0^2 Q_y} \tag{1.136}$$

A non zero real part of the impedance leads to an imaginary coherent tune shift, i.e. a damping or growth rate of the centroid depending on the sign of the tune shift. A non zero imaginary part of the impedance leads to a real coherent tune shift, measurable. Both tune shift are proportional to the beam intensity, meaning that while the number of particle increase in the beam, the stability of the bunch can be affected and/or the tune spread is large enough to provoke beam deterioration such as transverse emittance blow up and beam loss.

1.4.3 Beam Break-up Mechanism

This section will be devoted to the Beam Breakup instability, noted BBU. The theory will be described briefly, for more detailed explanations, the reader can refer to Ref. [37, 38] and to Ref. [39, 40] for its application in synchrotrons.

The Beam Breakup theory concerned mainly high-energy linacs since it was observed in linear accelerator. In these type of accelerator, the relative longitudinal positions of the beam particles inside the bunch do not change. The tail particles are always affected by the head particle and longitudinal wake can cause the particles at the tail to lose energy. In high energy linacs, this causes an energy spread, accumulating throughout the whole length of the linear accelerator, may be consequent and can increases the beam size and degrades the beam conditions for collisions in the case of a linear collider. This BBU formalism can be also applied in isochronous or quasi-isochronous rings, where the spread in η for all the particles in the bunch is very tiny, for example, $\Delta\eta < 10^{-6}$. In the case of the CERN PS, it is possible to apply the BBU formalism while the beam is crossing the transition energy, in which the synchrotron motion is slowing down.

If the beam is off center – e.g. due to betatron oscillations – a dipole wake field is excited by the head of the bunch and cause transverse deflection of the tail. For a high intensity beam, the betatron motion of the particles in the tail of the bunch can be seriously perturbed, leading to a transverse break-up of the beam. Let consider the simple two-particle model by which the bunch is represented by two particles of charge $\frac{1}{2}eN$ separated by a distance $\hat{z}$. The transverse displacements of the head, y_1, and the tail, y_2, satisfy

$$\frac{d^2y_1}{ds^2} + k_{\beta_1}^2 y_1 = 0 \tag{1.137}$$

$$\frac{d^2y_2}{ds^2} + k_{\beta_2}^2 y_2 = -\frac{e^2 N W_1(\hat{z})}{2LE} y_1 \tag{1.138}$$

where E is the energy of the beam particles, s the longitudinal distance measured along the designed particle path, W_1 is the transverse wake field, k_β is the betatron wave number, L is the length of the linac or the circumference of the accelerator. When the tune difference between the two particles approaches zero, the tail is driven resonantly the head and its displacement grows linearly with s

$$y_2(s) = y_1(s) - \frac{e^2 N W_1(\hat{z})}{4ELk_\beta}\left(y_{10}\sin k_{\beta_1} s\right) s \tag{1.139}$$

with y_{10} is the initial transverse displacement of the tail. While the beam is running on a length l, the displacement of the tail will grow by Γ folds

$$\Gamma = -\frac{e^2 N W_1(\hat{z}) l}{4ELk_\beta} = -\frac{e^2 N W_1(\hat{z}) \langle\beta\rangle l)}{4EL} \tag{1.140}$$

The growth is written in term beta function, since the transverse impedance initiates a kick y' to the beam and the size of the kick displacement depends on the beta function at the location of the impedance. For a broadband impedance, the transverse wake function at a distance z behind the source particle is, for $z > 0$,

$$W_1(z) = -\frac{\omega_r^2 Z_1^\perp}{Q\bar{\omega}} e^{-\alpha z/c} \sin\frac{\bar{\omega} z}{c} \tag{1.141}$$

where $Z_1^\perp$ is the transverse impedance at the angular resonant frequency ω_r, which is shifted to $\sqrt{\omega_r^2 - \alpha_r^2}$ by the decay rate $\alpha_r = \omega_r/(2Q)$ of the wake with Q being the quality factor. The two particle model cannot be applied for all the bunch length and if $\bar{z}$ falls on the first zero of $W_1(\bar{z})$, Eq. 1.140 says there is no growth at all. However, the particles in between will be deflected and they certainly affect the tail particles. The rms bunch length should be less than half the reduced wavelength λ_r of the resonant impedance.

$$\sigma_l << \frac{1}{2}\frac{\lambda_l}{2\pi} \tag{1.142}$$

Let consider a resonator broadband impedance with $Q = 1$ and $\omega_r = 1$ GHz, $\frac{1}{2}\frac{\lambda_l}{2\pi} = 15$ cm. In the case of the CERN PS, bunch length are of the order of meter at injection and transition, which is our interest in our studies. The two particles model cannot be applied in our case, which is the case for most protons bunches.

In Ref. [40], a formula has been derived for a single bunch BBU in circular machine from the theory developed by Yokoya. The bunch is approximated by a train of short bunchlets and apply the Yokoya formula for cumulative BBU in a train of bunches, with the initial condition that every bunch in the train has the same initial offset. Moreover, the computation has been done with the absence of acceleration and for the smooth approximation $Q_{x,y} = \beta_{x,y}/R$. The time between the bunchlets is assumed to be small compared to the decay time of the considered resonator $2Q/\omega_r$ and the wave period $T_r = 2\pi/\omega_r$. The ratio between the amplitude of the bunch tail after n turns in a circular machine, in the vertical plane

$$\frac{y_n}{y_0} = \frac{1}{2\sqrt{2\pi}} \times \left(\frac{\omega_0 L}{c}\right)^{1/4} \frac{c}{L\omega_r} \times e^{-\frac{\epsilon l}{c} + \sqrt{\frac{\omega_0 L}{c}}} \tag{1.143}$$

with

$$\frac{\omega_0 L}{c} = \frac{N_b e c}{\omega_{y0}(E/e)} \times \frac{\omega_r Z^\perp}{Q} n \tag{1.144}$$

with $\omega_{y0} = Q_{y0}\omega_0$ is the unperturbed betatron angular frequency and $\epsilon = \omega_r/Q$. As it was shown in Ref. [40] that the BBU mechanism is essentially described by the exponential term of Eq. 1.143.

2 The CERN Proton Synchrotron

Nowadays 53 years old, the CERN Proton Synchrotron belongs to the LHC injector chain. Beyond this role, the CERN PS has a central position in the accelerator complex and supplies beams for other important experiments. This chapter is devoted to the description of the PS to help the reader to understand not only the global operation of the machine but also the particularities that the user can be confronted with this machine. A brief description will be given of the different types of beam provided to experiments and to LHC. A particularity of the PS is the main magnet system which is composed by combined function magnets with special windings mounted on the poles, the so-called Pole Face Windings (PFW). They generate higher order components of the magnetic field and hence they can be used to setup the working point. A short description of the PFW operation will be given in this chapter.

2.1 General machine parameters

The final design of the CERN PS was adopted in 1954 and the PS was the first proton synchrotron with strong focusing ever built. The first beam accelerated up to 24 GeV happened in 1959 [7]. At that time, the linear acccelerator LINAC1 was the injector of PS with 50 MeV proton beams until the LINAC2 and the PSBooster took over in 1978. Today the PS accelerator complex is composed by the LINAC2 and LINAC3, PSBooster, LEIR (Low Energy Ions Ring), the Antiproton Deccelerator (AD) and the PS, as shown in Fig. 2.1. The CERN Proton Synchrotron is a ring of approximatively 628 m circumference composed by 100 main magnets and straight sections [41]. The number of betatron oscillation for the bare machine is 6.25 and 6.28 respectively in the horizontal and in the vertical plane. Table 2.1 summaries some important PS parameters. Over the years the injection kinetic energy of the proton beams changed and is currently set at 1.4 GeV. The extraction energy is not fixed and is different according to the beam purpose. Currently, the PS provides also lead ion beams [42] Pb^{54+} for the LHC experiments from the pre-injectors LINAC3 and LEIR [43].

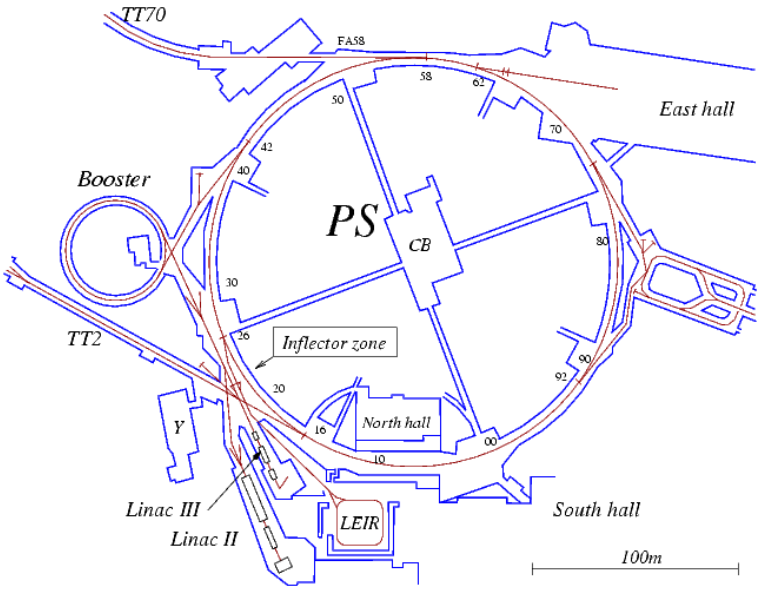

Figure 2.1: Proton Synchrotron complex layout [7]

General parameters	
Circumference [m]	$2\pi 100$
Number of straight sections	100
Vacuum chamber type	elliptical
Standard vacuum chamber aperture [mm]	140×70
Maximum dB/dt [Gauss/ms]	21
Bare Tunes $Q_{x,y}$	6.25/6.28
Bare chromaticities at injection $\xi_{x,y}$	$\sim -0.8/-1$

Table 2.1: General parameters of the CERN Proton Synchrotron

2.2 Beams in the CERN PS

A typical magnetic cycle duration of the PS is a multiple of 1.2 s and defined as a basic period. During this time, the beam is injected, accelerated, extracted and the time left is dedicated to the magnetic field decreasing as shown in Fig. 2.2a. Since the end of the 90's, the injection kinetic energy of the PS is 1.4 GeV for the proton beams. Fig. 2.2a shows that the protons are kept at constant magnetic field at least 30 ms on a flat bottom plateau in such a way the beam reaches an equilibrium state in the transverse and longitudinal planes, in case of injection errors. Indeed the beam can experiment a trajectory transient if injected at a wrong position in the phase space (x, x') and (y, y'), resulting in an emittance blow up. The beam is then accelerated with a magnetic field rate dB/dt of about 21 Gauss/ms or a momentum rate of 46 GeV/c/s. Finally the beam is extracted toward the SPS or a PS experiment. The Proton Synchrotron used to accelerate different types of particle: proton, electron/positrons, ions,

antiprotons and even deutons and α^- in the 80's [7, 44]. Currently only protons and ions are used in operation for the LHC and other experiments such as:

- nToF (Neutron Time of Flight) [45] is a PS dedicated experiment.
- AD is a ring decelerating antiprotons which are produced by 26 GeV/c protons hitting a target [46].
- the experiments in the East Area of the PS such as an irradiation zone or the DIRAC experiment [47] [48].
- beams are provided to the SPS experiment CNGS which aims to produce neutrinos observed in the OPERA detector in Italy [49].

The CERN PS will continue to provide beams during at least the next 25 years. The challenge is to continuously increase the number of proton for high intensity beams but also to produce high brightness beams, i.e. a larger beam intensity in small transverse emittance for the LHC. The Table 2.2 shows the beam parameters for two high intensity beams ToF and AD compared to the nominal LHC beam. Fig. 2.2a and 2.2b present respectively the magnetic field as a function of time of a ToF beam and of a LHC 25 ns. In particular, Fig. 2.2b shows that the flat bottom injection plateau is very long, about 1.2 s knowing that the beam goes in the PS at 170 ms. On this injection plateau, the PSBooster injects twice protons in the PS ring as it is also shown in Fig. 2.3. This is the so-called double batch Injection: a first injection is done in the PS from the four rings of the PSBooster at 170 ms and the second occurs about 500 ms after the first one. Therefore the bunches injected at 170 ms stay then 1.2 s on the flat bottom. The next paragraph will focus on the PS as LHC injector and how the LHC beams are produced.

Beam	ToF	AD	LHC Nominal (25 ns)
Maximum Intensity [10^{10}]	850	1600	940
# bunches	1	4	$6 \rightarrow 72$
Transverse emittance ($\epsilon^*_{x,y}$ (1 σ))	12.5/10.4	11.5/6.4	3/3
Longitudinal emittance (ϵ_l (2 σ))	2.3	1.8	0.35 (4 σ) at extraction
Bunch length at PS extraction [ns]	50	25	4

Table 2.2: Beam parameters of high intensity beam ToF and AD and the LHC 50ns or 25ns beam, where 50 and 25 refer to the bunch spacing at extraction energy. [12].

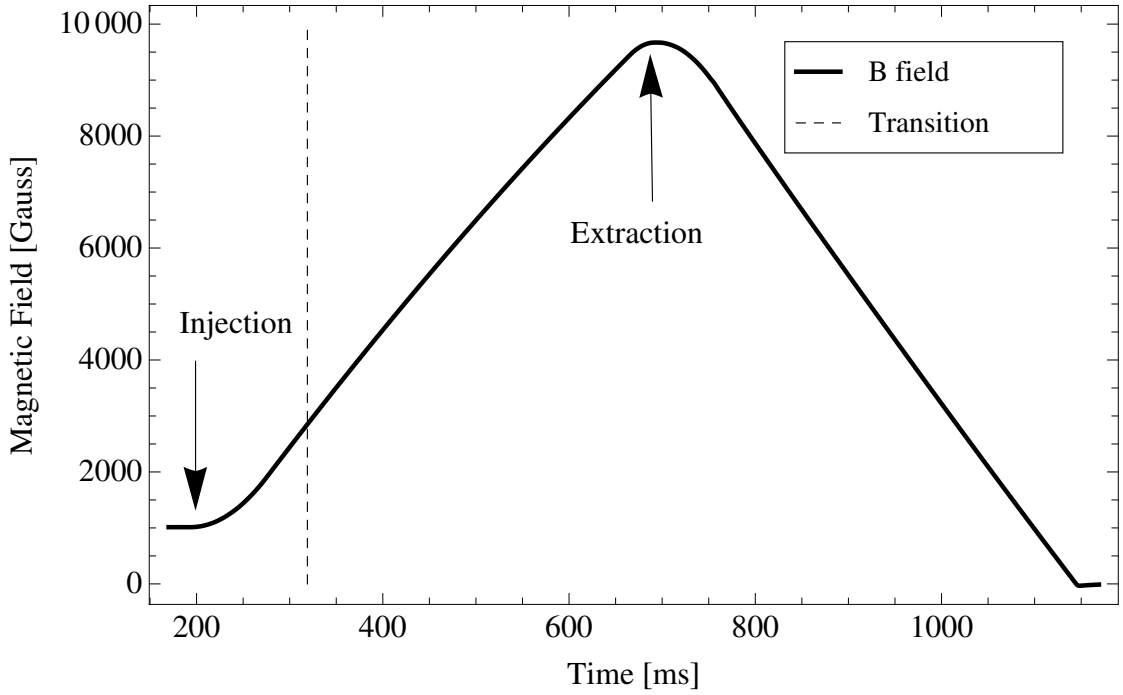

(a) Example of magnetic field in Gauss as a function of time for a ToF beam. At the 1.4 GeV injection kinetic energy, the magnetic field is about 1013.2 Gauss during the flat bottom plateau of about 30 ms. The beam is then accelerated and extracted.

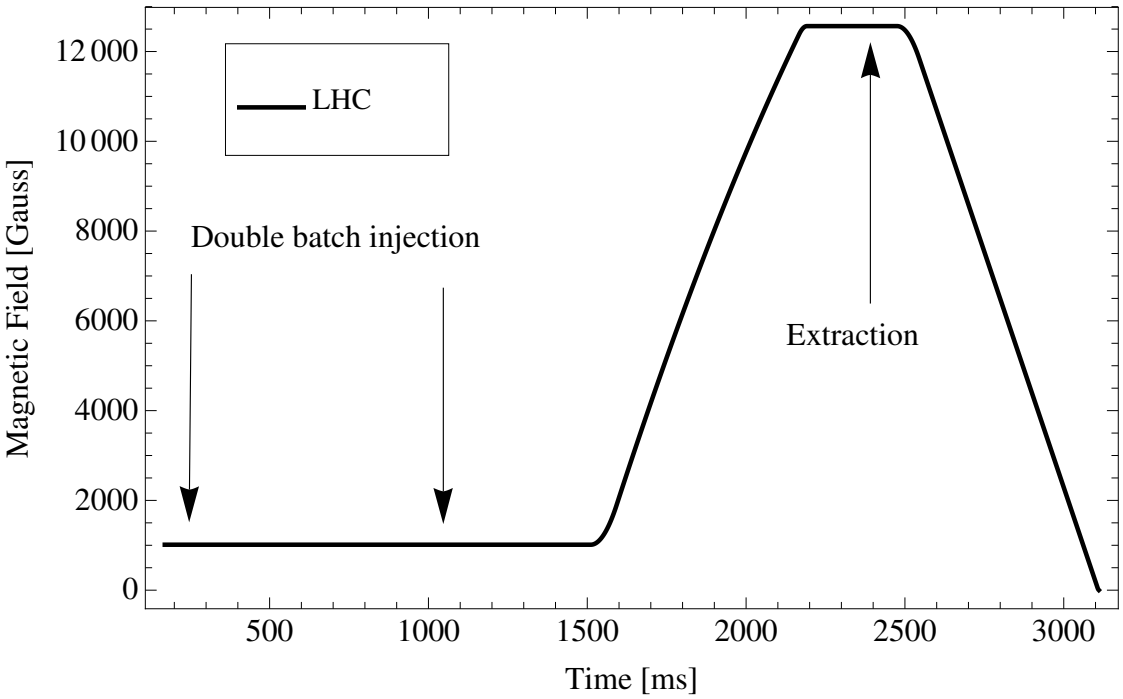

(b) Example of magnetic field in Gauss as a function of time for LHC 25 beam. The injection flat bottom is 1.2 s long.

Figure 2.2: Example of magnetic field cycle for the ToF and the nominal LHC 25 ns beams.

The PS as LHC Injector

This section provides a short description of the production of LHC multi-bunch beams in the PS meant for LHC physics experiments. According to the production scheme, the LHC-type beams transverse emittances should be defined in the PSBooster, whereas the longitudinal structure should be the result of a complicated series of RF gymnastics done in the PS. The beam should be cleaned by eventual tails in the SPS and eventually, the longitudinal and/or the transverse emittances might be increased by controlled blow-ups [50, 51]. Four different LHC multi bunch beams with the parameters of Table 2.3 are prepared in the PS. The differences come from the bunch spacing and the intensity per bunch at the extraction of the PS meant for different purposes.

Beam	# bunches	ϵ_l [eVs]	Intensity per bunch
LHC25	12 to 72	0.35	up to 1.3e11 ppb
LHC50	12 to 36	0.35	up to 1.9e11 ppb
LHC75	8 to 24	0.35	up to 1.3e11 ppb
LHC150	4 to 12	0.35	up to 1.3e11 ppb

Table 2.3: Parameters of the LHC beams produced in the PS at extraction [7, 13].

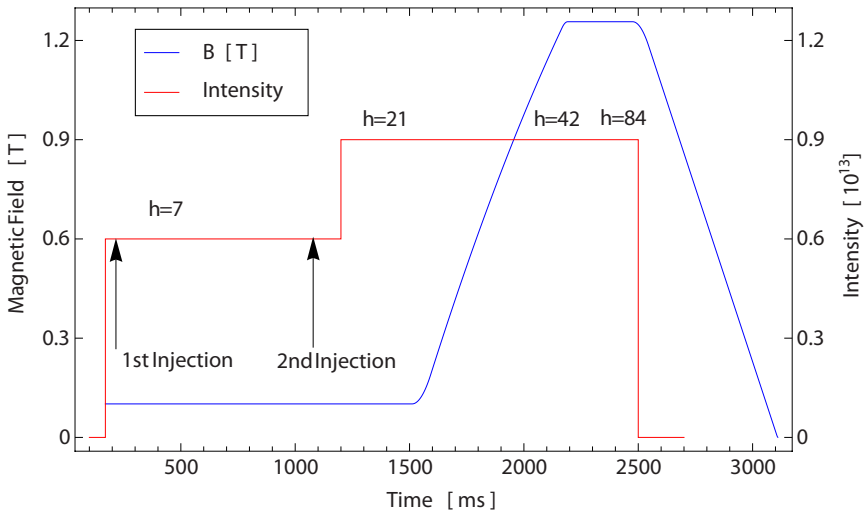

Figure 2.3: Production of the LHC 25 ns beam in the PS with the double batch injection on the 1.2 s long flat bottom plateau. The blue curve is the magnetic field as a function of time, the red is the beam intensity in number of protons and as a function of the harmonic number changed by the successive RF gymnastics.

In order to prepare the LHC 25 ns beam, a double batch injection from the PSBooster is needed in the PS: four bunches are injected on a long flat magnetic field plateau then completed by two other bunches later in the cycle, as shown in Fig. 2.3. The reason of the double batch injection is that the transverse emittance produced by the PSBooster is a linear function of the total beam intensity due to the multi-turn injection in the PSBooster [52] and the full intensity required for LHC beams cannot be achievable in a single injection in the PS without compromising the LHC requirements. The harmonic number h is 7 at 1.4 GeV, then right after the second injection, each bunch is triple splitted (Triple Splitting) as shown Fig. 2.4a, the process is described in Ref. [53]. The harmonic number changes then from $h = 7$ to $h = 21$. The bunches are then accelerated and again double splitted two consecutive times (Fig. 2.4b) at top energy to give finally 72 bunches. The harmonic number changes again from $21 \rightarrow 42 \rightarrow 84$. Each bunch is longitudinally rotated to fit in the 4 ns long SPS bucket. The beam is extracted in the TT2-TT10 transfer line with a single turn fast extraction toward the SPS.

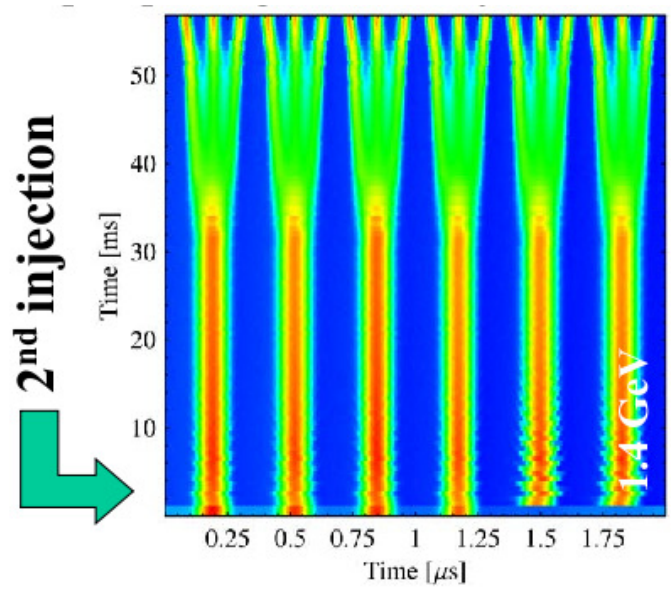

(a) Splitting in 3 bunches after the second injection.

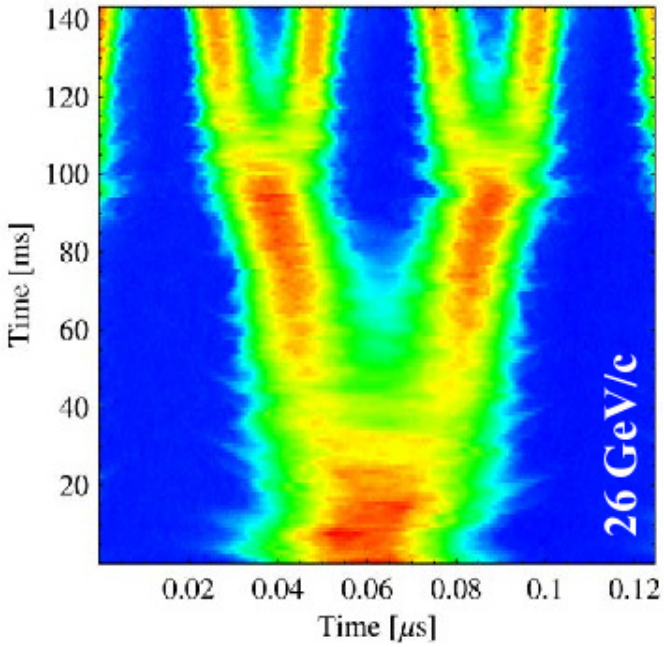

(b) Splitting in four beam before the extraction.

Figure 2.4: RF gymnastics for the production of the LHC 25 ns beam in the PS [13]: Fig. 2.4a at injection and Fig 2.4b.

2.3 The CERN PS Main Magnet System

The main magnet system of the PS consists of 100 combined-function normal conducting magnet units (MU), each composed of a focusing (F) half-unit and a defocusing (D) half-unit Fig. 2.5 [54].

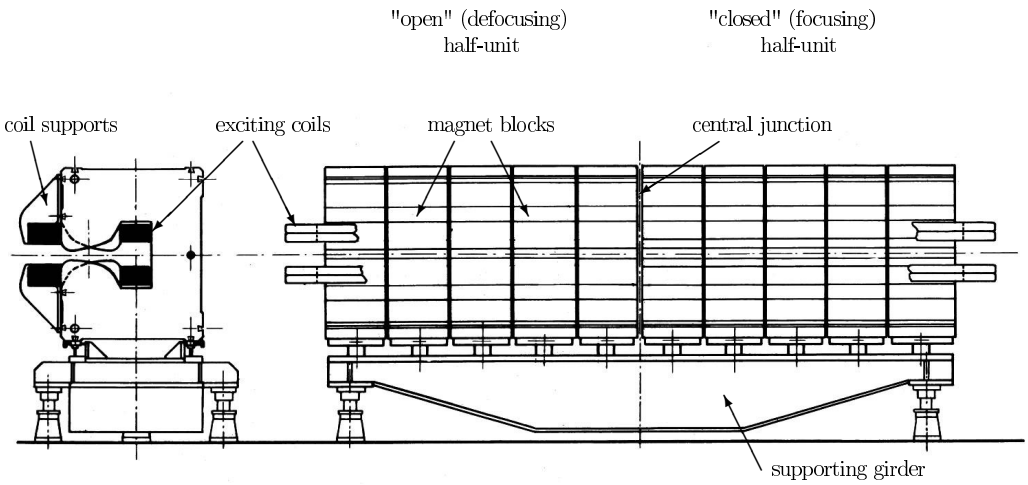

Figure 2.5: A CERN PS main magnet unit [8].

Between two magnet units, there is a straight section, which is field-free so that the PS lattice pattern is FOFDOD, see Fig 2.6, with F for focusing, D defocusing and O for the field free sections. A half-unit is composed of five adjacent magnet blocks, each 417 mm long. A block is a C-shaped structure of open or closed type Fig. 2.7 [7, 8, 41].

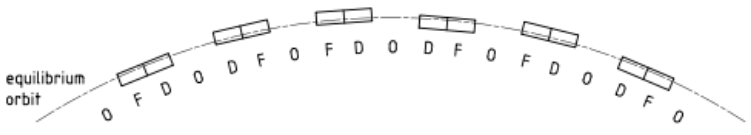

Figure 2.6: FOFDOD lattice structure of the CERN PS.

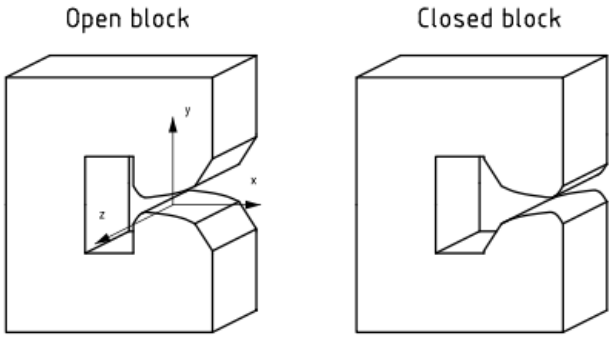

Figure 2.7: Iron block of the main unit magnet.

With local magnetic lenses, a correction can be made at given points in the straight sections between the main magnet units. Correction windings placed on the magnet poles Fig 2.8, namely Pole Face Windings (PFW) [7, 55, 56], act along the whole main magnet unit. The idea of the PFWs is to generate quadrupolar, sextupolar and octupolar components. The performance of the PFW is nevertheless limited by the relatively low currents which can be used [57]. The PFWs are divided into four independent circuits (Fig. 2.9). Two of them are mounted on the poles of the focusing (F) part of the main magnets, and the two others on the defocusing (D) part [57, 58]. The F and D circuits each are divided into a wide and a narrow circuit as shown in Fig. 2.9. The wide circuit winding (W) covers the whole magnet poles, while the narrow circuit winding (N) only covers the poles where the gap is narrow. The individual circuits are named DN, DW, FN, and FW. The 8L is a winding describing a figure-of-eight around the poles of both halfs of the magnet and therefore crosses between the focusing and defocusing part (Fig. 2.9).

The PFW are used in normal operation to setup the working point (Q_x,Q_y,ξ_x,ξ_y) with $Q_{x,y}$ the transverse tunes and $\xi_{x,y}$ the chromaticities [57–59]. Before 2007, the PFW and 8L were powered by three independent power converters, each controlled by their own current function generator [58]. The circuits were connected in series and parallel, which had the advantage to partly cancel the currents induced by the main magnetic field variations, i.e. the $\dot{B}$ [60] which is dB/dt. This mode of operation was called the three currents mode and the available currents are $I_F, I_D, I_{N,W}$ being respectively the currents in the PFW in the focusing and defocusing part and the currents in the narrow-wide circuits. In the three currents mode - circuit in series -, the Narrow N and Wide W are powered in the same way. Therefore three currents are available to control the four parameters of the working point. A renovation of the power converters led to one independent power supply per PFW and 8L, the five current mode [60, 61] - circuit in parallel -, which allows to set all the working point parameters. However this mode increases the magnetic field non-linearities. Chromaticity measurements done at injection energy

using the PFWs in 5-currents mode pointed out that this mode increases the higher order of chromaticity components. This aspect will be explained more in detail in Chap. 5. The comprehension of the PFWs operation is important to understand how was set the working point during the fast transverse instability measurements at transition energy described in Chap. 4.

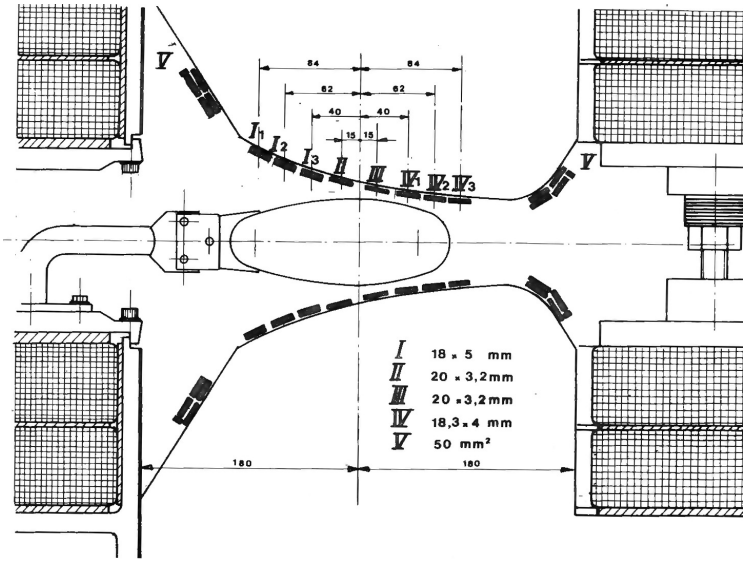

Figure 2.8: Cross section of a magnet pole with the Pole Face Windings.

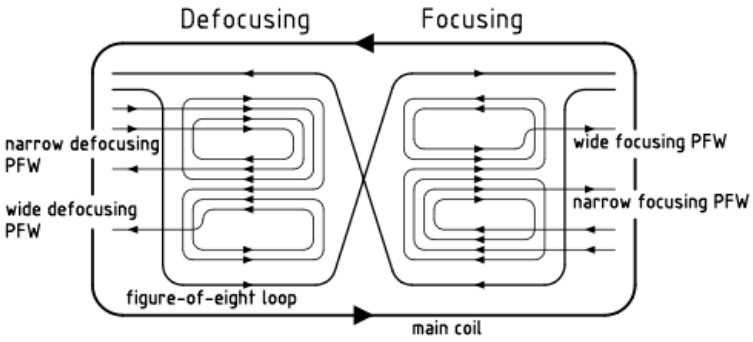

Figure 2.9: Pole Face Winding description.

2.4 Control of the Working Point

In most modern synchrotron, dedicated magnets are used to set chromaticities $\xi_{x,y}$, whereas the control of the working point (Q_x, Q_y, ξ_x, ξ_y) is achieved in the CERN PS by the PFWs and the figure of eight loop (8L). Beam-based measurements were performed in 2009 at different beam energies to correlate a variation of currents powering the PFW and the 8L to the parameters (Q_x, Q_y, ξ_x, ξ_y) starting from a working point used in normal operation. The complete procedure is described in Ref. [58]. The aim was to find the matrices M as different beam energies such as

$$\begin{pmatrix} \Delta Q_x \\ \Delta Q_y \\ \Delta \xi_x \\ \Delta \xi_y \end{pmatrix}_p = M(4\times 5)_p \begin{pmatrix} \Delta I_{FN} \\ \Delta I_{FW} \\ \Delta I_{DN} \\ \Delta I_{DW} \\ \Delta I_{8L} \end{pmatrix} \tag{2.1}$$

where $Q_{x,y}$ are the transverse tunes, $\xi_{x,y}$ the chromaticities respectively in the horizontal and vertical plane, p the beam momentum, $\Delta I_{FN}, \Delta I_{FW}$ are respectively the current variation in the focusing narrow and wide circuits of the PFW, $\Delta I_{DN}, \Delta I_{DW}$ are respectively the variation of the currents in the defocusing narrow and wide circuits of the PFW and finally ΔI_{8L} the variation of the current in the eight loop. The matrice measurements were performed from a ΔI variation of the currents powering the PFW, since the linear relation between physical parameter and current is assumed to be valid only around the predefined set of currents or physical parameters.

Chromaticity is measured by introducing a radial offset ΔR which modifies the revolution frequency of the beam by Δf. The momentum offset Δp is then calculated at the first order from

$$\frac{\Delta p}{p} = \frac{1}{\eta}\frac{\Delta f}{f} \tag{2.2}$$

The chromaticity is then obtained by acquiring the tune Q with respect to the introduced momentum offset

$$\frac{\Delta Q}{Q} = \xi \frac{\Delta p}{p} \tag{2.3}$$

At transition energy neighborhood, a radial offset does not change significantly the revolution frequency which makes chromaticity measurements difficult. This is also the reason why the PFW matrices M was not determined explicitly at this energy. An interpolated matrice is then used at transition as it will be explained in Sec 4.1.2.

2.5 Important remarks

In this section, we have voluntarily omitted to describe the injection and the transition process. Chap. 5 is entirely dedicated to injection studies in which will be described the transfer line between the PSBooster and PS and the single turn injection into the CERN Proton Synchrotron. Crossing Transition energy in the PS is explained in Chap. 1.3.

This chapter was dedicated to introduce the operation of CERN Proton Synchrotron. The commissioning of the accelerator occurred 53 years ago and since then the beam intensity delivered by the machine continuously increases over the years. Therefore the PS is nowadays confronted to numerous intensity limitations at injection, transition energy – which are the subjects of this thesis – and at extraction energies. The multiple extraction systems of the PS are not described here since there are not the subject of this thesis, however we can just cite that the CERN Proton Synchrotron includes several beam extraction systems such as

- a fast extraction at 26 GeV/c in which the beam extracted through the septum in one turn thanks to a the extraction kicker. This is used for LHC beams.
- a slow extraction at 24 GeV/c using the third order resonance [62] is performed on beams delivered to the EAST experimental areas.
- a continous transfer (CT) extraction at 14 GeV/c in which the beam is extracted in five turns but this method became problematic for high intensity beams due the induced irradiation in the ring [63]. This type of extraction is performed on beams for the CNGS experiment.
- a Multi Turn Extraction (MTE) was implemented in order to replace the CT extraction. It is a unique extraction system based on trapping in stable beam islands in the transverse phase space [64].

This chapter showed that the CERN PS is a versatile machine, accelerating various kind of particle up to different energies with a large range of beam intensity. For similar radiation constraints as the CT extraction [65], the injection of high intensity beams into the PS constitutes a limitation due multiple sources which are mainly based on aperture restriction and on collective effects. Chapter 5 describes the studies carried out at 1.4 GeV kinetic energy aim to understand the large amount of beam losses occurring during the injection process of high intensity beams.

3 Simulation Codes

3.1 MAD-X

The first version of the program MAD [66] (Methodical Accelerator Design) was developed at CERN in 1983. It is a tool for designing the optics of accelerators, storage rings and transport lines. The current version, which has been used throughout this thesis, is called MAD-X. A beginners guide can be found in Ref. [67], while a detailed description of the physics of the core module, which has not changed since the previous version MAD-8, can be found on the website [66].

MAD-X is a command-line driven program with a text-based interface. It uses a special language in which the user writes an input file. From this file, MAD-X reads definitions of magnetic elements and their sequence as well as the tasks that should be carried out. The sequence is used to calculate a closed orbit and the optical functions discussed in Sec. 1.1.

MAD-X has also a matching module, which can be used to find magnetic strengths that will produce desired values of the optical functions at given positions under certain constraints. MAD-X can also handle and correct possible machine imperfections and it can be used for both circular and linear accelerators.

3.2 FLUKA

The simulations of Sec. 5.6 were performed using the FLUKA program [68, 69], which is a Monte Carlo code for particle interaction and transport through a user-defined 3D geometry.

The first version of FLUKA was developed as long ago as in 1962 at CERN. This version handled only high energy proton beams and was used to design shieldings of high energy proton accelerators. Since then, the code has been continuously modified and improved in order to handle new particles, energy ranges and interactions. The physics has evolved over the years and FLUKA has been updated to include better and more accurate models.

FLUKA is based on five major modules, which are fully integrated with each other, that handle different interactions and particles: Hadrons, muons, electrons and photons, low-energy neutrons, and heavy ions. The code is based on nuclear models, except the low-energy neutron module, which handles neutrons with an energy below 20 MeV. This module uses instead a tabulated cross section library. A detailed description of the modules and the physical models they are based on is however beyond the scope of this thesis but can be found in the FLUKA manual and other online material [70].

In the default mode, FLUKA tracks every particle created in every interaction. This execution mode, which is called analogue, is very slow in terms of computational speed, especially at higher projectile energies. Therefore, different biasing techniques are used to speed up the simulation. Biasing was used in most simulations described in this thesis.

3.3 HEADTAIL

HEADTAIL is a simulation code developed by G. Rumolo et al. [71] which aims at simulating on successive turns the interaction of a bunch of particle with a source of impedance or with electron cloud driven instabilities [72]. The bunch is divided into slices and the user defines a number of macro particle of charge Q. Each macro particle in a slice gets a kick due to the wake field created by the preceding. Considering the vertical wake force generated by a source charge Q_1 on a test particle with a charge Q_2, the vertical angle kick $\Delta y'$ due to the force from the wake potential W_y^{pot} can be written as following [36]

$$\Delta y' = \int \frac{F_y}{m_0\gamma\beta^2c^2}ds = \frac{1}{m_0\gamma\beta^2c^2}\int F_y ds = Q_1Q_2\frac{W_y^{pot}}{m_0\gamma\beta^2c^2} \tag{3.1}$$

where m_0 is the mass of the particle, γ,β are the relativistic parameters, c is the speed of light. Let consider that the bunch is sliced from the head ($i = 1$) to the tail ($i = N_{slice}$). At a given turn in the simulation, a slice i contains $N(i)$ macro particles of charge Q with the total charge $Q_1 = N(i)Q$. The position of the center of mass of the slice i is located at $(\langle x(i)\rangle, \langle y(i)\rangle)$ at the location of the interaction between the beam and the perturbation. A macro particle of charge $Q_2 = Q$ at a transverse location (x, y) within a following slice j, with $j < i$, gets the total angle kick $\Delta y'(i)$ from the slice i [36], assuming that there is no coupling between the horizontal and the vertical plane,

$$\Delta y'(i) = \frac{N(i)Q^2}{m_0\gamma\beta^2c^2}W_y((j-i)\Delta z, x, \langle y(i)\rangle) \tag{3.2}$$

with Δz is the length of a slice and $W_y((j-i)\Delta z, x, \langle y(i)\rangle)$ is the wake function generated by a source slice at a vertical position $\langle y(i)\rangle$ on a test macroparticle at distance $(j-i)\Delta z$ from the source slice and a horizontal position x. Once the angle kick is given to the macro particles, the transverse position is tracked from one interaction point to another (turn by turn if there is only one kick) using the linear optics parameters of the machine provided by an input file. The

longitudinal coordinates are obtained by simple transport in the case of a linear longitudinal restoring force valid for small synchrotron oscillations as described in Sec. 1.2. More details about the use of the HEADTAIL code will be provided all along Sec 4.4.1.

4 Fast Transverse Instability at Transition Energy

In the previous paragraphs, it was pointed out that the CERN PS is a very versatile machine. During the last years it became a key-accelerator with a central position in the LHC accelerator chain and with the largest number of beam destinations in the CERN complex. Although a significant part of its working time is dedicated to providing beams to LHC, particular attention is given also to high intensity beams. As the intensity per bunch has increased over the years, limitations directly related to high intensity beams were discovered and constrained the number of particles that can be accelerated in the PS. This is a serious problem, since both CNGS and high-luminosity LHC require an increase in the number of protons per bunch. Therefore, an effort has to be done to understand these limitations and several studies are underway to improve the beams for the different experiments that the PS has to deliver beams for. Those issues are diverse and the current problems in the PS are beam losses caused by aperture restrictions and large transverse emittances, space charge, and beam instabilities driven by impedance.

The crossing of transition energy is also affected by these issues. The use of dedicated fast pulsed quadrupoles to perform the gamma transition jump increases the β-function and therefore the beam size in some parts of the machine, which provoke severe beam losses. They can be aggravated by longitudinal beam control problems [73]. Furthermore, transition energy is the moment when the synchrotron motion of the beam is frozen. When the particles do not move anymore in the bucket, they are particularly sensitive to wake forces from the machine impedance. While the beam intensity of the ToF single bunch beam was increased, a fast instability appeared around transition energy in the vertical plane, provoking a large emittance blow-up and beam losses [39]. The experiments of Ref. [39] considered the instability as being similar to the Beam Breakup in Linacs [37]: under the influence of a broadband wake field, the particles in the head excite those in the tails and the absence of synchrotron motion does not allow the beam to stabilize. Therefore the time the beam stays at transition neighbourhood with a very slow longitudinal motion has a strong influence on the instability mechanisms.

This instability is developing within a few hundred turns even with the use of the gamma transition jump [39], which is otherwise a good way to cure instabilities. The gamma transition

jump allows to cross quickly the nonadiabatic region as explained in Sec 1.3.6 by changing the unperturbed momentum compaction factor η shown in Fig. 1.18, reducing the zone in which the synchrotron motion is frozen. However, the instability can appear even in the presence of synchrotron motion if the rise time is faster than the synchrotron period T_s. Several formalisms exist for this kind of instability developing faster than T_s such as post headtail theory, Transverse Mode Coupling formalism [74]. However, they take into account synchrotron motion. The framework of the fast vertical instability occurring in the CERN PS is at the limit of those formalisms and also of the Beam Breakup theory [37] in which there is no synchrotron motion. The instability concerns mainly single bunch and high intensity beams. Up to now, the instability was cured by blowing up the longitudinal emittance. However, this solution has limitations, since it requires an increase of the RF voltage applied to the cavities, which are nowadays at their voltage limit. Therefore, it is important to further study and understand the instability in order to pave the way for future performance improvements.

In this chapter, new measurements of the fast transverse instability, performed around transition energy, are presented. This work consists of an extensive campaign of new measurements in much greater detail than previously and is meant to study the instability mechanisms. A particular attention was given to the setting up of the working point and especially the vertical chromaticity ξ_y. It induces a tune spread with the momentum of each particles, which is a way to increase the intensity threshold of transverse instabilities. Measurements of the transverse instability without gamma transition jump are described and the results discussed and compared to multi particle simulations using the *HEADTAIL* code in order identify the instability mechanisms and deduce an effective impedance using a simple broadband resonator model.

Measurements performed with the gamma jump are also presented in this chapter and then compared to the results of the unperturbed optics and to *HEADTAIL* simulations. As expected, the experiments show that the intensity thresholds of the instability can be considerably increased with the gamma transition jump and by an adequate adjustment of the chromaticity. Considerations about the role of the working point of the beam will also be discussed. The limitations of the model used in *HEADTAIL* are discussed, since the broadband impedance is not sufficient to match all the experimental observations. Modelled and measured instability parameters are compared to analytical formulas and other possible topics for future works will be discussed.

4.1 Beam setting up for measurements

This section describes the experimental conditions under which the measurements were performed as well as the detailed setting up of the beam. The most important parameters to adjust in these experiments are the time at which the stable phase shift must be done - see Sec. 1.3.2 - and the working point.

When the gamma jump is turned off, the energy of transition is changed as shown in Fig. 1.17. Therefore the instant when the stable phase shift is done has to be changed as well. This is

important to keep the longitudinal focusing in the bucket on both sides of transition energy and avoid longitudinal blow-up. The following paragraph explains an empirical way to identify the transition energy timing. Chromaticity is also a crucial parameter for thresholds in intensity of an instability. The setting up of the working point will be explained as well as the instrumentation used to observe the fast vertical instability. Experimental observations of the instability are also described in order to give to the reader a first overview of the instability development along the bunch.

4.1.1 Transition energy timing

A single bunch beam was set up without the gamma transition jump in order to study the dynamics of the fast transverse instability through transition energy with the nominal variation of η and without any complex change of the optics. This beam was made part of the PS super cycle and thus injected, accelerated and extracted a large number of times. The magnetic field cycle of the beam and the energy as a function of time are presented in Fig. 4.1. The beam parameters used during the measurements are presented in Table 4.1. The RF voltage of the cavities mentioned in Table 4.1 is the voltage used during the acceleration of the beam particle.

Total energy at γ_{tr} [GeV]	$E \simeq 6.1$
γ_t	6.12
Transverse tunes	$Q_x \simeq 6.22$, $Q_y \simeq 6.3$
RF Harmonic	h=8
Number of bunches	1
Total RF cavity voltage [kV]	145
Bunch intensity	$65 \cdot 10^{10}$-$165 \cdot 10^{10}$
Full bunch length [ns]	30
Longitudinal emittance (2σ) [eVs]	1.29 – 2.4
Transverse emittance norm. (1σ)[mm mrad]	$\epsilon_x = 1.17 - 2.38$ $\epsilon_y = 1.34 - 2.33$

Table 4.1: : Beam parameters during the measurements.

The longitudinal emittance is measured at the beginning of the acceleration as presented in Fig. 4.2. At t=170 ms the beam is injected. The RF voltage during the injection plateau, defined from t=170 ms to 200 ms, varies with respect to the requested value of the longitudinal emittance. Therefore, the first step of the experimental procedure is to adapt the RF voltage to the particular test beam in order to reduce a possible longitudinal mismatch between the incoming beam and the PS bucket. In the presence of longitudinal injection errors, the bunch oscillates in the bucket and filaments to give a larger emittance after few synchrotron periods. This is why ϵ_l is measured at the beginning of the acceleration at t=200 ms in order to get a value for a bunch matched to the bucket. The rms longitudinal emittance stays constant during the acceleration if no blow up occurs. The next step of the experimental procedure is to identify the transition energy during the ramp in order to set the shift of the RF stable

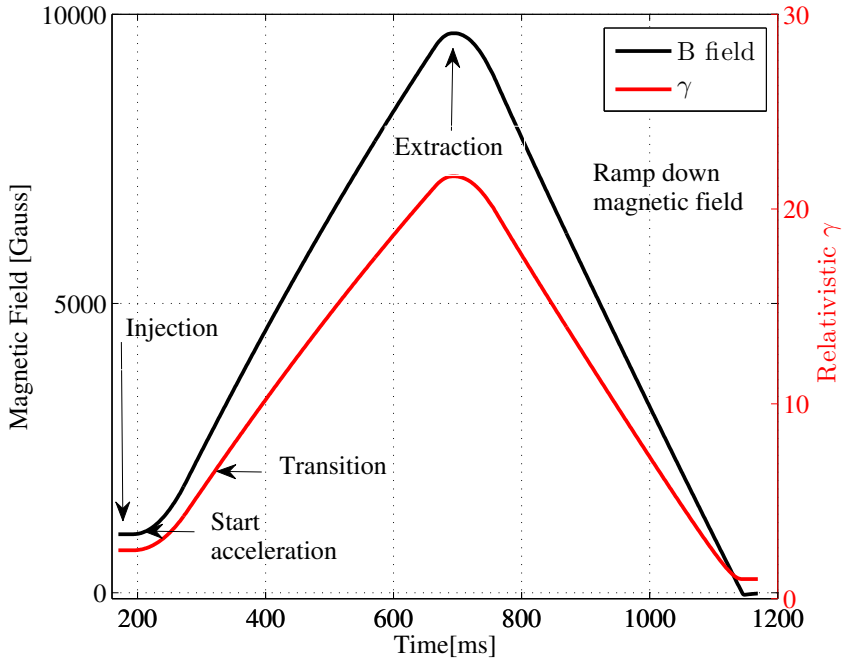

Figure 4.1: Magnetic cycle and relativistic parameter γ as a function of time. The cycle t starts at t=170 ms, i.e. when the beam is injected.

phase ϕ_s at the suitable moment. The time t at which the RF stable phase jump is performed must be correctly tuned in order to keep the longitudinal focusing below and above transition energy as we explained in Section 1.3.5. Ideally the RF stable phase should jump from ϕ_s to $\pi - \phi_s$ at a time t which satisfies

$$\eta(t) = \frac{1}{\gamma_t^2} - \frac{1}{\gamma^2(t)} = 0$$

The time t when the RF phase jump is performed will be considered in the measurements as the transition time.

A mistiming in the RF phase shift can cause bunch length oscillations and longitudinal blow up as described in Ref. [4]. However, it exists a time tolerance for the phase shift known to be about 1 ms [4] for the CERN PS. A mistiming within this tolerance is not critical due to the frozen synchrotron motion [23]: even if the beam is set at a wrong RF phase, the energy gain per turn weakly affects the revolution frequency, therefore the protons do not move in the bucket while they are in the nonadiabatic region. The setting up of the RF stable phase jump has to be at low intensity in order to alleviate bunch length oscillations excited by longitudinal space charge and longitudinal impedance [26][5], which are effects driven by high intensities.

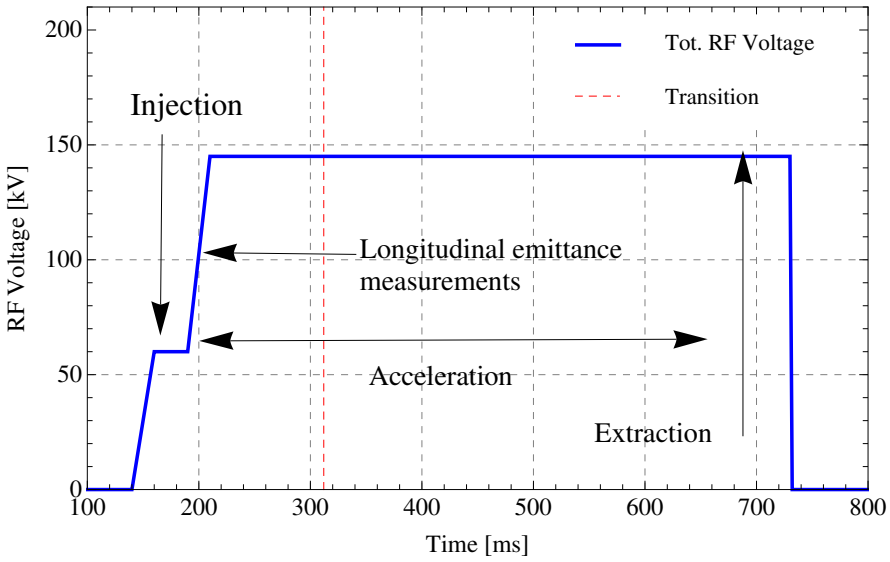

Figure 4.2: Example of total voltage applied on the RF cavities as a function of time. The longitudinal emittance is acquired at t=200 ms.

As described in Chap. 1.3, the bunch length is minimum at transition energy. This is used to set the right timing of the phase jump, which must be performed at the same moment as the bunch is the shortest. A device similar to a BPM pickup, called "Peak Detected" monitor [75], was used to identify the minimum of the bunch length. The monitor provides a signal proportional to the line charge density of the bunch, i.e. shorter the bunch is, higher is the signal. An example of a peak detected signal as a function of time is compared to a simulated bunch length with *HEADTAIL* in Fig. 4.3. Therefore the timing of the RF stable phase jump has been set at the same moment as the signal of the peak detected monitor is maximum.

Fig. 4.4a shows the measured peak detected for two intensities I=40×10^{10} and I=100×10^{10} protons. While the intensity in the beam is increasing, oscillations on the signal appear after transition energy as it can be seen for the case I=100×10^{10} protons. They correspond to bunch length oscillations as described in Sec. 1.3.5 due to longitudinal space charge and perhaps longitudinal impedance. On Fig. 4.4b, a delay in RF stable shift of 2 ms is applied at transition energy for a beam with an intensity I=100×10^{10} protons. Large oscillations are observed due to a mismatch of the beam in the bucket, while the bunch of particle goes out of the nonadiabatic region in a phase space which does not fit to the beam.

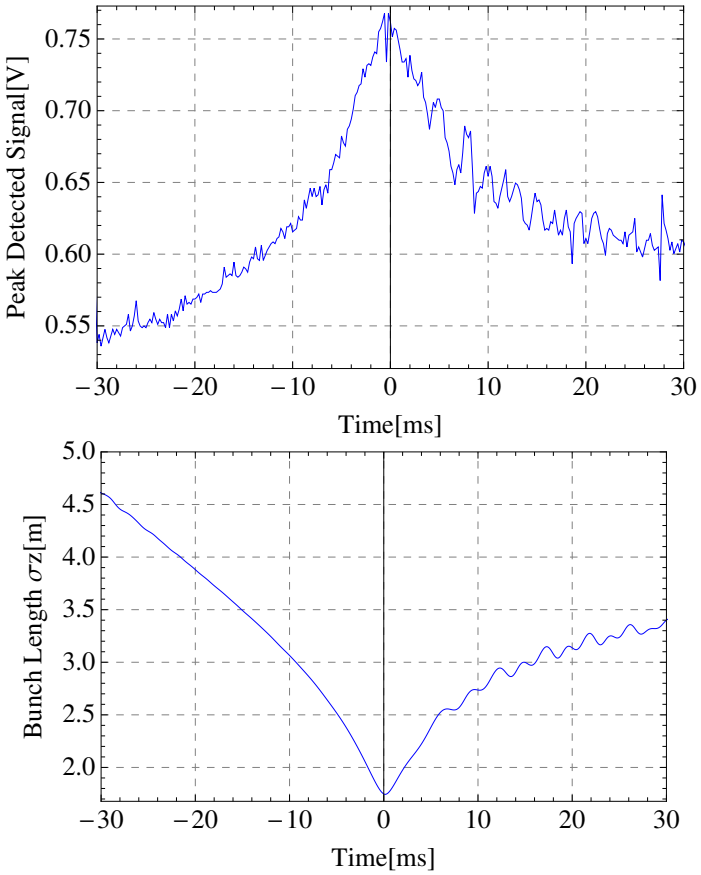

Figure 4.3: On the top: measured peak detected signal as a function of time, with time 0 identifies the transition energy. The maximum of the signal corresponds to the minimum of the bunch length as shown in the figure in the bottom, which corresponds to a *HEADTAIL* simulation of the rms bunch length.

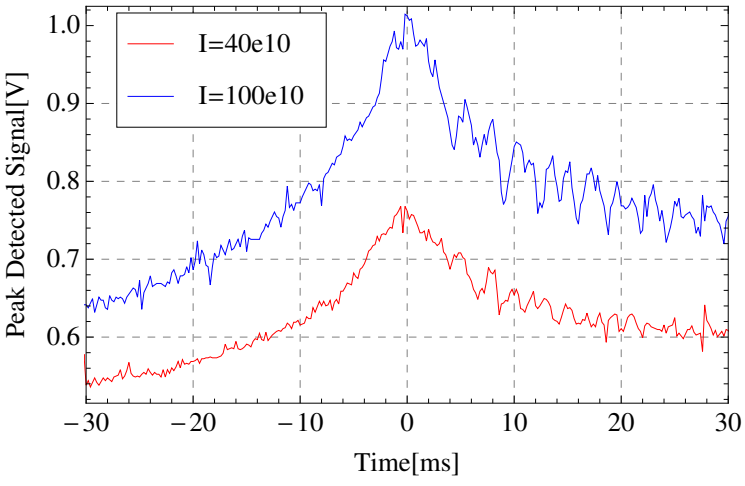

(a)

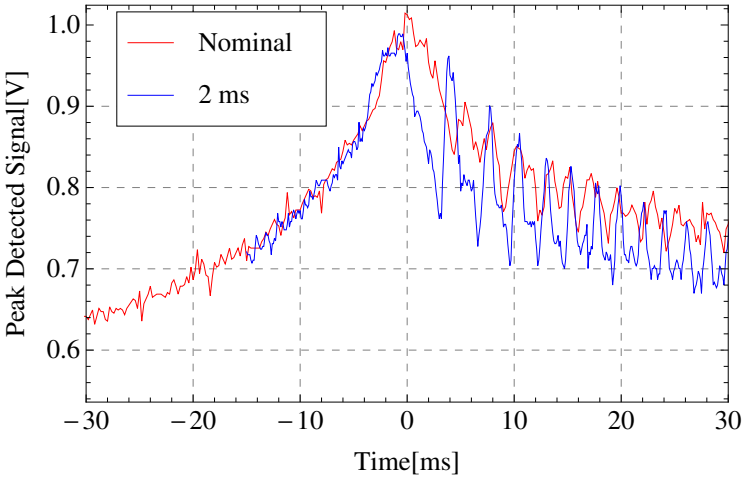

(b)

Figure 4.4: Peak detected signals through transition. Fig. (a) compares the signals of the monitor at two different intensities, the time 0 corresponds to the γ_t energy. Oscillations of the bunch length are observed on the signal corresponding to the beam intensity I=100 × 10^{10} protons. As explained in Chap. 1.3, they could be induced by longitudinal space charge and impedance Z_l. This explains why the timing of the RF phase shift must be determined at low intensity, here at I=40 × 10^{10} protons. Fig. (b) compares the peak detected signal for two beams with an intensity of I=100 × 10^{10} protons. A mistiming on the RF stable phase shift delayed by 2 ms is applied on the blue curve in which large bunch length oscillations are observed.

4.1.2 Chromaticity setting up

The chromaticity setting up represents the most important and delicate part of the beam preparation. It has been demonstrated that introducing chromaticity is an efficient way to damp transverse instabilities [76]. In fact the chromaticity introduces a betatron tune spread within the bunch, meaning that each particle is oscillating with different betatron frequency depending on their own momentum p. The motion of the particles is then incoherent, which helps to damp coherent instabilities in the bunch excited for example by machine impedance. This method can be used to increase the threshold in intensity of transverse instabilities.

For the following measurements, the vertical chromaticity is adjusted as small as possible in order to easily develop the fast transverse instability. In fact, ξ_y is kept at zero during several milliseconds to form a plateau through transition energy. In normal operation the chromaticities are usually brought to change sign at γ_t to avoid the head-tail mode m=0 to develop [24]. No sextupoles were used to adjust the working point, but instead the PFWs as it is done in normal operation.

In Sec. 2.3, it was explained how the PFWs control the working point in the PS with the use of the matrices Eq. 2.1 measured at different beam energies [58]. The adjustment of the working point were performed in 3-currents mode and Q_x is left as free parameter.

The variation of the currents ($\Delta I_{DN}, \Delta I_{DW}, \Delta I_{FN}, \Delta I_{FW}$) are then set in order to adjust the vertical chromaticity to zero through transition during several milliseconds, whereas ξ_x changes sign at γ_t in a similar way as in normal operation. Up to now, the fast instability was only observed in the vertical plane. For the need of the measurements, two different working points were adjusted with:

- a zero chromaticity plateau in the vertical plane only;
- a small and negative vertical chromaticity through transition energy ($\xi_v \simeq -0.1$).

The requested working points as a function of time are presented in Fig. 4.5a for the transverse tunes and Fig. 4.5b for the chromaticities. The time in Fig. 4.5 is expressed in unit of T_c, the nonadiabatic time defined in Sec. 1.3.4, which is about 2.2 ms. The reason for this choice of unit is to clearly identify the nonadiabatic zone. In Fig 4.6, it is checked that the beam does not cross destructive betatron resonances for the setting up of the zero chromaticity plateau.

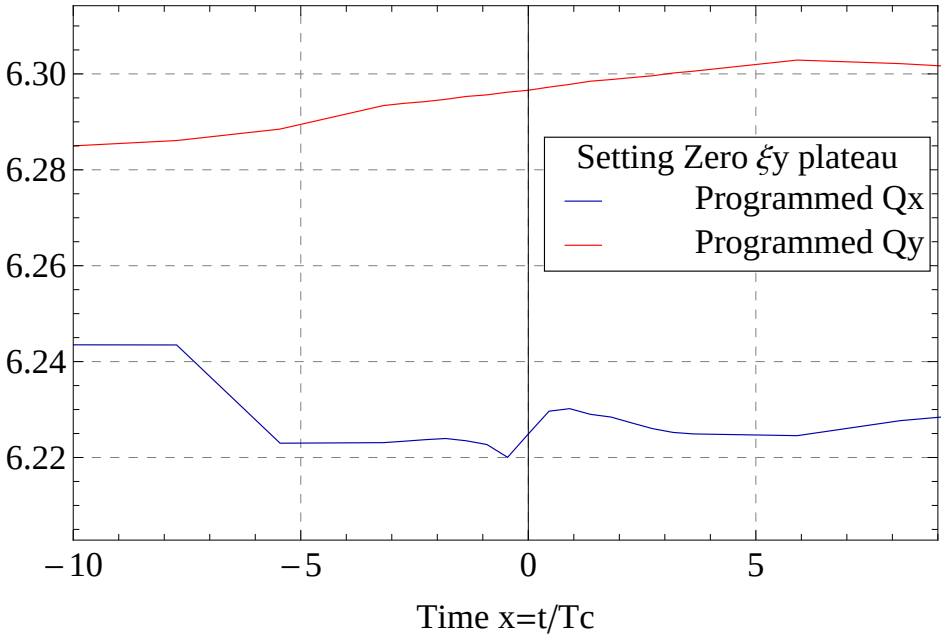

(a)

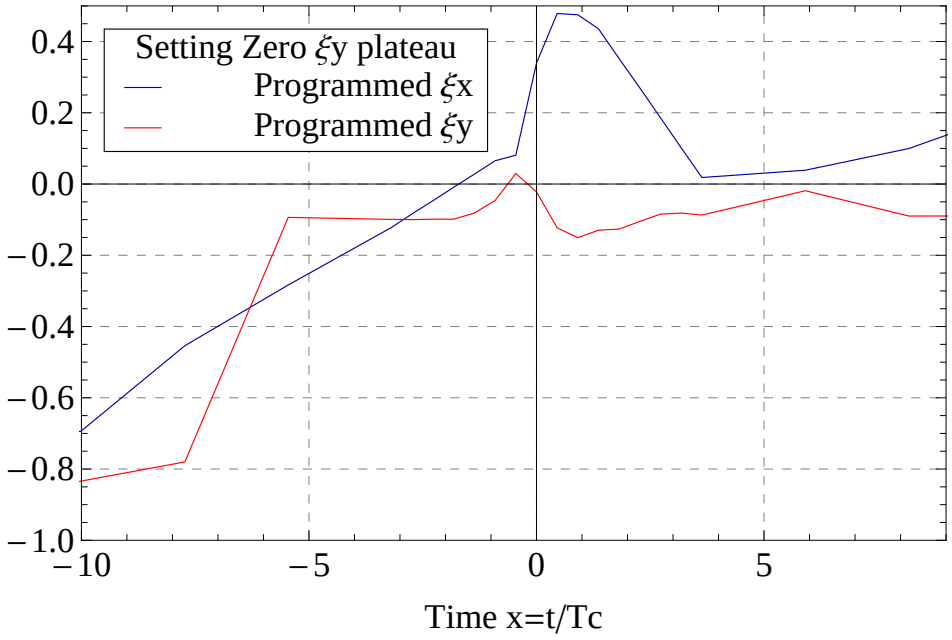

(b)

Figure 4.5: Working point programmed with the PFW for a zero chromaticity plateau in the vertical plane, Fig. 4.5a for the tunes and Fig. 4.5b for the chromaticities

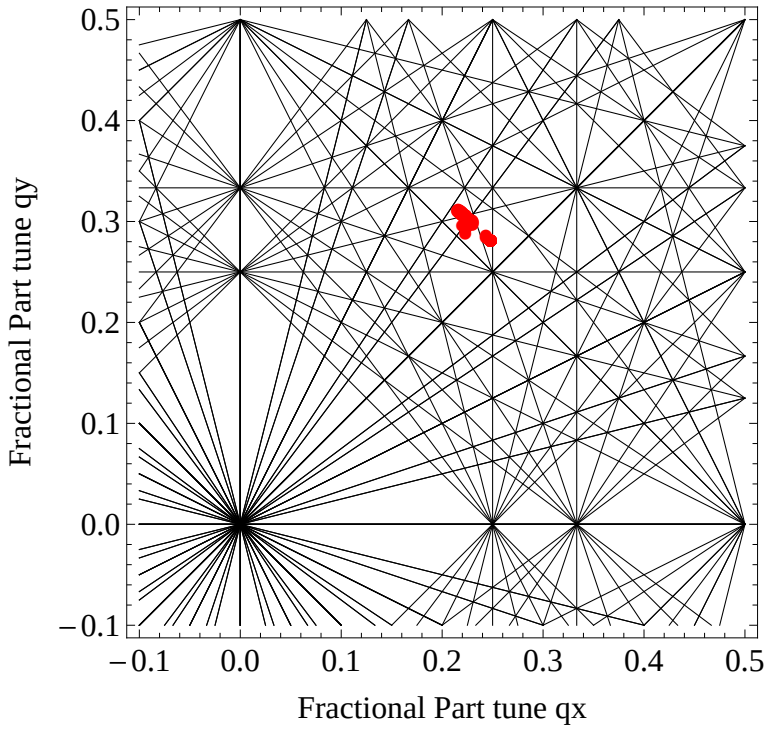

(a)

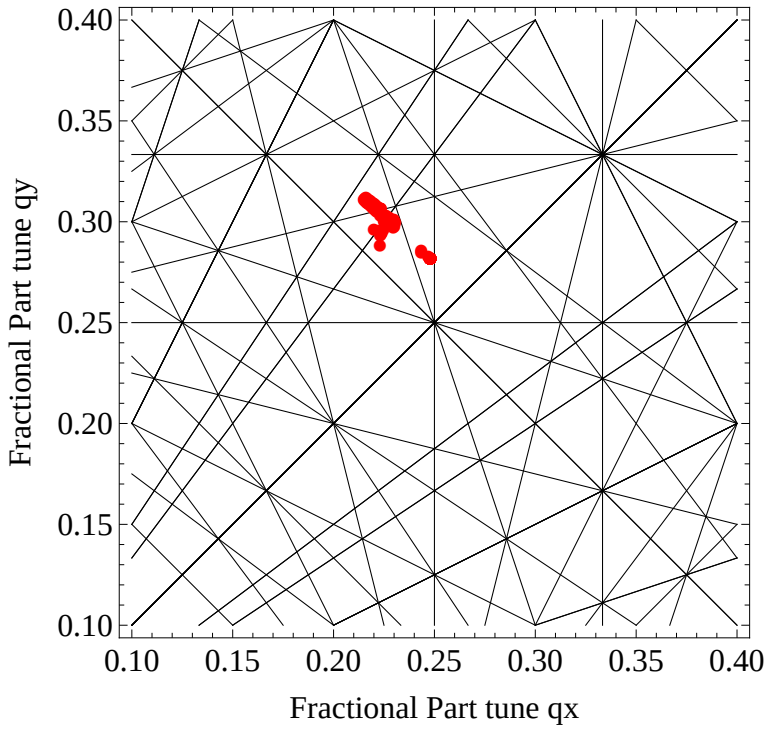

(b)

Figure 4.6: Tune diagram for a working point with the zero vertical chromaticity plateau.

The transverse tunes is measured in an accelerator by giving a transverse kick, i.e. an angle $\Delta x'$ or $\Delta y'$ to the particles. The beam performs then betatron oscillations and with the help of a beam position monitor [77], the position x or y can be measured turn by turn. A Fast Fourier Transform is then applied in order to deduce the number of betatron oscillation [75, 77].

The chromaticity is measured by acquiring the tune shift with the variation of the $\Delta p/p$ since $\Delta Q/Q = \xi \Delta p/p$. A momentum offset is introduced by changing the revolution frequency of the beam according to $\Delta f/f = \eta \Delta p/p$. The revolution frequency is changed by introducing a radial offset ΔR (or Δx) which moves radially the beam. At transition, chromaticity measurements are very difficult and are not reliable since $\eta \to 0$. The measurements are then very sensitive to errors on the measurements of the frequency but also to errors in the system which controls the energy of the beam [73]. Fig. 4.7 presents the measured frequency change $\Delta f/f$ as a function of a programmed radial offset for different time while the beam is coming through transition: the closer the beam is to this energy range, the smaller is the change in revolution frequency for a programmed radial offset. This makes the chromaticity measurements very difficult around transition.

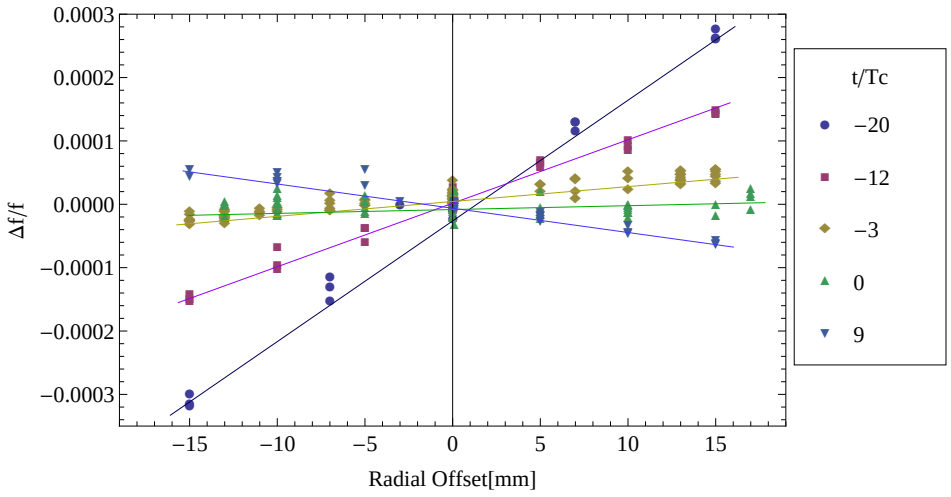

Figure 4.7: Measured frequency offset versus a programmed radial offset ΔR at different time during the acceleration expressed in units of the nonadiabatic time T_c.

The chromaticity is measured by acquiring the tune for a certain range of $\Delta p/p$. Q can be written as a Taylor series of $\Delta p/p$

$$Q(\Delta p/p) = Q_0 + Q'\Delta p/p + \frac{Q''}{2!}(\Delta p/p)^2 + ... + \frac{Q^{(n)}}{n!}(\Delta p/p)^n \tag{4.1}$$

with Q_0 being the unperturbed tune and $Q^{(n)}$ are the higher order terms of the tune spread. The chromaticity is deduced by applying a polynomial fit on the measured data and from the linear term is deduced the linear term of the chromaticity, $\xi_v = \frac{Q'}{Q_0}$. Fig. 4.8 and Fig. 4.9

show two different behaviors of the tune variation as function of the momentum offset for two different configurations of the PFWs. These data were acquired at two different instants during the cycle. In Fig. 4.8, a linear fit is used whereas Fig. 4.9 presents instead a parabolic behaviour of the tune with the momentum offset meaning that the PFWs introduced non-linear magnetic field components, here a octupolar term $Q'' = -50$.

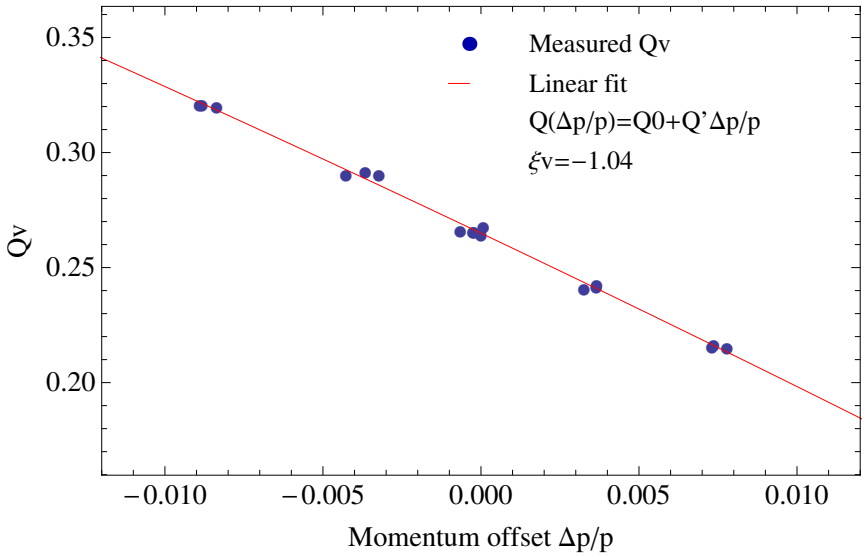

Figure 4.8: Example of vertical chromaticity measurement at $t = x/T_c = -20$. The vertical tune changes linearly with the momentum. The PFWs do not introduce any non linearity.

The obtained measured vertical chromaticity for the two sets in working point is presented in Fig. 4.10

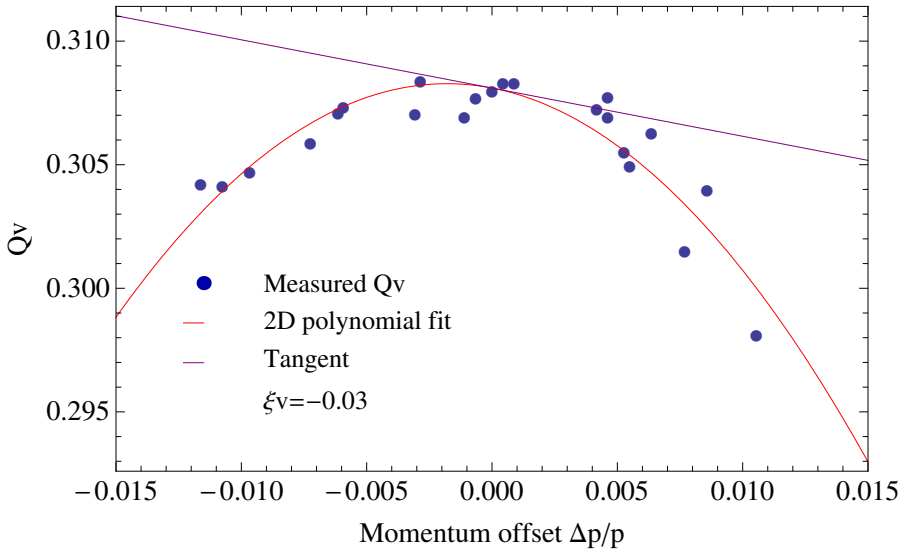

Figure 4.9: Example of vertical chromaticity measurement at $t = x/T_c = -5$. The vertical tune change quadratically with the momentum. The chromaticity Q' is deduced from the tangent to the origin. The PFW introduce non linearities in the magnetic field.

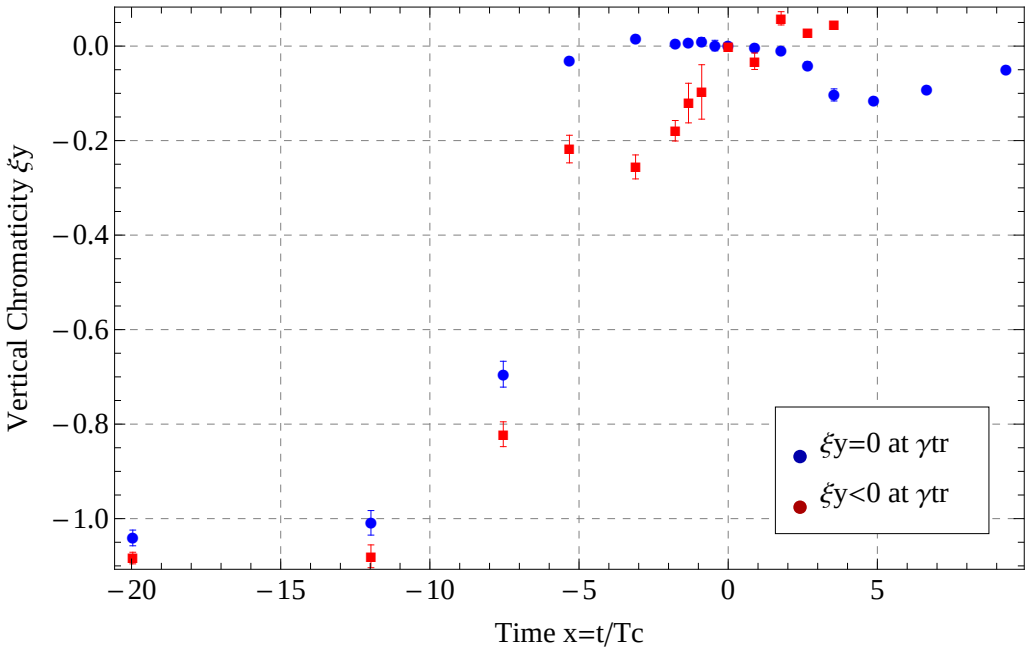

Figure 4.10: Measured vertical chromaticities for the two sets of working points as a function time expressed in units of the nonadiabatic time T_c.

Evaluation of chromaticity measurement uncertainty

A polynomial function is used to fit the tune shift as a function of the $\Delta p/p$. The linear component of the chromaticity, in which we are interested is deduce from the slope of the tangent at the origin for $\Delta p/p = 0$ as shown in Fig. 4.8 and Fig. 4.9

$$Q(x) = Q_0 + Q'\delta \tag{4.2}$$

where $\delta = \Delta p/p$. The total uncertainty on the ξ_y comes from the errors made by the fit on the regressed parameters Q' and Q_0 and from the standard deviation on the tune measurement. However, while transition energy is approaching, the change in revolution frequency is getting smaller. Eq. 2.2 shows that errors on $\Delta f/f$ (errors on the measurements of the revolution frequency for instance) will be amplified by the term $1/\eta$ with $\eta = 0$ at transition energy. It means that the fit should be not done considering the tune Q_y as an independent variable. The total uncertainty derivation of Q' and Q_0 should take into account the dependence of the uncertainty on the tune and on the momentum offset $\delta = \Delta p/p$. The error on the momentum can be written with the help of the uncertainty propagation on the revolution frequency measurement and Eq. 2.2 with $\delta = \Delta p/p$ and $\delta_f = \Delta f/f$,

$$\sigma\delta^2 = \left(\frac{\partial\delta}{\partial\delta_f}\right)^2 \cdot \sigma^2_{\delta f} \tag{4.3}$$

and the error on $\delta_f = \Delta f/f = (f_1 - f_0)/f_0$ is

$$\sigma^2_{\delta f} = \frac{\partial\delta_f}{\partial f_0}^2 \sigma^2_{f0} + \frac{\partial\delta_f}{\partial f_1}^2 \sigma^2_{f1} \tag{4.4}$$

Considering the standard deviation of $\sigma_{f1} = \sigma_{f0} = 1$ Hz [78], σ_f is constant whatever the value of the revolution frequency. Fig. 4.7 shows that the change in revolution frequency $\Delta f/f$ with the radial steering is maximum around 0.05% in the worse case, therefore considering that $f_1 \approx f_0$, Eq. 4.4 can be replaced in Eq. 4.3 and give

$$\begin{aligned}\sigma^2_\delta &= \left(\frac{\partial\delta}{\partial\delta_f}\right)^2 \frac{2}{f_0^2} \\ \sigma^2_\delta &= \frac{1}{\eta^2}\frac{2}{f_0^2}.\end{aligned}$$

Finally the momentum offset uncertainty can be written in the following form

$$\sigma_\delta = \left|\frac{1}{\eta}\right| \frac{\sqrt{2}}{f_0} \tag{4.5}$$

The evolution of the uncertainty on the momentum offset calculated from the measured frequency σ_δ given by Eq. 4.5 is shown in Fig. 4.11 as a function of time in units of the

nonadiabatic time.

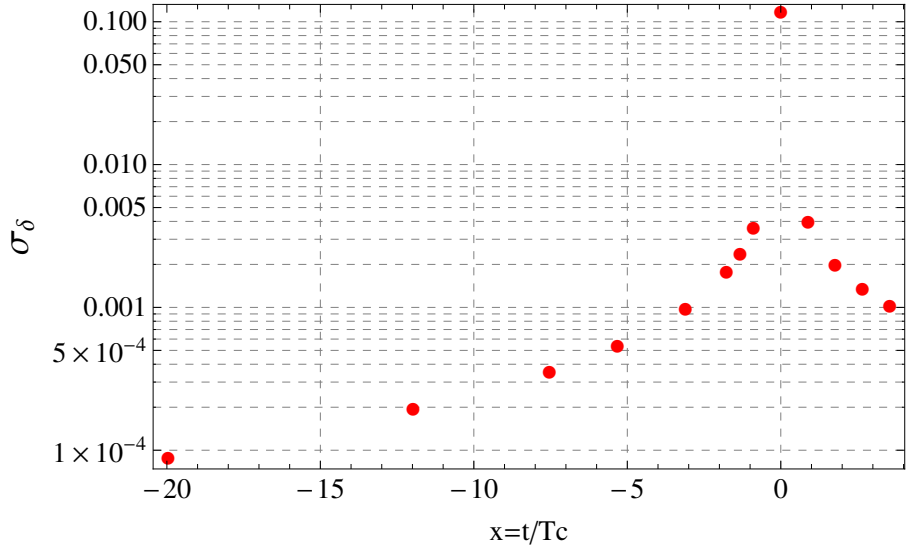

Figure 4.11: Error on the momentum offset $\Delta p/p$, calculated starting from the programmed radial offsets, at different time during the acceleration expressed in units of the nonadiabatic time T_c.

4.1.3 Experimental observations

The instrument used to measure the fast transverse instability is a wall-current monitor (WCM) with a suitable bandwidth to observe the instability pattern on the bunch. The complete description of the device can be found in Ref. [9].
A charged particle bunch moving with a highly relativistic speed in a well-conducting vacuum chamber is accompanied by a transverse electric field which induced a charge distribution in the wall. The knowledge of these image currents at four axis points A, B, C and D indicated in Fig. 4.12 is sufficient to determine the beam position and the intensity. The four voltages are measured at the points A, B, C and D and the differences $\Delta U = U_A - U_B = \Delta_y$ and $\Delta U = U_C - U_D = \Delta_x$ allow to determine the transverse beam position. If the beam is well centred in the vacuum pipe, no difference in voltage ΔU appears at the four axis points since the amount of image charges created are equally distributed. The signal ΔU is called Delta (noted Δ) and can be defined for the horizontal plane Δ_x and the vertical plane Δ_y. While the beam goes through wall current monitor, the voltages induced by the image current can be measured at the four points A,B,C and D. The sum of the these four voltages gives the so-called signal sum (noted Σ). The Σ signal corresponds to the longitudinal distribution of the bunch and its integral is related to the bunch intensity. An example of Δ and Σ signals are presented in Fig. 4.13 for a stable beam. Reference [9] points out that the bandwidth of the signal Σ (2.7 MHz-1.5 GHz) is different from the bandwidth of the signals $\Delta_{x,y}$ (9.4 MHz-1.5 GHz). Due to a different lower cut-off frequency, $\Delta_{x,y}$ filter differently the low frequencies and the shape of their signals are affected. The ratio $\Delta_{x,y}/\Sigma$ gives the transverse position of the beam. However it cannot be done since the bandwidth of the Δ and the Σ signals are different. Extra signal analysis are needed to correct it.

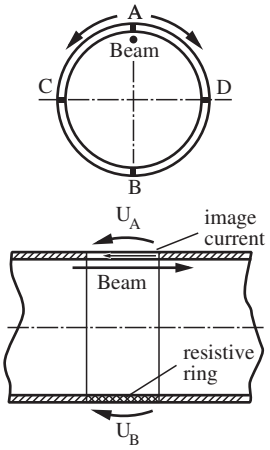

Figure 4.12: Description of the WCM [9].

In order to observe the transverse instability, the Δ_y and the Σ signals are acquired during the beam acceleration around transition energy. Fig. 4.15b shows the signals of the WCM for the intensity measured in Fig. 4.15a for a stable beam, this is an example before transition. Fig. 4.15c presents the same signals right after transition. Δ_y shows a high frequency oscillation along the bunch: the particles at head of the bunch are (particles close to the time position 100 ns in Fig. 4.15c) stable whereas at the maximum peak intensity, particles oscillates according to a travelling wave with a frequency of about 650-700 MHz. Once the particles at high amplitude hit the vacuum chamber, they are lost and a hole appears in the Σ signal, the longitudinal profile of the bunch, at the location of the lost particles. This hole is not immediately refilled due to the very slow synchrotron motion. The horizontal plane remains stable. The beam losses due to the transverse instability take place in less than 1 ms, which is fast compared to the synchrotron period T_s ($T_s \geq 10$ ms close to transition energy).

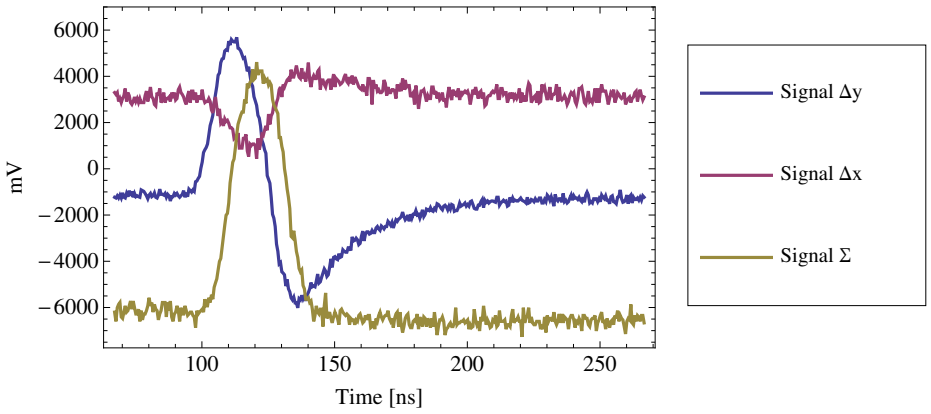

Figure 4.13: Transverse $\Delta_{x,y}$ and Sum Σ signals in mV of the WCM.

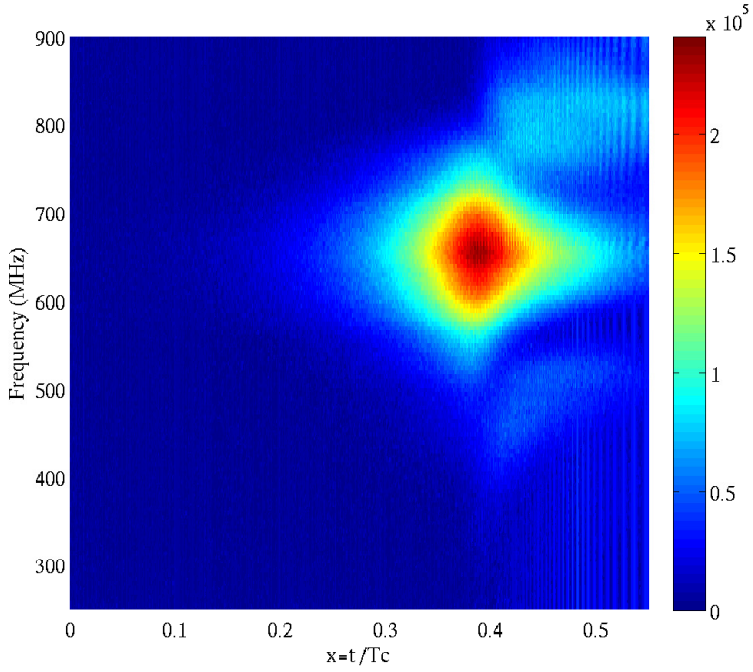

Figure 4.14: Travelling wave frequency of the vertical Δ_y signal acquired during several hundred consecutive turns around transition energy (x=0) as a function of time expressed in units of nonadiabatic time T_c for a 2 σ longitudinal emittance of 2 eVs.

The Δ_y and the Σ signals can be acquired on several thousands consecutive turns thanks to a multi-trigger system in order to observe the vertical instability developing. The signal sampling frequency is about 4 GSamp/s, which is sufficient to observe the high-frequency travelling wave on the Δ_y signal on 30 ns long bunches in the transition energy region. A Fast Fourier Transform (FFT) can be then applied on every trace of the Δ_y to determine the

spectrum in frequency of the signal as it is done on the waterfall plot Fig. 4.14. The spread in frequency of the travelling wave on the bunch goes from 600 to 700 MHz.

This section was dedicated to the first observation of the fast instability around transition energy, in the vertical plane. The particles close to the peak density, i.e. where the longitudinal density is maximum Fig. 4.15c, oscillate according to a travelling wave with a frequency of about 700 MHz. The protons oscillating at high amplitude hit the vacuum chamber and are lost in the machine. The instability rises in less than 1 ms in the example presented above which is faster than a synchrotron period, with $T_s \geq 10$ ms while the beam approaches transition energy. The fast instability develops even without chromaticity, therefore it is not a classical head-tail kind. Indeed, the head-tail instability needs chromaticity and it takes several synchrotron period to grow. In the next section, extensive rise time measurements as a function of the beam intensity are presented.

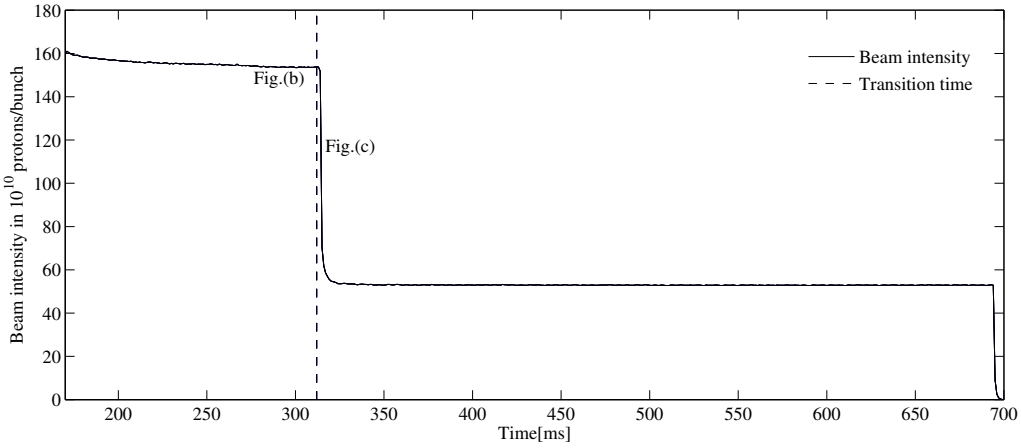

(a) Beam intensity as a function of time. The dashed line shows the time of transition energy crossing.

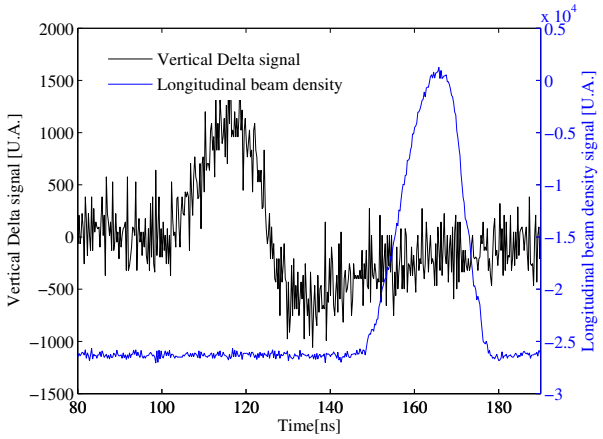

(b) Vertical Δ and Σ signal of the WCM before transition.

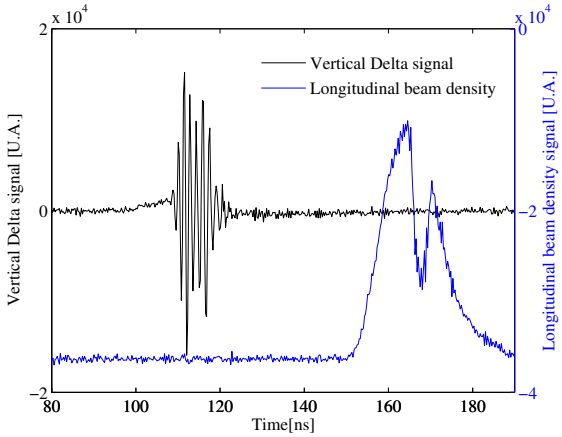

(c) Vertical Δ and Σ signal of the WCM after transition.

Figure 4.15: Fast transverse instability observation close to transition energy with the WCM at an intensity presented in the Fig. (a) and a longitudinal emittance of 2 eVs at 2 σ, well before transition, the beam is stable, Fig. (b) and after transition, the vertical signal of the WCM shows that the beam is unstable Fig. (c)

4.2 Instability Rise Time Measurements

In the formalisms describing transverse instabilities rising faster than the synchrotron period [79], such as the coasting beam theory, the beam spectrum is interacting with the machine impedance, producing a complex tune shift as it was described in Chap. 1.4.2. Above a certain intensity threshold, the imaginary part of the coherent angular frequency $\Delta\omega_y$ [74] is non zero and the motion of the particles are growing in a exponential way [10]

$$Im(\Delta\omega_y) \propto -Re(Z_\perp^y(\omega'))h(\omega' - \omega_\xi) > 0$$

where $Re(Z_\perp^y(\omega))$ is the real part of the transverse impedance, $h(\omega)$ is the bunch spectrum in frequency domain with $\omega' = \omega_0 p + \omega_s$, ω_0 the angular revolution frequency, p is an integer, ω_s the angular synchrotron frequency and ω_ξ is the chromatic angular frequency. In the BBU theory, the ratio y_n/y_0 between the vertical amplitudes of the tail of the beam after n turns and an injection offset is mainly described by the exponential term of Eq. 1.143. In both cases, the analytic formulas for the growing motion of the particles are proportional to the impedance, considered as broadband in Ref. [39, 74]. τ represents the rise time and the inverse of τ is the growth rate such as $a = 1/\tau$ and,

$$\tau = \frac{-1}{Im(\Delta\omega_y)}$$

This section presents the extensive measurements of the fast vertical instability through transition energy. The influence of different parameters, such as the beam intensity and the longitudinal emittance, on the instability threshold and on the rise time, are studied. The experiments were performed for different longitudinal emittance ϵ_l and the resulting rise times and intensity thresholds will allow to determine an impedance model for the PS, that we suppose to be broadband. The reason of this is that previous head-tail measurements [10] by varying the chromaticity have shown that the transverse impedance can be approximated to a broadband model. The other reason is that a detailed impedance model element by element, as done for LHC and the SPS, does not exist for the PS. The experiments were performed for the two chromaticity settings mentioned in Sect. 4.1.2 in Fig. 4.10.

For the need of the measurements, the Δ_y and the Σ signals are acquired over 5000 consecutive turns (i.e. around 10.5 ms) through transition energy as well as the beam intensity N_b and the longitudinal emittance ϵ_l. The intensity is recorded over the magnetic cycle every millisecond as shown in Fig. 4.15a and the longitudinal emittance is measured at the very beginning of the acceleration. For one set of measurement, i.e. for a given N_b, ϵ_l and working point, a fast Fourier transform is applied on each traces Σ_y to extract turn by turn the frequency range [400 MHz-1 GHz] of the travelling wave developing along the bunch beam. The maximum of the frequency spectrum is then identified and its time evolution turn by turn can be represented. An example of analysis is shown in Fig. 4.16 and Fig. 4.17. Fig. 4.16a presents a Δ_y signal while the instability is developing and Fig. 4.16b is the frequency spectrum of the

Δ_y. The maximum of the spectrum is extracted, by applying this method on all the traces of the data set, Fig. 4.17a is obtained. The maximum of the frequency spectrum is evolving exponentially as a function of time.

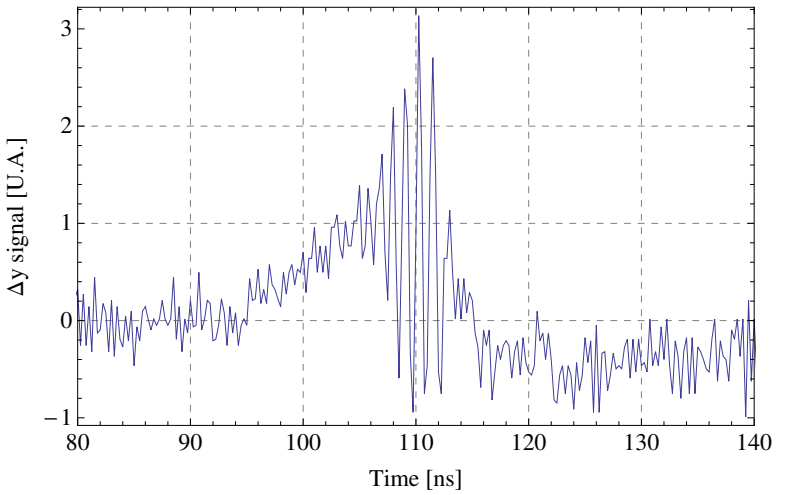

(a)

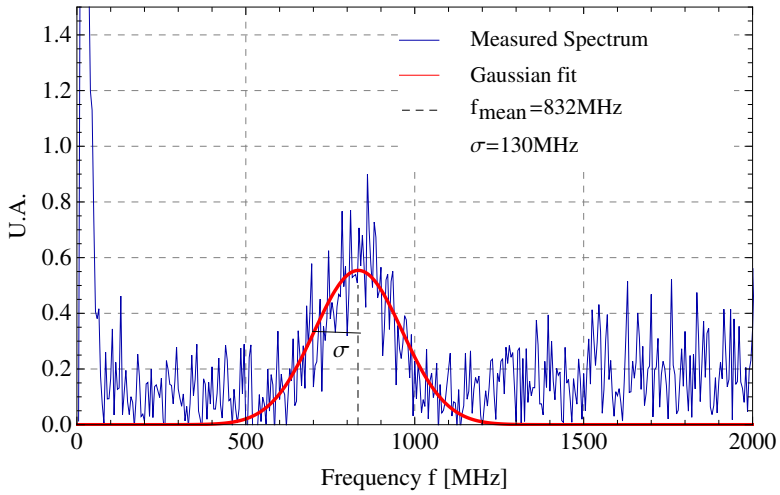

(b)

Figure 4.16: Fig. (a) shows an example of Δ_y signal while the travelling wave along the bunch is developing. Fig. (b) is the beam frequency spectrum resulting from a fast Fourier transform applied of the single trace of Fig. (a). A Gaussian fit is applied to find the central frequency and the frequency width σ.

Fig. 4.17b can be also set in logarithm scale. The maximum of the frequency spectrum as a function of time is growing. The linear part is selected and a linear least square regression can

be applied as done in Fig. 4.17b

$$f(t) = B \exp\left[\frac{t}{\tau}\right]$$
$$\ln f(t) = a \times t + b$$

where $f(t)$ is the maximum frequency time evolution turn-by-turn, B, b are constant, t is the time, a is the growth rate in s^{-1} and τ the rise time can be then deduced.

Results of the Scan in Beam Intensity

For each longitudinal emittance ϵ_l and working point, a scan in beam intensity was performed. At each measurement point (ϵ_l, chromaticity, and intensity) the signals Δ_y and Σ were acquired.

Considering the two-particle model with a particle p_1 placed at the head of the bunch and a particle p_2 placed at a distance z behind p_1, p_2 is excited by p_1 through the wake force F, expressed as (see Sec. 1.4.3),

$$F = e(Ne/2)\, y_1 W_1 \tag{4.6}$$

with e the electron charge, Ne the bunch charge, y_1 the displacement of the particle 1 and W_1 the wake field per meter of the structure. One can see that the more intense is the bunch, the larger is the wake force. This is why a scan over the number of particle in the bunch is performed. Moreover, the rise time of the instability and its intensity threshold are important parameters to understand the dynamics of the transverse instability.

The measured rise times as function of bunch intensity, for the two working points, are shown in Fig. 4.18a for $\epsilon_l \simeq 1.5$ eVs, Fig. 4.18b for $\epsilon_l \simeq 1.9$ eVs and Fig. 4.19a for $\epsilon_l \simeq 2.3$ eVs. The rise time is given in number of turns and the chromaticities $\xi_v \simeq 0$ and $\xi_v < 0$ refer to Fig. 4.10.

Independently of the chromaticity and the longitudinal emittance, each figures shows that there exists an intensity threshold I_{th} below which the instability does not develop. The existence of an intensity threshold is predicted by the theory of instability faster than the synchrotron period such as for coasting beam theory [79]. Eq. 4.6 shows that the wake force excited by a particle 1 and applied on a particle 2 becomes larger with the beam intensity and the instability develops faster: the rise time becomes smaller. The results of the measurements show that the chromaticity acts on the intensity threshold whereas when $I >> I_{th}$, the rise times are comparable regardless the longitudinal emittance.

Three different regimes in intensity can be distinguished for the instability rise time:

- When the intensity is decreased towards I_{th} and below, the rise time becomes very large: closer the intensity is from I_{th}, slower the instability will develop. While the intensity is

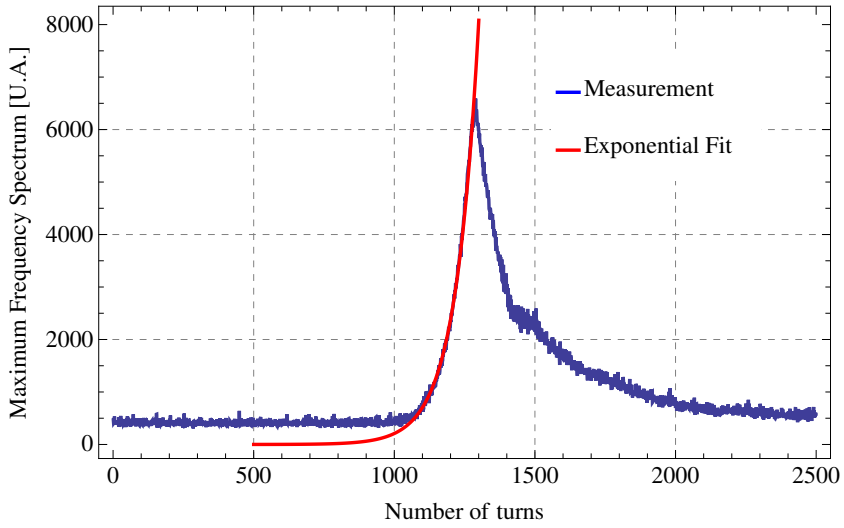

(a)

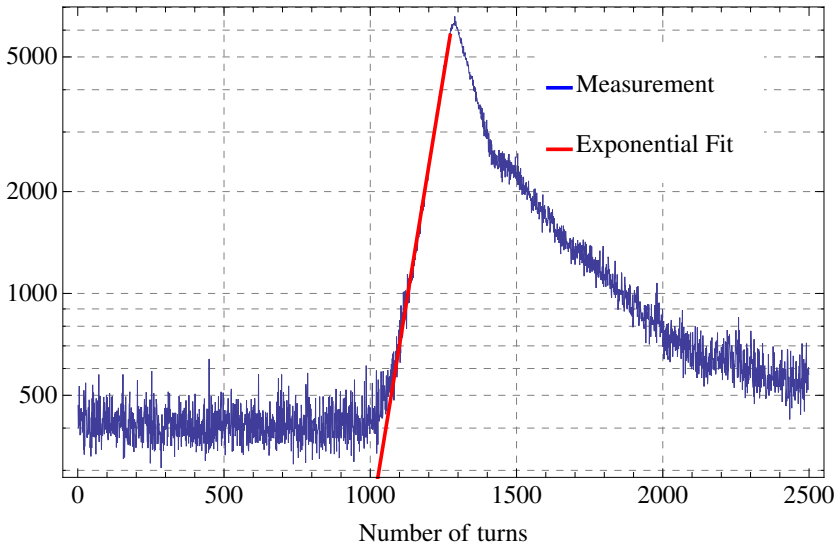

(b)

Figure 4.17: Maximum frequency of the travelling wave observed in the vertical Δ_y signal with an example of exponential fit presented in the Fig. (a) and in logarithmic scale in Fig. (b). The slope determines how fast the vertical instability grows with time. Only 2500 turns over the 5000 acquired, are presented. Transition is situated in this case at the turn 0.

approaching I_{th}, the rise time is going to infinity.

- The rise time evolution seems to be linear with the intensity for $I >> I_{th}$ and it even reaches a saturation regime for the case of an 1.5 eVs longitudinal emittance;

- A non-linear regime can be applied between these two limits.

The rise time as a function of the beam intensity is inversely proportional to the number of particle in the beam, as expected from the theoretical formula developed in Ref. [79]. This reference compares different formalisms of fast transverse instability such as Beam Breakup, Transverse Mode Coupling, coasting beam and Post Head-tail theory. Using simple formulae, rise time are computed and the different formalisms lead to the same expressions of rise time under a certain numeric factor. Fig. 4.21 shows the growth rate for the longitudinal emittance of 1.5 and 1.9 eVs for the two in chromaticity and Fig. 4.22 for the case 2.3 eVs. Fig. 4.23a and Fig. 4.23b compares the growth rate by chromaticity. If the rise time as a function of the intensity is inversely proportional, then the growth rate as a function of the intensity is a linear function when $I >> I_{th}$ and this is the case on the figures mentioned above.

The rise times of the instability are then compared for the two working point sets. They look similar in the linear/saturation regime ($I >> I_{th}$) and the major difference comes from instability threshold in intensity in the non-linear and the low-intensity regime. As excepted, ξ_v modifies I_{th} according the coasting beam theory which will be explained in Sec.4.8. This effect is clearly visible for the longitudinal emittances ϵ_l = 2 eVs and 2.3 eVs in Fig. 4.18b and Fig. 4.19a but less visible for the case 1.5 eVs. This is explained by the fact that the real longitudinal emittance could not be well controlled for this last measurement set. Further measurements showed that indeed the ϵ_l = 1.29 eVs set for beam intensities close to the instability threshold for the set of negative chromaticity as illustrated in Fig. 4.19b. The underlying reason for the observed emittance variation is left as a future study.

A systematic study of ϵ_l shows that it can vary by 20% from shot-to-shot as presented in Fig. 4.20. The machine is not very reproducible. This contributes further to the spread of the measured rise times.

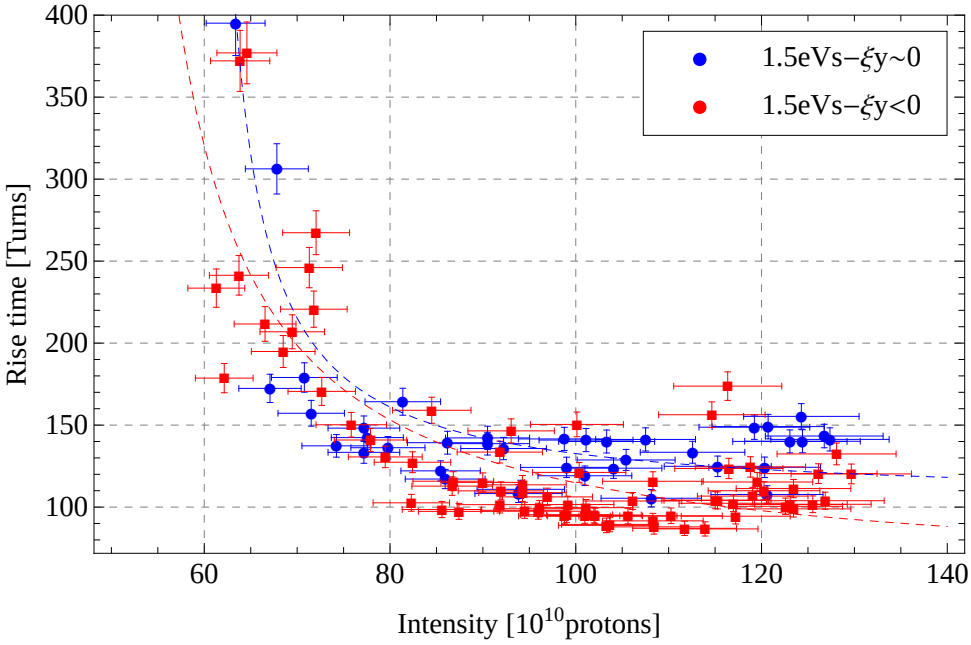

(a)

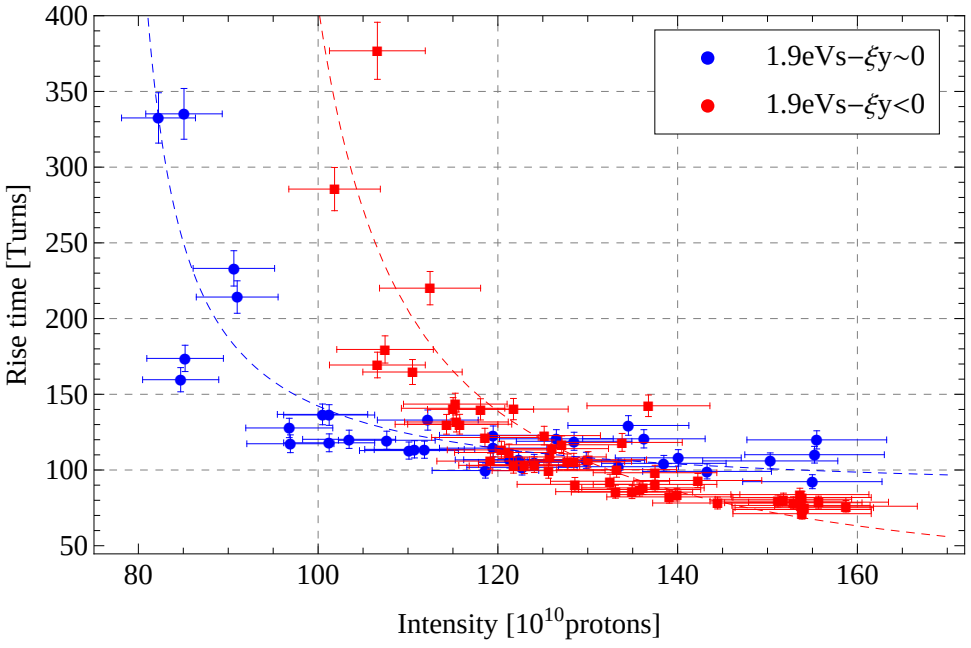

(b)

Figure 4.18: Measured instability rise time as a function of the intensity and the vertical chromaticity. The measurements were repeated for three different longitudinal emittances presented in Fig. (a) for 1.5 eVs, 1.9 eVs.

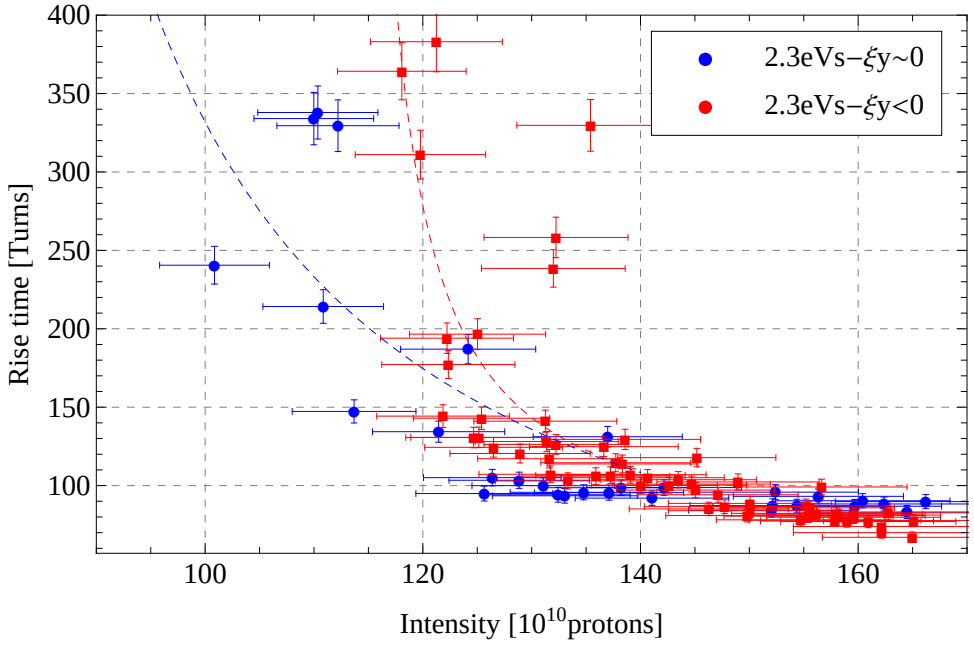

(a)

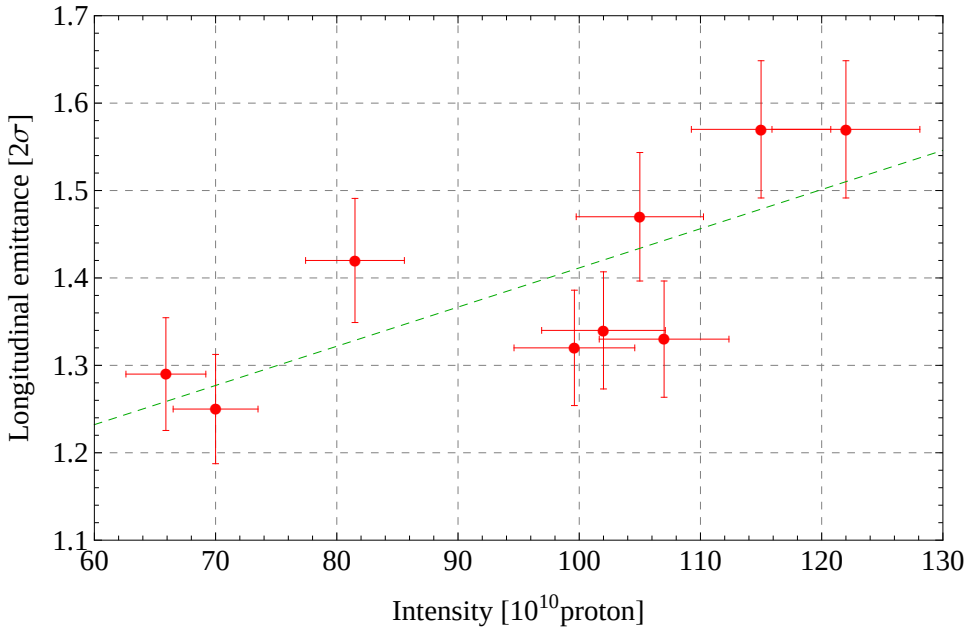

(b)

Figure 4.19: Measured instability rise time as a function of the intensity and the vertical chromaticity. The measurements were repeated for three different longitudinal emittances presented in Fig. (b) and 2.3 eVs in Fig. (a). Fig. 4.19b shows the measured longitudinal emittance as a function of the beam intensity for the set with a negative chromaticity. It can seen that ϵ decreased with the beam intensity. This explains the lower measured intensity threshold for a negative chromaticity.

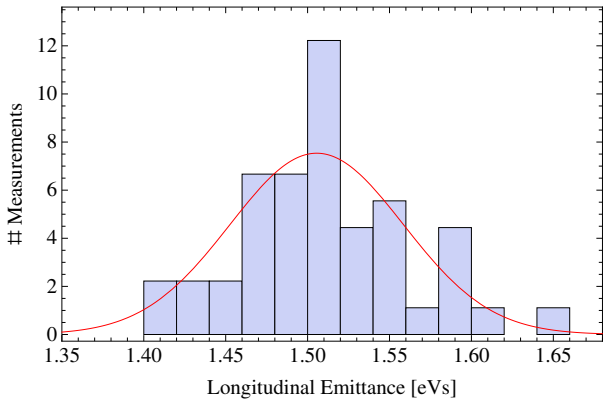

Figure 4.20: Histogram of systematic measurements of the longitudinal emittance for ϵ_l = 1.5 eVs.

It can be more convenient to look at the growth rate, the inverse the the rise time. When the growth rate as a function of the intensity is linear, it means that the instability is well above the threshold. The results are presented in Fig. 4.21 for the longitudinal emittance of 1.5 and 1.9 eVs for the two in chromaticity and in Fig. 4.22 for the case 2.3 eVs. Fig. 4.23a and Fig. 4.23b compares the growth rate by chromaticity. It can be already seen that a working point with chromaticity increases the intensity threshold of the instability, probably by Landau Damping and the spread in tune introduced by chromaticity. The growth rates at the highest intensities –in the linear regime– looks higher with chromaticity than without. The reason is yet understood and is left to further studies.

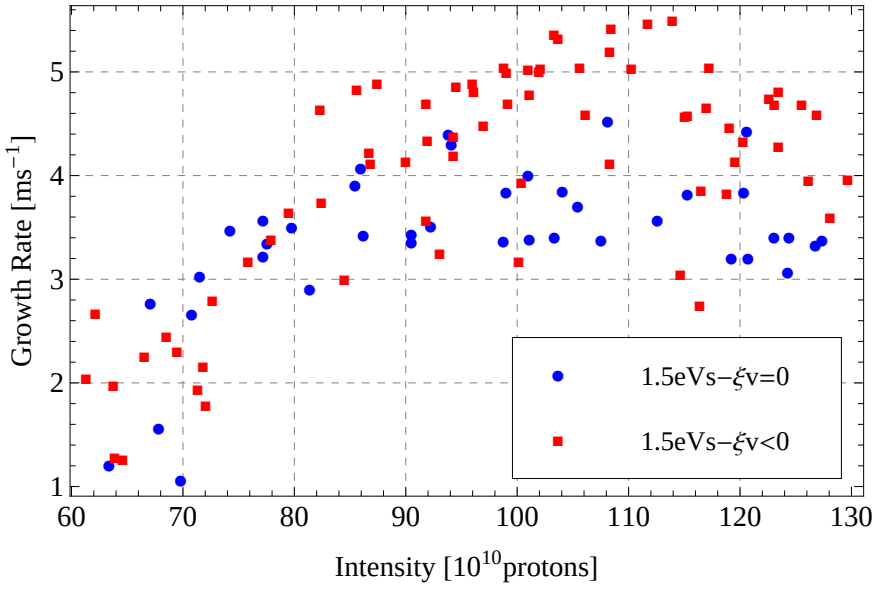

(a)

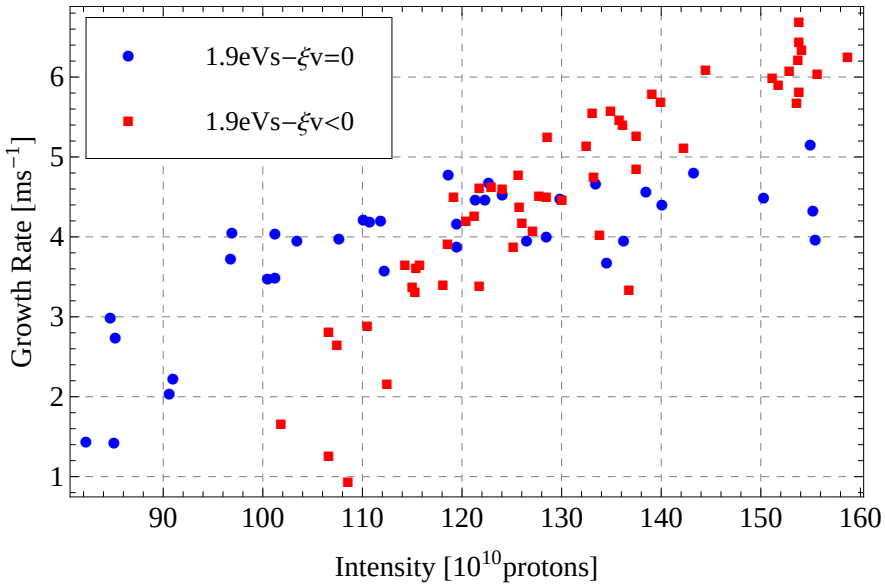

(b)

Figure 4.21: Measured instability growth rate as a function of the intensity and the vertical chromaticity .

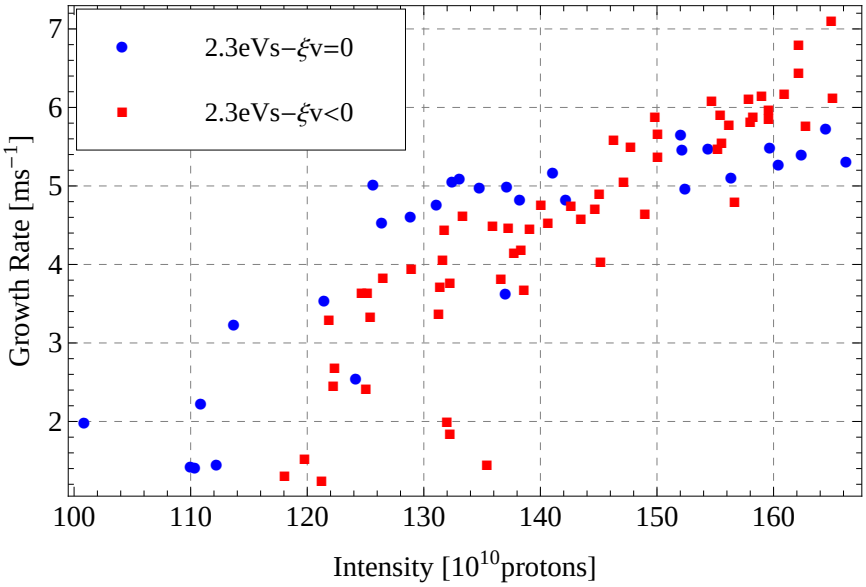

Figure 4.22: Measured instability growth rate as a function of the intensity for $\epsilon_l = 2.3$ eVs.

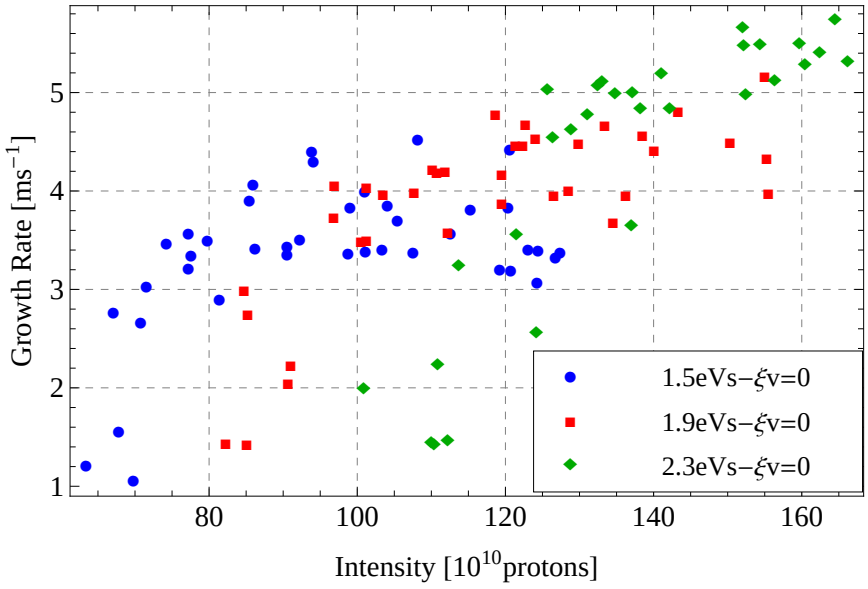

(a)

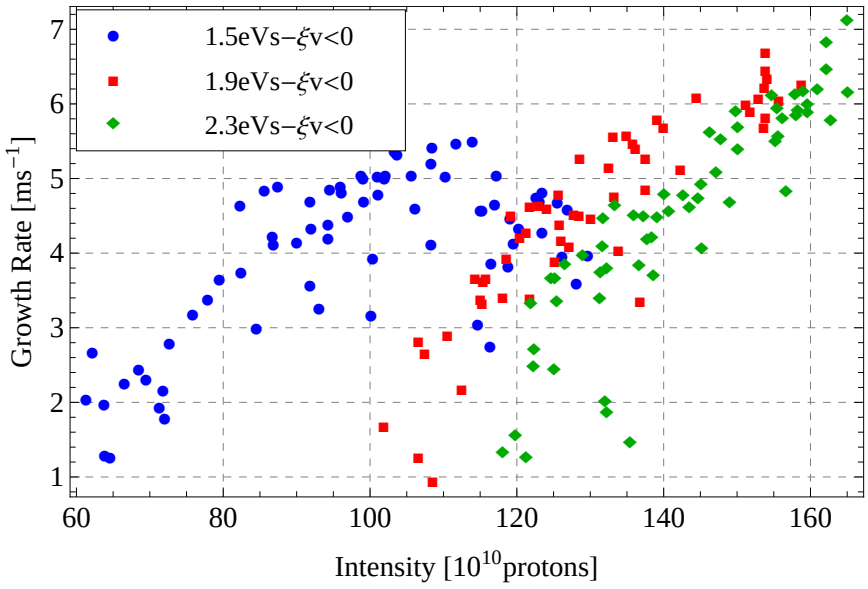

(b)

Figure 4.23: Measured instability growth rate as a function of the intensity for the two sets of chromaticity.

4.3 Instability Threshold Parameters

4.3.1 Intensity Threshold I_{th}

This section is focused on the measurements of the instability threshold in intensity as a function of ϵ_l. A good understanding of this behaviour is fundamental for the determination of the PS impedance model that is used in the multi-particle simulations described in Sec 4.4. The influence of the distance from the transition energy, i.e. the parameter η, will be also discussed.

As the beam intensity approaches the intensity threshold I_{th}, the rise time of the instability tends to infinity. For the different longitudinal emittances, I_{th} is estimated from Fig. 4.18a, Fig. 4.18b and Fig. 4.19a by extrapolating the number of particles in the bunch in the low-intensity regime of the rise time. Then the dependence of I_{th} on ϵ_l is analysed. Additional intensity threshold measurements were performed for several values of ϵ_l and for the two chromaticity points defined in Sec. 4.1.2. The results are presented in Fig. 4.24. The complementary measurements were done by varying the beam intensity and by observing the signal of the WCM until the instability appears. They verify the estimated I_{th} for e_l = 1.9 eVs and 2.3 eVs and confirm that the intensity threshold measured in Fig. 4.18a corresponds to a longitudinal emittance of about 1.3 eVs. Fig. 4.24 shows first that I_{th} is varying linearly with the longitudinal emittance and that the intensity thresholds of the instability are higher with chromaticity. This confirms that a possible cure would be to introduce a betatron frequency spread in the bunch. The linear dependency of I_{th} is predicted by the coasting beam theory of instabilities faster than the synchrotron period,

$$I^{th} = \frac{32\sqrt{2}}{3}\frac{Q_{y0}|\eta|\epsilon_l}{e\beta^2 c} \times \frac{f_r}{|Z_y^{BB}|} \tag{4.7}$$

with Q_{y0} is the vertical tune, f_r is the cut-off frequency of the broad-band impedance model, Z_y^{BB} is the value of the vertical broad-band impedance. This will be explained in more detail in Sec. 4.8 and in Sec. 4.4.

At this point, rise times and intensity thresholds of the instability were extracted from the measurements. To do so, the time at which the instability appears on the Δ_y signal is identified for each set of data and related to the relativistic energy mass factor γ and therefore to the synchrotron angular frequency ω_s and the synchrotron period T_s:

$$\omega_s = \sqrt{\left(-\frac{eV_{rf}h\eta\cos\phi_s}{2\pi\beta^2 E_{tot}}\right)\omega_0^2} \qquad T_s = \frac{2\pi}{\omega_s} \tag{4.8}$$

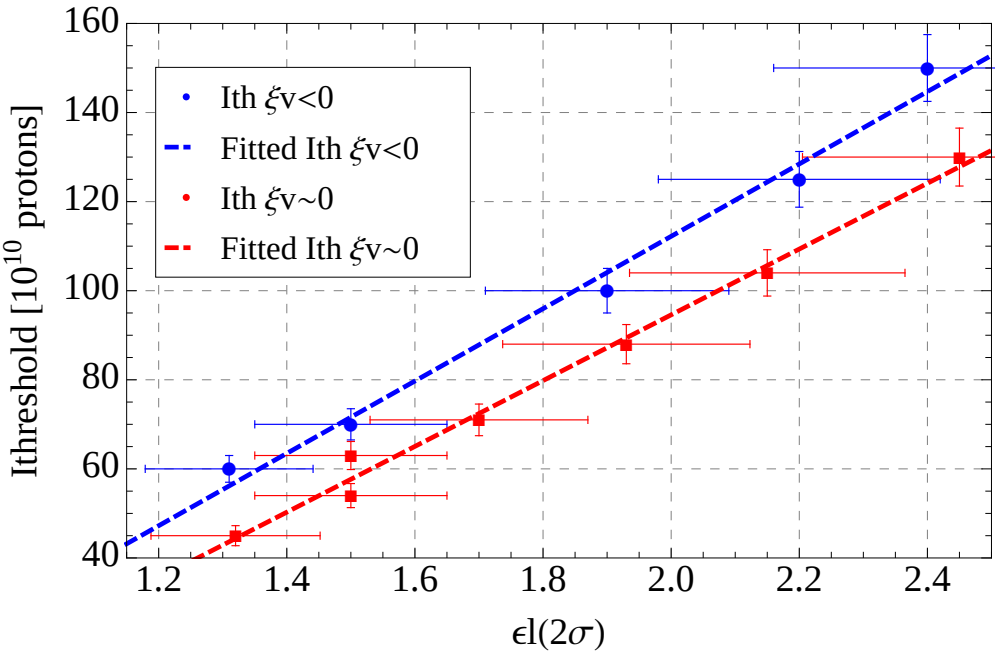

Figure 4.24: Measured intensity threshold of the instability as a function of the longitudinal emittance for the two sets in chromaticity.

The time at which the bunch starts to be unstable was identified relative to the RF phase shift supposed to be exactly the transition energy. If this RF gymnastic is not set at transition, the values of T_s might be false due to an incorrect estimation of η. However, there exists a way to determine at which turn exactly during the acceleration the transition occurs, different from the empirical method already described in Section 4.1.1. Fig. 4.25 presents the synchrotron period as a function of the momentum compaction factor η at which the instability is triggered in the measurements. In the presentation of the results, the rise time computed from each set of data is divided by the corresponding synchrotron period, in order to conveniently relate the rise time to the time scale of the synchrotron motion close to transition, and the intensity is normalized to I_{th}. This allows to compare the rise time measurements for the different longitudinal emittances and the results are presented in Fig. 4.26 and Fig. 4.27. It shows that the rise time evolution, normalized by the synchrotron period, is similar regardless of the longitudinal emittance for a given chromaticity. Fig. 4.26 confirms that $\tau / T_s << 1$, therefore the instability develops much faster than the synchrotron period. It confirms that the fast vertical instability is not of head-tail type, which needs several synchrotron periods to develop.

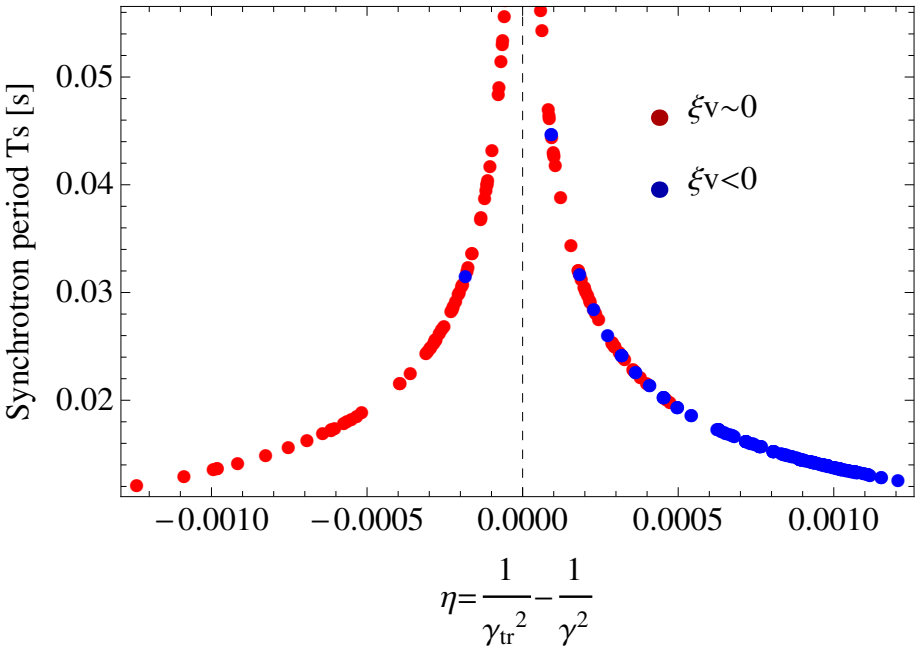

Figure 4.25: Synchrotron period sampled during the rise time instability measurements. Each point corresponds to one measurement where the instability was observed at this particular combination of η and T_s.

Since the instability is developing during the acceleration, the relativistic γ does not stay constant and the momentum compaction factor η is changing as well. Regardless the formalism adopted, η is an important parameter. In the Transverse Mode Coupling theory [11] or in the coasting beam formalism [74] presented in Eq. 4.7, the threshold in intensity I_{th} is strongly dependent of $|\eta|$ and the momentum compaction factor changes the interaction of the bunch spectrum with impedance particularly in presence of chromaticity with the chro-

matic frequency $\omega_\xi = Q\xi\omega_0/\eta$. In the Beam Breakup theory (BBU), there is no synchrotron motion and no transition energy, therefore the η is not taken into account. While the motion becomes nonadiabatic near transition energy, boundaries in η can be defined at the limits of the nonadiabatic zone and from the analysis performed below for the synchrotron period, one can determined which η_{th} triggers the instability in the measurements.

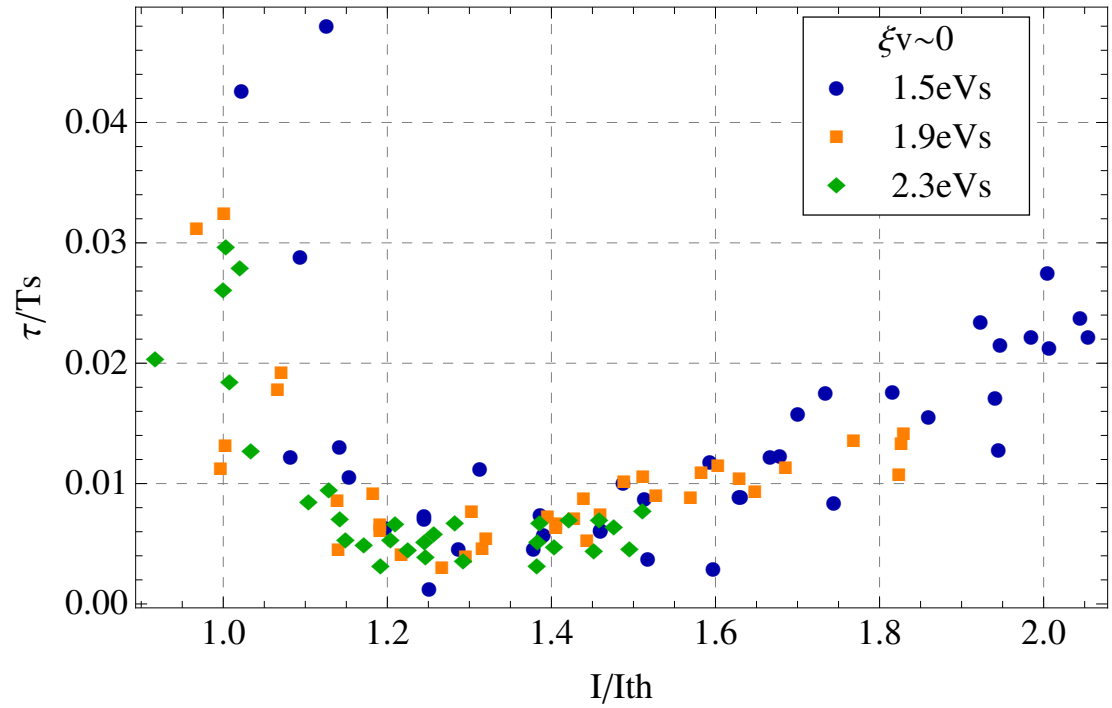

(a)

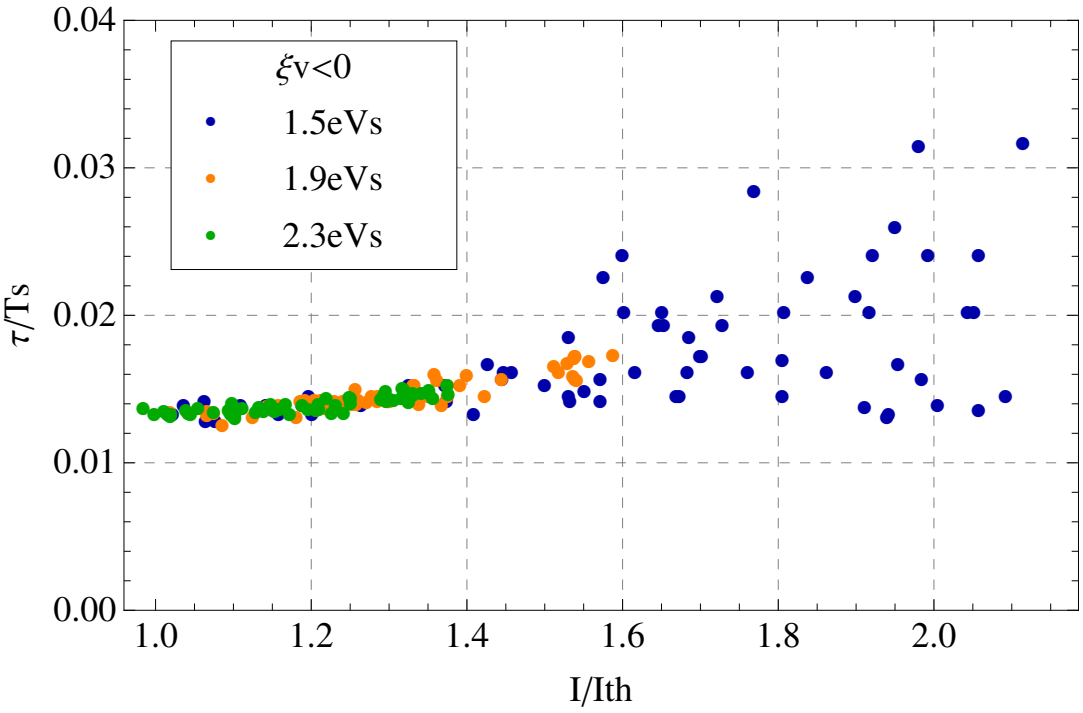

(b)

Figure 4.26: Measured rise time divided by its synchrotron period as a function of the beam intensity divided by the I_{th} corresponding to the longitudinal emittance of the data set, for a chromaticity close to zero in Fig. (a) and for a negative chromaticity in Fig. (b). The local minimum observed in Fig. (a) is caused by T_s tending to infinity at transition. This effect is not seen in Fig. (b), since all the points correspond to times after transition.

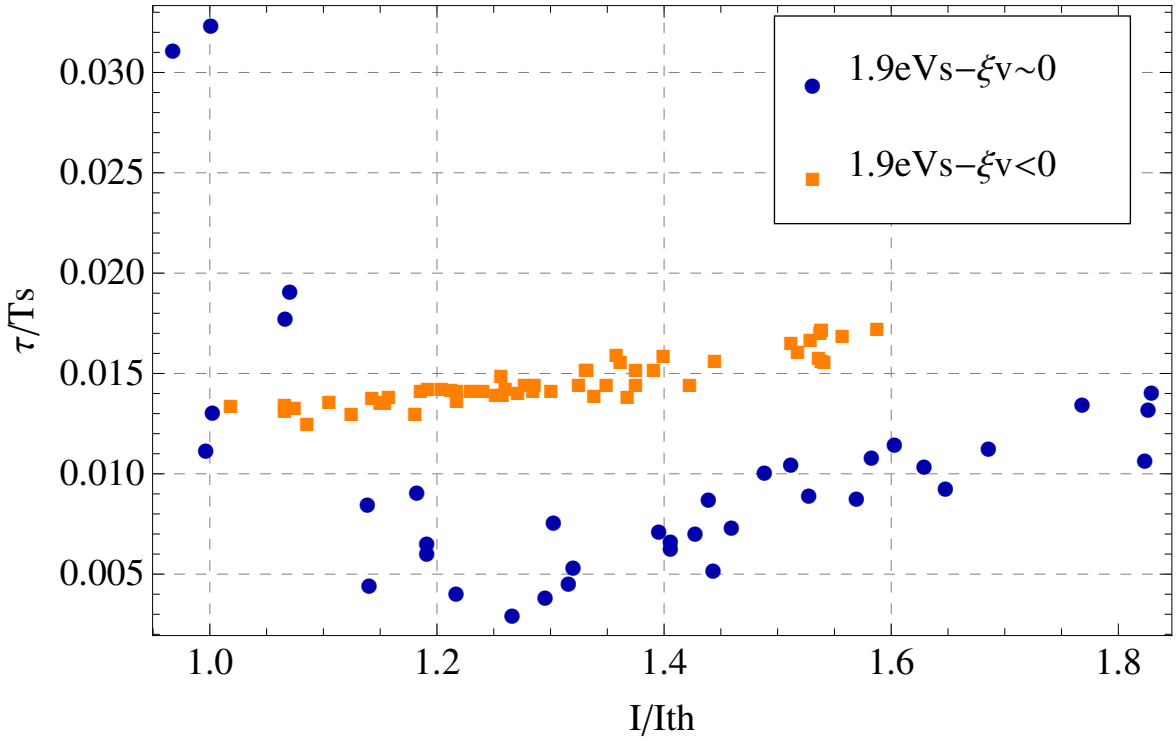

Figure 4.27: Measured rise time related to the synchrotron period as a function of the beam intensity divided by the I_{th} for ϵ_l =1.9 eVs and for the two sets in chromaticity.

4.3.2 Momentum Compaction Factor Threshold η_{th}

The fast transverse instability is not triggered at the same energy for increasing beam intensity increases. The time when instability starts during the acceleration can be related to a η_{th}, i.e. a distance from the transition energy. In particular, the main difference between the two sets in chromaticity is the time - or η - at which the instability starts. Whereas the fast turbulence is triggered few hundred turns on both sides of the supposed transition energy for $\xi_v \simeq 0$, a clear delay in time is observed when chromaticity is introduced, in our case $\xi_v \simeq -0.1$, the instability appears most of the time for positive value of η, up to 2 ms after transition energy. In this paragraph, the threshold in η is determined as a function of the beam intensity for each set of data and the results are presented in Fig. 4.28. We proceed in a similar way as the previous paragraph by identify the moment at which the instability starts with respect to the transition timing. Fig. 4.28a and Fig. 4.28b shows that it exists a threshold in η, η_{th}, below the instability is not triggered. η_{th} is a linear function of the beam intensity. Another remark is η_{th} is not a function of the longitudinal emittance, i.e. the instability is triggered at the same time close to the intensity threshold regardless ϵ_l. Fig. 4.28a and Fig. 4.28b allows to determine η_{th} for both sets in chromaticity:

- Figure. 4.28a shows that, for a vertical chromaticity close to zero, $\eta_{th} \simeq 0.00045$, when the beam intensity is closed to the intensity threshold;
- Figure. 4.28b shows that, for a vertical chromaticity of about -0.1 at transition, $\eta_{th} \simeq 0.0012$,when the beam intensity is closed to the intensity threshold;

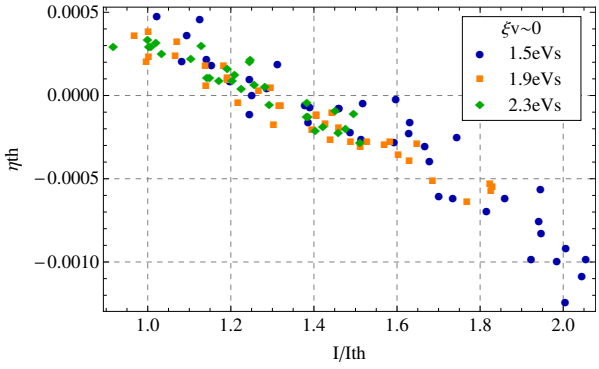

(a) η threshold, $\xi_y = 0$, normalized intensity

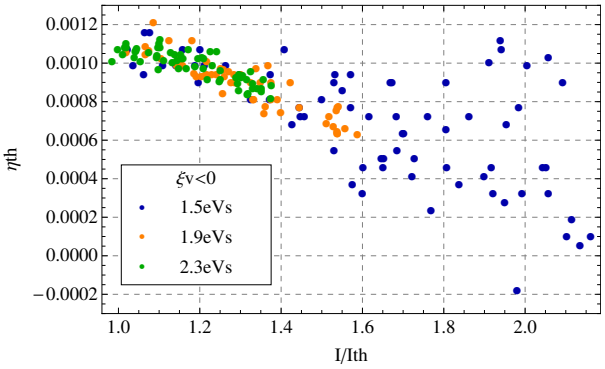

(b) η threshold $\xi_y < 0$, normalized intensity.

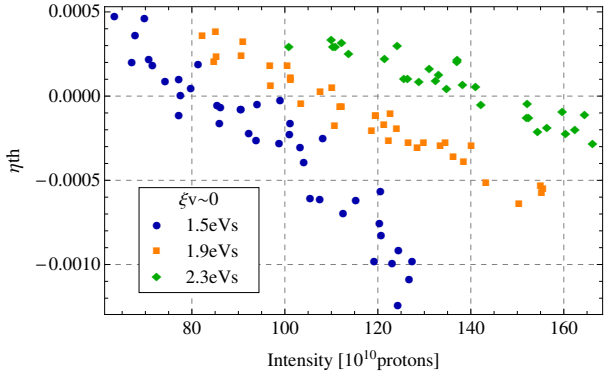

(c) η threshold,$\xi_y = 0$.

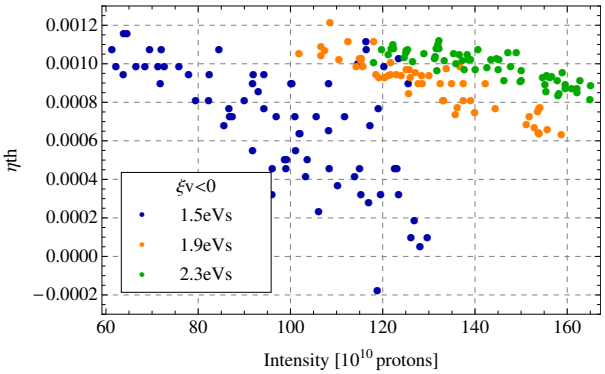

(d) η threshold, $\xi_y < 0$.

Figure 4.28: Instability threshold in η as a function of the beam intensity for no chromaticity - negative chromaticity - Fig. (a) - Fig. (b) - and as a function of the beam intensity in unit of I_{th} Fig. (c) - Fig. (d)

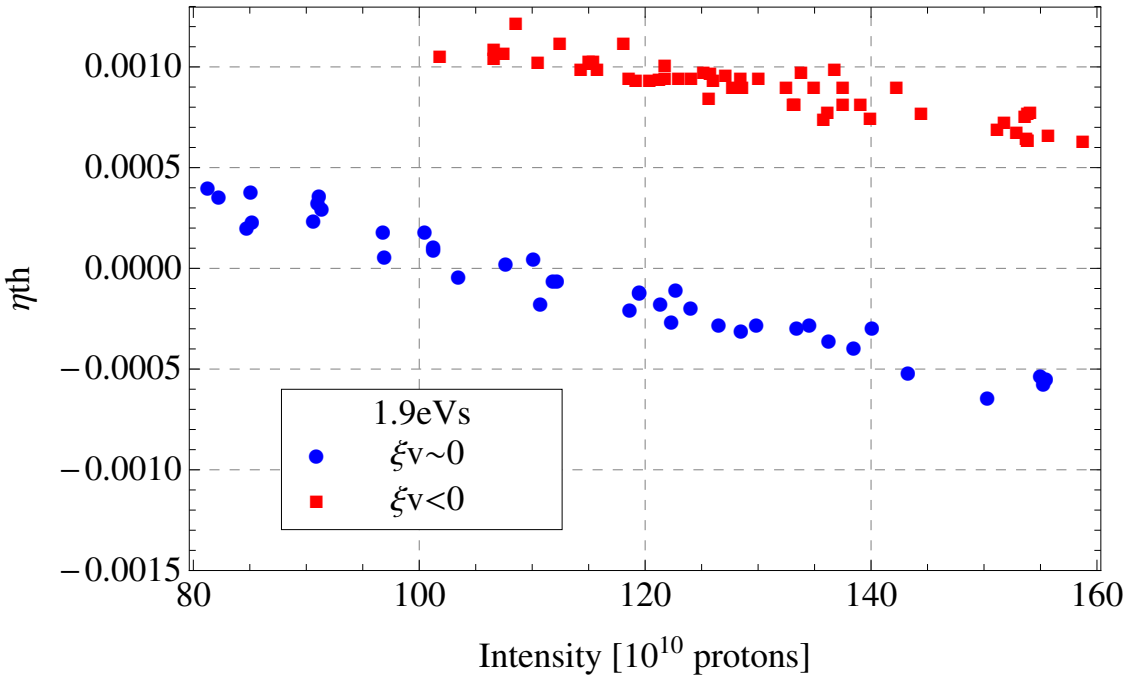

Figure 4.29: η threshold as a function of the beam intensity for a longitudinal emittance of 1.9 eVs for a chromaticity close to zero and negative.

Let extract η_{th} from the measurements and from Fig. 4.29 and check at which longitudinal regime - adiabatic or nonadiabatic - they belong. We introduce here the nonadibatic time $T_c = 2.2$ ms in the PS. The result is presented in Fig. 4.30 in which we see that the instability is triggered for times x expressed in unit of the nonadiabatic time which belong to the interval $-T_c < t < T_c$ or $-1 < x < 1$. Therefore the fast turbulence is observed in the measurements in the nonadiabatic longitudinal regime. Considering these results, one can observe that:

- during the measurements, we supposed the transition time is the same as the timing at which the RF stable phase shift is performed. However the setting of the jump was done in an empirical way and an uncertainty of few hundred turns can be admitted. In this case, the instability might start to develop in the adiabatic regime.
- Fig. 4.30 shows that higher is the beam intensity, earlier the instability will appears regardless the chromaticity. One can make the hypothesis that for beam intensity large enough, the instability will be triggered in the adiabatic regime, i.e. $x > 1$. In the BBU formalism, it would mean, even in presence of synchrotron motion, the movement which exchanges the particles between the head and the tail of the bunch is not strong enough to stabilize the fast transverse instability in a longitudinal regime too close to the nonadiabatic region. The reason why the beam intensity was not pushed so far is due to the very large losses.

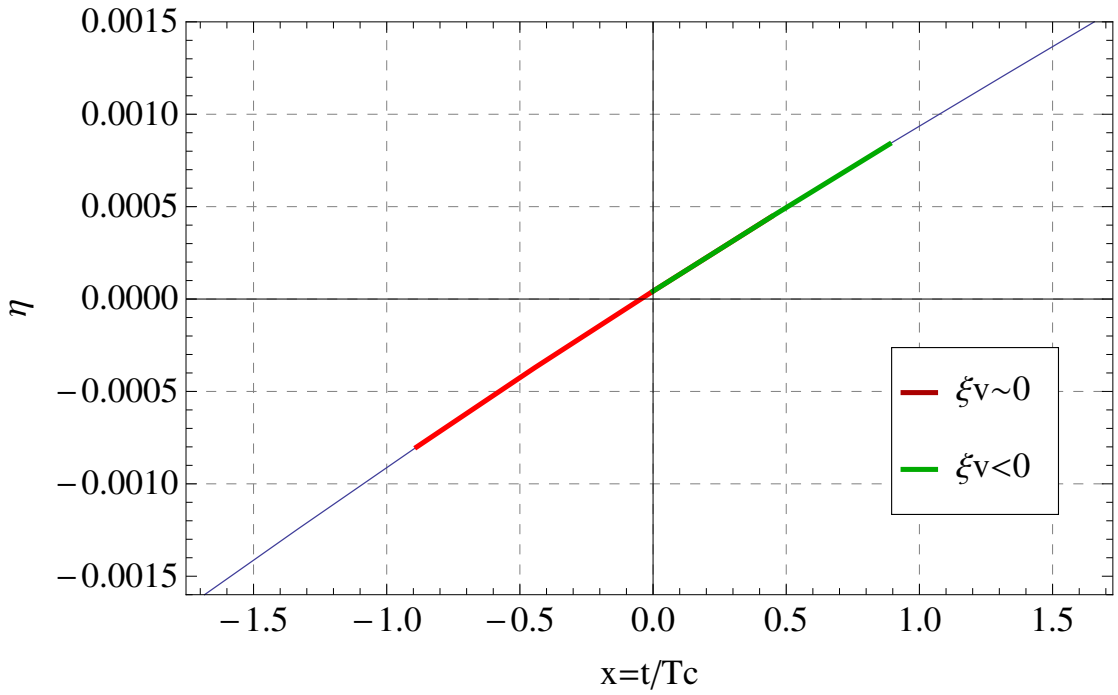

Figure 4.30: Measured η threshold as a function of time in unit of the nonadiabatic time T_c. The green and the red curve can be superposed for the $T_c > 0$.

Conclusions

In this section, the fast transverse instability measurements at transition energy without any gamma jump scheme were presented. We described in detail the experimental conditions under which the measurements were performed. The vertical chromaticity was set in two ways: a first set of data was taken with $\xi_v \simeq 0$ and another with $\xi_v \simeq -0.1$ as shown in Fig. 4.10. As discussed in Sec. 4.1.2, the working point setting up was tuned by PFWs and the vertical chromaticity was measured through transition. The fast instability is observed in the vertical plane but can be also present in the horizontal one due to a strong transverse coupling and if the horizontal chromaticity is not set in a suitable way. The instability was observed on the Δ_y signal of a wide band pickup and it manifests itself through a high frequency wave traveling along the bunch. The head is stable whereas the particles at the peak density are excited by a short range wake field and oscillate with high amplitudes until they hit the vacuum chamber. Systematic measurements were performed for different longitudinal emittances by varying the beam intensity for both sets in chromaticity. The rise times were extracted from the data and intensity thresholds as a function of the longitudinal emittance were then established. The results show that the larger the intensity, the faster the instability develops and the smaller is the rise time τ. By comparing τ with the synchrotron period, it was deduced that $\tau << T_s$. Then Fig. 4.24 presents that I_{th} is linearly varying with the longitudinal emittance and is also strongly dependent on the chromaticity. Therefore two ways to cure the instability can be explored:

- a blow up in longitudinal emittance used up to now in normal machine operation to alleviate the instability.
- use a suitable chromaticity setting.

The notion of threshold in momentum compaction factor η_{th} has been introduced, i.e. the needed distance from transition energy for a given chromaticity to develop the instability. In first approximation η_{th} does not depend of the longitudinal emittance, i.e. on the bunch length, but only of ξ_y:

- Fig. 4.28a shows for a vertical chromaticity close to zero, $\eta_{th} \simeq 0.00045$;
- Fig. 4.28b shows for a vertical chromaticity of about -0.1 at transition, $\eta_{th} \simeq 0.0012$;

Finally, by extracting η_{th} as a function of the beam intensity for both sets in chromaticity, Fig. 4.30 shows the measured instability appears in the nonadiabatic regime. Investigations with *HEADTAIL* simulations have to be performed to check if the transverse instability can be developed in the adiabatic regime. This is the subject of the next section in which a benchmark of the measurements will be presented.

4.4 Macroparticles simulations with *HEADTAIL*

4.4.1 Effect of a Broad-Band Impedance on the Beam Stability through Transition Energy

The *HEADTAIL* code takes as an input a configuration file (.cfg) in which the user defines divers parameters needed to performed the simulation. In the following some frequently used parameters are explained:

`Number_of_particles_per_bunch` defines the bunch population N_b.

`Bunch_length` sets the rms bunch length in m.

`Longitudinal_momentum_spread` defines longitudinal momentum spread or energy spread $\Delta p/p_0$ in rms units.

`Relativistic_gamma` defines the relativistic mass factor at which the simulation starts.

The bunch length and the momentum spread have to satisfy the well known matching condition in a stationary bucket in order to start the simulation

$$\frac{R_0|\eta|\Delta p/p_0}{Q_s\sigma_z} = 1 \tag{4.9}$$

with R_0 the machine radius, $R_0 = 100$ m for the CERN PS. The simulation is started far from transition energy in order to let the bunch filamented longitudinally in the bucket due to a small mismatch appearing in the first hundred turns. η is deduced from $1/\gamma_t^2 - 1/\gamma^2$ and the synchrotron tune Q_s is deduced. The expression of the longitudinal emittance is given at 2 σ as second conditions to deduce the rms bunch length and the longitudinal momentum spread since

$$\epsilon_l = 4\pi\frac{p\beta}{e}\sigma_z\Delta p/p_0 \tag{4.10}$$

with p the momentum, e the electron charge and β the relativistic parameter. The factor $p\beta/e$ is meant to get the rms bunch length from meter to second. Therefore from Eq. 4.10 and Eq. 4.9, σ_z and $\Delta p/p_0$ can be deduced.

`Synchrotron_tune:` sets the synchrotron tune Q_s.

`Momentum_compaction_factor:` sets the momentum compaction α_p the the value for the gamma transition γ_t where $\gamma_t = 1/\sqrt{\alpha_p}$.

`Number_of_turns:` define the number of turns the simulation has to be performed.

`Horizontal_chromaticity_[Q'x]:` sets the horizontal chromaticity Q' which is get from $Q' = Q_h\xi_h$.

`Vertical_chromaticity_[Q'x]`: sets the vertical chromaticity Q' which is get from $Q' = Q_y \xi_y$.

`Flag_for_synchrotron_motion`: sets the dynamics of the longitudinal phase space: stationary bucket, accelerating bucket, presence of longitudinal space charge, double RF harmonic. In our case, we choose the case with acceleration.

In the following paragraph, the beam-impedance interaction is defined in the configuration file. In our case a broad band impedance model is chosen and is general enough to model pipe discontinuities, tapers, non-resonant structures like pick-ups, kickers bellows etc. The resonant structure is characterized by the typical resonator impedances [72]:

$$Z_\perp(\omega) = \frac{\omega_r}{\omega} \frac{R_s}{1 + iQ\left(\frac{\omega_r}{\omega} - \frac{\omega}{\omega_r}\right)} \tag{4.11}$$

`Res_frequency_of_broad_band_resonator_[GHz]`: sets the ω_r parameter which is the cut-off frequency of the resonator.

`Transverse_quality_factor`: sets the Q parameter of the resonator.

`Transverse_shunt_impedance_[MOhm/m]`: sets the R_s parameter, the shunt impedance. The real and imaginary part of resonator model can be represented as in Fig. 4.31 as a function of the angular frequency ω.

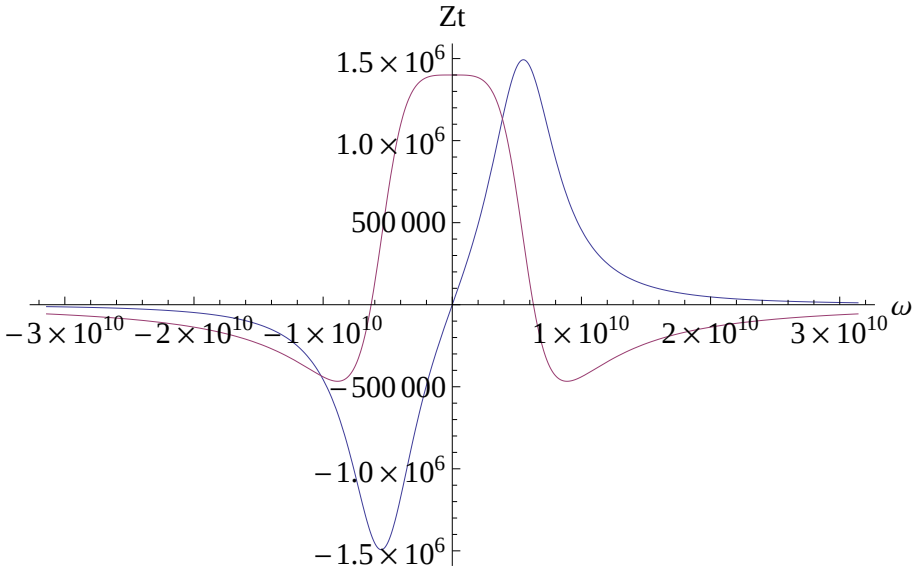

Figure 4.31: Real part in blue and imaginary part in purple of a broadband resonator as a function of the angular frequency.

`Number_of_kick_sections:` This parameter sets the number of kicks received by the bunch per turn to model its interaction with the impedance. In our case, since the PS impedance model is unknown, this number is set to 1.

`Switch_for_pipe_geometry_(0->round_1->flat):` this option defined the shape of the vacuum chamber. In the case of the CERN PS machine, the chamber are considered as flat. This switches artificially [72] the horizontal wake field keeping the vertical on and an incoherent quadrupole field is adding. Ref. [72] set that a chamber can be considered as flat if $(a-b)/(a+b) > 0.2$ with $2a$ is the width and $2b$ is the height of the vacuum chamber. In the case of the PS, $a = 75$ cm and $b = 35$ cm and $(a-b)/(a+b) = 0.333 > 0.2$

`Number_of_turns_for_the_wake:` this line determies if the wake field is computed only once at the beginning of the simulation and is kept the same during the simulation. One can write the expression of the wake field of the broadband resonator

$$W_{BB} = \omega_r^2 \frac{R_s}{\omega_r \sqrt{1-\frac{1}{4Q^2}}} e^{-\frac{\omega_r}{2Q}t} \sin\left(\omega_r \sqrt{1-\frac{1}{4Q^2}}\, t\right) \qquad \text{with} \quad t = z/(\beta c) \tag{4.12}$$

`y-kick_amplitude_at_t=0_[sigmas]:` allows to displace vertically the beam at the beginnng of the simulation in number of sigma $\sigma = \sqrt{\beta_v \epsilon_v}$ with β_v is the beta-function in the vertical plane and ϵ_v is the rms vertical emittance. The initial distribution of bunch particles is transversely centered around the values input at this line.

`Switch_for_losses_(0->no_losses_1->losses):` allows beam losses either transversally when the particles exceed the dimensions of the vacuum chamber or longitudinally, ie. the particles are considered lying in the separatrix and get lost.

`Main_rf_voltage_[V]:` sets the RF voltage of the radio-frequency cavities.

`Main_rf_harmonic_number:` sets h the RF harmonic, in our case $h = 8$.

`Max_phase_shift_delay_after_transition_crossing_[turns]:` allows to set a delay for the RF stable phase jump at transition energy.

Headtail instability measurements done at the CERN PS in 1974 in Ref. [10] and [80] (Fig. 6 of the references) have shown experimentally that the PS impedance is consistent with a broad-band model. A frequency resonator of 1 GHz with quality factor Q of 1 were found. In this thesis, we will show that those parameters are consistent with the observation of the fast vertical instability. The general wake field expression is given in Eq. 4.12. Hence, a broad-band impedance model is set up in *HEADTAIL* with the beam characteristics presented in Table 4.2 for two different intensities. The simulation is started far from transition, at a beam energy of $\gamma = 4$, corresponding to 50 ms before transition in real time machine. The reason is to leave the beam filament in the bucket during the first hundred turns since the beam is not perfectly matched to the bucket due to matching errors of the beam distribution with respect

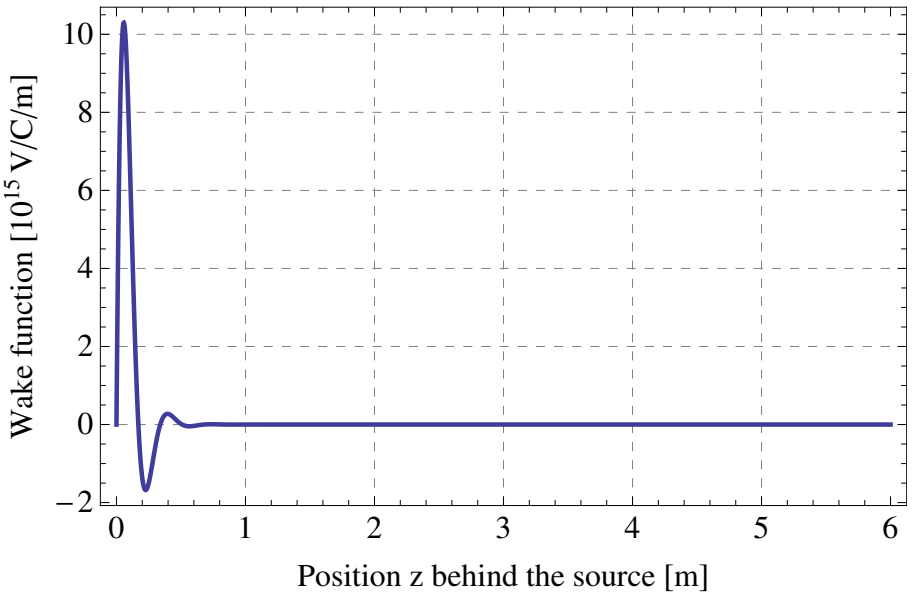

Figure 4.32: Wake function for the broadband impedance model with the parameters of Table 4.2

to the accelerating bucket. The chromaticities are set to zero in both planes and the switch for the impedance is on in such a way that the beam-impedance interaction is performed with the wake plotted in Fig. 4.32. At the beginning of the simulation, *HEADTAIL* generates the particle distributions. The longitudinal one is created from the rms bunch length and the momentum spread given in the configuration file. These values are obtained from the longitudinal matching of a stationary bucket and a bi-gaussian distribution is then generated in an accelerating bucket. Fig 4.33 represents the bunch distribution evolution during the simulation, in particular the initial bunch distribution. No space charge is taken into account in the simulation.

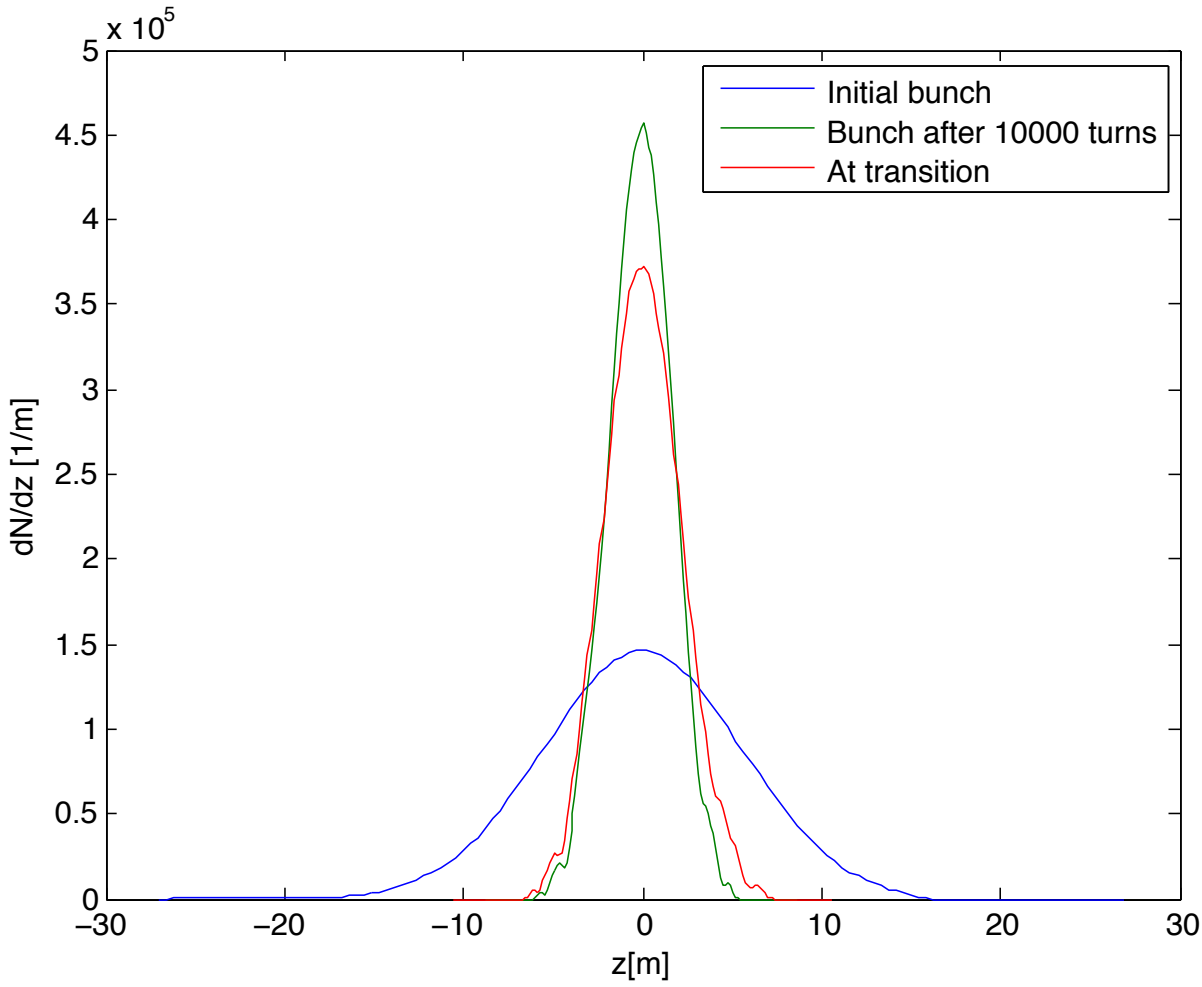

Figure 4.33: Bunch distribution from *HEADTAIL* at the beginning of the simulation, at transition energy and 500 turns after.

Momentum change rate	46 GeV/c/s
Machine radius R_0	100 m
γ_t	$\simeq$ 6.11
Starting γ	4
RF Voltage	200 kV
Bunch length rms σ_z	5.521 m
Momentum spread rms $\delta p/p$	0.0023
Longitudinal emittance (2 σ)	1.9 eVs
Norm. transverse emittance (1σ) $\epsilon_{x,y}$	5 mm·mrad
Transverse tunes $Q_{x,y}$	6.22/ 6.28
Chromaticity $\xi_{x,y}$	0/0
RF Harmonic h	8
Number of bunches	1
Synchrotron tune Q_s	0.0015
Shunt Impedance R_s	1.6 MOhm/m
Resonator frequency f_r	1 GHz
Quality factor Q	1
Number of simulated turns	50000

Table 4.2: Beam parameters in the cfg file at the beginning of the *HEADTAIL* simulation.

Beam parameters during the acceleration are extracted from the *HEADTAIL* simulation. Fig. 4.34 the RF stable phase ϕ_s, in which the phase shift at transition energy is performed in order to keep the longitudinal focusing below and above γ_{tr}. Fig. 4.35a presents the time evolution of the relativistic γ compared to the gamma transition of the bare machine. Fig. 4.35b shows the momentum compaction factor η as a function of γ.

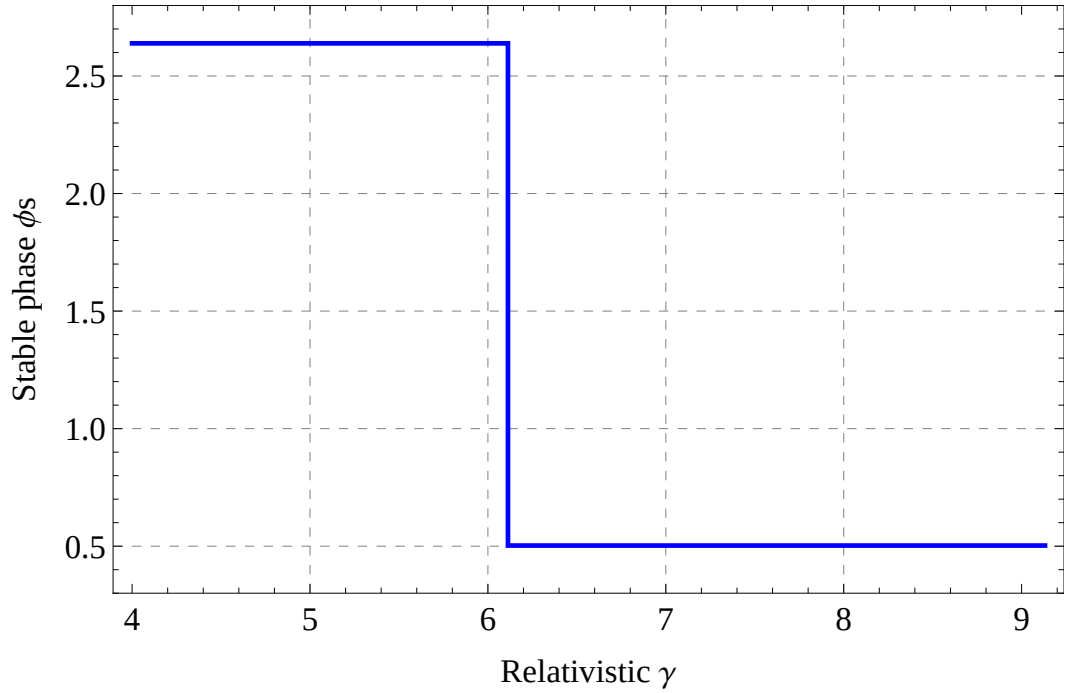

Figure 4.34: Stable phase ϕ_s evolution during the *HEADTAIL* simulation. The phase shift is performed at transition energy.

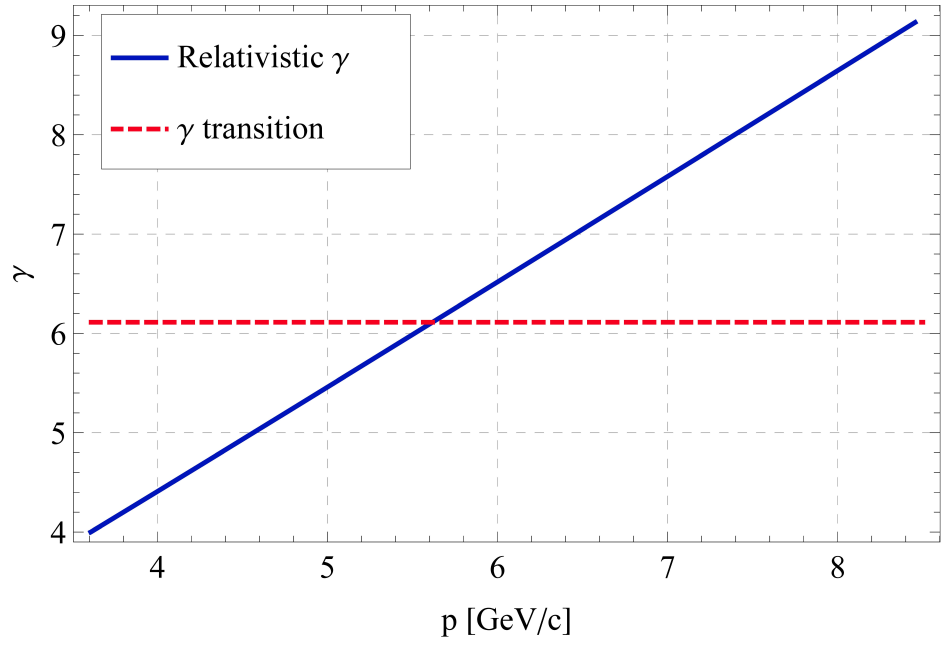

(a)

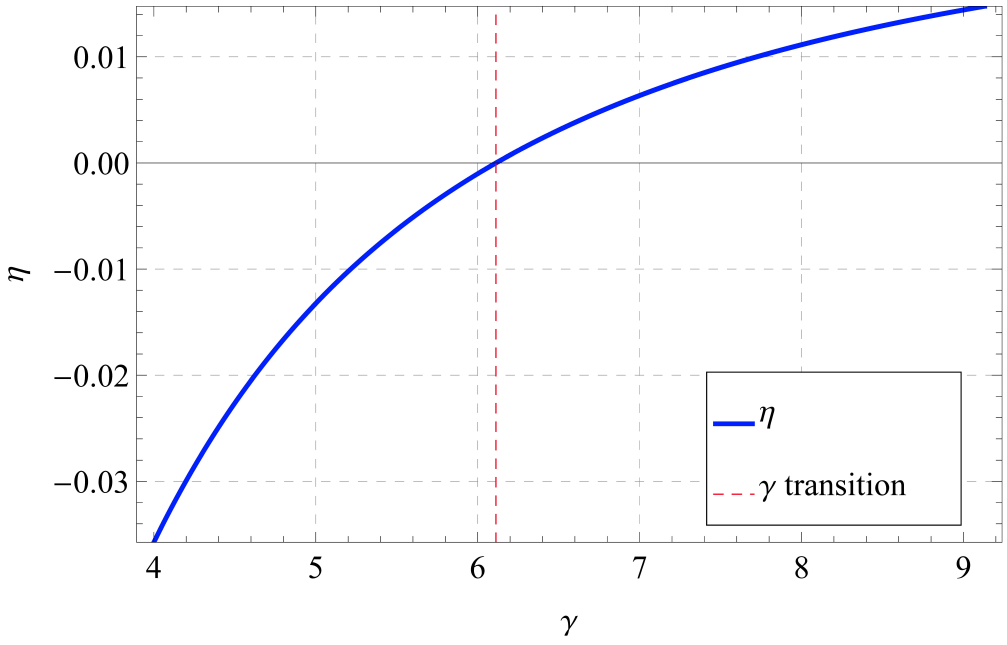

(b)

Figure 4.35: Fig. (a) is the Lorentz factor γ evolution during the acceleration simulation by *HEADTAIL*. Fig. (b) is the momentum compaction factor η variation with the beam energy.

The full bunch length ($4\sigma_z$) simulated by *HEADTAIL* is presented in Fig. 4.36a. As described in Sec. 1.3.4, σ_z reaches a minimum at transition energy as expected from the nonadiabatic longitudinal theory. At the same time, the momentum spread $\delta p/p$ in Fig. 4.36b is maximum. This confirms that the acceleration module of *HEADTAIL* is behaving as expected inside and outside of the nonadiabatic regime. From Fig. 4.36a, the bunch length is slightly oscillating at the beginning of the simulation due to a small longitudinal mismatch of the beam in the RF bucket.

The longitudinal initial parameters $\sigma_z, \delta p/p$ given in Table 4.2 are calculated from a stationary bucket while *HEADTAIL* generates the distribution in an accelerating phase space which is not completely matched to the beam. The particles are captured and the beam will filament to occupy the phase space. It can be seen in Fig. 4.33 the bunch distribution is not completely Gaussian since some tails are developed. Due to the slowing down synchrotron motion the bunch length oscillations are damped around transition to appear again after.

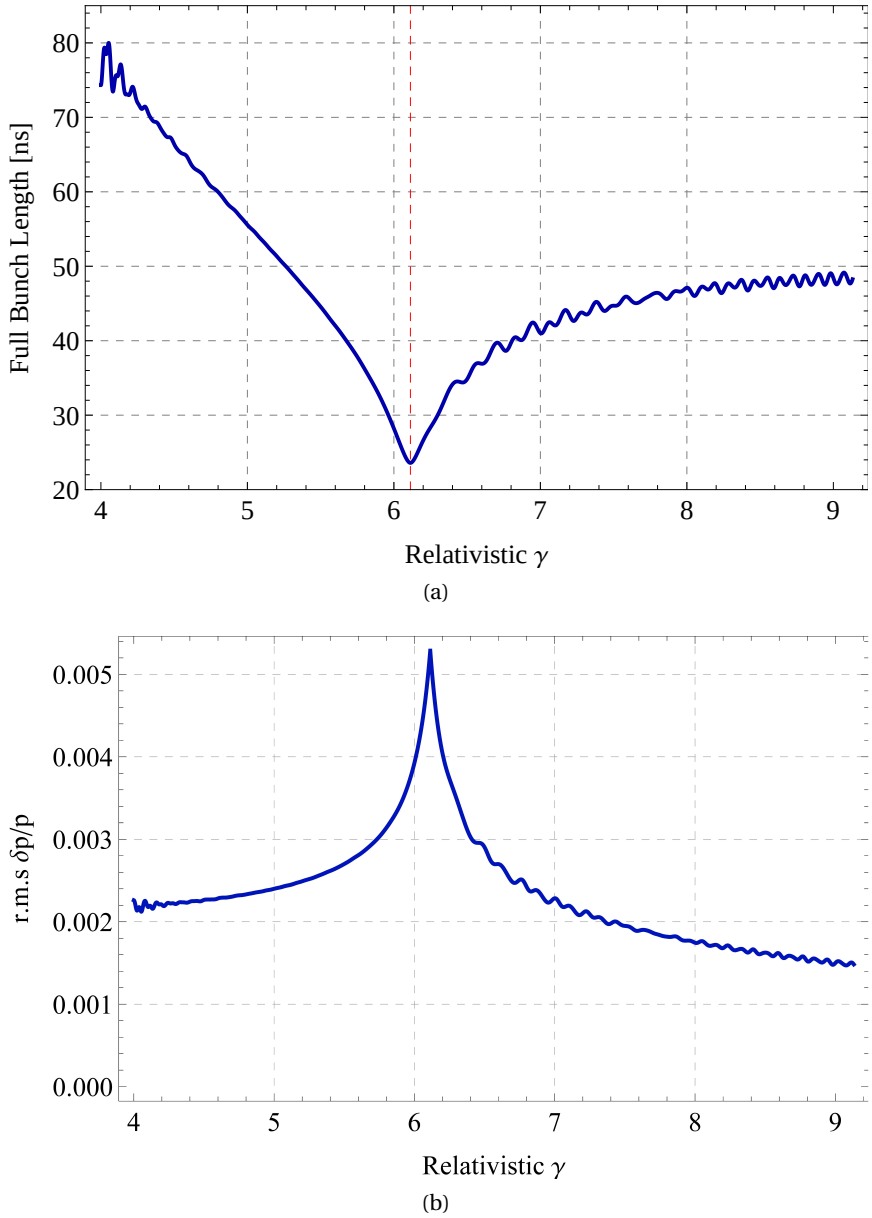

Figure 4.36: Fig. (a) is the full bunch length evolution during the acceleration computed by *HEADTAIL*. Fig. (b) is the energy spread variation with the beam energy.

The simulation is performed for two beam intensities $N_b = 10 \cdot 10^{10}$ and $N_b = 90 \cdot 10^{10}$ protons for which we expect that the beam is either stable or unstable. The vertical position of the beam centroid for the two intensities is presented in linear scale in Fig. 4.37a and in logarithm scale in Fig. 4.37b. The oscillations at low energy are caused by the vertical offset given to the beam at the beginning of the simulation. The beam remains stable for the intensity of $N_b = 10 \cdot 10^{10}$ whereas the vertical position of the centroid grows exponentially for $N_b = 90 \cdot 10^{10}$, confirmed by Fig. 4.37b in which a linear behaviour is observed in logarithm scale. The vertical normalized emittance in Fig. 4.38 blows up while the instability is developing.

The Δ and longitudinal density signals are also provided by *HEADTAIL*. Fig. 4.39a presents the vertical Δ signal and the longitudinal beam distribution. The particles start to oscillate around the peak density which is consistent with the measurements. Fig. 4.39b shows again the Δ_y signal around transition energy while the instability is well developed. A Fast Fourier Transform is applied on every trace to identify the frequency spectrum of the instability as a function of the beam energy during the acceleration as shown in Fig. 4.40. One can compare Fig. 4.40 with the measurements of Fig. 4.14. Similar frequency ranges of about 500 MHz up to 1 GHz are observed on simulated vertical profiles. As first approximation, the broadband impedance model allows to reproduce the measured travelling wave with similar frequency.

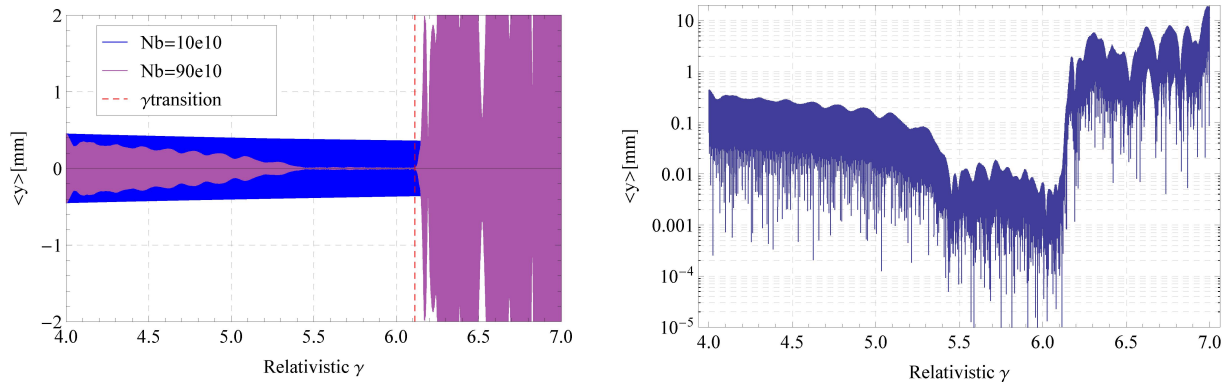

(a) Vertical centroid motion for $N_b = 90 \cdot 10^{10}$ and $N_b = 10 \cdot 10^{10}$ (b) Vertical centroid motion for $N_b = 90 \cdot 10^{10}$ in logscale.

Figure 4.37: Fig. (a) is the vertical position of the beam centroid in linear scale and in logarithm scale in Fig. (b).

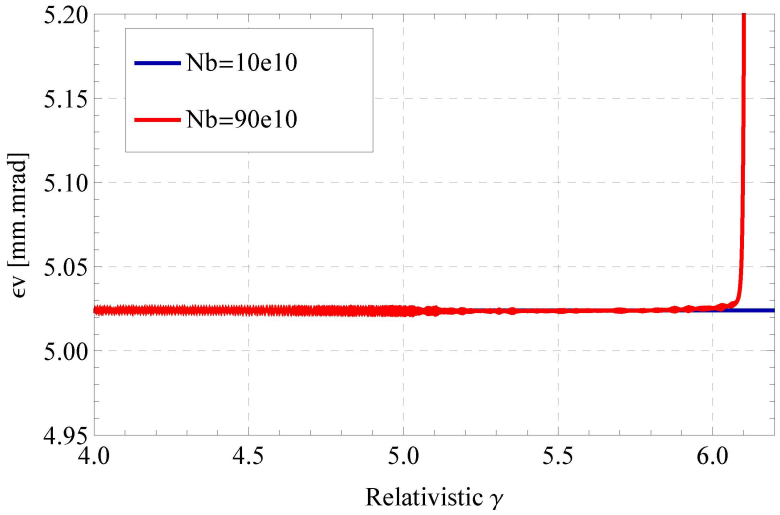

Figure 4.38: Vertical r.m.s emittance as a function of beam energy.

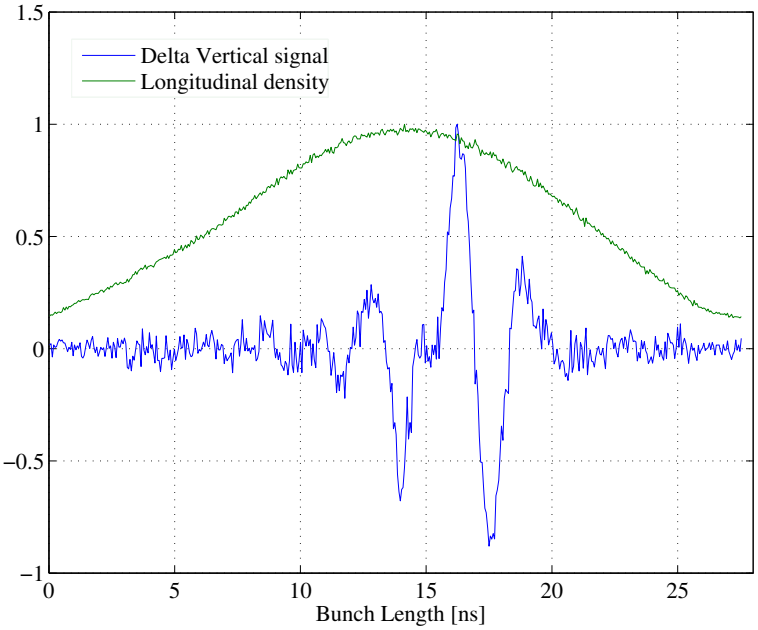

(a) Δ_y and longitudinal beam distribution signals computed by *HEADTAIL* while the instability is starting.

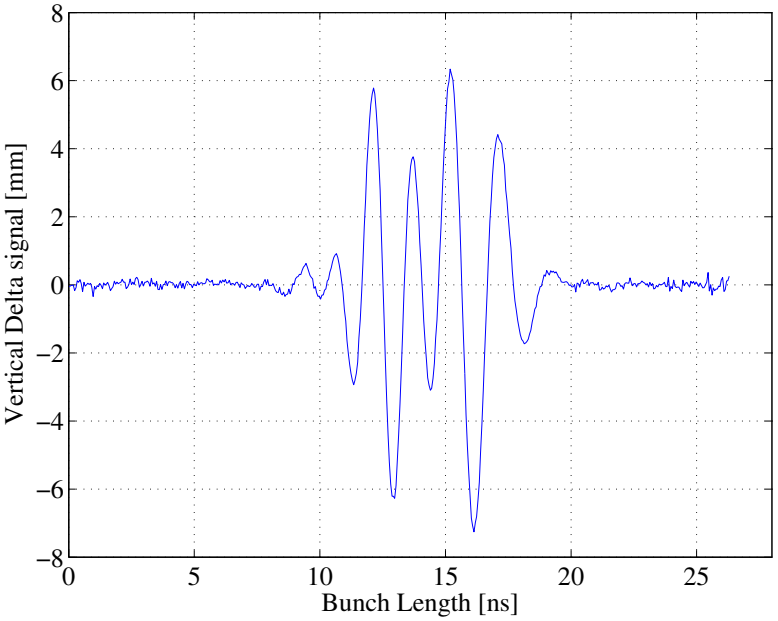

(b) Δ_y signal computed by *HEADTAIL* while the instability is well developed.

Figure 4.39: Δ_y and longitudinal beam distribution signals computed by *HEADTAIL*

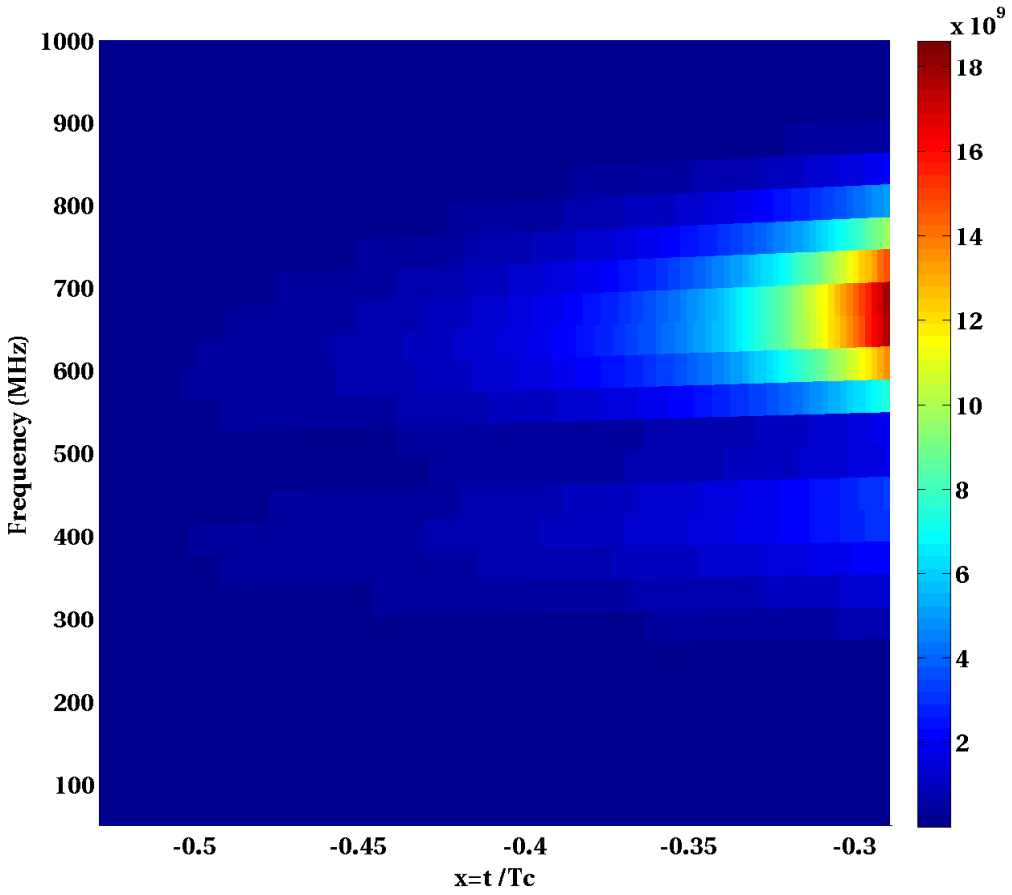

Figure 4.40: Frequency of the travelling wave simulated by HEADTAIL as a function of time expressed in unti of T_c.

4.4.2 Conclusions

Macro particle simulations with *HEADTAIL* using a broad-band impedance have shown that the beam can be unstable through transition energy. The instability appears in the vertical plane and the centroid is affected by an exponential growth. By comparing the Δ_y signal to the longitudinal density simulated by *HEADTAIL*, one can see that an oscillation is developing near the peak density as observed in the measurements and with the frequency of the travelling wave. This is a first very important result.

In the next paragraph, a scan in beam intensity scan is performed with *HEADTAIL*. The results are compared to experimental data in order to find the suitable matching impedance parameters and study in more detail the dynamics of the fast vertical instability.

4.5 Broad-Band Impedance Matching

This section will focus on the dynamics of the instability in macroparticle simulations with *HEADTAIL*. In a similar way as the experiments, scans in beam intensity are performed in order to compute the rise time of the instability. The results are compared to the experimental data. Intensity thresholds as a function of the longitudinal emittance, if exist, are defined. The parameters of the PS effective broad-band impedance interacting with the beam at transition energy are matched. The simulations are performed without and with chromaticity, which might be a damping mechanism.

4.5.1 Impedance matching for $\epsilon_l = 1.9$ eV.s

A series of macro particle simulations *HEADTAIL* has been performed for a longitudinal emittance of 1.9 eV.s without any chromaticity. The beam characteristics in the simulations are presented in Table 4.3. The beam intensity is varying as well as the shunt impedance R_s with the parameters of Table 4.4 in order to find the impedance model which roughly fits the measurements in term of rise time and instability threshold.

Beam intensity	$0.01 \cdot 10^{10} \rightarrow 160 \cdot 10^{10}$ protons
Starting relativistic γ	4
η at $\gamma = 4$	-0.035
RF Voltage V	200 → 145 kV
Transverse tune $Q_{x,y}$	6.22/6.28
Chromaticity $\xi_{x,y}$	0/0
Norm. rms emittance $\epsilon_{x,y}$	5 mm·mrad

Table 4.3: Beam parameters in *HEADTAIL* simulations. The number of proton in the bunch is varied.

As already explained in Sec. 4.4.1, longitudinal parameters has to be provided to *HEADTAIL* to generate the beam distribution. Energy spread and rms bunch length are deduced from the condition of a matched stationary bucket and using the expression of the longitudinal emittance, here with a value of 1.9 eV.s, the longitudinal parameters σ_δ, σ_z are deduced from Eq. 4.10 and Eq. 4.9. The rms bunch length and energy spread are found in order to obtain a longitudinal emittance at 2σ in a matched stationary bucket. The results are shown in Table 4.5.

Resonator frequency f_r	1 GHz
Quality factor Q	1
Shunt impedance R_s	0.1→2.5 MOhm/m

Table 4.4: Broad-band impedance parameters in *HEADTAIL* simulations. The shunt impedance is varying in the code.

Fig. 4.41a presents the RF bucket computed with the beam parameters of Table 4.3, i.e. the separatrix Eq. 1.58 with a RF voltage of $V = 200$ kV. The solution of the matched beam solved is a solution of the general equation of the longitudinal motion Eq. 1.48. *HEADTAIL* generates a

RF Voltage V	200 kV
σ_z	5.52 m
σ_δ	0.0023
Synchrotron tune Q_s	0.0015
η	-0.035

Table 4.5: Results of the longitudinal matching for a longitudinal emittance 2 σ of 1.9 eV.s.

bi-Gaussian distribution in the accelerating bucket using the equation of the separatrix Eq. 1.58. Up to now, the total RF voltage applied on the cavities used in the calculation was 200 kV. However, the measurements were performed with 145 kV, which reduces the height of the bucket and the RF acceptance from $(\Delta E/E_s)_{max,(V=200\ kV)} = 0.0228$ to $(\Delta E/E_s)_{max,(V=145\ kV)} = 0.0194$. It is important is to check that the longitudinal emittance during the simulation is conserved. In an accelerating bucket, the product of the rms energy spread and the rms bunch length $\sigma_\delta \sigma_z$ has to be constant to conserve the longitudinal emittance. Therefore, we monitor this quantity during the simulation in Fig. 4.42. In the case of a 145 kV RF voltage, the product of the rms energy spread and the rms bunch length $\sigma_\delta \sigma_z$ is lower by 20% at the beginning of the simulation due to the mismatch between the initial conditions, generated for a stationary bucket, and the accelerating bucket and also due to also to the small bucket height if the total voltage is 145 kV.

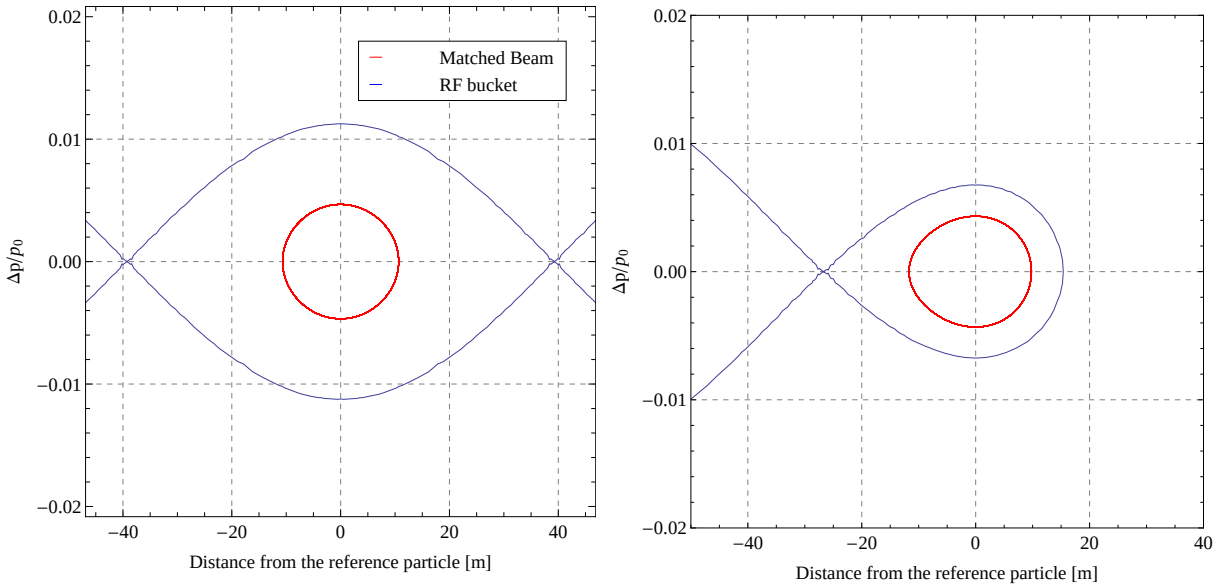

Figure 4.41: Fig. (a) presents the PS RF bucket computed from Eq. 1.58 and the solution of a matched beam with the parameters of Table 4.3 and Fig. (b) is the PS accelerating at the same energy.

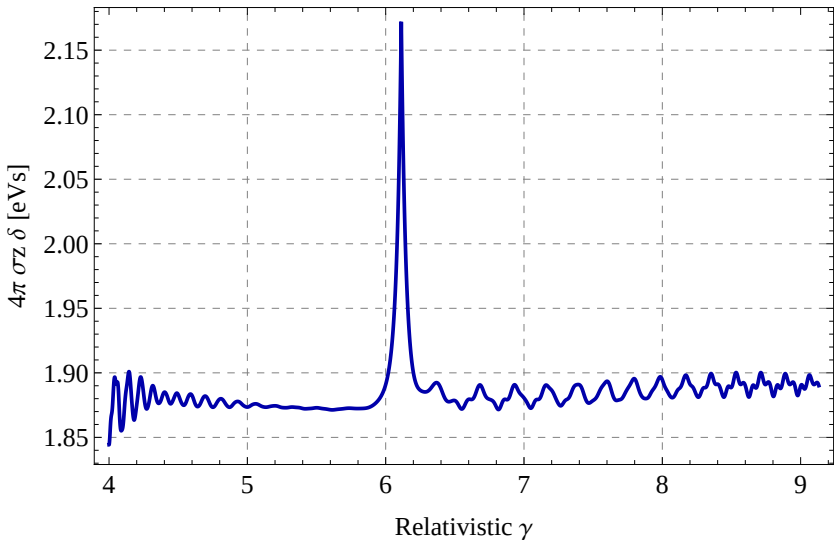

Figure 4.42: Bunch length and energy spread product evolution as a function of the beam energy during the acceleration for a RF voltage of 200 kV.

Fig. 4.43a and Fig. 4.43b show the RF accelerating bucket respectively for 200 kV and 145 kV for the same longitudinal emittance of 1.9 eVs and the blue dots are initial particle distribution generated by *HEADTAIL* at the very beginning of the simulation, before the particles complete the first turn. The bucket with 200 kV is less full with respect to the case 145 kV, in particularly at the boundaries of the fish-shape bucket. The longitudinal beam distribution can be projected for $\Delta p/p = 0$ and for the case of 200 kV, Fig. 4.44a, the distribution is Gaussian, at the opposite of Fig. 4.44b, which corresponds to the case 145 kV. In this example, the longitudinal distrubution gets some long tails and is not Gaussian. The most convenient case for the particle generation in the bucket seems to be in favour to the total RF voltage of 200 kV. However, in order to decrease bunch length oscillation after transition energy, the reduction of the RF voltage is convenient, the risk being if the reduction is excessive that the beam experiences non-linear synchrotron motion. It is very common in normal operation to perform an adiabatic reduction of the RF cavity voltage in order to prevent some longitudinal instability to develop.

The measurements were performed with a total RF voltage applied on the cavities of about 145 kV. Keeping the same longitudinal emittance, the bunch length is changed by about 20%. It is important to keep the longitudinal conditions in the simulations as close as possible as in the experiments. Hence it was necessary to implement in the code a quasi-adiabatic reduction of the RF voltage from 200 kV to 145 kV as illustrated in Fig. 4.45 and the resulting bunch length is shown in Fig. 4.45b. The bunch length is then shorter at transition energy and while the RF voltage reaches the minimum voltage of 145 kV, σ_z slightly increases. Some particles populate the tails of the distribution and they are lost when the voltage is not sufficient to keep them in the bucket. *HEADTAIL* computes the bunch length by evaluating the standard deviation of the distance between each macroparticle and the reference particle. Therefore if many protons populate the tails of the distribution, the bunch length increases until they are lost. This reduction of the RF voltage in the simulation is not performed in an adiabatic way. In the real machine, the decrease evolves over at least 100 ms, which would mean a twice as long simulation time for a computing time that is already very long (>24 hours).

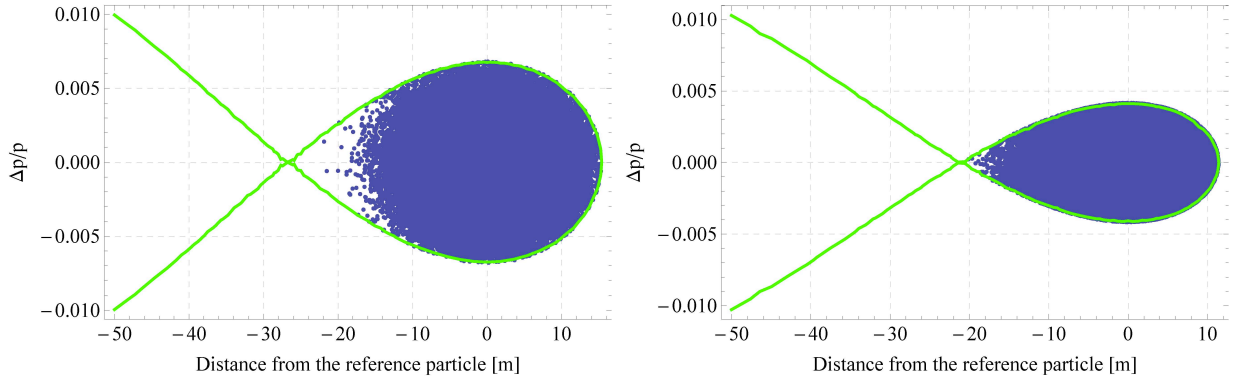

(a) Total RF voltage 200 kV (b) Total RF voltage 145 kV

Figure 4.43: Fig. (a) presents the PS RF bucket for a total RF voltage of 200 kV with the particles generated by *HEADTAIL*. The same is done in Fig. (b) with a total RF voltage of 145 kV in which the bucket is full whereas Fig. (a) seems to be more adapted.

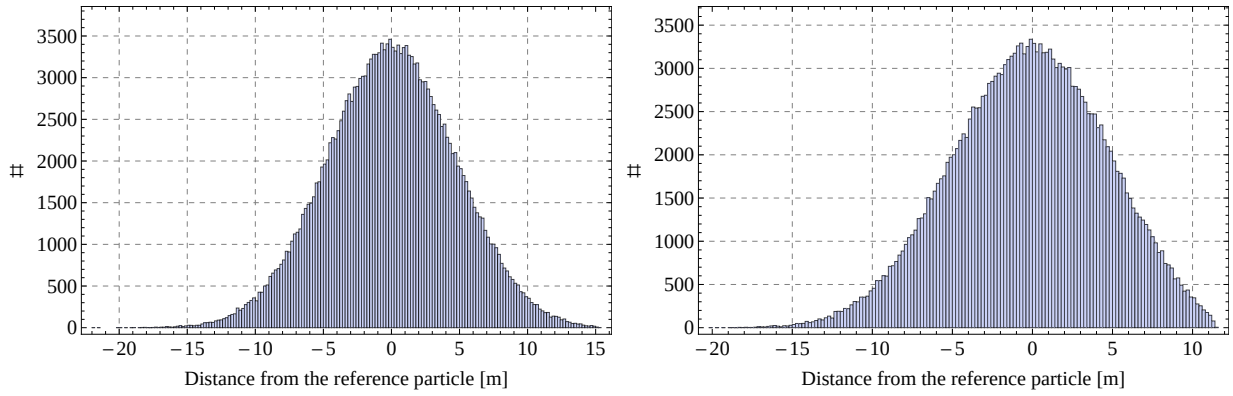

(a) Total RF voltage 200 kV (b) Total RF voltage 145 kV

Figure 4.44: Fig. (a) presents the initial beam distribution for a total RF voltage of 200 kV generated by *HEADTAIL*. The same is done in Fig. (b) with a total RF voltage of 145 kV.

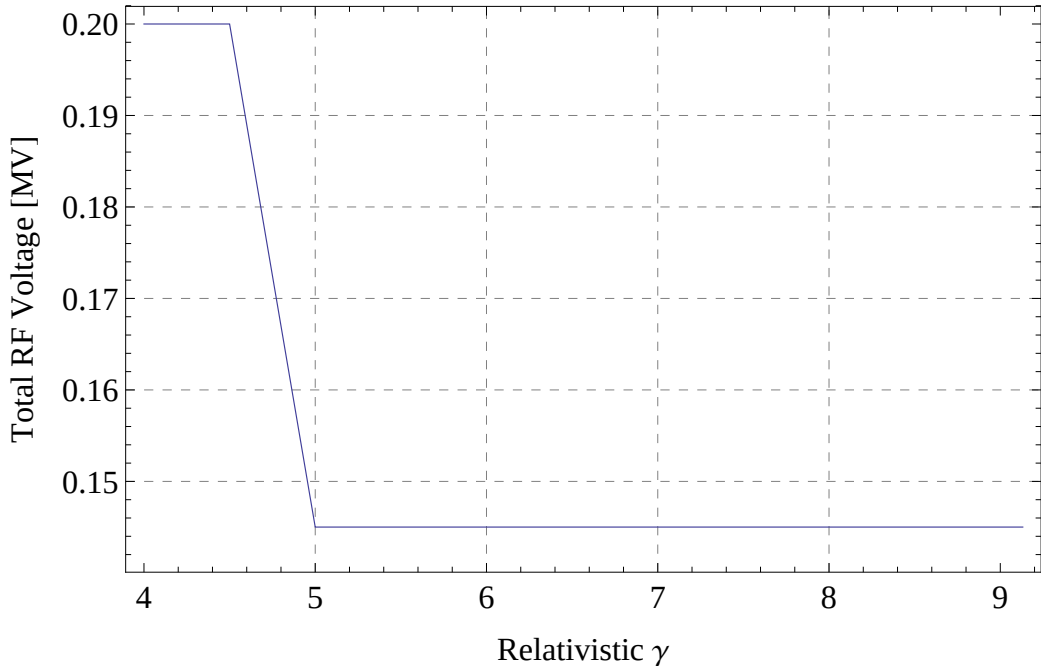

(a) .

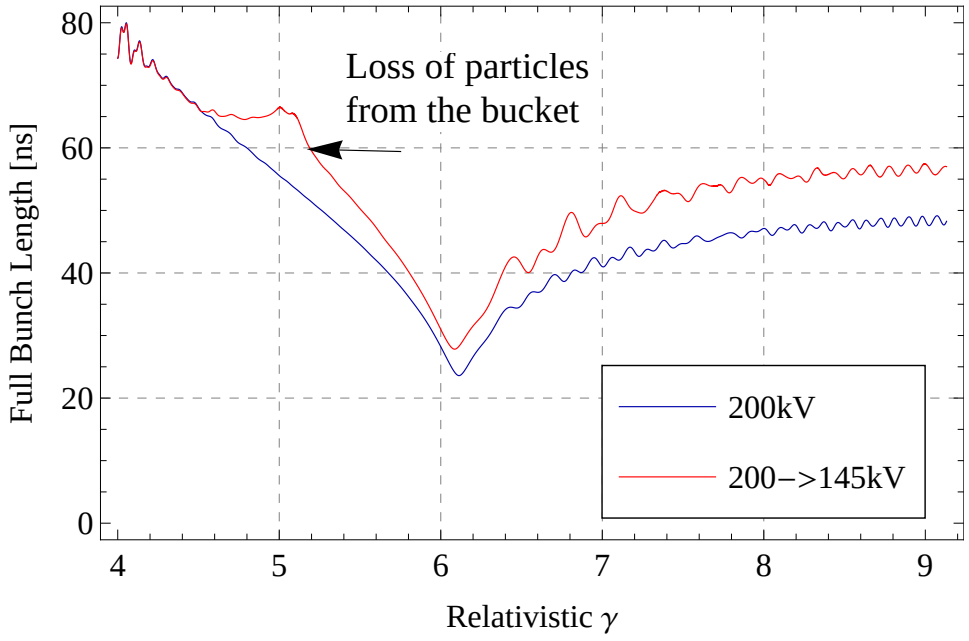

(b)

Figure 4.45: Fig. (a) presents the almost adiabatic reduction of the RF voltage implemented in *HEADTAIL*. The resulting bunch length evolution is presented in Fig. 4.45b compared to the bunch length computed if the RF voltage at 200 kV is kept constant along the simulation.

The broad-band impedance model is composed by three parameters: the resonator frequency f_r, here about 1 GHz [39, 81], the quality factor Q, here about 1 for the moment, and the shunt impedance R_s, which is unknown. Hence, this parameter has to be matched to fit the thresholds in number of protons and in momentum compaction measured in Sec. 4. The effect on the bunch length of the longitudinal space charge is neglected for the moment. A series of simulations is launched using the longitudinal matched parameters of Table 4.5 and Table. 4.3. The beam intensity is scanned as well as the shunt impedance. Measurements have shown that the fast vertical instability appears below a certain threshold in intensity which can be well seen on the wallcurrent monitor signal. Several outputs are available from *HEADTAIL* to observe the instability. In many studies, the beam centroid of the beam is used which averages the transverse position of each slices, implying that the beam experiments a coherent motion [36]. Fig. 4.47 presents the vertical beam centroid as a function of the relativistic γ factor for a shunt impedance of $R_s = 1.5$ MΩ/m and for different beam intensities indicated in the label of each plot. The reader is reminded that the effect of the impedance is to provoke a complex tune shift ΔQ. If $\mathrm{Im}(\Delta Q)$ is non-zero, it triggers a growth rate, i.e. the motion of the single particles increases exponentially. Hence, in order to identify an exponential growth on the beam centroid, the figures are presented in semi-logarithm scale. The beam intensity needed to observe such a behaviour is about $75 \cdot 10^{10}$ protons which is very close to the $80 \cdot 10^{10}$ measured for the same longitudinal emittance.

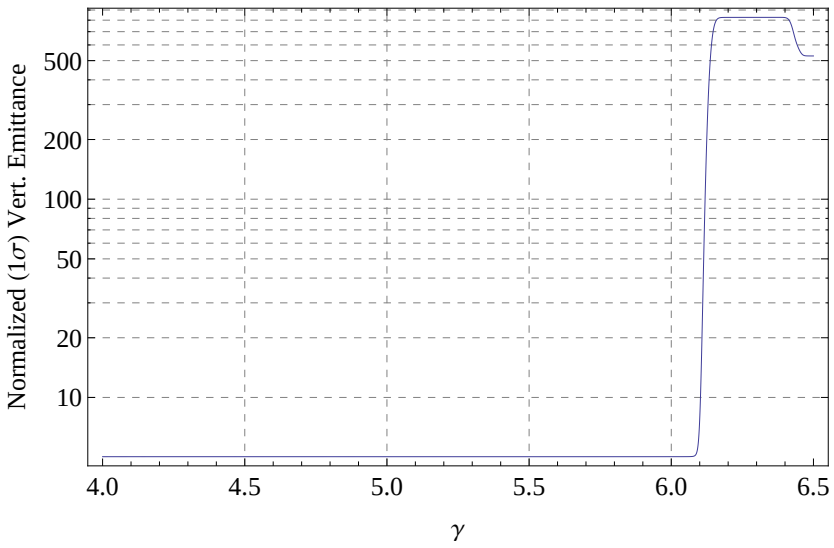

Figure 4.46: Vertical normalized 1σ emittance computed by *HEADTAIL* as a function of the beam energy for $N = 80 \times 10^{10}$ protons. The shunt impedance is $R_s = 1.5$ MΩ/m.

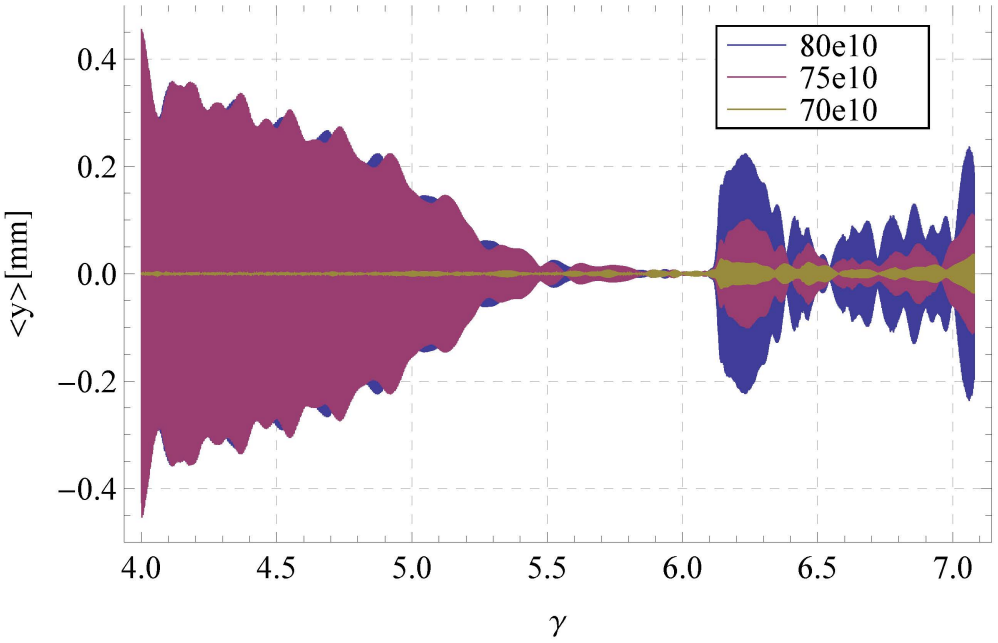

(a) .

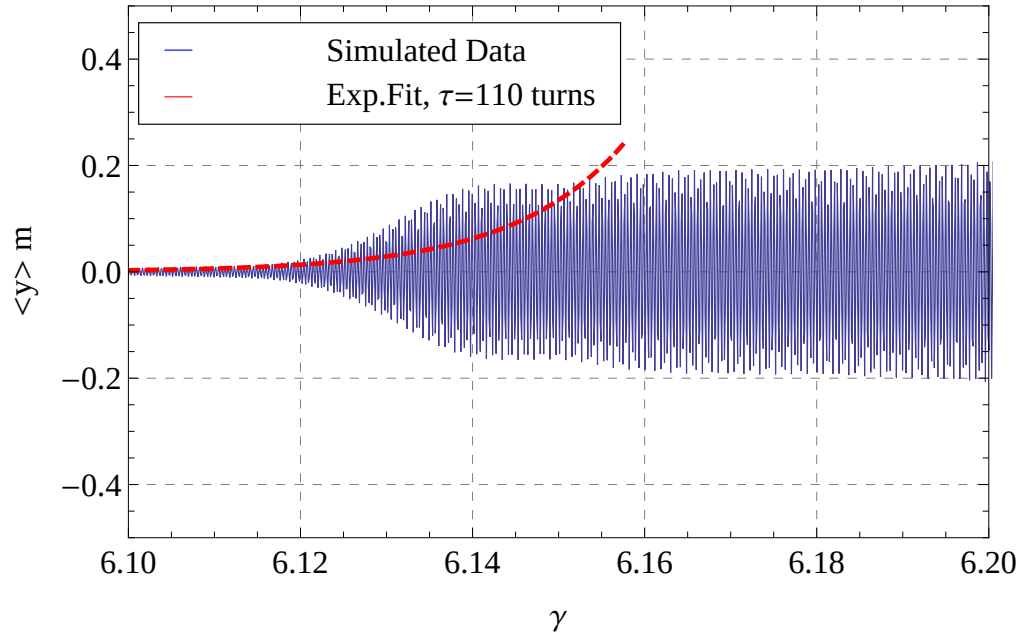

(b)

Figure 4.47: Fig. (a) presents the vertical beam centroid for the intensities of $70 \cdot 10^{10}$ and $80 \cdot 10^{10}$. An exponential fit is applied in Fig. 4.47b.

The corresponding vertical emittance growth for $R_s = 1.5$ MΩ/m and $N = 85 \cdot 10^{10}$ protons is shown in Fig. 4.46. A large blow up of about more than 100 times the initial vertical emittance of 5 mm.mrad normalized is observed, which implies that the instability is already well developed and the impedance is overestimated. The large emittance blow up is consequence of the time evolution of the vertical distribution. Fig. 4.48 presents the positions of 4000 macroparticles computed by the code in the vertical phase space (y, y') at different beam energies during the acceleration. As expected, below $\gamma \simeq 6$, the beam is stable in the phase space until it approaches transition energy, where particles oscillate with large amplitudes. At these energies, the transverse distributions in y shown in Fig. 4.49 is no more Gaussian and the high amplitude particles populate the tails of the distribution. The transverse emittance is computed in *HEADTAIL* as the standard deviation of the positions of the macro particles—this is why the vertical emittance is blowing up so rapidly. In a similar way as in the longitudinal plane, a switch is available in *HEADTAIL* to introduce an aperture constraint in order to lose the particle when they are oscillating at amplitudes above the real vacuum chamber dimension. *HEADTAIL* uses an average aperture.

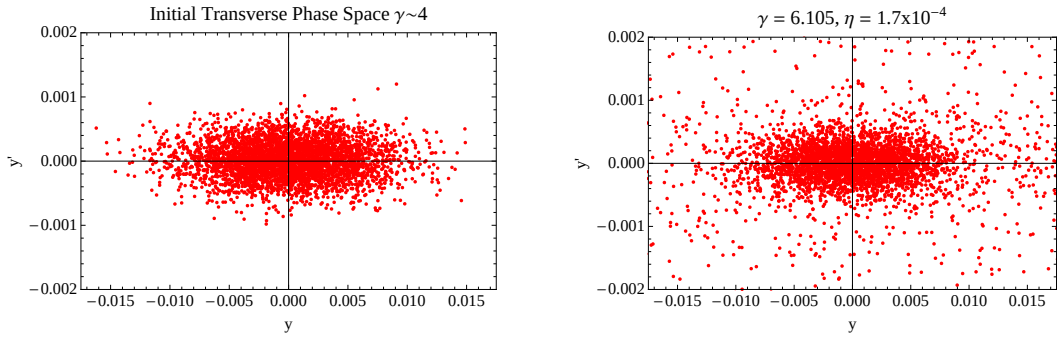

Figure 4.48: Vertical phase space of 4000 macroparticles calculated by *HEADTAIL*: at the beginning of the simulation, the beam is stable, and for an energy close to transition, the phase space occupied by the beam is blowing up ($N = 85 \cdot 10^{10}$ protons, $R_s = 1.5$ MΩ/m)

It is possible to obtain the beam survival from the simulation as illustrated in Fig 4.50, similar to the beam intensity measurements - Fig. 4.15a for example - of the experiments. The resulting vertical emittance is also presented in Fig. 4.51. The fraction of surviving beam in Fig. 4.50 shows that half of the particles from the initial beam intensity are lost on the vacuum chamber, which in the experiment did not happen for a number of particle close the intensity threshold. In our study, the vertical shunt impedance is overestimated by fitting the rise time using only the position of the vertical centroid. If R_s is decreased, no exponential growth of the centroid is observed and it is then not possible to fit a rise time.

As in the experiments, *HEADTAIL* allows to simulate the Δ_y signal of a pickup similar to the wall current monitor installed in the PS. By getting the Δ_y each or every two turns, the same method applied to the measurements to extract the rise time can be also used for the simulated signal. Figure 4.52 compares the rise times calculated from the centroid and from the Δ_y signals. No significant difference in rise time between the two methods is observed for the

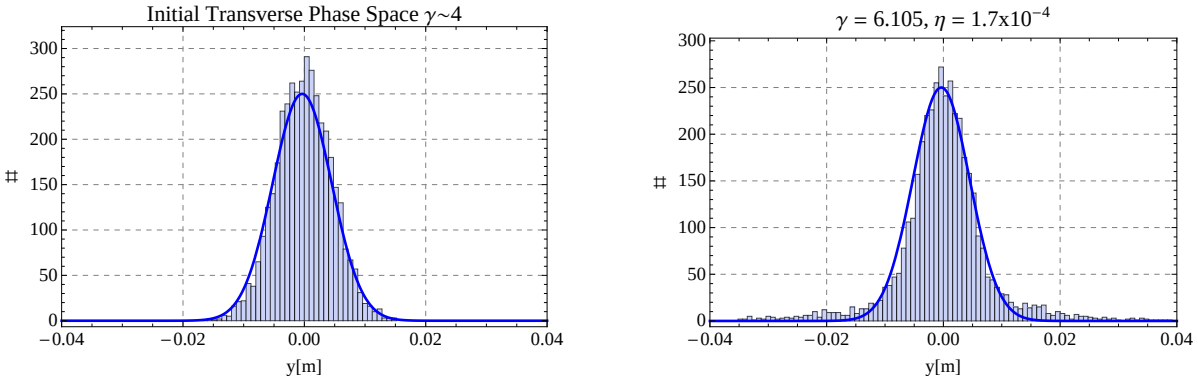

Figure 4.49: Vertical distribution of 4000 macroparticles calculated by *HEADTAIL*: at the beginning of the simulation, the beam is stable, and for an energy close to transition, the tails of the distribution are populated due to the instability ($N = 85 \cdot 10^{10}$ protons, $R_s = 1.5$ MΩ/m)

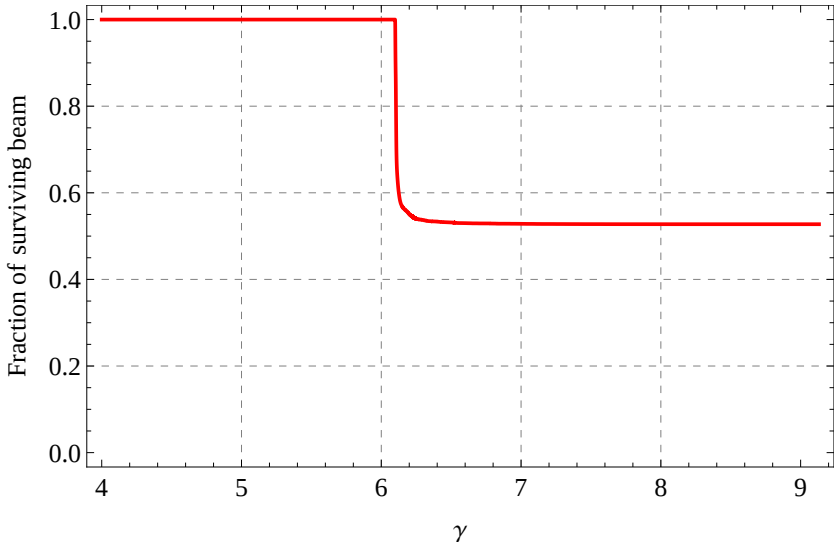

Figure 4.50: Fraction of surviving beam computed by*HEADTAIL* along the acceleration. Half of the beam is lost due to the blow up of the emittance ($N = 8510^{10}$ protons, $R_s = 1.5$ MΩ/m)

highest intensities while the rise times are different closer to the threshold in intensity, with I_{th} about 3 times lower than with the centroid method. In both cases, an offset of 50 turns is observed with respect to the measurements for the rise time for the highest intensities Fig. 4.52. Therefore, by considering only the centroid of the beam, a significant source of uncertainty may be done on the determination of intensity threshold in this study and the impedance overestimated. Close the intensity threshold, the instability does not develop an exponential growth of the motion of the beam centroid. Since the measurements were done by using studying the Δy signal while the instability is developing along the bunch, therefore, the simulated Δy will be used in order to compute rise time.

The matching impedance is deduced from Fig. 4.53 showing the rise time τ of the instability

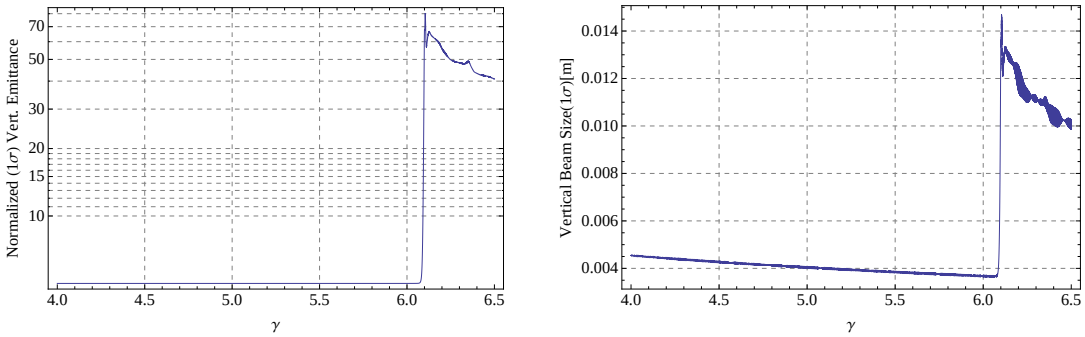

Figure 4.51: On the left, the vertical normalized emittance resulting from the simulation in which an aperture restriction. On the right, the resulting vertical beam size ($N = 8510^{10}$ protons, $R_s = 1.5$ MΩ/m)

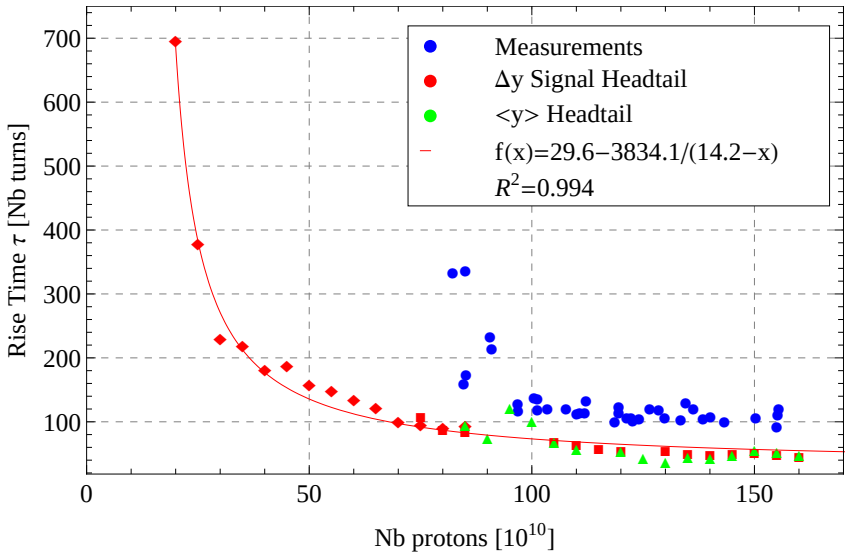

Figure 4.52: Rise time of the instability for $R_s = 1.5$ MΩ/m, $\epsilon_l = 1.9$ eV.s as a function of the intensity in 10^{10} protons, computed from the vertical centroid and from the Δ_y signals given by *HEADTAIL*. For the highest intensity, no difference is observed in term of rise time between the two methods, whereas the threshold I_{th} are strongly different.

computed from the simulated Δ_y signals as a function of the shunt impedance parameter R_s. For a beam intensity of $N = 85 \cdot 10^{10}$ protons, which corresponds to the intensity threshold I_{th} in the measurements for a longitudinal emittance of $\epsilon_l(2\sigma) = 1.9$ eV.s, the needed shunt impedance to reproduce I_{th} is about $R_s = 0.7$ MΩ/m. Below this value, no exponential growth is observed from the Δ_y signals, that is too small to be distinguish from the numerical noise. It should be noted that the found value of R_s is thus less than half of the value found with the method of the centroid.

The number of protons in the beam is then varied keeping the shunt impedance constant

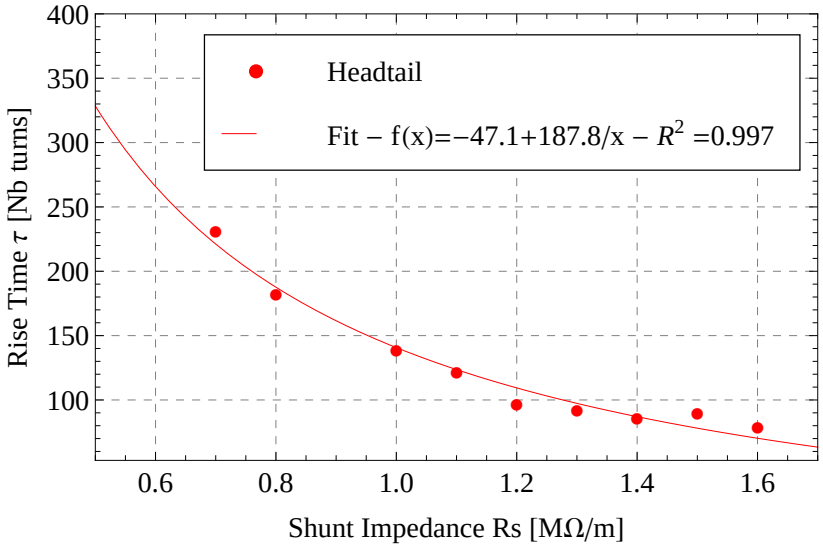

Figure 4.53: Rise time of the instability in number of turn as a function of the shunt impedance R_s for a beam intensity of $N = 85 \cdot 10^{10}$ protons. The instability threshold in intensity is identified for $R_s = 0.7$ MΩ/m

$R_s = 0.7$ MΩ/m. The rise time of the instability is extracted for each beam intensity from the simulated Δ_y signals in a similar way as performed in the measurements and the result is shown in Fig. 4.54 in which they are also compared to the measurements. The order of

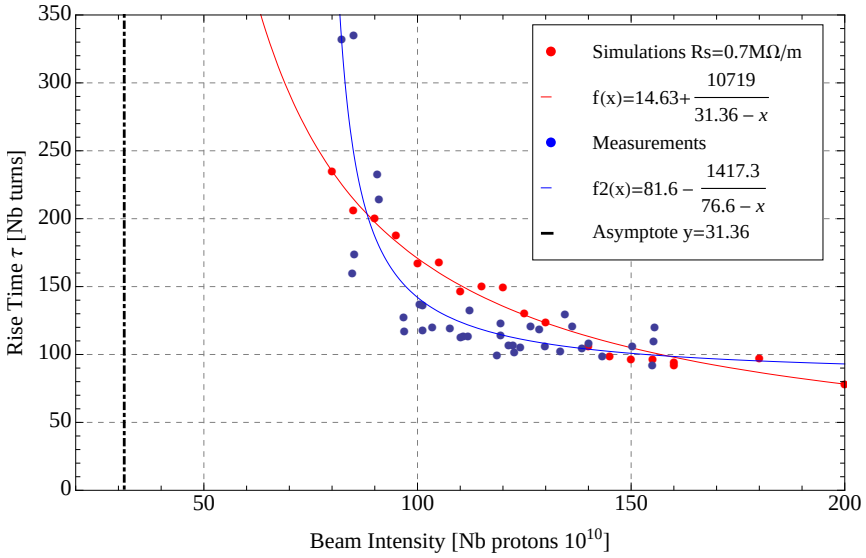

Figure 4.54: (Rise time of the instability in number of turn as a function of the beam intensity for a shunt impedance of $R_s = 0.7$ MΩ/m

magnitude of the simulated rise times τ of the instability is consistent with the measured rise time. The computed τ as a function of the beam intensity are well fitted with a function

$f(x) = a + b/(c - x)$ meaning that τ has an asymptotic behaviour, also presented in Fig. 4.55. The lower the number of protons in the beam, the larger the rise time, and it goes to infinity for intensities tending to an asymptotic value, in this case of Fig. 4.54, $N_b = 31.16 \cdot 10^{10}$ protons. This asymptotic function has been obtained by performing a scan over a large range of beam intensities in order to get more points to perform the fit shown in Fig. 4.55. In a similar way as in the measurements, the simulated rise time is inversely proportional to the beam intensity and the asymptotic value in Fig. 4.55 shows that the instability has a threshold in intensity, which is behaviour comparable to the measurements.

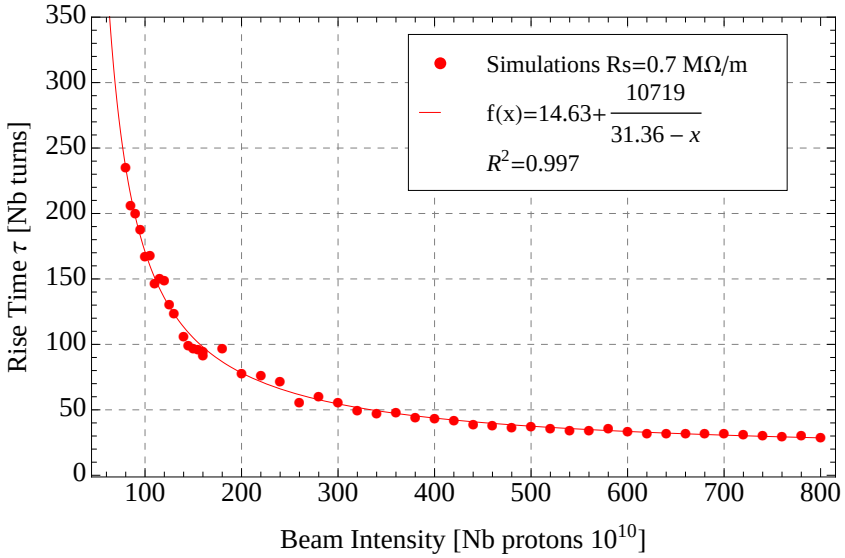

Figure 4.55: (Rise time of the instability in number of turn as a function of a large beam intensity range for $R_s = 0.7$ MΩ/m

A difference in behaviour is observed between the simulated rise times and the measured rise times:

- For intensities above $100 \cdot 10^{10}$ protons, both the simulated and measured rise time evolve in a linear regime and even a saturation regime in which the rise time does not vary so much with the intensity. However, the measured rise times evolve more rapidly in this regime than the simulated.
- The rise time reaches more quickly the asymptotic regime in the measurements while the beam intensity approaches to the threshold.

It is interesting to study the ratio I_{linear}/I_{th} where I_{th} is the intensity threshold and I_{linear} the intensity at which the linear regime of the rise time as a function of the intensity starts.

- In the measurements, $I_{th} = 80 \cdot 10^{10}$ protons and $I_{linear} = 120 \cdot 10^{10}$ protons therefore $I_{linear}/I_{th} = 1.5$.

- In *HEADTAIL*, $I_{th} = 75{\cdot}10^{10}$ protons and $I_{linear} = 400{\cdot}10^{10}$ protons therefore $I_{linear}/I_{th} = 5$.

The rise time in the measurements reaches 3 times more rapidly the threshold in intensity than in the simulations. This difference may be explained by the use of a simple broadband impedance model in the simulations. It is very likely that real the PS impedance is more complex. However, presently a detailed impedance model does not exist. This is an important future work.

Other cases with $R_s = 0.9, 1$ MΩ/m were computed to show that they have the same hyperbola behaviour for the rise as a function of the beam intensity. Furthermore, checks were done to see if the ratio I_{linear}/I_{th} can be changed by modifying the shunt impedance. Fig. 4.53 presents scan in intensity for $R_s = 0.7, 0.9, 1, 1.5$ MΩ/m. The higher is R_s, the lower is the intensity threshold and lower is I_{linear} and finally the ratio I_{linear}/I_{th} remains the same.

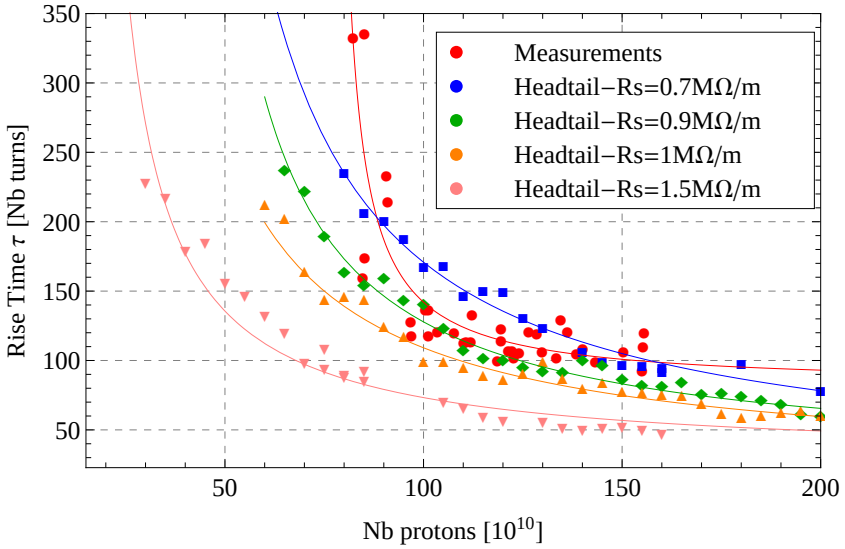

Figure 4.56: (Rise time of the instability in number of turn as a function of the shunt impedance R_s for a beam intensity of $N_b = 85\dot{1}0^{10}$ protons. The instability threshold in intensity is identified for $R_s = 0.7$ MΩ/m

The accuracy of the rise time in the measurements as well as in the simulations depends on the number of points fitted during the exponential growth of the particle motion. We estimated that a particle oscillation below an amplitude of 0.04 mm might not be detected by the wall current monitor. Let consider an unstable beam with particles oscillating with amplitudes comparable to 0.04 mm. With the WCM used in the experiments, the oscillations in the first part of the exponential growth might not be possible to detect. Therefore the rise time computation is affected, since the fit is performed with less points. For higher intensities, the error achieved on the rise time is smaller due the strength of the instability. Therefore the rise times measured close to the supposed I_{th} may belong to the non-linear regime, explaining

the difference in behaviour of the the rise time with the number of protons in the beam.

Macro particle simulations with *HEADTAIL* have been used to model the fast vertical instability around transition energy. As opposed to the SPS or LHC Ref. [36][82], no detailed impedance model exists for the PS, thus a simple broadband model was used in *HEADTAIL*. This is nevertheless sufficient to reproduce the bunch oscillations observed in the measurements on the Δ_y signal. The threshold in intensity was reproduced and the rise time as a function of the intensity computed from simulation are of the same order of magnitude as those observed in the measurements. It was previously discussed that the simulations shows that the instability has a threshold in beam intensity, which is non-zero, due to the hyperbola behaviour of τ with the number of proton in the bunch.

In the Beam Breakup formalism used in Linac, in presence of a broadband wake field, the head of the beam excites the particles behind and the tail is then always unstable. In our study, this is not the case: the instability in both simulation and experiments shows a threshold in intensity. This behaviour is comparable to the theory of instabilities faster than the synchrotron period for coasting beam. In the case of a synchrotron, the particles are exchanged between the head and the tail due to synchrotron motion, which stabilizes the beam breakup instability. At transition energy, the synchrotron motion is slowing down while the beam is getting closer to the nonadiabatic zone. The instability appears when the exchange of the particles between the head and the tail is not fast enough to stabilize the beam and this might depend also on the beam intensity and therefore the force of the wake.

Up to now, only a bunch length corresponding to a longitudinal emittance of 1.9 eVs was considered. However, the instability was measured for different ϵ_l and therefore for different bunch lengths. In the next paragraph, the influence of the bunch length on the intensity threshold will be studied.

4.5.2 Impedance Matching with Bunch Length

In the previous paragraph, a shunt impedance has been deduced from the threshold in intensity measured for the case of a longitudinal emittance of $\epsilon_l = 1.9$ eVs. Then, the beam intensity was varied to reproduce the measured rise time of the instability as a function of the number of protons in the bunched beam. The same analysis is done for the other sets of measured longitudinal emittance studied in Sec. 4.3.1, i.e. $\epsilon_l(2\sigma) = 1.3, 1.5, 2.15, 2.3$ eVs. As in the case $\epsilon_l = 1.9$ eVs, the longitudinal parameters in term of bunch length and momentum spread are computed at the energy $\gamma = 4$ for a stationary bucket and presented in Table 4.6. Except the rms bunch length and momentum spread, the beam parameters in terms of chromaticity, tune and RF voltage remain the same as Table 4.2. They are then used in *HEADTAIL* as starting conditions for the bucket at the beginning of the simulation. The bunch length evolution with the beam energy along the simulation is presented in Fig. 4.57 for the different longitudinal beam emittances. The matched shunt impedance for each longitudinal emittance has been determined by comparing the corresponding simulated rise times to those obtained in the measurements while the beam intensity is at the threshold.

Longitudinal emittance ($2\,\sigma$)	1.3 eVs	1.5 eVs	2.15 eVs	2.3 eVs
Bunch length rms [m] σ_z	4.602	4.906	5.873	6.075
Momentum spread rms $\delta p/p$	0.0019	0.0021	0.0024	0.0026
Synchrotron tune Q_s	0.0015	0.0015	0.0015	0.0015

Table 4.6: Longitudinal beam parameters for the bucket at the energy $\gamma = 4$ in *HEADTAIL* simulation.

Following the same method as in the previous paragraph, the shunt impedance is varied while the intensity is kept constant at the thresholds. The scan was done for the different measured thresholds shown in Fig. 4.24. The results in shunt impedance scan for each measured longitudinal emittance are presented in Fig. 4.58a and Fig. 4.58b for respectively $\epsilon_l = 1.3$ eVs and $\epsilon_l = 1.5$ eVs, and in Fig. 4.59a and Fig. 4.59b for $\epsilon_l = 2.15$ eVs and $\epsilon_l = 2.3$ eVs.

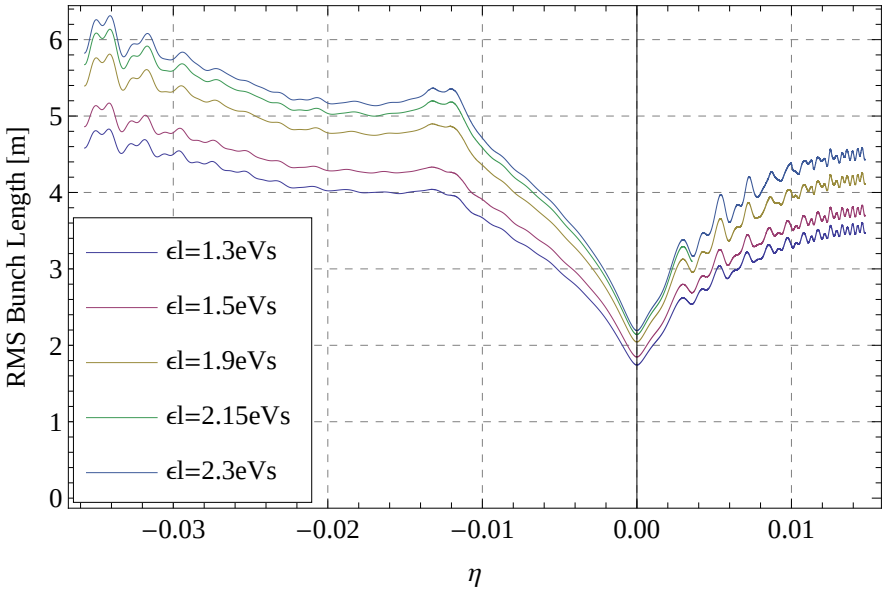

(a)

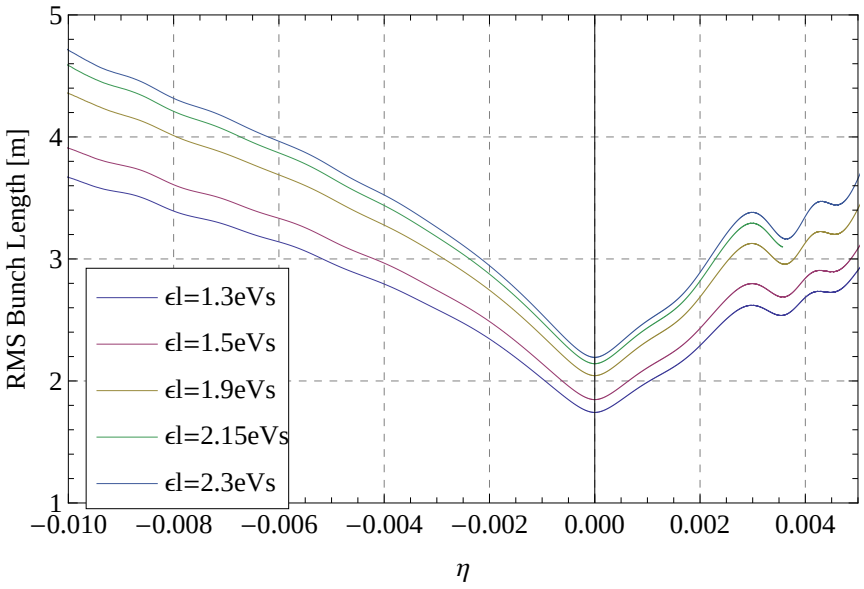

(b)

Figure 4.57: Bunch length evolution as a function of η for the different longitudinal emittances measured in the experiment.

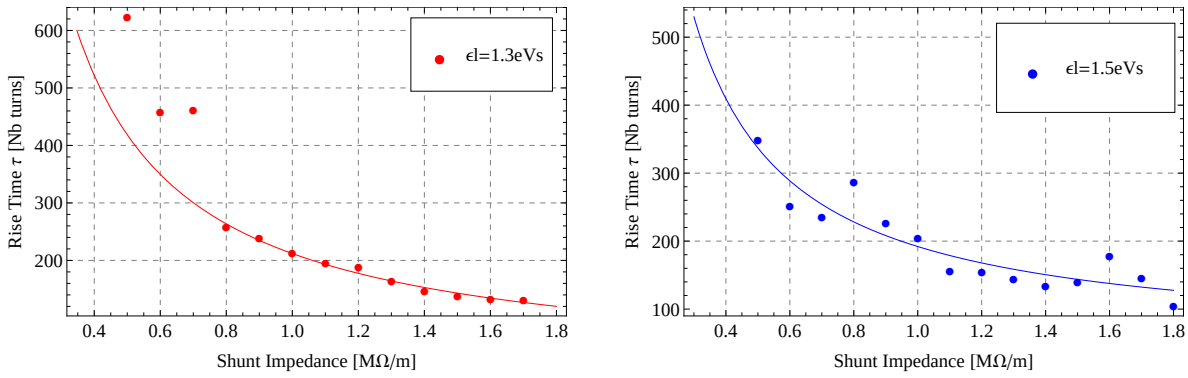

(a) (b)

Figure 4.58: Results of the impedance scan R_s for $\epsilon_l = 1.3$ eVs in Fig. (a) for a threshold in intensity of $45 \cdot 10^{10}$ and Fig. (b) for $\epsilon_l = 1.5$ eVs for threshold in intensity of $58 \cdot 10^{10}$

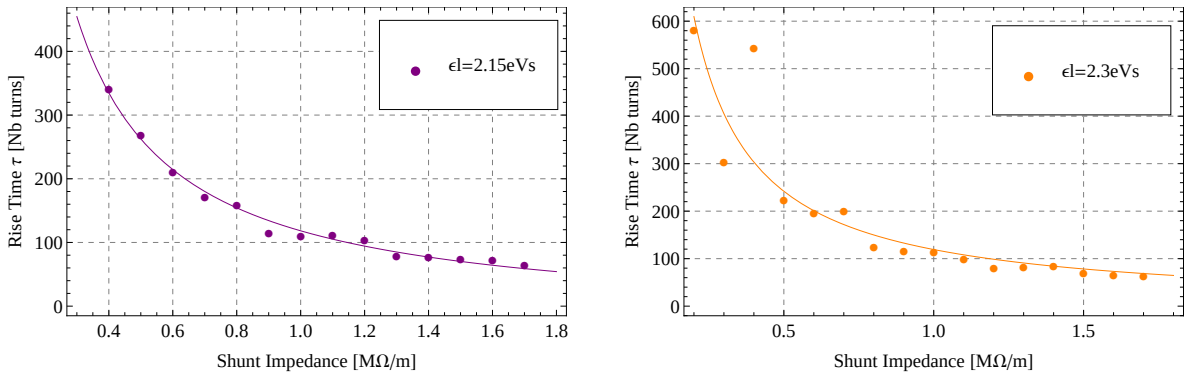

(a) (b)

Figure 4.59: Results of the impedance scan R_s for $\epsilon_l = 2.15$ eVs in Fig. (a) for a threshold in intensity of $104 \cdot 10^{10}$ and Fig. (b) for $\epsilon_l = 2.3$ eVs for threshold in intensity of $117 \cdot 10^{10}$

In each case, the rise time as a function of the shunt impedance R_s is fitted by hyperbola function where the fits are summarized with the quality of the fit for all the measured longitudinal emittances in Table 4.7. They are also summarized in Fig. 4.60 and the impedance thresholds needed to reproduce the intensity thresholds observed in the measurements are shown in Fig. 4.61 as a function of the longitudinal emittance.

Longitudinal emittance ($2\,\sigma$)	Hyperbola fit function R_s in MΩ/m	R^2
1.3 eVs	$f(R_s) = (5.423 \pm 8.278) + \frac{(206.474 \pm 9.495)}{R_s}$	0.999
1.5 eVs	$f(R_s) = (47.154 \pm 19.312) + \frac{(144.854 \pm 17.67)}{R_s}$	0.984
1.9 eVs	$f(R_s) = (-47.09 \pm 1.38) + \frac{(187.76 \pm 10.77)}{R_s}$	0.997
2.15 eVs	$f(R_s) = (-25.85 \pm 5.55) + \frac{(144.135 \pm 34.51)}{R_s}$	0.997
2.3 eVs	$f(R_s) = (-3.42 \pm 30.59) + \frac{(122.608 \pm 15.95)}{R_s}$	0.923

Table 4.7: For each longitudinal emittance, a hyperbolic function is applied to the simulated rise time as a function of the impedance given to *HEADTAIL*. The results of these fits are given in this table as well as its goodness.

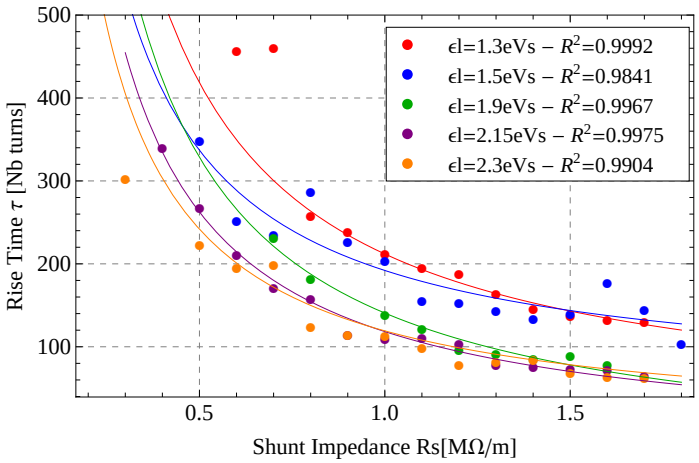

Figure 4.60: Rise time computed by *HEADTAIL* as a function of the shunt impedance for the different measured longitudinal at the intensity threshold identified in Fig. 4.24.

At this point, the notion of effective impedance has to be introduced. Fig. 4.61 shows that the matched shunt impedance that reproduces the threshold in intensity of the instability is not constant and is strongly dependent of the longitudinal emittance, i.e. of the bunch length.

In the previous paragraph, it has been demonstrated that the order of magnitude of the measured rise time for $\epsilon_l = 1.9$ eV.s can be reproduced with *HEADTAIL* for an impedance of

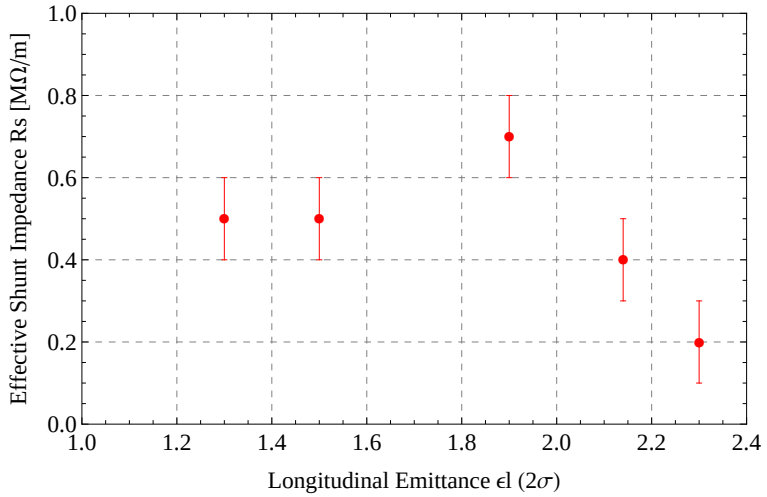

Figure 4.61: Effective impedance for each measured longitudinal emittance deduced from Fig. 4.60.

$R_s = 0.7$ MΩ/m. Thresholds in R_s were found for each longitudinal emittance in Fig. 4.61 and it appears that they are not constant with ϵ_l. Scans in intensity were performed for $\epsilon_l = 1.5, 2.3$eVs to benchmark the measured rise times with *HEADTAIL* simulations for other bunch lengths. Fig. 4.62a and Fig. 4.59b present the results for respectively $\epsilon_l = 1.5$ and $\epsilon_l = 2.3$eV.s for two shunt impedances, their respective R_s threshold and $R_s = 0.7$ MΩ/m. Their rise times are compared to the measurements. The order of the magnitude is reproduced for $R_s = 0.7$ MΩ/m whereas a difference of a factor 2 is found in Fig. 4.62a, with $R = 0.5$ MΩ/m and $\epsilon_l = 1.5$ eV.s. It goes to a factor 4 with the set $\epsilon_l = 2.3$ eV.s in Fig. 4.63 if $R_s = 0.2$ MΩ/m. The error then on the estimation of the threshold in intensity is about 30%, i.e. $I_{th} \simeq 40 \times 10^{10}$ protons instead of 63×10^{10} for $\epsilon_l = 1.5$ eVs (See measured intensity threshold in Fig 4.24), $I_{th} \simeq 90 \times 10^{10}$ protons instead of 100×10^{10} for $\epsilon_l = 2.3$ eVs. In the case of non-zero chromaticity, $R_s = 0.7$ MΩ/m is a good approximation to estimate the order of magnitude of the rise time of the fast transverse instability, regardless the longitudinal emittance.

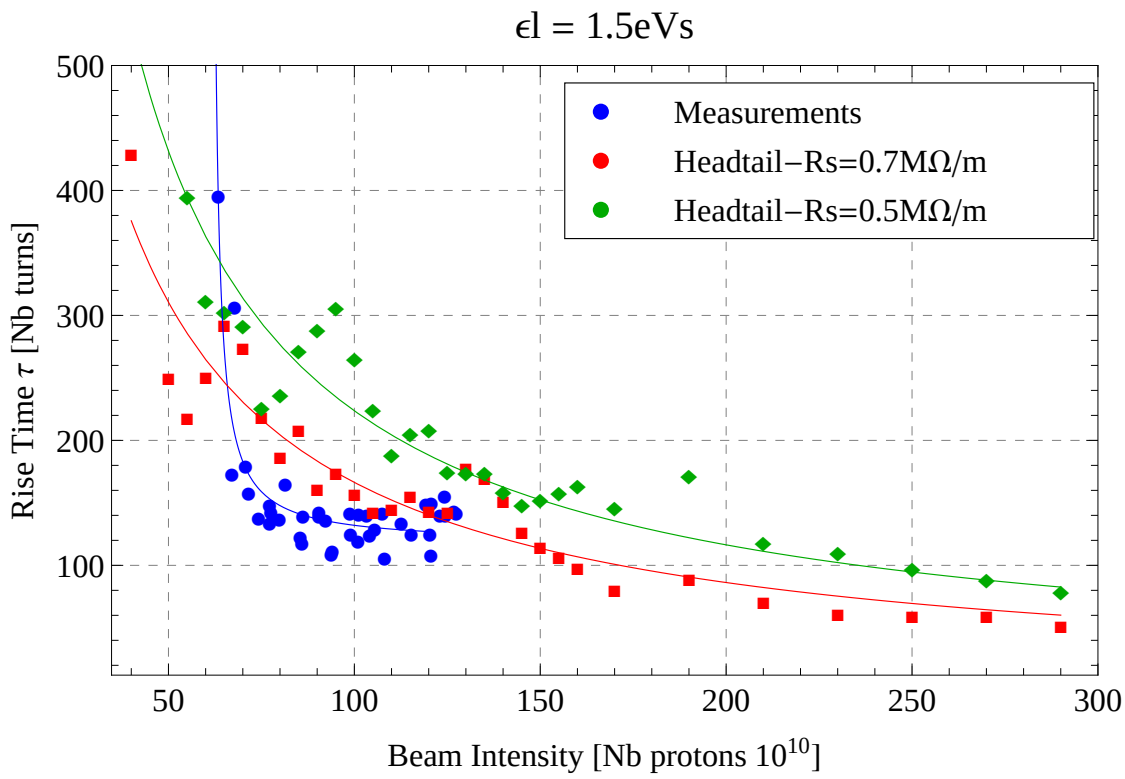

(a)

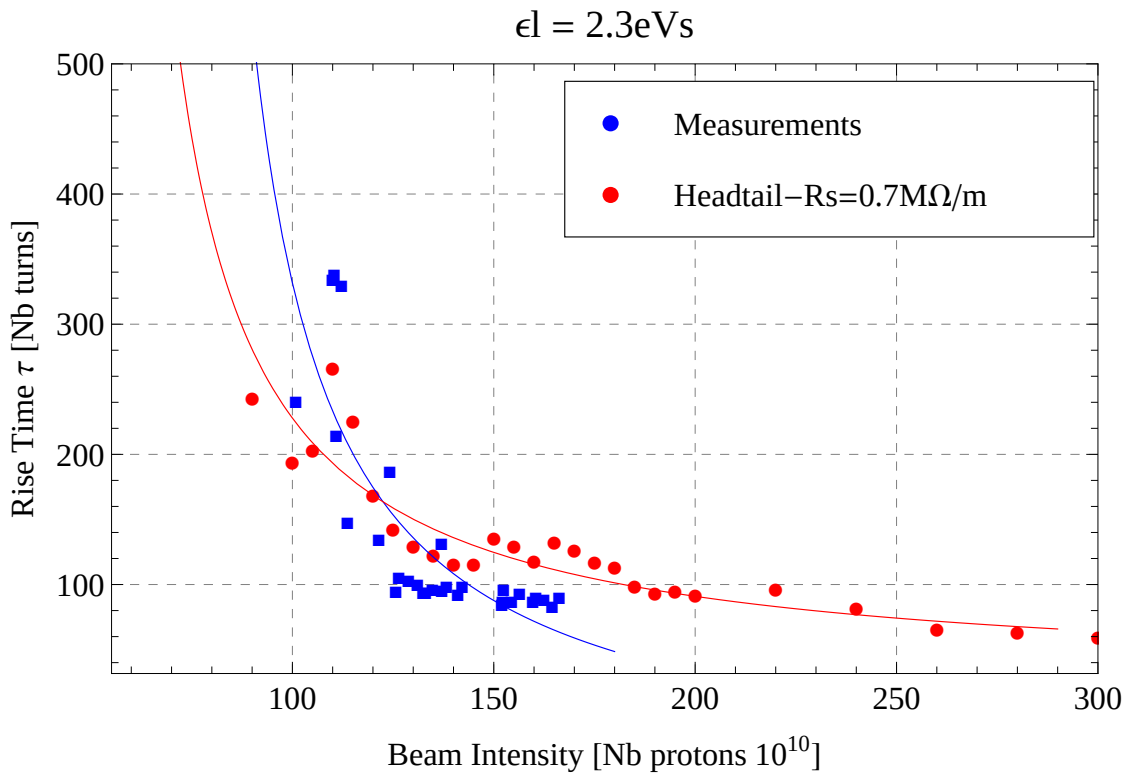

(b)

Figure 4.62: Instability rise times computed by *HEADTAIL* for ϵ_l = 1.5 eVs in Fig. (a) and in Fig. (b) for ϵ_l = 2.3eVs.

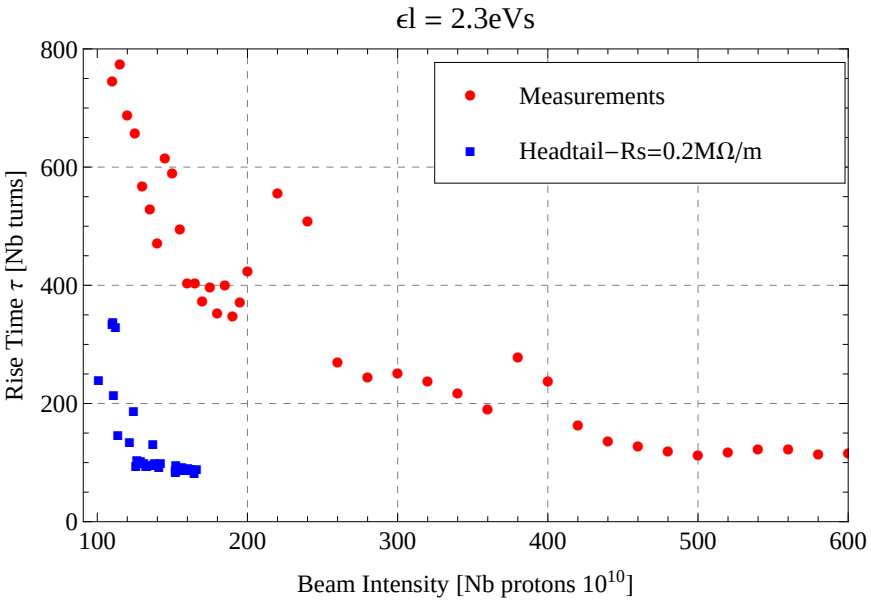

Figure 4.63: Instability rise times computed by *HEADTAIL* for $\epsilon_l = 2.3$ eVs for an impedance of $R_s = 0.2$ MΩ/m. The results are compared to the measurements and an error of a factor 4 is found with respect to the experimental data.

The vertical impedance has been matched for different longitudinal emittances for a beam without chromaticity. The order of magnitude of the measured rise times can be found with *HEADTAIL* simulations considering a vertical shunt impedance of 0.7 MΩ/m, with an estimated error of about 30%, as illustrated in Fig. 4.64 which compares the simulated intensity threshold as a function of the longitudinale emittance to the measured intensity threshold. Considering the very simple impedance model unsed in *HEADTAIL*, this agreement is good.

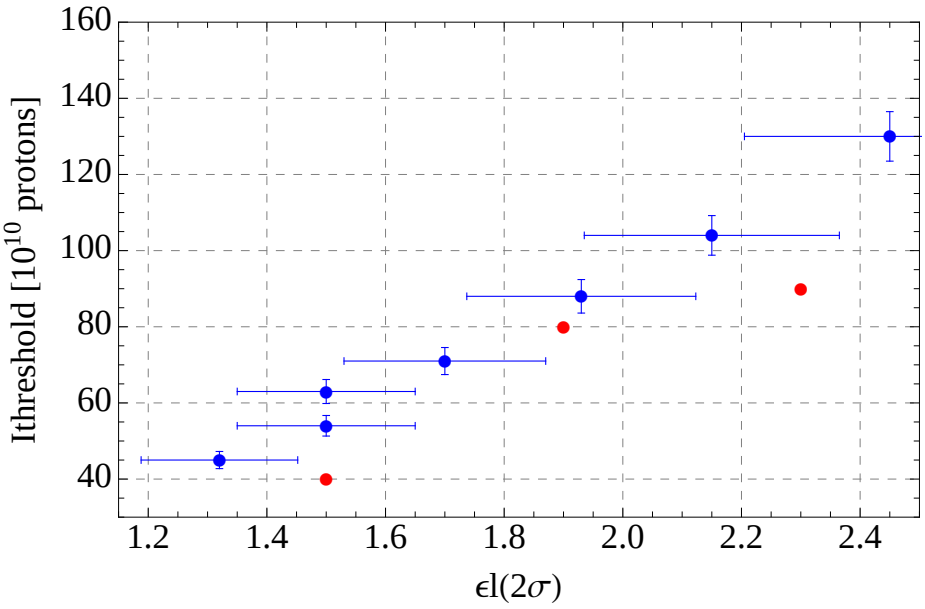

Figure 4.64: Instability rise times computed by *HEADTAIL* for different longitudinal emittances compared to the measured I_{th}: in red are the simulated intensity thresholds with *HEADTAIL* and in blue are the measured I_{th}.

4.6 Fast Transverse Instability with Chromaticity

Up to this point, only a beam without chromaticity was considered in the simulations. However, chromaticity introduces incoherent motion, which can increase the threshold in intensity of transverse instabilities. Sec. 4.3.1 describes also the fast transverse instability with a small negative chromaticity as presented in Fig. 4.10. Measurements show also that the thresholds in intensity and in η are higher with a small chromaticity, even negative, as shown in Fig. 4.24 for I_{th} and in Fig.4.28 for η_{th}. In this paragraph, a vertical chromaticity is introduced in the code *HEADTAIL*. The code was modified in order to implement a vertical chromaticity varying with time as in the measurement in Fig. 4.10, where ξ_y is slightly negative while the beam is crossing transition energy. When this energy is crossed, the sign of the chromaticities has to be changed, otherwise the headtail mode $m = 0$ can get unstable as shown in Fig. 4.65. These examples of unstable $m = 0$ headtail instability were taken in PSB [10] in the 70's.

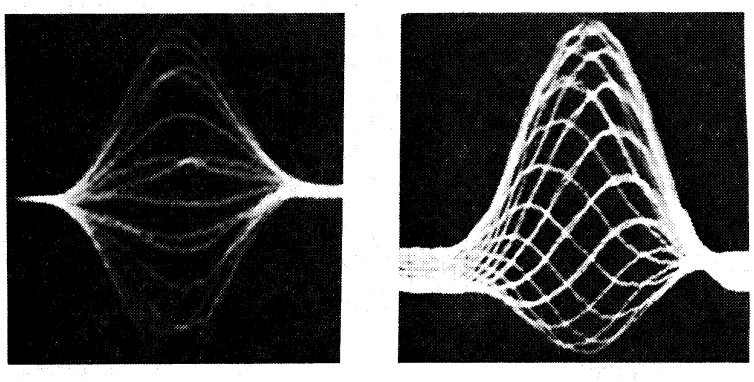

Figure 4.65: Example of headtail instability with $m = 0$ unstable. These data were taken in the PSB in Ref. [10].

The analysis performed in the previous paragraph is applied again in the case with a vertical non-zero chromaticity. The shunt impedance R_s is varied in order to match the measured the rise time. Fig. 4.66 presents the vertical chromaticity as implemented in *HEADTAIL* as a function of η and compared to the measured chromaticity.

In Fig. 4.67, the simulated Δ_y signal for a zero and a slightly negative chromaticity are compared for a beam intensity of 100×10^{10} protons, $\eta = 2 \times 10^{-4}$ and $R_s = 0.7$ MΩ/m. Like in the measurements, the oscillation along the bunch is damped by the spread in tune introduced by the chromaticity.

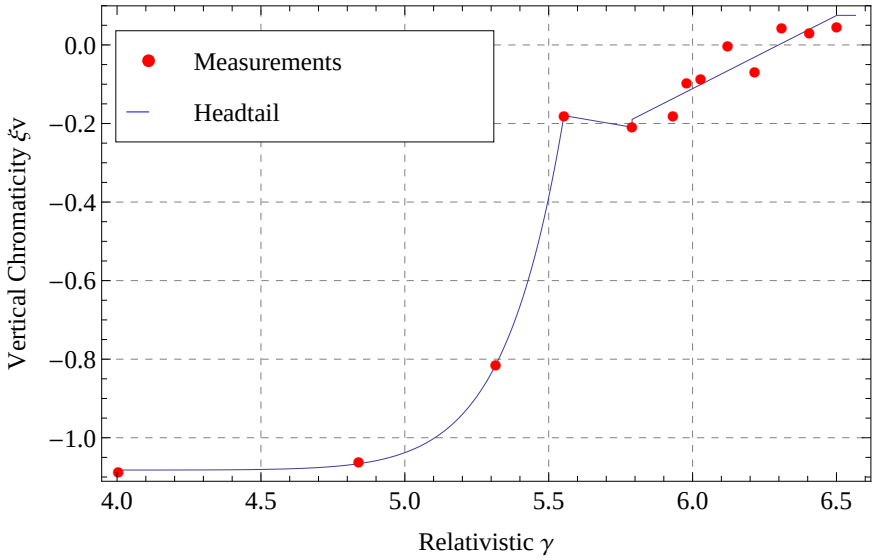

Figure 4.66: Vertical chromaticity ξ_y simulated by *HEADTAIL* compared to the measurements.

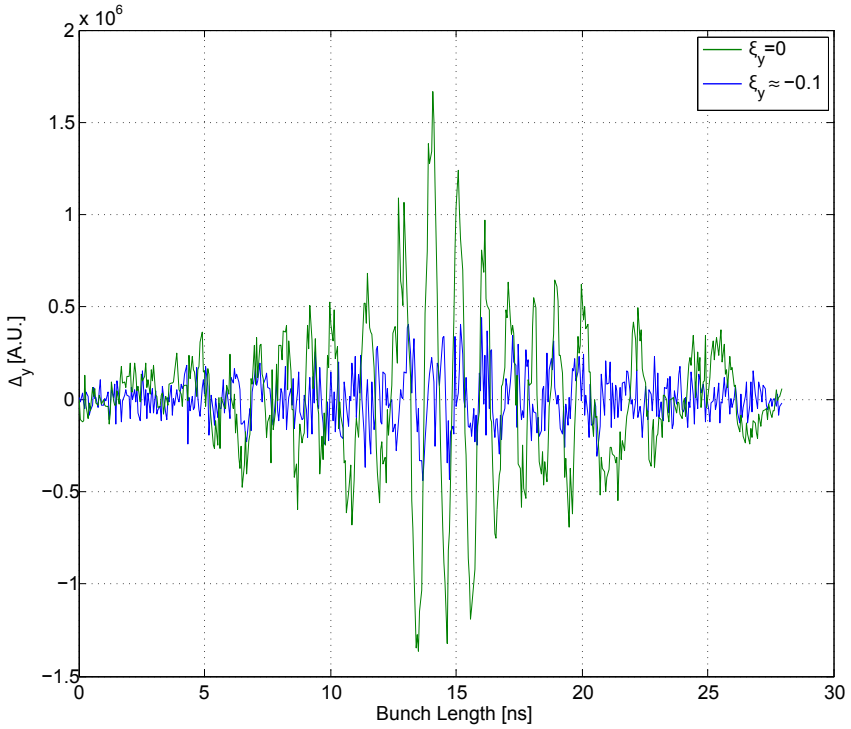

Figure 4.67: Comparison of Δ_y signals computed by *HEADTAIL* with and without vertical chromaticity ξ_y for a beam intensity of 100×10^{10} protons and at $\eta \simeq 0.002$.

A scan in shunt impedance R_s has been performed with the set of chromaticities presented in Fig. 4.66. The rise time of the instability is computed for each vertical impedance in Fig. 4.68a. The best values in R_s that matched the order of magnitude of the measured rise time are $R_s = 0.5$ and 0.7 MΩ/m. The value of the impedance is chosen to give the same order of magnitude as in the measurements. Fig. 4.68b shows that, with this set of chromaticities, the intensity threshold is $I_{th} \simeq 80 \times 10^{10}$ protons whereas in the measurements, the threshold is identified at $I_{th} \simeq 100 \times 10^{10}$. A disagreement of 20% is then visible. Fig. 4.69 compares the rise time as a function of the intensity for a beam with and without chromaticity and no significant difference is observed, whereas the measurements show a clear difference of about 20% in intensity and in η threshold. To fit I_{th} of about 100×10^{10} observed in the experiments with ξ_y -0.1, the impedance has to be $R_s \simeq 0.5$ M Ω/m, however the rise times for higher intensities are underestimated. As a conclusion, the real part of the broadband impedance is fitted at the value $Z_y^{\perp} = [0.5, 0.7]$ MΩ/m.

In the simulations with and without chromaticity, the rise times agree well with the measurements and an error of 20%-30% is made on the estimation of the intensity threshold. This could mean that some damping could be present in the real machine which are are not in the code.

In particular, no octupolar component of the field and higher component of the non-linear chromaticity was taken into account in the simulations. If this component is large, it can contributes to increase the threshold in intensity. However, as explained in Sec. 4.1.2, the error on the chromaticity measurements close to transition is rather high, therefore the non-linear chromaticity is hard to estimated. Even small, it might have an effect since the dp/p close to γ_{tr} energy is maximum.

Other incoherent effects can change the threshold, such as transverse space charge and the impedance model used in the simulations. In particular, only a simple broadband impedance model was used in the code, which is a purely dipolar. However, a detuning part of the impedance as explained Sec. 1.4.1 has to be considered as well since the PS contains many asymmetric structures and ferrite kickers [64]. In this case, considering a force applied on a trailing particle due a source particle, the wake force depends also on the position of the trailing particles. This introduces a incoherent effect of the force applied on each particle and might be a source of damping close to the intensity threshold. However, this effect cannot be estimated because the quadrupolar part of the impedance is unknown.

Up to this point, only the rise time and the intensity threshold were considered. However, the distance from the transition energy of the onset of the instability, i.e. η, is also a fundamental parameter. It allows to define at which energy the beam enters in the nonadiabatic region.

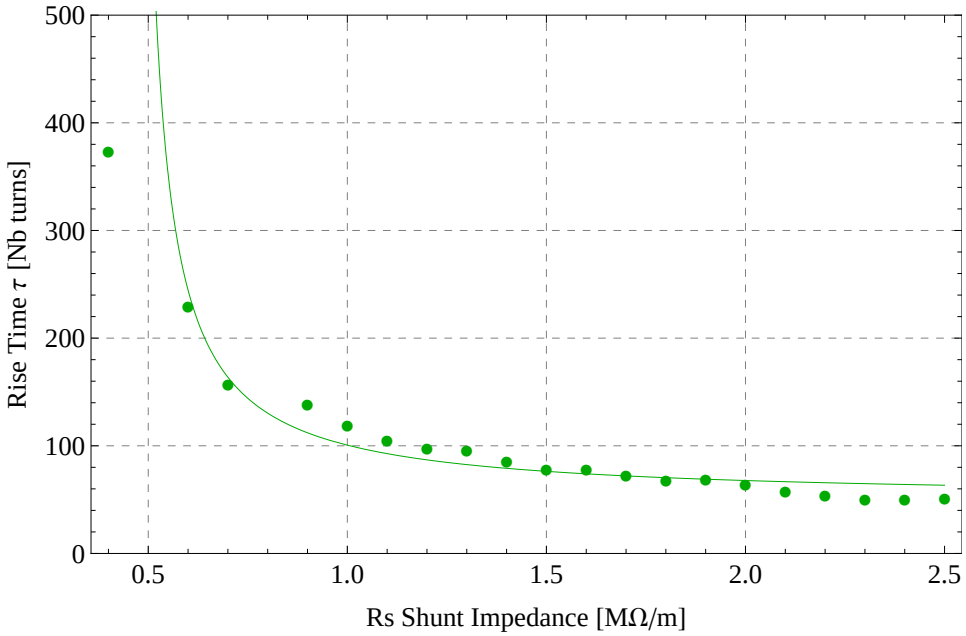

(a)

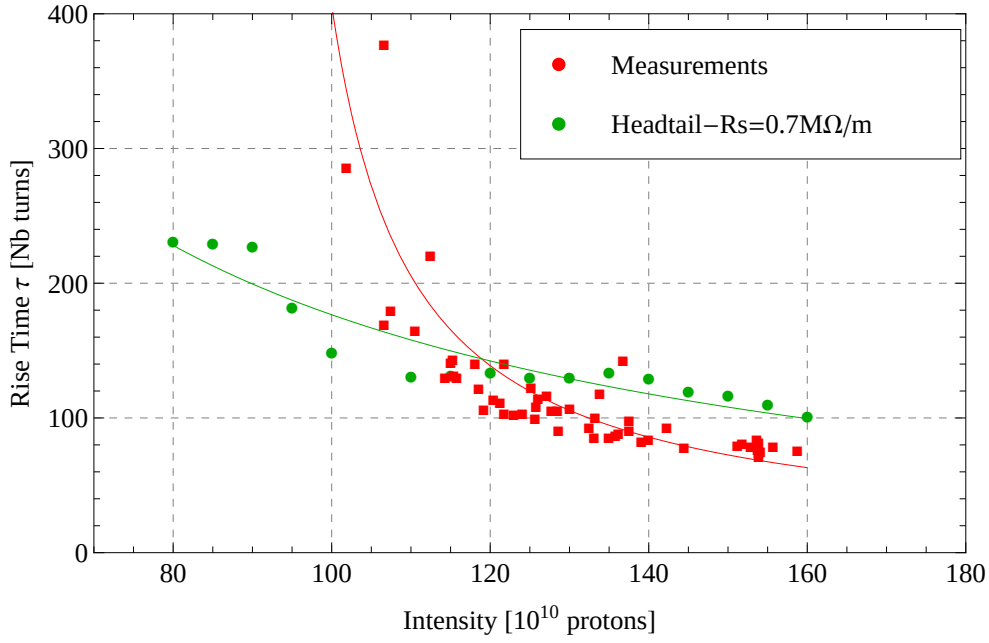

(b)

Figure 4.68: Fig. (a) Rise time of the fast transverse instability as a function of the shunt impedance in *HEADTAIL* with vertical chromaticity ξ_y as in the measurements for a beam intensity of 100×10^{10} protons. Fig. (b) presents the intensity variation for a vertical impedance of 0.7 M Ω/m.

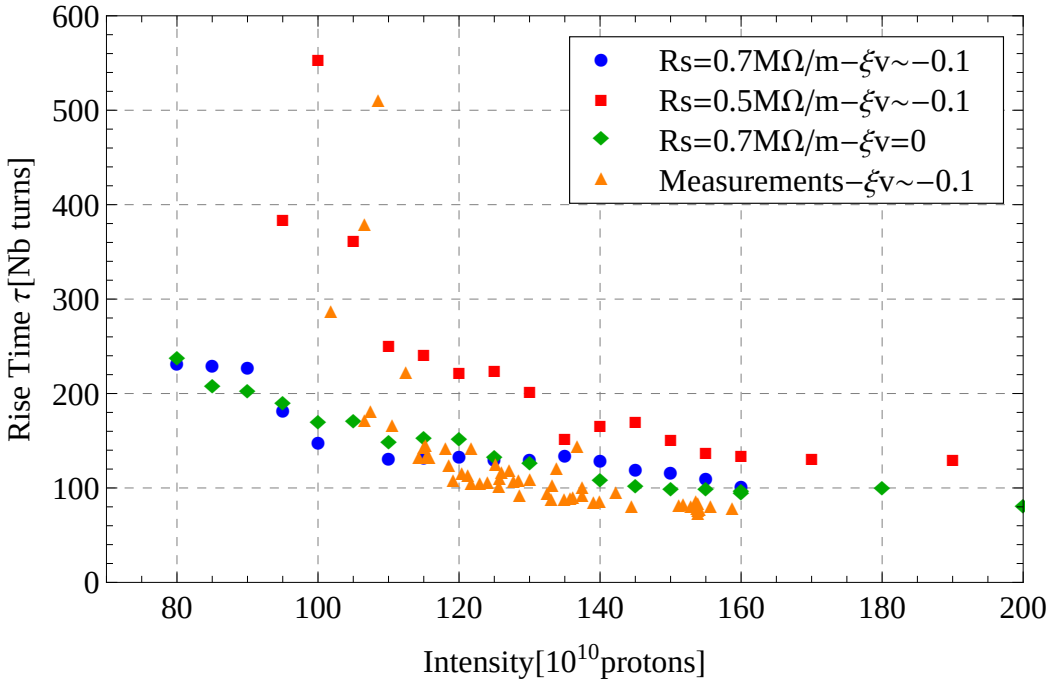

Figure 4.69: Comparison of the rise time with and without chromaticity for $\epsilon_l = 1.9$ eVs for $Rs = 0.5 - 0.7$ MΩ/m.

4.7 Threshold in η and bucket adiabaticity

The measurements presented in Sec. 4.3.2 show that a threshold in momentum compaction factor η could be determined. Up to now, we have seen that the instability occurs during a few hundred turns around transition energy, when the synchrotron motion is very slow. This is why the reference [10] assumed that the fast vertical instability observed in the PS since 2000 can be treated with the Beam Breakup theory. This formalism considers a beam without any longitudinal motion. Now one can understand why it is important to estimate at which distance from transition energy the instability occurs. Concerning the TMC formalism, the simplified condition to get the motion unstable is [10]

$$\Gamma = \frac{\pi N e 2 W_1}{4 m_0 \gamma \beta \omega_s} \geq 2 \tag{4.13}$$

which depends on the synchrotron angular frequency. Transition energy is at the limit of the TMC theory since $\omega_s \rightarrow 0$. It means that not only the beam intensity is a factor which can trigger the fast transverse instability, but there might be a threshold η_{th} also in the momentum compaction factor. The measurements show that for all longitudinal emittances, η_{th} is a constant for a given intensity. In this section, η_{th} will be determined with *HEADTAIL* simulations and compared with the measured $\eta_{th} \simeq 0.0004$ without chromaticity and $\eta_{th} \simeq 0.001$ with chromaticity.

Using the same method as in the experiments, a scan in beam intensity is performed for a beam with and without chromaticity. The implemented ξ_y in *HEADTAIL* is the chromaticity presented in Fig. 4.66. The threshold η_{th} is determined with the same method as the rise time. *HEADTAIL* provides the Δ_y signal turn by turn. By applying a FFT at each signal, every turns, the frequency bandwidth around 700 MHz is selected. The power of the frequency is then shown in Fig. 4.17 as a function of the number of turns. A linear fit is applied to determine the growth rate of the instability. η_{th} is deduced as the value of η where the linear fit meets the noise of the signal. The noise is estimated by taking an average of the power frequency on a window preceding the instability.

Fig. 4.70 presents the η_{th} as a function of the beam intensity for $\epsilon = 1.5, 1.9, 2.3$ eVs. The x-axis is the intensity normalized to the measured intensity threshold for the considered longitudinal emittance. Fig. 4.70 shows that η_{th} is rather linear with the beam intensity and when the intensity is normalized by I_{th}, the curves look rather similar. η_{th} does not depend on the bunch length or longitudinal emittance, but only on the intensity. This is exactly the behaviour observed in the measurements in Fig. 4.28a.

Then the simulated η_{th} are compared to the measurements in Fig. 4.71. The measured data show $\eta_{th} \simeq 0.0004$ for beam intensities close I_{th}, whereas the simulations shows that $\eta_{th} \simeq 0$ - the fast instability starts always before or at transition energy for a beam without chromaticity. A very likely explanation of this difference comes from the setting up of the transition energy timing in the experiments. As already explained in Sec 4.1.1, the stable phase shift performed

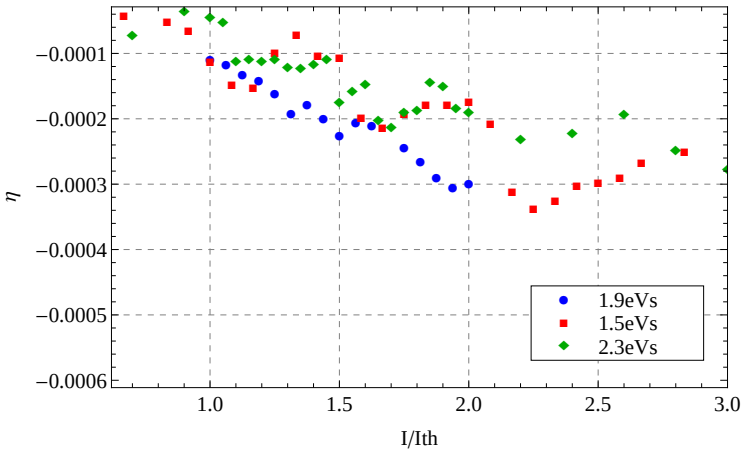

Figure 4.70: Simulated η_{th} as a function of the beam intensity normalized to the intensity threshold I_{th} obtained by measurements for different longitudinal emittance.

at transition energy is set by a timing which was tuned with 1 ms steps, so an error of 1 ms is realistic. The error bars on the measured data of Fig. 4.71 and in Fig. 4.72 include this timing error. These error bars represents an uncertainty in timing of 1 ms, which is a systematic error. As a consequence, the fact to observe systematically the instability after the supposed transition energy can be explained by an error of 250 turns on the estimation of the timing of the stable phase ϕ_s shift. The minimum η_{th} would not be 0.0004 but 0 and this would be consistent with the simulations. A linear fit is applied on the experimental data in Fig 4.71 and on the simulated η_{th}:

$$\begin{aligned}\eta_{th}(I/I_{th}) &= -0.00014 \pm 7\times10^{-6} + 0.00005 \pm 0.00002 \quad \text{simulations}\\ \eta_{th}(I/I_{th}) &= -0.001 \pm 0.00004 + 0.0013 \pm 0.00006 \quad \text{measurements}\end{aligned} \tag{4.14}$$

It can be seen that a factor 7 differs between the measured and the simulated slopes. In the real machine, while the beam intensity is increasing, η_{th} evolves 7 times faster than in the simulations.

When I increases by a factor 2, the measured η_{th} is multiplied by a factor 10 whereas it is multiplied by a factor 2 in the simulation. A large disagreement is observed for the measured and the simulated η_{th} as a function of the beam intensity and the first explanation is that the impedance model between the real machine and the broadband model are different. This is one of the limits of the use of a simple broadband impedance model in *HEADTAIL*.

Then a vertical chromaticity is added in the simulations in order to study the impact of a tune spread on η_{th}. The result is presented in Fig 4.72. An offset of 0.0002 towards positive values of η is observed. Even if no significant difference in intensity threshold and in rise time was observed with $\xi_y < 0$ in Fig. 4.69 in the simulations, a significant increase of the threshold

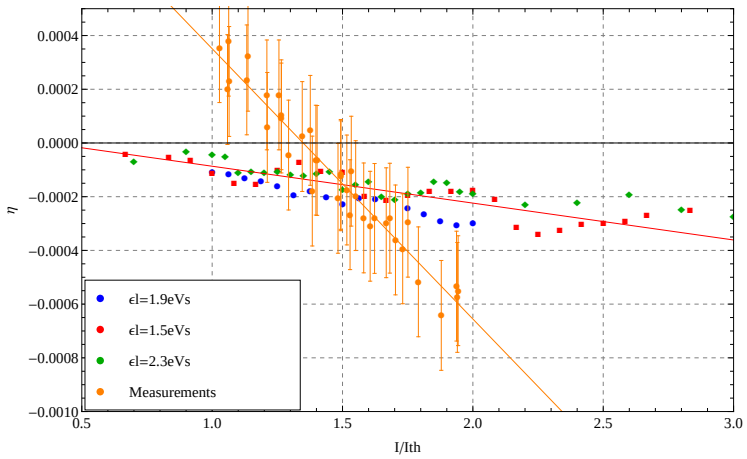

Figure 4.71: Simulated η_{th} as a function of the beam intensity normalized to the intensity threshold I_{th} obtained by measurements for different longitudinal emittance and for no chromaticity.

in η is computed by *HEADTAIL* and measured in the real machine. Fig. 4.72 compares the simulated η_{th} to the experimental η_{th}. Again, by applying a linear fit on the measured and simulated η_{th} with ξ_y, the obtained slopes differ again by a factor 7.

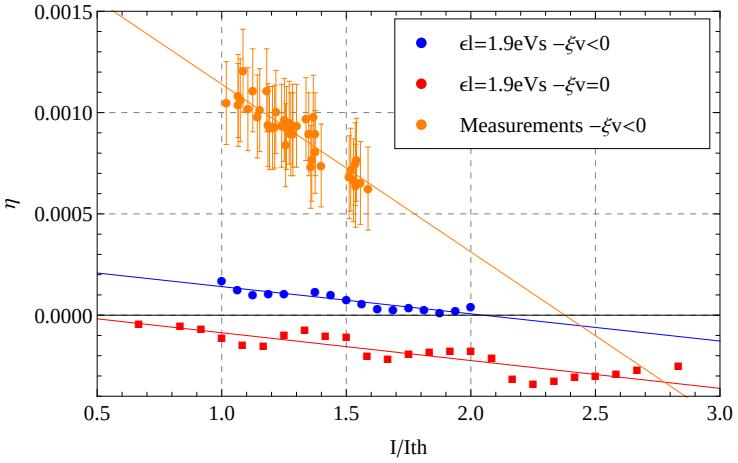

Figure 4.72: Simulated η_{th} as a function of the beam intensity normalized to the intensity threshold I_{th} obtained by measurements for different longitudinal emittance and a vertical chromaticity $\xi\ -0.1$ at transition energy.

With the presence of chromaticity, the instability is triggered after transition energy, both in the measurements and in the simulations. For intensities close to $I/I_{th} \simeq 1$, a factor 5 difference is observed between the computed $\eta_{th} \simeq 0.0002$ and the measured $\eta_{th} \simeq 0.001$. On the contrary to the case without chromaticity, this difference cannot be explained by an error on the estimation of the timing of the transition energy, since the discrepancy is too large. Two possible explanations of these observations are mentioned:

- the instrumentation is not capable to detect very small particle oscillations when the beam intensity is close to the intensity threshold of the instability. An estimation of the resolution was 0.04 mm. This has a direct impact on the quality of the rise time estimation. The error on the linear fit to deduce the growth rate is based on fewer points and the moment at which the instability is detected is therefore slightly shifted. A difference in η of 0.0002 concerns only a few hundred turns.
- As already observed for the benchmark of the intensity threshold, incoherent effects such as space charge and higher order components of the magnetic field are certainly present in the machine, contributing to the increase of the thresholds in intensity and in η.

As a conclusion, the comparison between the threshold in momentum compaction in the experimental data and the simulations shows a fair agreement considering an error on the timing on the transition energy of half a millisecond in advance with respect to its real value. In addition, *HEADTAIL* does not allow to reproduce the same η_{th} evolution as a function of the beam intensity, since a factor 7 is observed between the experimental data and the simulations.

4.8 Comparison with Theories

4.8.1 Beam Breakup

In Sec. 1.4.3, the BBU mechanism was briefly described and Ref. [39] applies this formalism at the fast vertical instability of the PS. Here, we compute the ratio between the amplitude of the bunch tail at the turn n and the first turn for a circular machine, in the vertical plane, from Eq. 1.143, with the parameters of Table 4.8. This formula does not take into account any chromaticity.

Beam intensity [10^{10} protons]	130
Resonator frequency f_r [GHz]	1
Radius [m]	100
Full bunch length [ns]	30
Shunt Impedance MΩ/m	0.7 and 3.1
Total Energy [GeV]	6.1
Vertical tune Q_{y0}	6.28
Vertical average PS aperture [mm]	35

Table 4.8: : Beam parameters for the application of the BBU formalism.

Fig. 4.73 and Fig. 4.74 show after how many turns the particles excited by the impedance oscillate at an amplitude such that they reach the vacuum chamber dimension and are lost in the machine. The computations were done for the shunt impedance found by the experiment, i.e. 0.7 MΩ/m in Fig. 4.73. The particles would need at least 4000 turns, i.e. 8 ms, to reach the aperture. In the experiment, large losses occurs within 2 ms for such intensity and bunch length and no vertical chromaticity. The impedance has to be increase up to 3.1 MΩ/m match the losses in 2 ms and therefore a disagreement of more than a factor 4 is made.

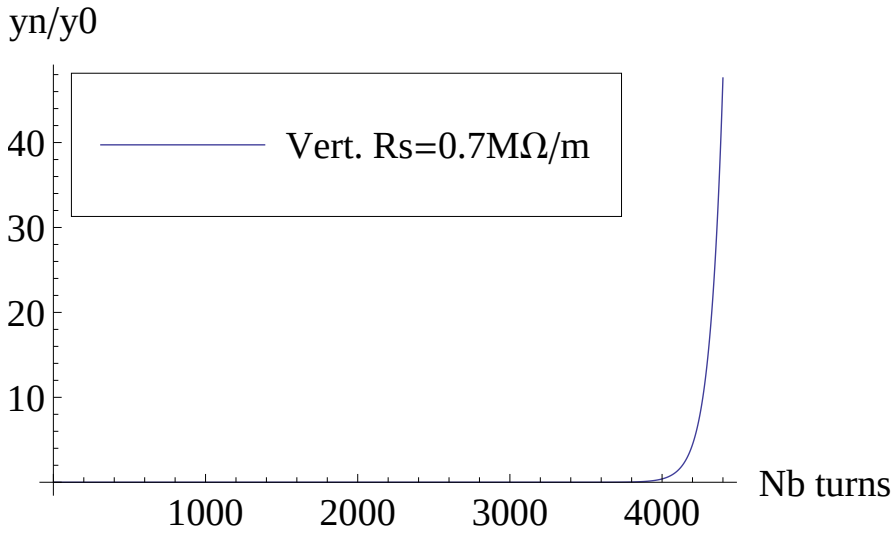

Figure 4.73: Amplitude evolution computed with the Beam Breakup formula with a shunt impedance of R_s=0.7 MΩ/m.

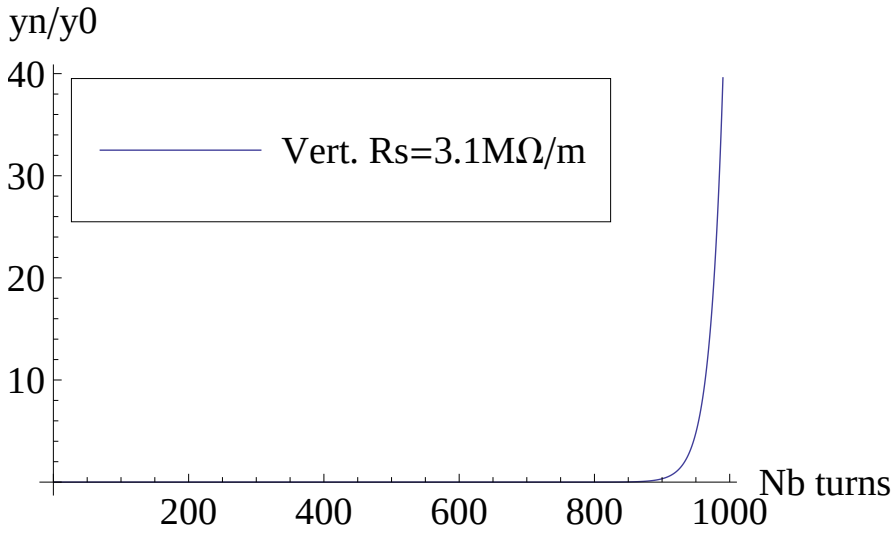

Figure 4.74: Amplitude evolution computed with the Beam Breakup formula with a shunt impedance of R_s=3.1 MΩ/m.

4.9 Effect of Higher Quality Factor Q

Up to this point, only a broad-band impedance with a quality factor of $Q = 1$ was considered. From the previous studies, in a similar way as the measurements, it was shown that the instability starts at the peak density of the bunched beam. In this paragraph, the effect on the instability of higher quality factor Q will be studied. In the Beam Break Up formalism applied to rings Ref. [38], the longitudinal positions z between the particles is assumed to be unchanged due to the frozen synchrotron motion. In the two-particle model, the transverse displacement of the head, y_1, and the tail, y_2, affected by the transverse wake potential W_1, satisfy

$$\begin{aligned} \frac{d^2 y_1}{ds^2} + k_{\beta_1}^2 y_1 &= 0 \\ \frac{d^2 y_2}{ds^2} + k_{\beta_2}^2 y_2 &= \frac{-e^2 N W_1(\hat{z})}{2LE_0} y_1 \end{aligned} \tag{4.15}$$

where E_0 is the energy of the beam particle, $\hat{z}$ is the longitudinal distance measured along the designed particle path, W_1 is the transverse wake function, k_β is the betatron wave number, and N the number of particle in the beam. The wake function is given by

$$W_1(\hat{z}) = -\frac{\omega_r^2 Z_1^\perp}{Q\sqrt{\omega_r^2 - \alpha^2}} e^{-\alpha z/c} \sin \frac{\sqrt{\omega_r^2 - \alpha^2}\, z}{c}$$

with $(\omega_r, Z_1^\perp, Q)$ being the parameters of the broad-band impedance, and $\alpha = \omega_r/(2Q)$ the decay rate. One can see that

$$\lim [W_1(\hat{z}, Q \to +\infty)] = 0, \tag{4.16}$$

so the higher is the quality factor, the weaker is the wake transverse force along the bunch. Therefore, a scan over different values of Q was done with *HEADTAIL* for a study of the effect of the quality factor on the instability through transition. The threshold and the rise time of the fast vertical instability might be changed as well as the pattern on the Δy signal. A broad-band impedance is declared in *HEADTAIL* with $f_r = 1GHz, R_s = 1.6$ MOhm/m (these simulations were done before the matching in impedance), and the quality factor is scanned with the values $Q = (1, 2, 3, 5, 8, 10, 20)$. The beam parameters are presented in Table. 4.9. The wake function are plotted in Fig. 4.75 and Fig. 4.76.

The vertical position of the centroid as a function of the momentum compaction factor η and for the different values of quality factor is presented in Fig. 4.77 for $Q = (1, 2, 3, 5)$, in Fig. 4.78 for $Q = (8, 10)$ and in Fig. 4.79a for $Q = 20$. As expected, the higher the quality factor, the weaker

Beam intensity [10^{10} protons]	90
Longitudinal emittance (2 σ)	1.9 eVs
Norm. transverse emittance (1σ) $\epsilon_{x,y}$	5 mm·mrad
Transverse tunes $Q_{x,y}$	6.22/ 6.28
Chromaticity $\xi_{x,y}$	0/0
RF Harmonic h	8
Number of turns	50000

Table 4.9: Beam parameters in the cfg file at the beginning of the *HEADTAIL* simulation.

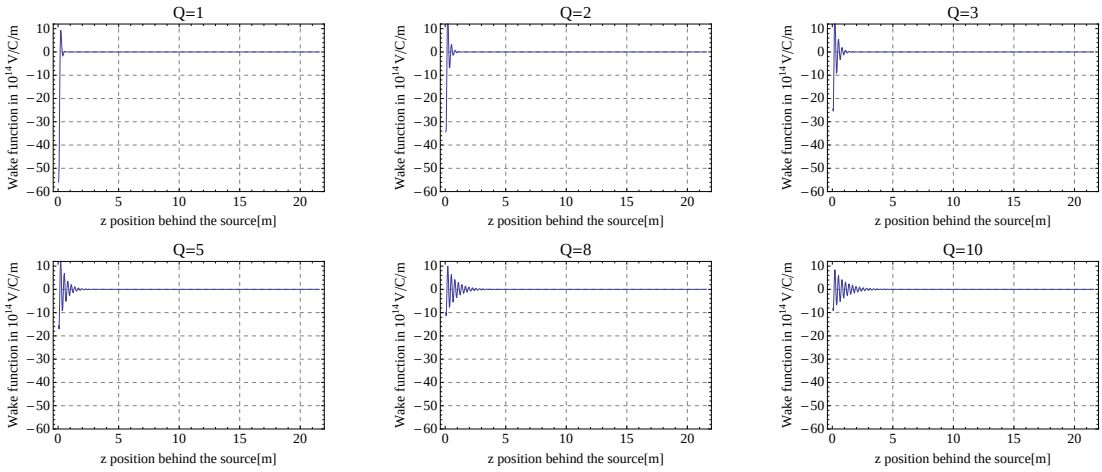

Figure 4.75: Wake function for a broad-band impedance for values of quality factor $Q = 1, 2, 3, 5$ and 10.

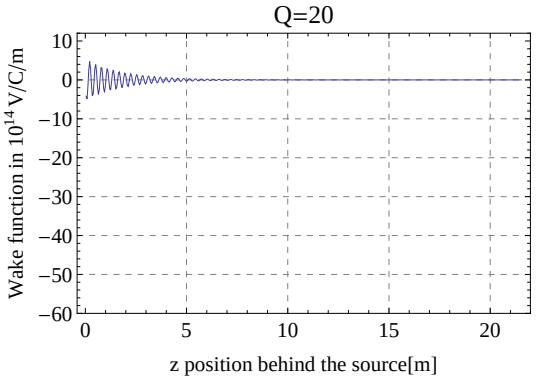

Figure 4.76: Wake function for a broad-band impedance for values of quality factor $Q = 20$.

is the instability. As a consequence, the rise time is slower as shown in Fig. 4.79b and the instability threshold is affected. For values of the quality factor $Q > 3$ and for a beam intensity of $90 \cdot 10^{10}$ protons, the beam is stable.

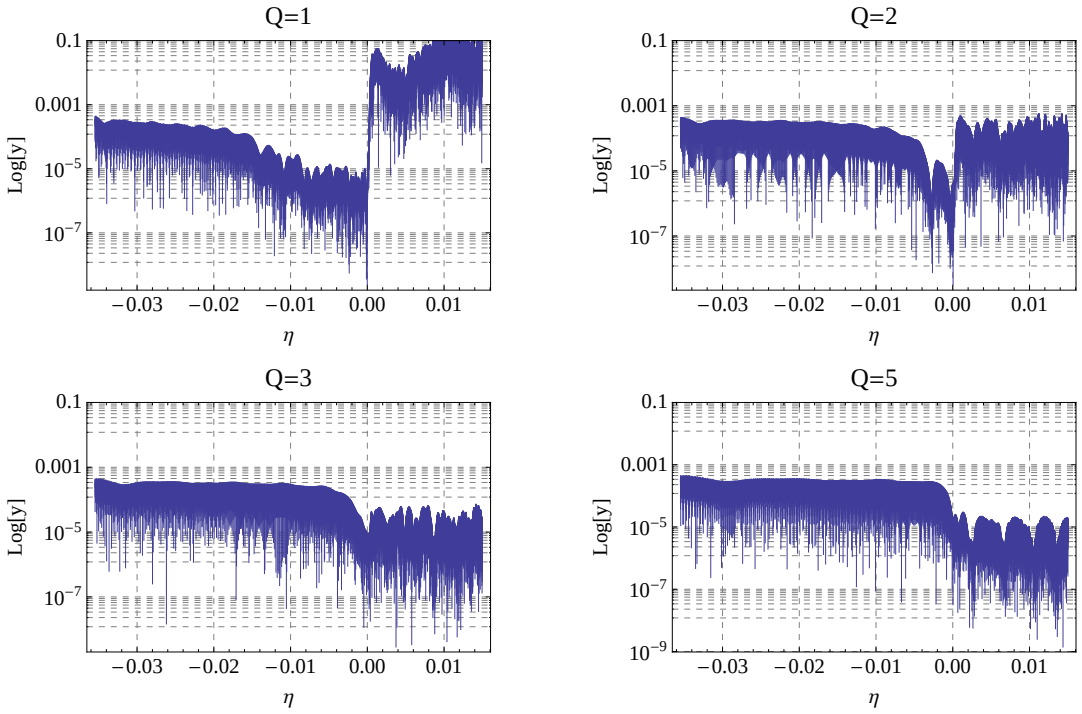

Figure 4.77: Vertical bunch centroid evolution as a function of the momentum compaction η for values of quality factor $Q = 1, 2, 3$ and 5.

The effect on the rise time of the instability is easily seen on the formula Ref. [39] with the term $\alpha = \omega_r/(2Q)$ which become smaller while Q is increasing.

$$\frac{y_n}{y_0} = \frac{1}{2\sqrt{2\pi}} \left(\frac{\omega L}{\beta c}\right)^{\frac{1}{4}} \frac{\beta c}{L\omega_r} e^{-\alpha L/(\beta c)\sqrt{\frac{\omega L}{\beta c}}} \tag{4.17}$$

The shape of broad-band wake function might influence also the Δ_y signal and the way the oscillation develops along the bunched beam. In the following paragraph, the measured Δ_y signal is compared to the *HEADTAIL* signals for the cases of the quality factor simulated below. Fig. 4.80 shows a measured Δ_y signal for a bunched beam of $90 \cdot 10^{10}$ protons around transition energy. The measurement shows that the oscillation is developing around the peak density of the beam, i.e. where the particle density is the highest. The head of the bunch seems stable - particles in the head arrive at small value in time. This means that the mechanism responsible for this instability is a single-bunch effect with a short-range wake field.

The signals presented in Fig. 4.80 can be compared to the signals of Fig. 4.81a for $Q = 1$, Fig. 4.81b for $Q = 2$, Fig. 4.82a for $Q = 5$ and Fig. 4.82b for $Q = 10$. One can notice that higher is

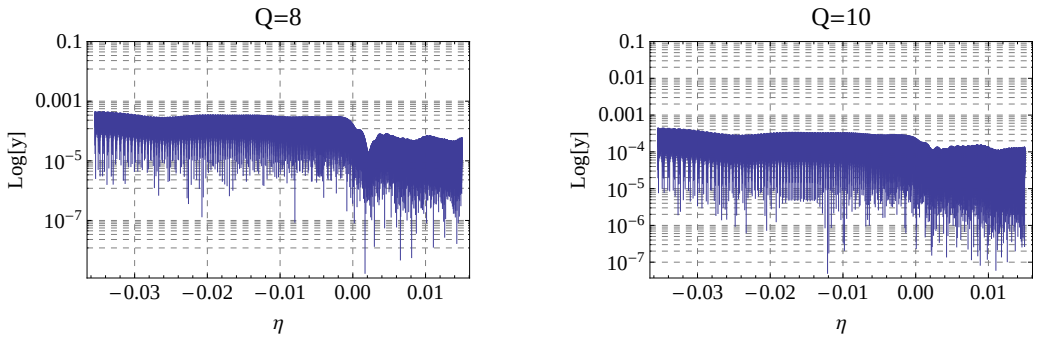

Figure 4.78: Vertical bunch centroid evolution as a function of the momentum compaction η for values of quality factor $Q = 8, 10$.

the quality factor Q, longer is the range of z in which the particles are oscillating due the wake. Whereas the measurements show a short range effect in which mostly the particles at the peak density are unstable, the case $Q = 10$ presents that the tail of the bunch is very unstable. By increasing the quality factor Q of the broad-band impedance, the range of the wake fields becomes longer. The case $Q = 1$ Fig. 4.81a appears to be the most suitable to reproduce the oscillation observed in the measurements Fig. 4.80.

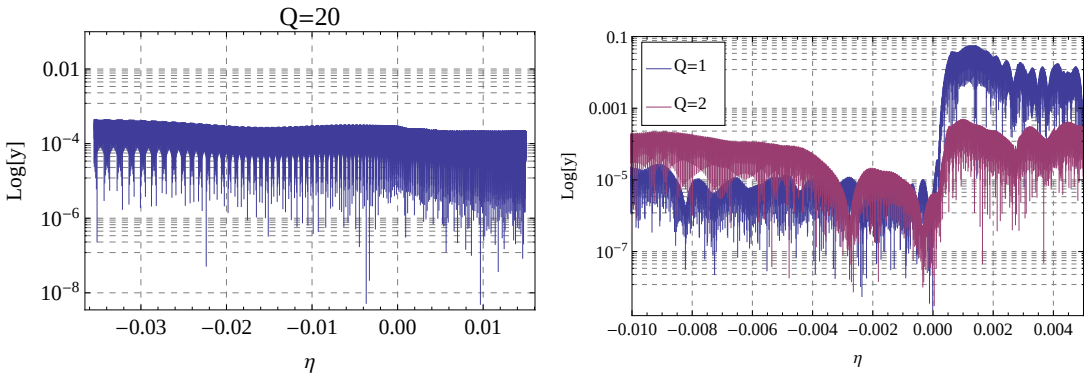

Figure 4.79: Fig. (a) is the vertical beam centroid in logarithm scale for a broad-band impedance with a quality factor $Q = 20$. Fig. (b) compares the vertical beam centroid for $Q = 1$ and $Q = 2$ in which it can be seen that the instability rises slower while Q is higher.

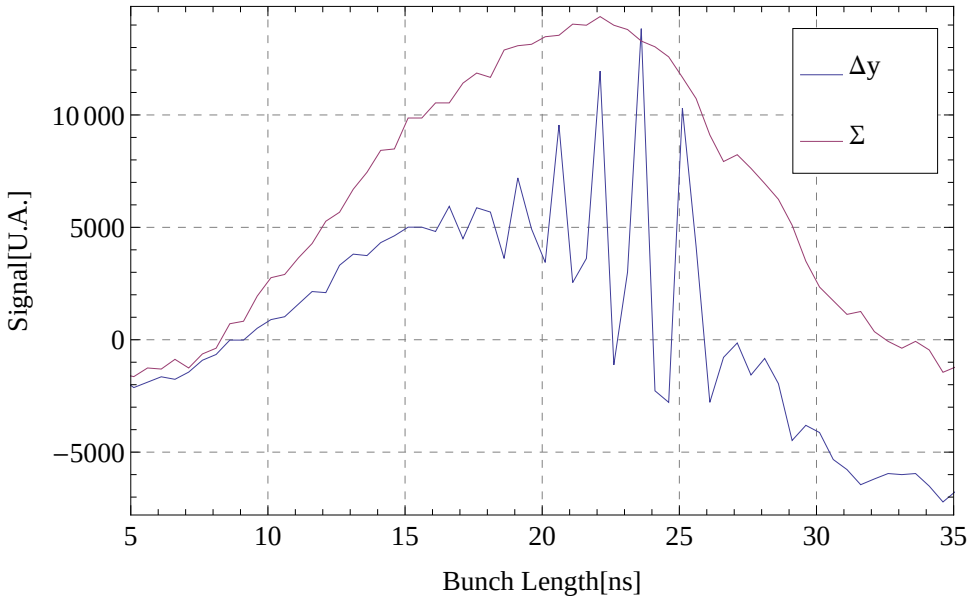

Figure 4.80: Measured Δ_y signal for a beam intensity of $90 \cdot 10^{10}$ protons around transition energy.

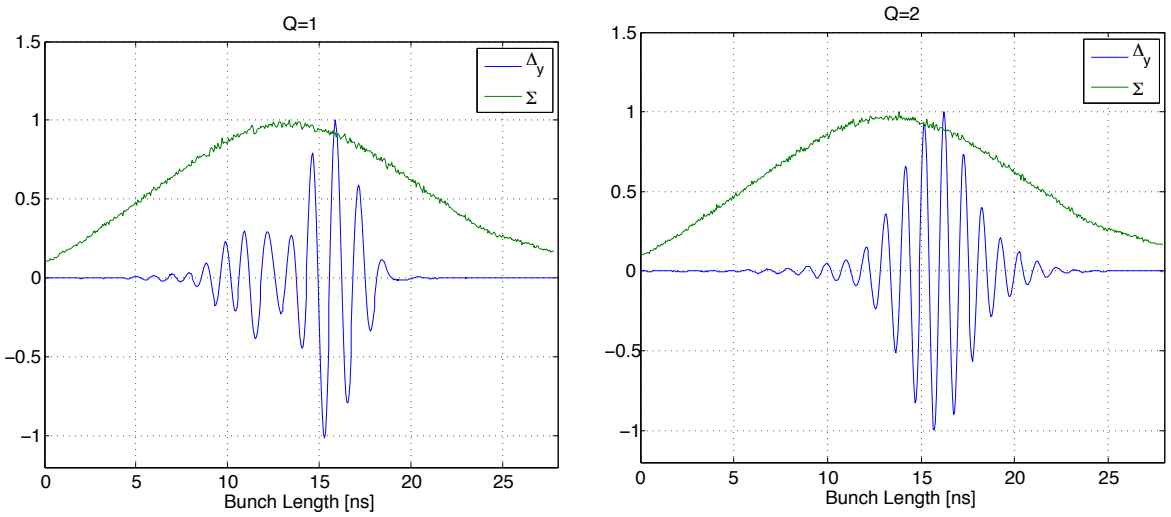

(a) (b)

Figure 4.81: Δ_y signal computed by *HEADTAIL* with a broad-band impedance and for different value of quality factor $Q = (1,2)$ presented respectively in Fig. (a) and in Fig. (b). For each case, the longitudinal density is also plotted.

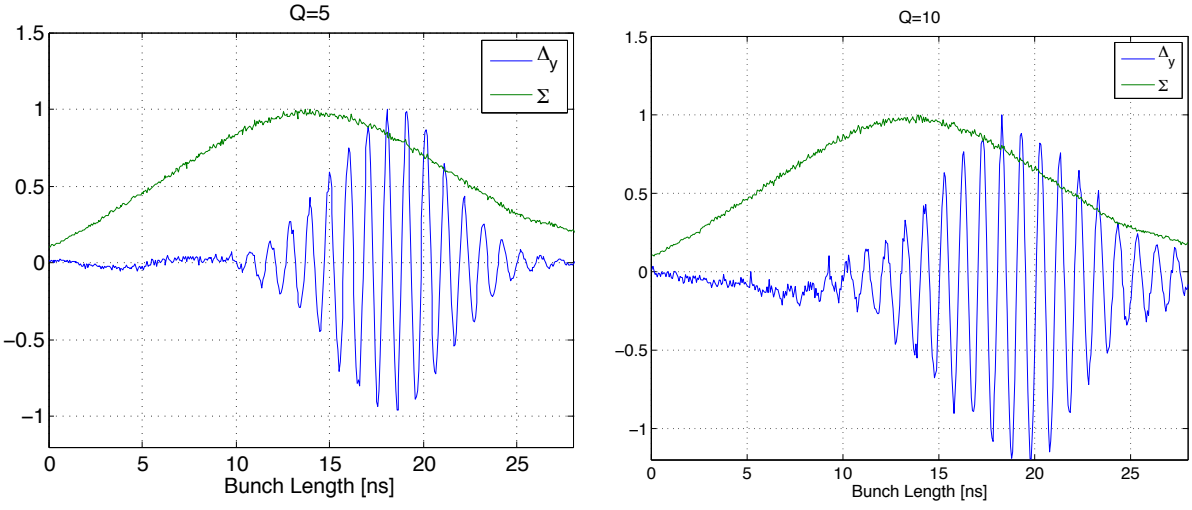

(a) (b)

Figure 4.82: Δ_y signal computed by *HEADTAIL* with a broad-band impedance and for different values of the quality factor $Q = (5,10)$ presented respectively in Fig. (a) and in Fig. (b). For each case, the longitudinal density is also plotted.

4.10 Fast Vertical Instability Measurements with Gamma Transition Jump

Up to this point, only beams crossing transition energy without complex change in gamma transition, were considered. In normal operation and since 30 years, the CERN PS uses a gamma jump in order to cross in a faster way transition energy, as explained in Sec. 1.3.6. The lattice of the machine is changed in order modify the gamma transition energy as well and therefore η. In the previous section, the fast vertical instability measurements demonstrated that η is a fundamental parameter. The measurements shows also that it exists threshold in η, depending on the intensity and on the chromaticity, which trigger the fast instability. The gamma transition jump changes strongly η in order to keep the beam at safe distance from $\eta = 0$ before and right after the jump: the gamma transition jump is a powerful way to alleviate the instability and allows to considerably increase I_{th}. In this section, experimental results of the fast vertical instability with the application of a gamma transition jump are presented.

4.10.1 Beam Setting Up

As for the experiments without γ_{tr}-jump, the setting up of the beam is fundamental. The measurements are performed with a single bunch beam with the parameters of Table 4.10. The total voltage applied on the RF cavities in these sets of measurement were kept higher than previously, i.e. at 200 kV instead of 145 kV due to longitudinal losses during the acceleration. Indeed, with smaller RF voltages, slow beam losses were observed 50 ms before transition energy while the quadrupoles of the gamma jump start to pulse. They were cured by increasing the RF voltage of the cavities which increases the height of the bucket as well. The explanation is that the voltage was not large enough to keep the particles in the linear bucket and the protons reaching the separatrix were lost.

Total energy at γ_{tr} [GeV]	$E \simeq 6$
γ_t	6.44
RF Harmonic	h=8
Number of bunches	1
Total RF cavity voltage [kV]	200
Full bunch length [ns]	50
Longitudinal emittance (2σ) [eVs]	1.29 - 2.4

Table 4.10: Beam parameters with for the measurements with gamma jump.

The gamma jump used here is the one performed on the high intensity beam ToF since it is the most concerned by this type of instability. γ_{tr}-jump is done with doublets and triplets of quadrupoles located all around the ring. Fig. 4.83a presents the evolution of the currents powering the magnets. They are sampled as a function of the beam energy and, using an optics model of the PS and the simulation code MADX, the gamma transition γ_{tr} is computed for each couple of currents of doublets and triplets of quadrupole. Fig. 4.83b presents the results of the change in γ_{tr} during the acceleration – i.e. the gamma transition jump – and while the currents of Fig. 4.83a are pulsing. γ_{tr} is changing in 500 μs by $\Delta\gamma_{tr} = 1.89$. The transition energy γ_{tr} is about 6.44.

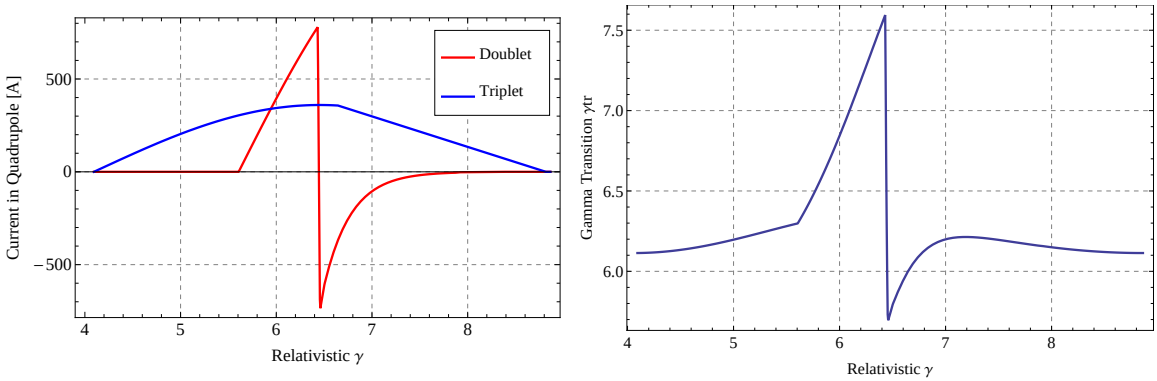

(a) (b)

Figure 4.83: Fig. (a) presents the currents of the gammajump quadrupoles as a function of the beam energy. Fig. (b) shows the resulting change .

The resulting momentum compaction factor η is then presented in Fig. 4.84a. In previous studies [29], a stability criteria for η was defined for the longitudinal microwave instability as η should not be smaller than 0.004 for more than 1 ms around transition energy. In this case, $|\eta|$ stays under the limit for 0.1 ms (Fig. 4.85).

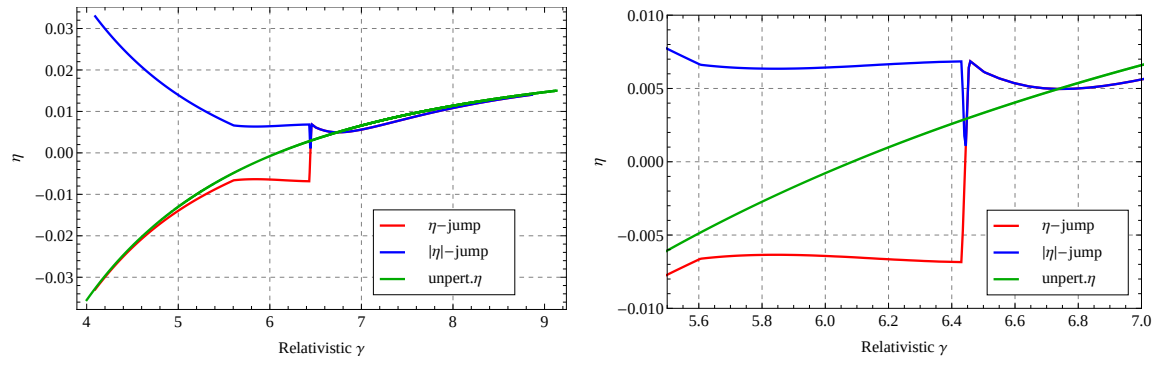

(a) (b)

Figure 4.84: Fig. (a) is the resulting η evolution during the gammajump. Fig. (a) zooms in the region of the gammajump.

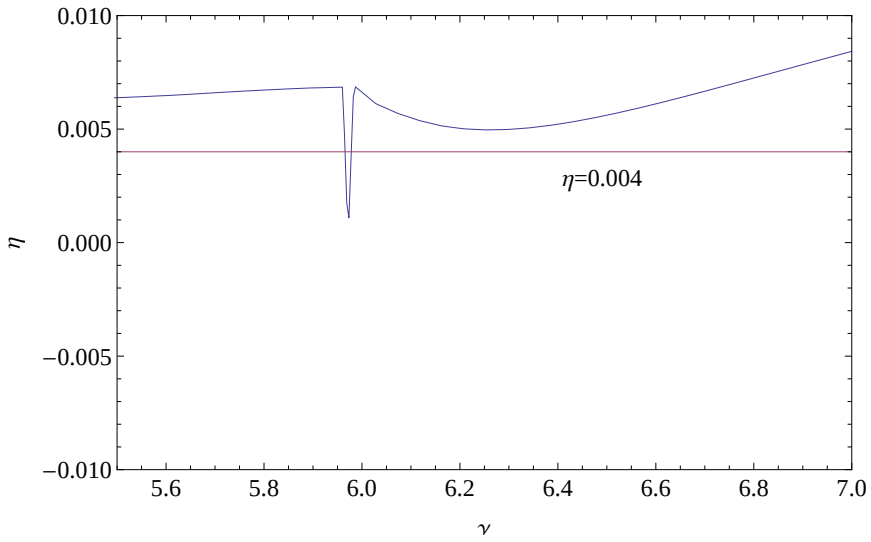

Figure 4.85: Absolute value of $|\eta|$ as a function of the beam energy with the stability limit of the microwave instability $|\eta| = 0.004$.

As for the measurements without gamma jump, the time of the RF stable phase jump has to be tuned. This timing is not the same as the one set during the previous measurements since the transition energy is increased on a beam with gamma jump. In a similar way as in Sec.4.1.2, this timing is scanned and again the Peak Detected signal is acquired in order to find the time at which the bunch length oscillations are minimum after the jump of γ_{tr}. Such scans and signals of the Peak Detected pickup are presented in Fig. 4.86. The timing of the RF stable phase shift is linked to the timing when the jump of the currents of the doublets is performed.

The optics functions such the beta and the dispersion function are perturbed by the gamma transition jump, and the envelope of the beam strongly increases while the currents of the quadrupoles are at their maximum. This is one of the unfavourable effect of the gamma transition jump. The beta function increases by a factor 4 in certain locations of the ring [30], which can be the cause of serious beam losses, as explained in Reference [30]. The perturbed beta and dispersion functions due to the gamma jump averaged around the ring are presented in Fig. 4.87a and in Fig. 4.87b. For the rest of the study, only the average of the beta and dispersion functions will considered since the simulations with *HEADTAIL* are done a single kick due to the impedance therefore only averages in optical function can be given.

As in the experiment without gamma jump, the chromaticity is a crucial parameter to control. Initially, the aim was to perform a zero-chromaticity plateau as in the previous measurements detailed in Sec. 4.1.2. However, due to the gamma transition jump and the PFWs, this was not possible. First of all, as explained previously, the control of the working point is very delicate in the PS and while an aimed chromaticity is programmed, a certain amount of time is needed to the power supplies of the PFWs to reach the current which will provide the desired value in chromaticity. Then, the matrices relating the currents of the PFWs at this energy

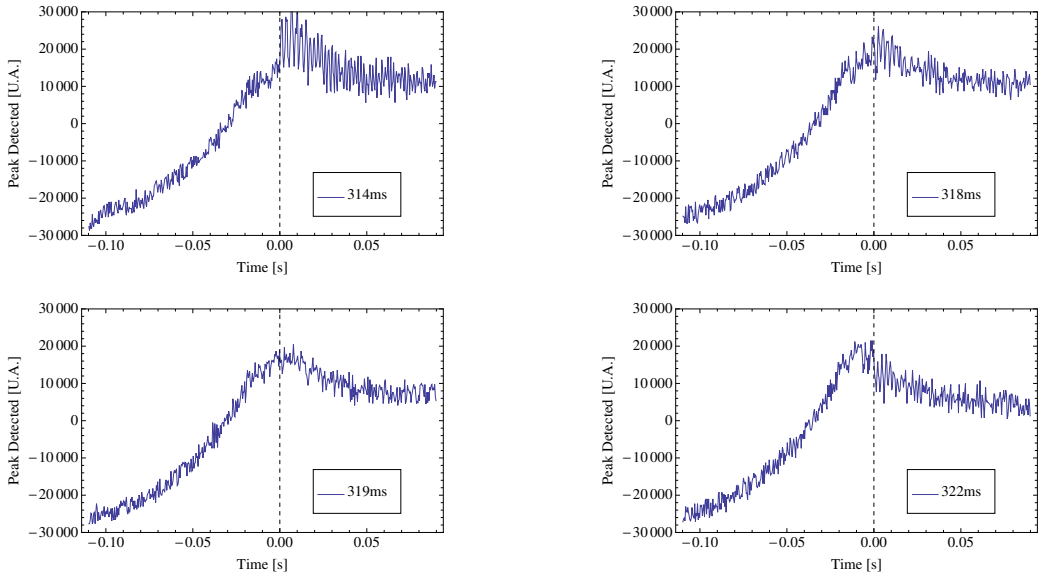

Figure 4.86: The time when the jump in η is done is scanned in order to identify the minimum residual bunch length mismatch.

and the working point are extrapolated as explained in Sec. 2.4.Then the gamma jump itself is changing the working point, since it changes the tunes – $\Delta\gamma_{tr}$ is performed with a non zero tune shift. Therefore the chromaticities are affected by the rapid change in quadrupolar component of the field. It was decided, instead of a zero chromaticity plateau, to program a vertical chromaticity which is negative below transition and positive above. One has to pay attention that the chromaticities are computed from the tune measurements as a function of the $\Delta p/p$ and η is modified by the gamma jump according Fig. 4.84a.

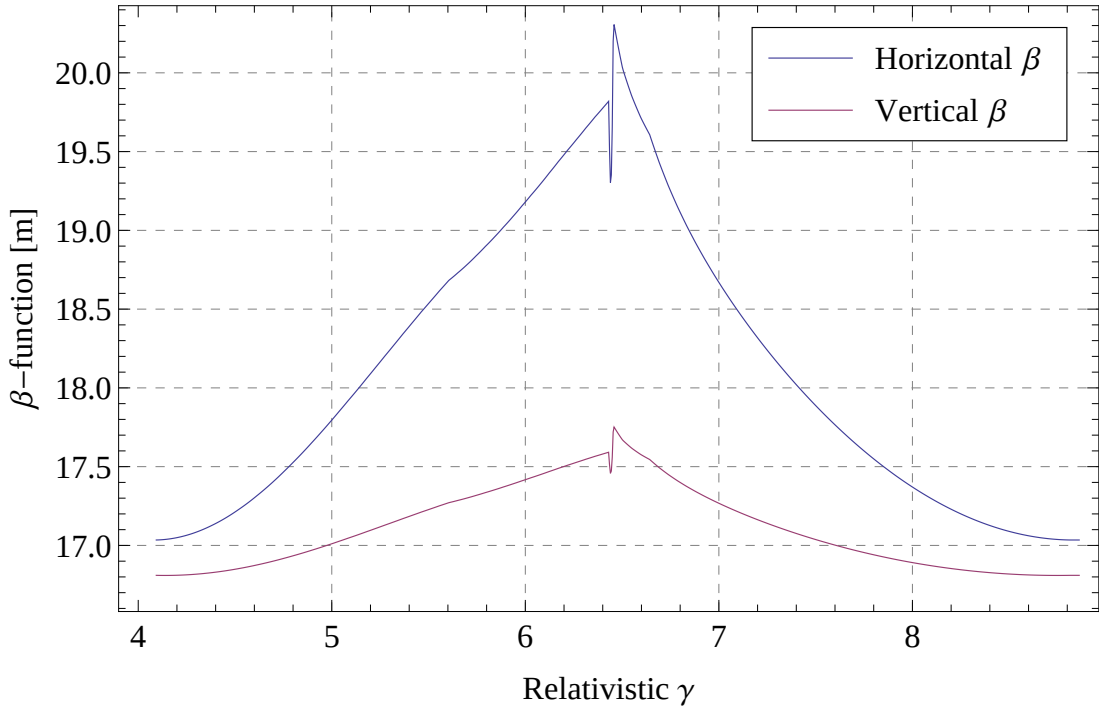

(a)

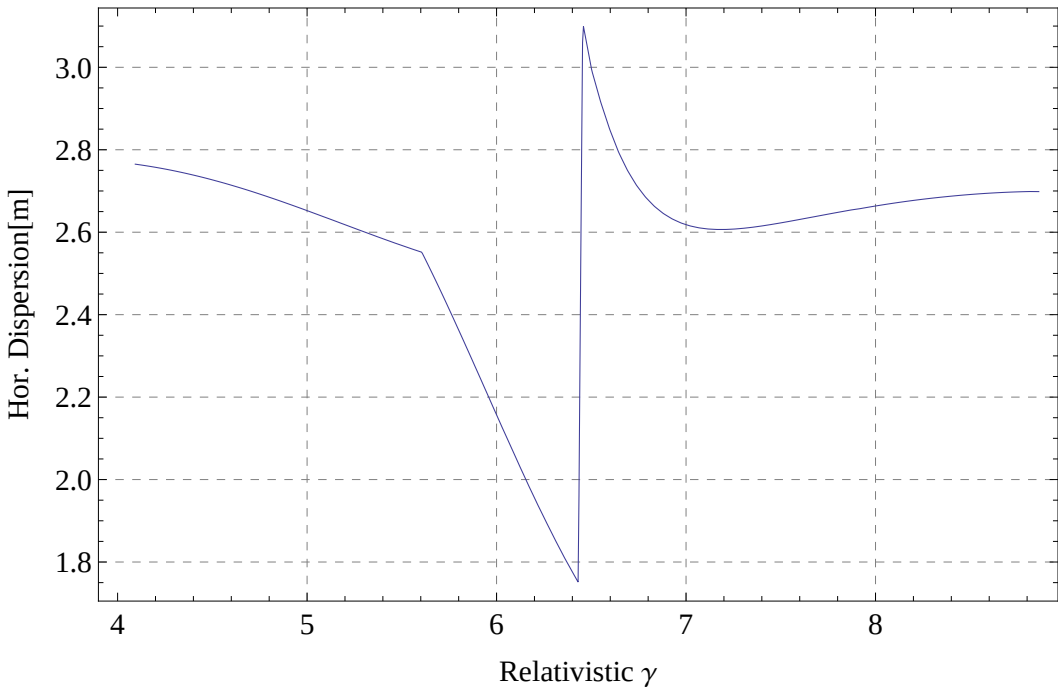

(b)

Figure 4.87: Optics functions as a function of the beam energy while the quadrupoles of the gamma jump are pulsing.

4.10.2 Fast Vertical Instability Observation with a Gamma Transition Jump

This section will be dedicated to experimental observations of the fast vertical instability while the gamma transition jump quadrupoles are pulsing. The differences with the previous experiments are that the η function is modified by the quadrupoles, jumping from -0.007 to 0.007 in 500 μs, and that the vertical chromaticity ξ_y is changing as well partly due to the optics change. The ξ_y evolution with time is the results of the gamma jump and also of the programmed working point. Fig. 4.90 summarizes the fast vertical instability development with the use of a γ_{tr}-jump. Fig. 4.90 presents η, ξ_y and beam intensity evolution as a function of time around the transition energy for a beam of $I = 630 \cdot 10^{10}$ protons with a longitudinal emittance of 2.1 eVs. In the left bottom of Fig. 4.90 is drawn a waterfall plot of the strength of the travelling wave frequency caused by the instability as a function of time around γ_{tr} energy. The time on the figures of Fig. 4.90 is given with respect to the time of γ_{tr} timing, thus 0 ms is the moment when $\eta = 0$. Therefore Fig. 4.90 allows to follow the instability development while the γ_{tr}-jump is performed. Fig. 4.90 A, B, C and D present measured Δ_y and Σ signals of the WCM while the fast vertical instability is developing.

A first observation from the waterfall plot is the travelling wave frequency can be found around 700 MHz even with the use of a gamma transition jump. With the γ_{tr}-jump, the instability does not develop for small values of η contrary to the measurements presented in Sec. 4.1.3.

For $I \simeq 630 \times 10^{10}$ protons with a longitudinal emittance 2.1 eVs and a vertical chromaticity $\xi_y \simeq 0.1$ after the γ_{tr}-jump, the waterfall plot is related to the evolution of η and one can observe that the instability starts for a threshold $\eta_{th} = 0.005$ at $t = 5$ ms after transition energy. The beam intensity decreases slightly before due to aperture restriction [30] since the beam size is very large around the inversion of the currents of the doublets of quadrupoles. Fig. 4.90 A shows that the particles are not oscillating at high amplitude whereas the beam intensity is decreasing due to other mechanisms such as aperture restrictions or eventually resonances crossing since the gamma jump occurs with a non zero tune shift. With slow losses, a reshuffling of the particles in the bunch occurs which might contribute to the stabilization of the instability up to $t \simeq 8$ ms.

From $t \simeq 8$ ms with $\xi_y = 0.15$, the instability develops in a stronger way, see the waterfall plot of Fig. 4.90. The beam losses occur within 3 ms and the rise times are about the same order of magnitude as the measurements without gamma jump as shown in Fig. 4.88. It is then interesting to relate Fig. 4.88 to the bunch length measured from the Σ signal acquired also turn by turn on the same time scale as the Δ_y signal. The result is shown in Fig. 4.89. The bunch length oscillates after the gamma jump which occurs at $t = 0$ ms, meaning that the beam is not matched to the bucket. The γ_{tr}-jump brings the bunch length to a shorter value. If the gamma jump is well adapted to the beam, the bunch length stays constant without any oscillations. The jump in η has to be larger, because the gamma jump brings the beam to a non adapted bunch length. This gamma jump is then slightly not adapted for a beam with such intensity.

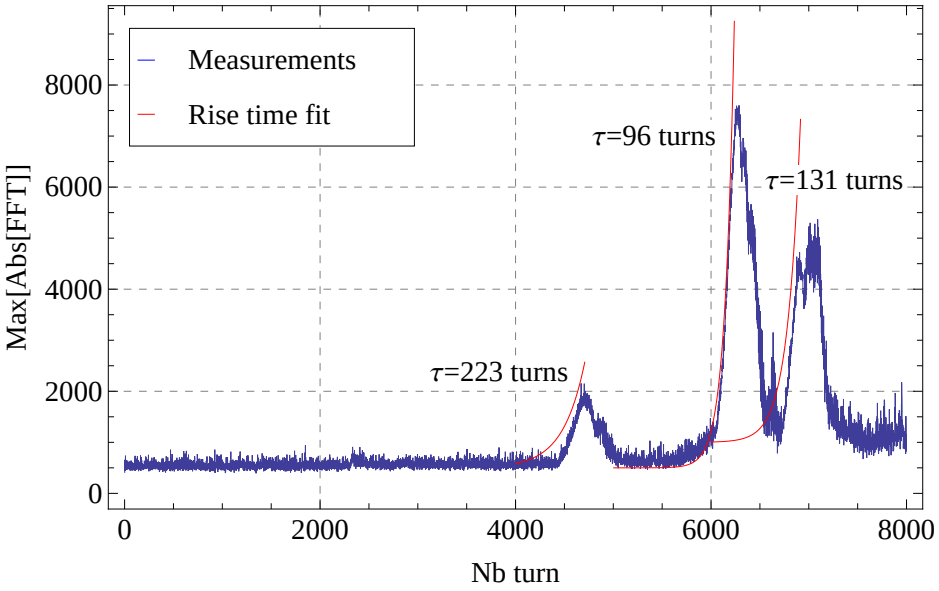

Figure 4.88: Rise time of the fast vertical instability with a gamma jump for a beam intensity of $I \simeq 630 \times 10^{10}$ protons, $\epsilon_l = 2.1$ eVs.

By comparing the bunch length oscillations after the gamma jump to the evolution of the maximum frequency spectrum evolution Fig. 4.89, a correlation between the oscillation of the bunch length with the growth of the intensity can be done: the instability is rising faster while the peak density is maximum, i.e. while the bunch length reaches a local minimum. Therefore, the instability seems to be dependent of the peak density than the bunch length which would then rather corresponds to the coasting beam formalism: the peak density is varying with time after the gamma jump making the instability non-linear. The reason why the instability is not growing at each maximum of the peak density, might come from the losses.

Fig. 4.90 B presents the Δ_y signal while the instability is well developed ($t \simeq 8$ ms). The spread of the travelling wave is then shifting to oscillation frequencies of 400 MHz while the beam loses particles. Then Fig. 4.90 C shows a hole in the longitudinal profile, the shift in frequency which might be due to the beam losses. Finally, η increases to values larger than 0.006 and the beam is stabilized 10 ms after transition energy.

As a conclusion, the fast transverse instability does not occur while the η-jump is performed. The change in η is either too fast compared to the instability rise time or since the PFWs are changing rapidly, higher components of the field can act also on the beam. Transverse space charge has also to be considered and since it can change the instability threshold [83] . The instability appears then while η decreases down to 0.005 after the η-jump. The rise time of the instability seems to be also triggered by the variation of the peak density while the bunch length is oscillating after the gamma jump. This leads to the hypothesis that the instability can be related to the coasting beam formalism. However other mechanisms are present in the machine and they stabilize the beam: beam losses, higher component of the magnetic fields

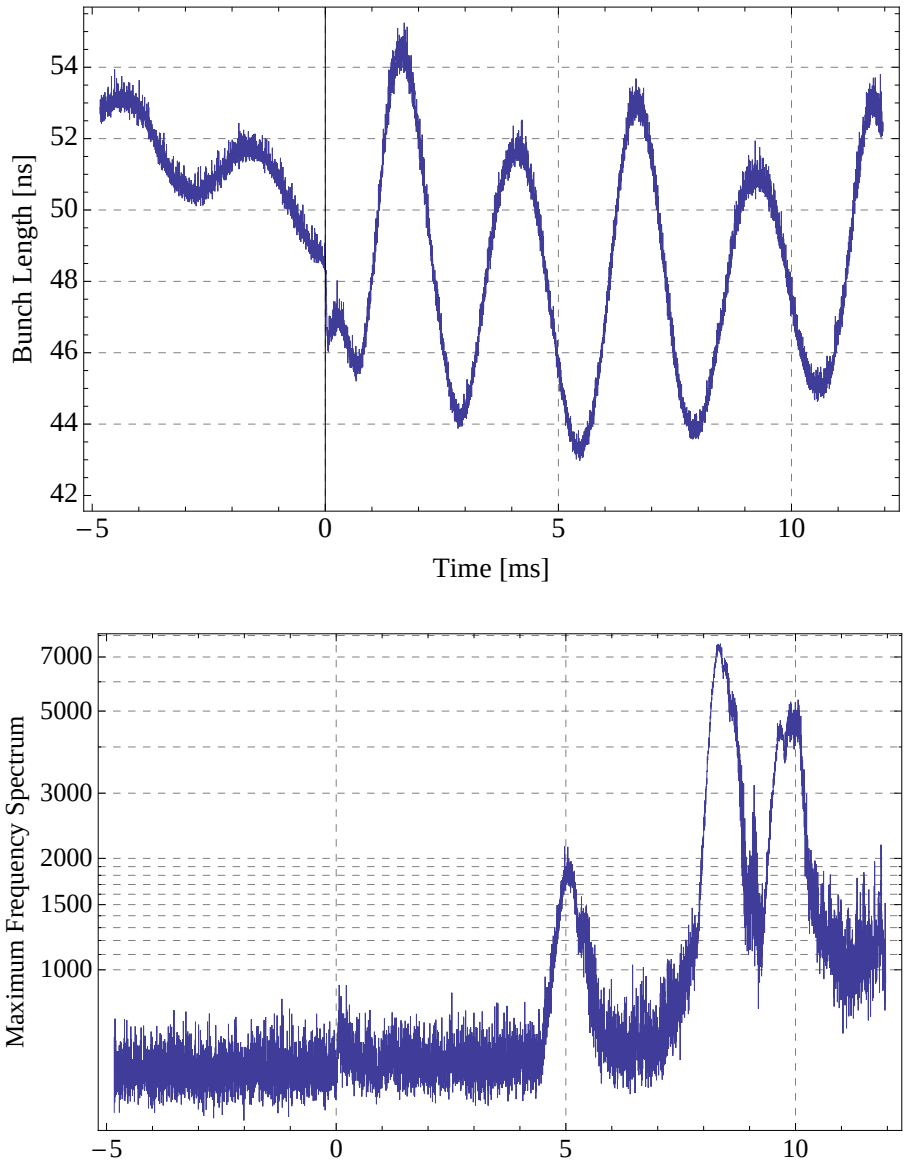

Figure 4.89: Maximum of the frequency spectrum as a function of time on the top and measured full bunch length evolution for a beam with a gamma jump and an intensity of $I \simeq 630 \times 10^{10}$ protons, $\epsilon_l = 2.1$ eVs.

and transverse space charge with such beam intensity.

With the use of a gamma transition jump, the threshold in intensity has been strongly increased. With a longitudinal emittance of 2.1 eVs, $I_{th} = 90 \times 10^{10}$ protons without gamma jump. In the case of Fig. 4.90, the beam intensity is already $I \simeq 630 \times 10^{10}$ protons. Therefore using larger values of η and therefore larger synchrotron tune Q_s can stabilize the beam. Considering the

BBU formalism in circulating beam, this means that particles between the tail and the head are exchanged and it helps to damp the instability. The next section is devoted to intensity threshold measurements with the gamma jump in order to establish the gain in I_{th} with respect to the case without γ_{tr}-jump.

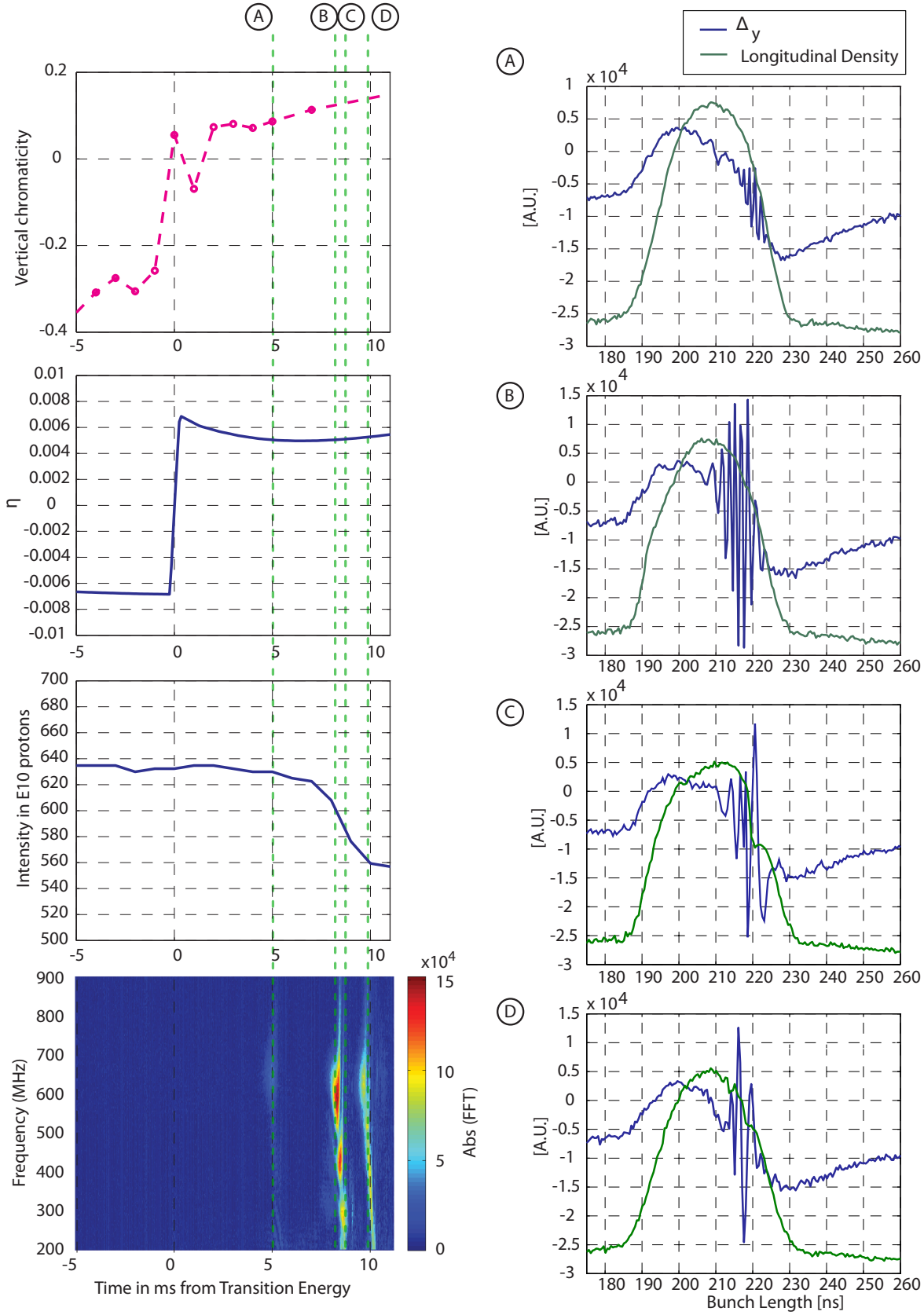

Figure 4.90: Description of the measured fast vertical instability with the use of a gamma jump.

4.10.3 Intensity Threshold with Gamma Transition Jump

No systematic rise time measurements with the beam intensity were performed since the fast vertical instability does not develop in once, but occurs while the peak density is varying. Efforts were then concentrated on the determination of intensity thresholds as a function of the longitudinal emittance as in Sec. 4.3.1 concerning the experiments without the γ_{tr}-jump. Therefore the intensity thresholds were determined by observing the Δ_y signals of the WCM while the number of protons in the single bunch beam is varied from high to lower intensities. The experiments was performed for the two sets in chromaticity presented in Fig. 4.91b. The results of the corresponding measured I_{th} are shown in Fig. 4.91a for the measured chromaticities as a function of time. Here two set of working points are presented, i.e. two ways for programming (Q_y, ξ_x, ξ_y), Q_x is left as free parameters in the context of the PFWs used in 3 currents mode. It has been observed while the setting up of the vertical chromaticity that the intensity threshold is very sensitive to the way how the working point is programmed. By slightly changing the targeted ξ_y, I_{th} can be strong decreased. As example, in Fig. 4.91, $I_{th}(\epsilon_l = 1.9)$ eVs $= 455 \times 10^{10}$ protons for the set 1 in chromaticity whereas $I_{th}(\epsilon_l = 1.9$ eVs$) = 324 \times 10^{10}$ protons for the set 2, so I_{th} has been divided by a factor 1.4. However, Sec. 4.6 has shown that the vertical chromaticity did not have as strong effect on the intensity threshold as measured in the real machine. Therefore one can expect the same effect with the gamma transition jump.

In particular, Fig. 4.91b shows that the change in chromaticity is particularly quick, meaning that the dI/dt of PFWs has to change quickly as well. Investigations on dI/dt powering the PFWs shows that the quadrupolar component is different according to the dI/dt programmed in the PFWs. Investigations on this phenomena are on going (Eddy currents). However, this effect can impact the instability behaviour since the quadrupolar component is affected and therefore the tune, the tune spread and the chromaticity. Therefore one has to keep in mind that not only the final obtained chromaticity is important but also the way how the working point is obtained.

An experiment has been carried out to study the influence on the I_{th} of the amplitude of γ_{tr}-jump induced by the jump in current of doublets of quadrupoles. Unfortunately, the experiments has been only done the for the set 2 in chromaticity due to lack of time. The beam intensity started at $\simeq 270 \times 10^{10}$ protons for a longitudinal emittance of 1.7 eVs measured before the acceleration. The current powering the doublet of quadrupoles reaches a maximum from which the currents jumps to change the γ_{tr}. The experiment starts from the currents of Fig. 4.83. The triplets were changed by the same ratio. The result is presented in Fig. 4.92. The $\Delta\gamma_{tr}$ is therefore decreasing while the maximum current applied to the doublet before the gamma jump is going down. Fig. 4.92 shows that the intensity threshold of the instability is linearly decreasing with the rapid current change of the currents of doublet ΔI_{db} and therefore in $\Delta\gamma_{tr}$. This experiment shows that the gamma jump can strongly increase the intensity threshold of the fast vertical instability due to the value of η before and after the γ_{tr}-jump.

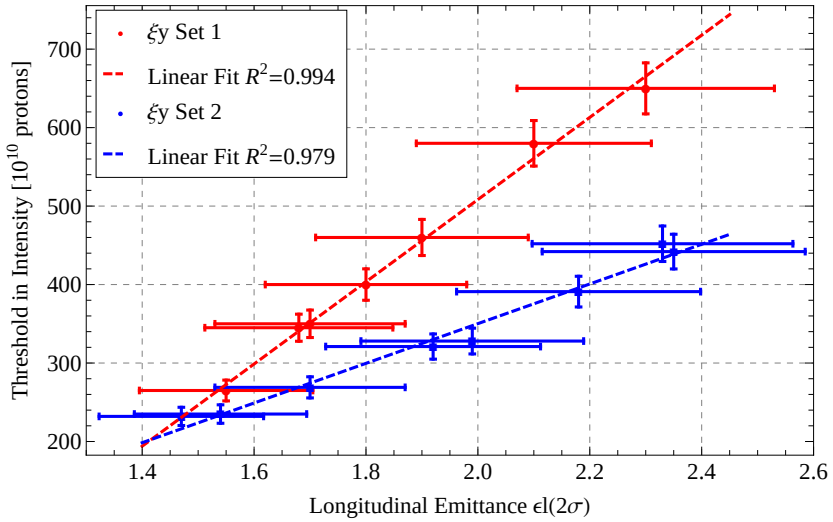

(a)

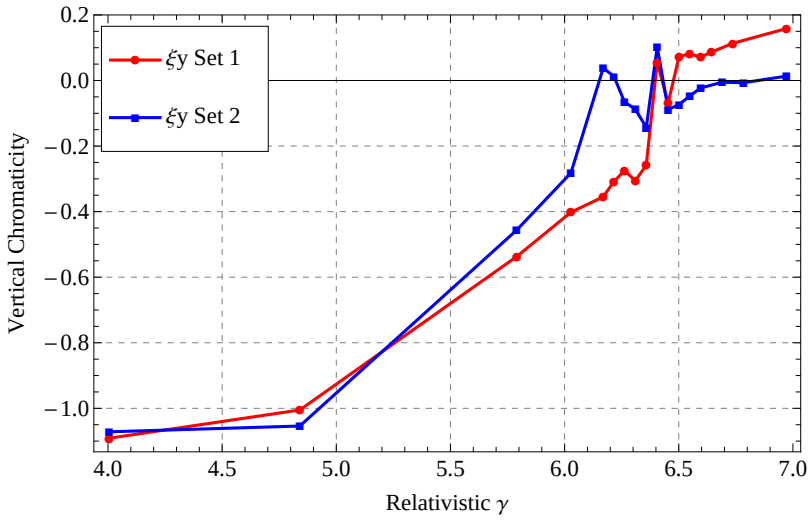

(b)

Figure 4.91: Fig. (a) presents the measured intensity threshold as a function of the longitudinal emittance for the two sets of measured vertical chromaticity of Fig. (b)

4.10.4 Macro particle simulation with a gamma transition jump

A gamma transition jump has been implemented in *HEADTAIL*: the code updates turn by turn the value of the momentum compaction η and in addition a change of chromaticity as in the measurements was also taken into account, but these simulations are not finished. However, by including the same broadband impedance as found for the case without gamma jump, for ϵ_l = 1.9 eVs, the intensity threshold is well above of the measured one of about 456×10^{10} protons of Fig. 4.91. Therefore the gamma transition jump by simulations and by measurements increases the intensity thresholds.

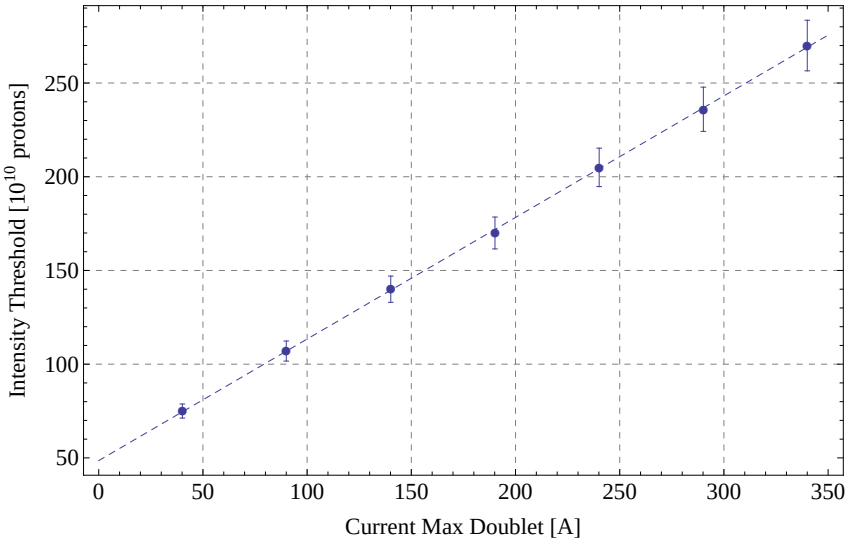

Figure 4.92: Intensity threshold variation with the maximum current applied on the doublets before the γ_{tr}-jump.

Fig. 4.93 compares the simulated bunch length with gamma jump to the maximum frequency spectrum of the travelling wave as a function of the number of turn. Transition energy is identified on the figure. Both are normalized to their maximum in order to be able to compare them. As in the measurements, the strength of the instability is modulated by the variation of the peak density. A waterfall plot of the frequency of the travelling wave is presented in Fig. 4.94 and it can be compared to the measurements Fig. 4.92 In the simulations, the frequency of the travelling wave is more shifted to 900 MHz instead of 700 MHz for the measurements without gamma jump. This is a limitation of the impedance model.

4.10.5 Conclusion

This paragraph was dedicated to the measurements of intensity threshold of the fast vertical instability. The experiment was performed for two working points according to Fig. 4.91b. In one set, ξ_y changes sign around transition energy but not as quickly as the gamma jump. The other set gets a vertical chromaticity slightly negative. Fig. 4.91a shows that the working point strongly changes I_{th}. A convenient way appears to change the vertical chromaticity quickly while the gamma transition jump is performed and gets a negative ξ_y before transition energy and a high positive chromaticity after. The experiments shows that the working point is a strong parameter to cure the fast vertical instability. A scan in $\Delta\gamma_{tr}$ was studied and the results show that the intensity threshold of the instability can be strongly increased while the targeted value of $|\eta|$ is then large. The measurements point out the working point and $\Delta\gamma_{tr}$ are the main parameters to cure the instability.

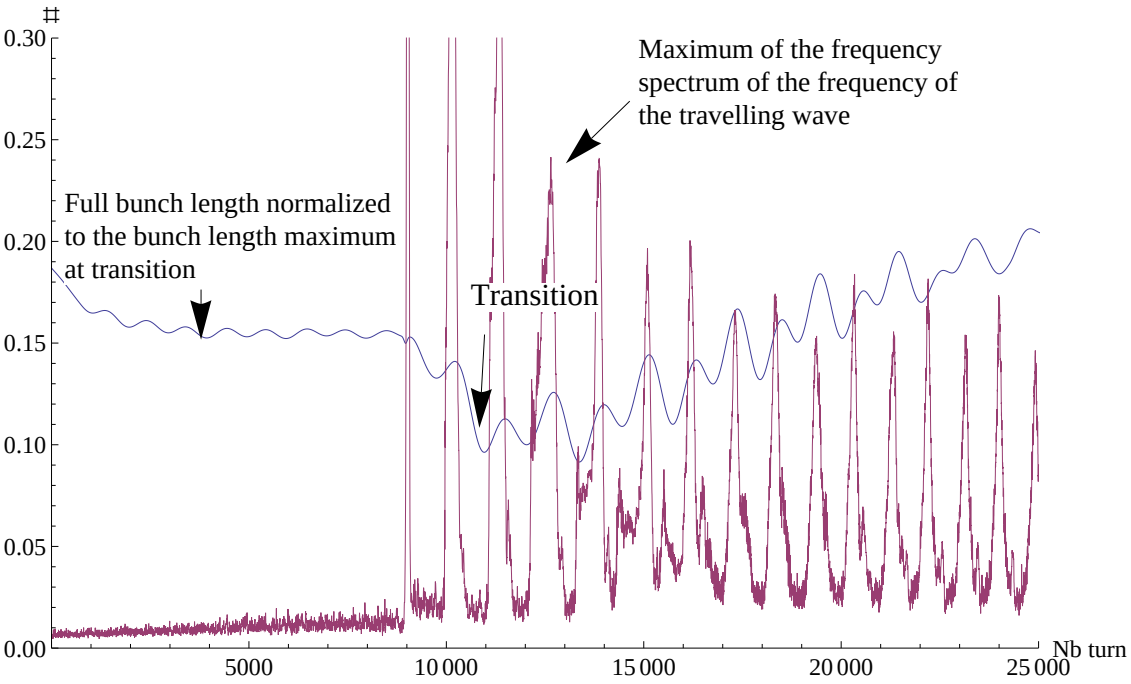

Figure 4.93: Intensity threshold variation with the maximum current applied on the doublets before the γ_{tr}-jump.

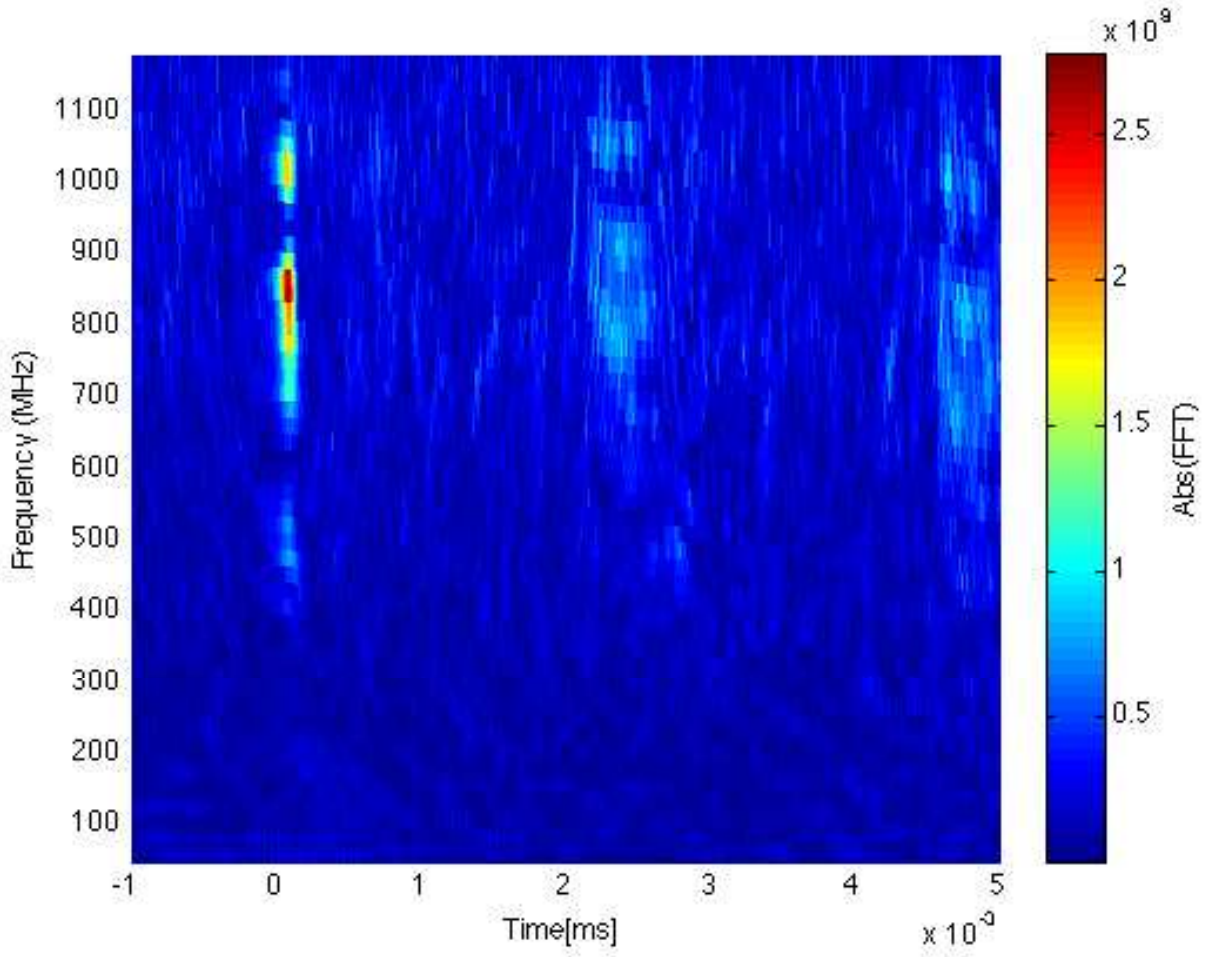

Figure 4.94: Simulated frequency map as a function of time with the γ_{tr}-jump.

4.11 Limitations and open questions

The study of *HEADTAIL* simulations have shown that a simple broadband impedance model cannot matched entirely the dynamics of the fast vertical instability measured in the real machine. However, this very simple impedance model and in particular the measurements can be used in the future to cross check high intensity beam stability with the use of a more complete impedance model.

This section is devoted to present the main limitations of the use of a simple broadband impedance model and of the *HEADTAIL* code with respect to the instability measurements. Several possible improvements for a better understanding of this instability while the beam crosses transition energy are discussed. They contributes also to improve the knowledge of the machine, in particular with the presence of the PFWs to control the working point. This section is meant to provide openings for future works.

Impedance model

The first limitation of the use of a broadband impedance model is that it is certainly not the real impedance of the PS. It is an rough estimation and several formalisms such as BBU and coasting beam formulae [74] were derived with such resonator impedance. However, in first approximation, it reproduces quite well the travelling wave along the bunch with a resonator frequency of about f_r =1 GHz and a quality factor of $Q = 1$. The measurements and in particular those with the gamma jump showed that the wake field is acting as short range, confirming that the quality factor is rather close to 1.

The travelling wave frequency with a gamma transition jump stays around 700 MHz while the simulated frequency is shifted around 900 MHz-1 GHz. This is a difference which can come from the impedance model.

In the simulations, only a resonator impedance has been used, which is purely dipolar, see Sec. 1.4.1. However, as explained in Sec. 1.4.1 and later in Sec.5.8.3, the real impedance consists of a dipolar and a quadrupolar part if the higher order components of the magnetic field are neglected. The quadrupolar part of the wake force produced a dependance of the force of an offset of the trailing particle, which contributes to incoherent effects. Asymmetries in the vacuum chamber can increase the threshold in intensity of transverse instabilities as explained in Ref. [84]. Therefore the difficulty to reproduce the measured intensity threshold and the rise time as a function of the intensity close the intensity threshold, and then I_{th} itself, can come from the fact that only pure dipolar impedance were taken into account. With an impedance model done element by element as in the SPS [36], it will be a good input to study the effect of such impedance on the intensity threshold of the fast vertical instability.

The threshold in η as a function of the beam intensity for a given chromaticity and a longitudinal emittance were determined in both measurements and simulations. In the two cases,

η_{th} grows linearly with the intensity but not with the same slope. η_{th} is proportional to the intensity via the impedance as in the coasting beam formalism but in the measurements, η_{th} is decreasing more rapidly, meaning that when the intensity is going to higher values, the instability will appear at much more earlier energies in the cycle than in the simulations. Therefore the instability reaches more quickly the adiabatic regime than in the simulations. This might come from the impedance model.

Studies are currently ongoing to determine a complete impedance model, element by element, as it is done in the SPS [36]. The different electromagnetic field generated by the beam at different devices such as kicker magnet, are modelized in a simulation code and the wake force is then defined for each element. In parallel, there is a way to identify the different source of impedance. Coherent tune shift measurements can also be done as a function of the beam intensity at different locations of the ring, recording the turn by turn beam position at all the BPMs placed around the accelerator. At each location, the localized transverse tune shift can be then computed and the large $Q_{x,y}$ depressions as a function of the intensity allow to identify and locate the source of impedance. In Sec. 5.8, measurements of the betatron frequency shift with the intensity are presented but for one single BPM and they were used to deduce the value of the imaginary part of the transverse effective impedance at injection and at extraction energy. The work performed for this thesis is not only important to predict threshold in intensity of the instability, but this study can be used also as an important cross check to validate the complete impedance model, when it will be ready. As a conclusion, the first main limitation of this study is the very simple impedance model used in *HEADTAIL*.

Higher order components of the magnetic field due to the PFW

Chromaticity is a good way to increase intensity threshold for at a given η but it appears not to be sufficient to reproduce the measured I_{th} for each longitudinal emittance presented in Fig. 4.24. The simulations provides a good benchmark of the rise time of the instability for a R_s = 0.7 MΩ/m, but an error of about 20% is done on the intensity threshold. This difference can come from mechanisms which damp the instability close to the threshold and can increase I_{th} and most of them are incoherent effect. In particular, octupole magnets are sometimes used as a cure to damp transverse instability as described in Ref. [85]. The octupole field creates a betatron frequency spread due to amplitude-dependent tune shift and thus enhances Landau damping.

The chromaticity measurements show that before and after coming into the nonadiabatic region, the variation of the transverse tune with $\Delta p/p$ is not linear but can be fitted by a parabolic function, meaning that the PFWs induce an octupolar component in the magnetic field and a non-linear coupling between the transverse planes. Since the measurements around transition energy of such parameters is very difficult, it is necessary to evaluate analytically or with the help of magnetic model of a PS main magnet with the PFWs. This is actually under study but not yet finalized [86]. Therefore, the measured matrices for the working point have to use, extrapolated at transition energy. Using MADX-PTC, the multipoles defining

the PFWs in MADX are matched to reproduce the working point and therefore the higher components of the field generated by the PFWs can be deduced. However, it is accurate if the chromaticity is well measured, which is not the case around transition energy. Therefore a complete PS main magnet model is needed to evaluate the octupolar component present during the instability measurements.

To take into account such component of the field, it is then necessary to provide a link between MADX and *HEADTAIL*. In particular case of the simulations with gamma jump, the working point is changed. Tunes, chromaticities and higher components of the field are changing as well. For such simulations, these parameters have to updated turn by turn to take into account the change in optics. The idea would be to perform optics computation with MADX inside the *HEADTAIL* simulations.

Future works on the fast vertical instability have to study the impact of the octupolar component on the dynamics of the instability. The measurements with gamma jump showed that a rapid change in working point helps to increase I_{th}. When the different components of the field will be well defined, it will then possible to use the PFWs to cure the instability with the octupolar component they generated. The disadvantage is that such method decreases the dynamics aperture.

Transverse Space Charge

It is well know that transverse space charge can modify the threshold in intensity of transverse instability, in particular the TMCI [42]. Transverse space charge can create a tune spread, which acts as damping mechanism. Transverse space charge is not well implemented in *HEADTAIL* and works are ongoing to improve it. In this thesis work, no extensive simulations with transverse space charge were performed. The tune shift due to space charge is related to the optics of the machine and in particular to the beam size. The Laslett tune shift are expressed as

$$\Delta Q = \frac{r_p N_b}{(2\pi)^{2/3}\gamma^2\beta\sigma_z}\oint \frac{\beta_{x,y}(s)ds}{\sqrt{\epsilon_{x,y}\beta_{x,y}(s)}(\sqrt{\epsilon_x\beta_x(s)}+\sqrt{\epsilon_y\beta_y(s)})} \tag{4.18}$$

The *HEADTAIL* simulations done in this thesis were done for a single kick of the impedance and the current code does not take into account a change in optics, which would be very useful for the modelization of the fast vertical instability with gamma jump, since the optics is perturbed with the fast quadrupoles and therefore the dispersion and β-function are changed. In the framework of a collaboration between the GSI for the FAIR project and the PS Upgrade team at CERN, fast transverse instabilities measurements at transition energy are planed to study the impact of the transverse space charge on the threshold in instability, by varying for instance the bunch length. Transverse space charge is then an important damping mechanism which is important to evaluate.

4.12 Conclusions

The aim of this study was to perform extensive measurements of the fast vertical instability at transition energy in order to bring a solid experimental part to the previous study done about this subject in Ref. [39]. The dynamics of the instability was studied in detail with and without the application of a gamma transition jump via experiments and macro particle simulations.

The single bunch beams are the most perturbed by this instability. However the goal was also to identify whether this issue would be a limitation for the High Luminosity LHC beam which requires a larger beam current per bunch in the same longitudinal emittance as currently produced by the PS.

Transition is a range in energy in which the beam is very sensitive to wake forces and if the beam current is sufficiently large, instabilities can develop. The reason is that the synchrotron motion is to slow to counteract instabilities faster than the synchrotron period. Synchrotron motion is a way of stabilization by the exchange of the particles between the head and the tail. This is the reason why the fast vertical instability is developing first in the nonadiabatic region.

The experiments showed that the instability grows in the vertical plane. It has been never observed in the horizontal plane, except due to the linear coupling of the machine. By observing the signals of a WCM with an adequate bandwidth, the Δ_y is showing that the particles close to the peak density of the bunched beam are oscillating according to a travelling wave of about 700 MHz while the beam is crossing transition energy. Fast losses occur within a synchrotron period, i.e. in 1 or 2 ms, with $T_s \geq 10$ ms when the beam is in the nonadiabatic region.

The dynamics of the fast instability was studied by acquiring the Δ_y signals on 5000 successive turns for an increasing beam intensity, i.e. for stronger transverse wake forces. The working point was set with the PFWs and a vertical chromaticity plateau was programmed. This was checked by ξ_y measurements well below and above transition energy. However, as explained in Sec. 4.1.2, the chromaticity is hardly measured in nonadiabatic regime. As complement, the decoherence of the beam position due to a vertical kick was observed instead. Smaller is the chromaticity, longer the beam will perform betatron oscillation excited by a angle given by a kicker.

The rise time of the instability was determined as a function of the beam current in the machine and the result showed that higher is the intensity in the bunch, faster the instability is rising. Then, it exists clearly in the measurements a threshold in intensity below which the instability does not develop. The experiment was repeated for several longitudinal emittances, i.e. different peak density and the threshold in intensity of the instability is linearly increasing with the longitudinal emittance. Up to now, the instability was cured by blowing up longitudinally the beam at each increase of the single bunch beam ToF intensity. However, this method has a limit which is the voltage applied on the RF cavities. Currently, 200 kV is the standard voltage during the acceleration of the particles and there is not so much margin any more. The bucket of the ToF beam at $850 \cdot 10^{10}$ is already particularly full. This study was aimed to provide other

ways to increase the threshold in intensity of the instability.

The particularity of this work is that the instability is developing during the acceleration, while many fast transverse instabilities in other machines occur when the energy of the beam is stabilized, i.e. either at injection or extraction. Not only the intensity was a fundamental parameters in these studies, but the momentum compaction η factor is also important. It allows to know at which distance the beam is from the transition energy and η is directly linked to the synchrotron motion, i.e. smaller η is, slower are moving the particles in the bucket: they are then more sensitive to wake forces. At transition energy, $\eta = 0$ and the swap between the head and the tail of the beam, which is a natural way to damp instabilities, vanishes for few turns. Therefore the determination of the momentum compaction factor which triggers the instability is fundamental. It determines whether the instability develops in the nonadiabatic or in the adiabatic regime. The experiments showed that when the beam intensity is close to the threshold and dependently of the bunch length, i.e. here the longitudinal emittance, it starts in the nonadiabatic regime. For each intensity, a threshold in η is measured, and higher is the beam current, higher in absolute value is the threshold in η. The intensity scan stops at the limit of the nonadiabatic zone, but if an error of about 300 turns on the setting of the RF stable phase is considered, higher intensities make the instability develop in the adiabatic region, i.e. while $|T_c| \geq 1$. When the number of protons is increased in the beam, the instability will develop earlier during the acceleration.

Chromaticity in the vertical plane was introduced, i.e. small negative before and small positive after. But it appears that $\xi_y \simeq -0.1$ while $\eta = 0$. The working point is programmed with the PFWs. The intensity scan in this configuration showed that the intensity thresholds increased by 20% with respect to a beam without vertical chromaticity. The thresholds in η are higher as well by a factor 2. The conclusion is that, for each set in chromaticity, thresholds in η are independent of the bunch length. The choice of a working point is therefore an alternative solution to cure the instability instead of changing the longitudinal density.

In order to understand in a deeper way the dynamics of the instability, macro particle simulations were performed with the *HEADTAIL* code. The main goals are to benchmark the simulations with measurements and find an equivalent impedance model which matches as close as possible the measured rise time and intensity thresholds. This is why the code was adapted to reproduce the beam conditions as close as possible to the real machine and the vertical chromaticity change was implemented, since the *HEADTAIL* allows only to do simulations with a fixed chromaticity. The simulations were performed with a simple broadband impedance model since the exact modelization of the PS impedance does not exist yet. The parameters of the broadband resonator with $f_r = 1$ GHz, $Q = 1$, $R_s = 0.7$ MΩ/m were matched to reproduce the travelling wave of 700 MHz which comes from a short range wake field and the order of magnitude of measured rise times are fairly well similar to the measurements. With this model, the intensity thresholds can be reproduced with an error of 20%-40%.

In order to understand this difference, the ratio I_{lin}/I_{th} was introduced. It defines the increase

intensity needed to reach the linear regime of the rise time with respect to the threshold in intensity. This ratio is about 1.5 in the measurements whereas it is 5 in the simulations, meaning that immediately above the threshold, the rise time evolves quickly in the linear regime in which the rise time does not change so such. This difference might come from the impedance model used in the simulations, being different from the real machine impedance model and it can from damping mechanisms, which increase I_{th}. No additional incoherent effects except chromaticity were introduced in *HEADTAIL*, and the presence of betatron tune spread in the calculations does not reproduce the global increase of the threshold in intensity. However, *HEADTAIL* simulations agrees with the measurements by increasing significantly η_{th} with presence of chromaticity: the accelerated intensity becomes larger without developing the instability for the same η with respect to a simulation without ξ_y. This is an important agreement with the measurements. However, the amplitude of the damping is not the same and the evolution of η_{th} with the beam intensity is smaller than in the simulation, explaining then the difference in ratio I_{lin}/I_{th} between the calculations and the experiments. For example, the η_{th} for a beam intensity equivalent to the ToF beam $800 \cdot 10^{10}$ protons is still developing in the nonadiabatic zone ($\eta_{th} \simeq -0.0012$), which disagrees with the measurements. Few comparisons with the formalism coasting beam for fast transverse instability shows that the agreement is good for the simulations but not as good for the measurements by a factor 2 lower in η_{th}.

The next step of this study was to see the impact of a significant increase of η using a gamma transition jump. This allows to cross as fast as possible the transition energy, in such as a way to overtake the rise time of longitudinal and transverse instabilities. Another single bunch beam was set with a gamma transition jump and with two different working points. A zero chromaticity plateau appears to be impossible to do with the current PFWs, therefore a rapid change in chromaticity was programmed from negative to positive values. The intensity thresholds are significantly increased with the gamma jump by a factor 6 as well as the η_{th} also by a factor 6. The γ_{tr}-jump has been implemented in *HEADTAIL* to take into account the perturbation of η-function. As in the measurements, intensity thresholds are much higher by the same order of magnitude. The difference comes from the η_{th}: the instability is triggered at $\eta = 0$ close the threshold in intensity in the simulations. Even with chromaticity and a jump performed in 500 μs, the rise time of the instability is faster. The jump is obviously not fast enough to overcome the instability at $\eta = 0$. No instability is developing while the gamma jump is performed in the measurements, confirming that damping mechanisms, present in the real machine, are not taken into account in the simulations.

Several hypothesis are considered. The first of them is the higher components of the magnetic field generated by the PFWs, such as octupolar components, which can be seen on the chromaticity measurements by a significant term in second order of chromaticity Q''. While ξ_y is rapidly changing, the other components of the magnetic field are changing as well. This might be the reason why the beam is stable while the particles are crossing transition in the experiments with a gamma jump. The application of a Q'' in *HEADTAIL* showed an increase of the rise times. However, more studies with an exact magnetic model of the main PS magnet

and the PFWs is needed to simulate the exact components generated by the PFWs. This is not done by *HEADTAIL*. The other damping mechanism is the transverse space charge which introduces an additional tune spread. The very simple model of impedance could be also a source for the differences observed between the measurements and the simulations.

The goals of the study were to find an equivalent broadband impedance model to benchmark the fast vertical instability measurements performed at transition energy, then check with a gamma transition jump by *HEADTAIL* and by measurements that the intensity thresholds are significantly increasing, and finally study the dynamics of this fast instability. Up to now, the longitudinal emittance blow-up was used as cure, but with this study, we show that the η-jump is by far the most efficient way to damp the instability with the choice of an adequate working point. The intensity threshold could be pushed higher if the different components of the field are controlled, as for example the octupoles. It is well known that they constitute a strong damping mechanism for transverse instability. However, the drawback is the reduction of the dynamics aperture.

Studies are currently ongoing in the framework of the PS Upgrade project to simulate element by element the wake functions and then establish a more exact impedance model. Beyond the fact that this study allows to better understand the PS machine, these measurements can be used as an important support to validate a complete impedance model.

5 High intensity beams issues at Injection

With its 52 years old, the total beam intensity delivered by the CERN Proton Synchrotron continuously increases since its commissioning in 1959. Whereas the total number of protons in the beam was nearly few 10^{10} early in the 60's, this intensity has been multiplied nowadays by a factor 4000 as illustrated in Fig. 5.1. Today the intensity record per bunch is held by the single bunch beam for the nToF experiment with $850 \cdot 10^{10}$ protons whereas the multi bunch beam for the CNGS experiment is accelerated with $2500 \cdot 10^{10}$ protons on 8 bunches at PS injection [12]. With such high intensity, unfavourable effects might occur at low and medium energy such as space charge forces, partly responsible of transverse emittance blow up in low energy machines. The transverse emittance delivered by the PSBooster increases with the number of protons in the bunch due its multi turn injection system [52]. The transverse phase space at injection in PSBooster is "painted" in order to accumulate the required number of protons. Using the betatron oscillations in the phase space of the successive injected beams, the (x, x') and (y, y') planes are filled. Due to non-linearities and Colombian repulsion between the particles (space charge), the beam will occupy after a few turns the full phase space. The direct space charge force is then very strong at PSBooster injection. In the future, LINAC 2 will be replaced by LINAC 4 and a new injection system based on a H^- charge exchange injection, is foreseen allowing to improve considerably the production of beam with higher brightness for LHC beams. Since the number of protons per bunch, and therefore the emittances, has grown over the years, the transverse beam size $\sigma_{x,y} = \sqrt{\beta_{x,y}\epsilon_{x,y}}$ has risen in the same way, meaning that the machine acceptance became smaller. Important beam losses are measured in the CERN PS and the highest spots were identified at extraction [65] and at 1.4 GeV injection energy. In this Chapter, the studies will focus on beam issues at 1.4 GeV only. The large losses induced became a radiation protection problem since a non negligible amount of them are located in a part of the PS ring where the shielding of the tunnel is the weakest. Beyond the irradiation problem, a significant intensity increase is investigated for an experiment similar to the CNGS with an intensity up to $4000 \cdot 10^{10}$ protons. Such increase would required an important improvement of the PS injection efficiency.

The causes of these beam losses will be studied in this chapter. The complete injection system

of the PS will be described in details. The matching of the injection line with respect to the PS ring has been measured in order to identify whether the losses are induced by injection errors and by possible aperture limitations. It appeared that the loss mechanism is composed by two different processes related to the optics of the line and to the PS orbit perturbation at injection. Possible issues due to space charge forces and impedance effects will be considered and for this reason, coherent tune shift measurements were carried out in order to estimate the effective impedance of the CERN PS at injection energy.

Potential cures of the beam losses will be explored such as an increase of the injection kinetic energy from 1.4 GeV to 2 GeV, which would favour space charge effect reduction. The different possible solutions concerning optics upgrade of the transfer line and of the PS ring will also be discussed.

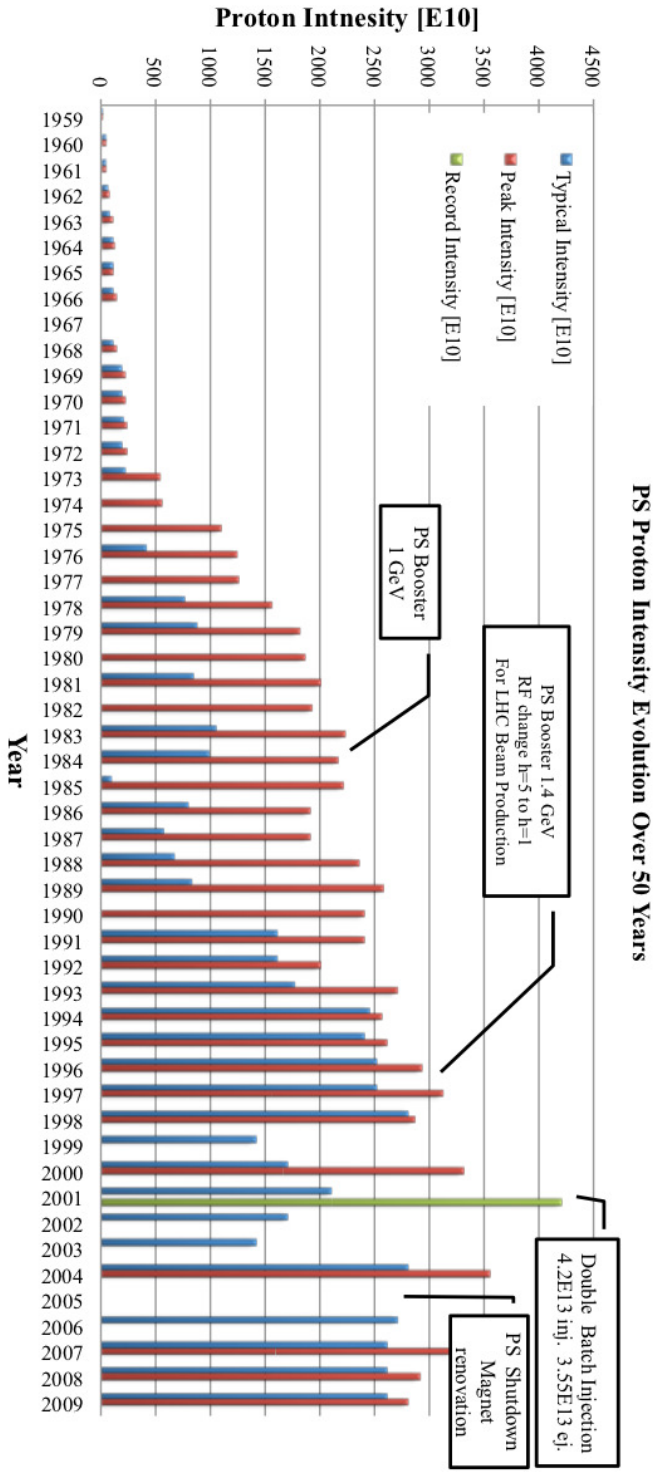

Figure 5.1: Time evolution of the beam intensity delivered by the CERN PS over 50 years [7].

5.1 Single-turn injection system

The injection system is composed by the transfer lines from the Booster to the PS, the BT-BTP line, and by a single turn injection into the Proton Synchrotron. The PSBooster is an accelerator composed by 4 superposed ring from which 4 extraction lines are vertically recombined in order to obtain only one line to inject proton beams into the PS. Fig. 5.2 proposes an overall schematic view of the recombination whereas Fig. 5.6 and Fig. 5.7 show a more detailed layout with the elements composing the lattice of the four transfer lines. The first part of the line is called BT Fig. 5.6 and the second is named BTP Fig. 5.7. The vertical recombination is performed with vertical dipoles - called BVT10, BVT20 and and SMV10, SMV20 in Fig. 5.6 - except the extraction line from Ring 3 being at the same level as the PS. From Fig. 5.6, one can see that Ring 4 and 3 are recombined into BT-Up (BTU) and Ring 1 and 2 into BT-Low (BTL). The resulting lines are merged into one vacuum pipe at the BT-MTV40 Fig. 5.6. After this point, the BT line is splitted in two toward either the measurement line BTM and the ISOLDE experiment, or to the PS through the BTP transfer line (Booster to PS) presented in Fig. 5.7. The switch between the two destinations is made with the help of a horizontal dipole, the BT-BHZ10.

The proton beams are injected from the BTP line into the CERN PS through a septum magnet thanks to a single-turn injection. A schematic layout of the elements is drawn in Fig 5.3. The septum is a special dipole magnet with a thin partition which encloses the deflecting field. The stray field outside the septum, where the circulating beam passes, is made as a nearly zero as possible. A cross section of the PS injection septum is shown in Fig 5.4. In the single-turn injection scheme Fig 5.3, a fast kicker is installed at phase advance $\Delta\mu$ in order to kick the beam on the closed orbit. The kicker is a pulsed dipole magnet with rise and fall times that are short on the time scale of the bunch spacing. The incoming beam is injected with an offset x_s with respect to the closed orbit and angle x'_s. β_s, α_s are the optics functions at the septum noted with the subscript s and β_k, α_k are the optics functions at the kicker noted the the subscript k. The application of boundary conditions at the kickers ($x_k = 0, x'_k = \delta_k$) in the trajectory equations 1.22 determines the subsequent position and angle of the beam at the septum.

$$x_s = \delta_k \sqrt{\beta_k \beta_s} \sin \Delta\mu \tag{5.1}$$

$$x'_s = \delta_k \sqrt{\frac{\beta_k}{\beta_s}} (\cos \Delta\mu - \alpha_s \sin \Delta\mu) \tag{5.2}$$

The trajectory from the kicker must match the design orbit in the septum, so that

$$\delta_k = \frac{x_s}{\sqrt{\beta_k \beta_s}} \frac{1}{\sin \Delta\mu} \tag{5.3}$$

$$x'_s = \frac{x_s}{\beta_s} (\cot \Delta\mu - \alpha_s) \tag{5.4}$$

The kicker strength is usually limited by technology and/or economics, so it is advantageous to make either $\Delta\mu$ close to $\pi/2$, or either large β_k so δ_k is reduced. The disadvantage is the increase of the beam size since $\sigma_k = \sqrt{\epsilon\beta_k}$. In the case of the CERN PS, the offset x_s is large - more than 30 mm - and the needed kicker strength is important. This is why an orbit perturbation - called orbit bump - is additionally used to adjust the closed orbit in the injection region and therefore reduces x_s, as shown in Fig 5.3. The orbit bump is performed with 4 bumpers, noted BSM, presented in Fig. 5.5, which are placed in straight section (SS) 40, 42, 43 and 44. The injection kicker and the septum are respectively located in SS45 and SS42.

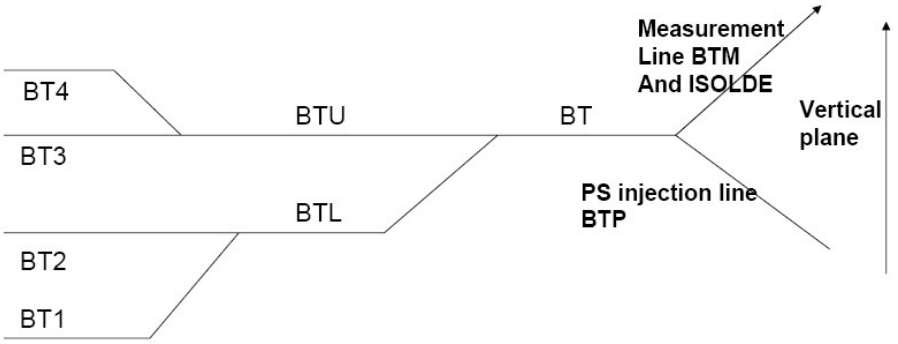

Figure 5.2: Extraction layout.

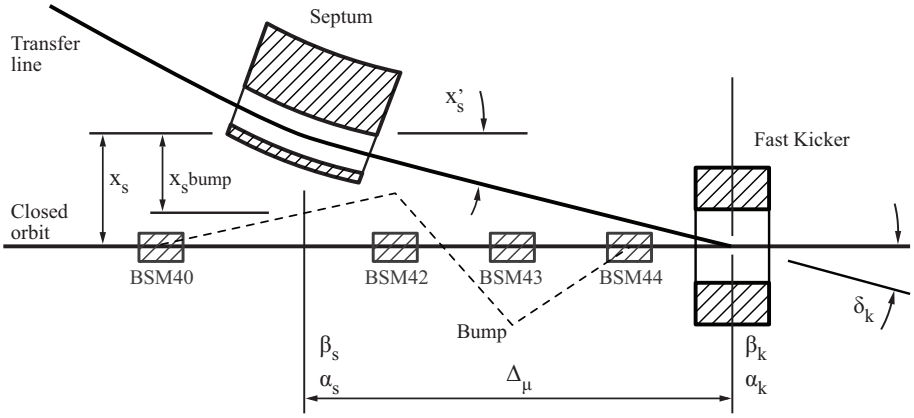

Figure 5.3: Injection closed orbit bump performed with 4 magnets in the CERN PS.

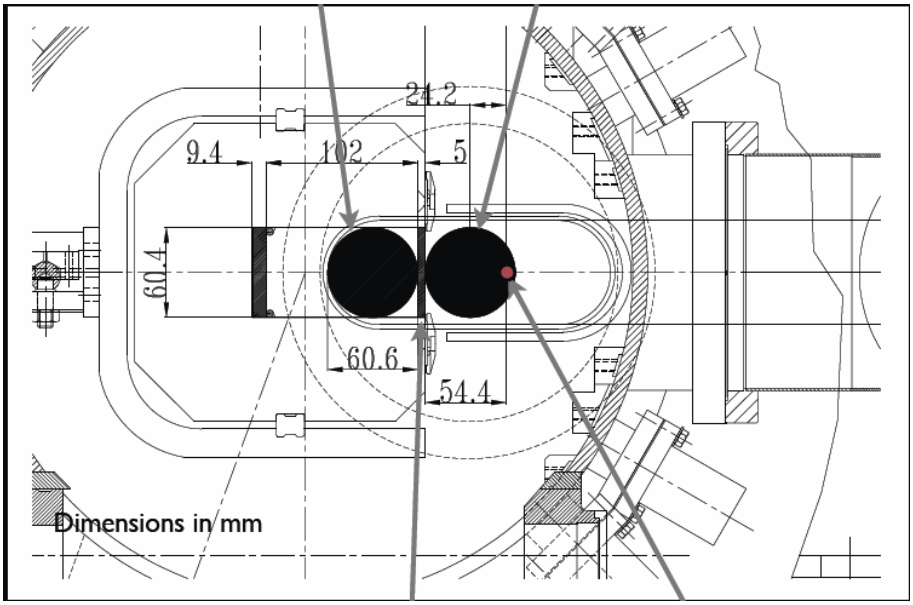

Figure 5.4: Cross section layout of the injection septum. The dipole is divided into two part: one part encloses the magnetic field, bending the particles to inject the beam into the ring. The other part is field free and the circulating beam is going through it every turn. Courtesy to J. Borburgh.

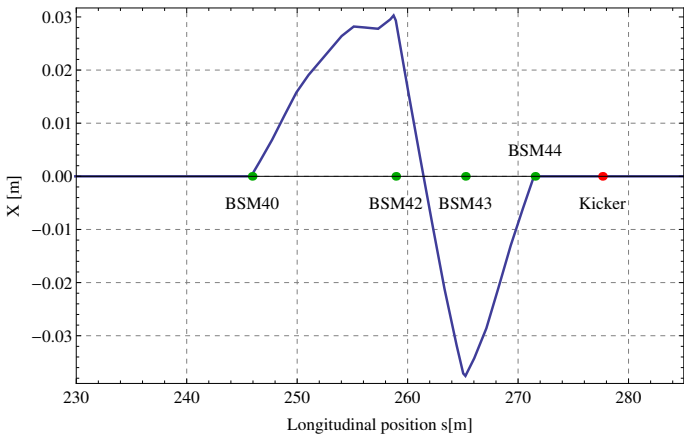

Figure 5.5: Injection closed orbit bump performed with 4 magnets in the CERN PS.

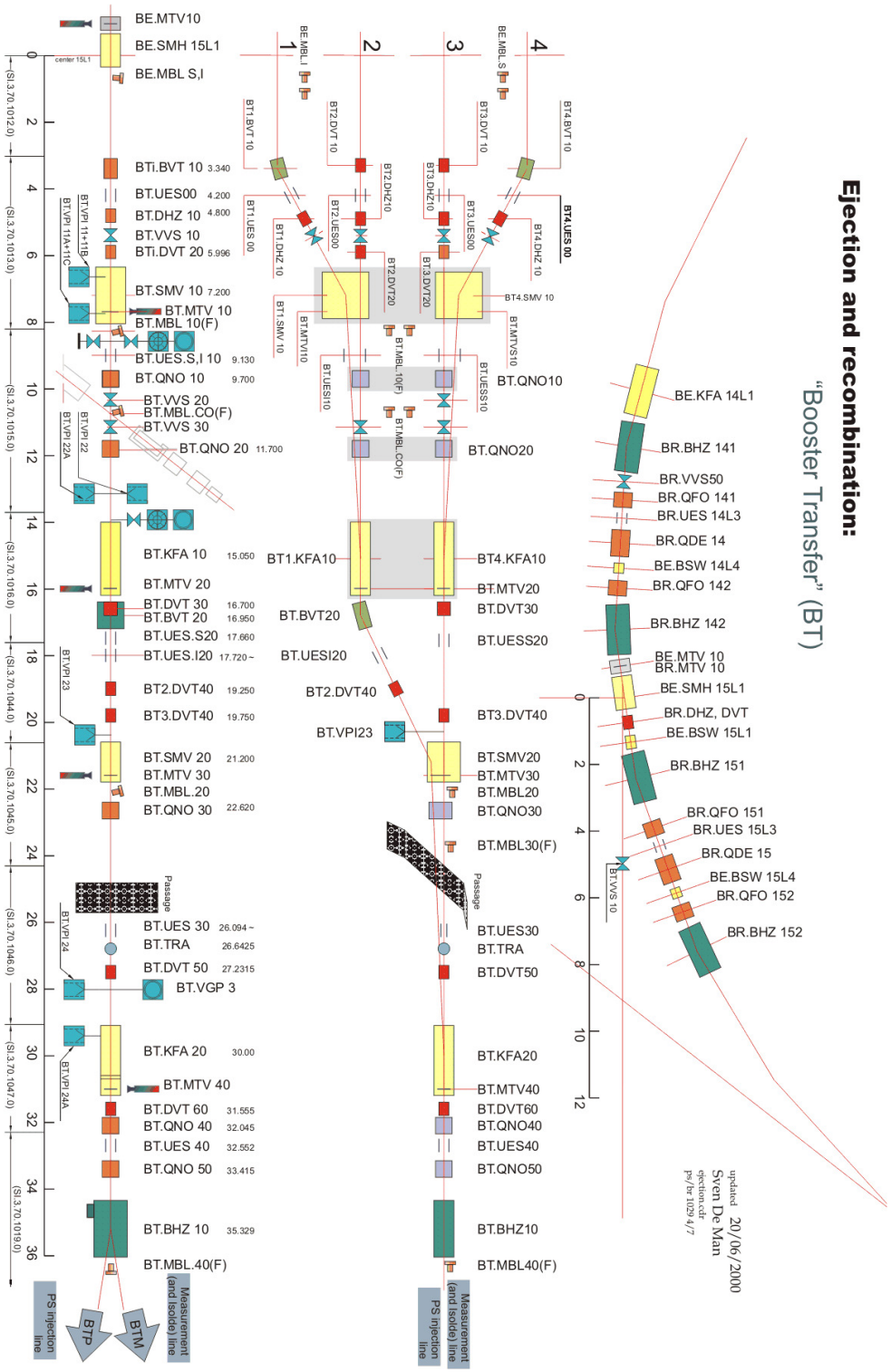

Figure 5.6: PSBooster extraction layout from the PSB to the BT.BHZ10 splitting the transfer line in two: one line is going to the measurement line and the other is continuing to the PS via the BTP line presented in Fig. 5.7. Courtesy to S. De Man.

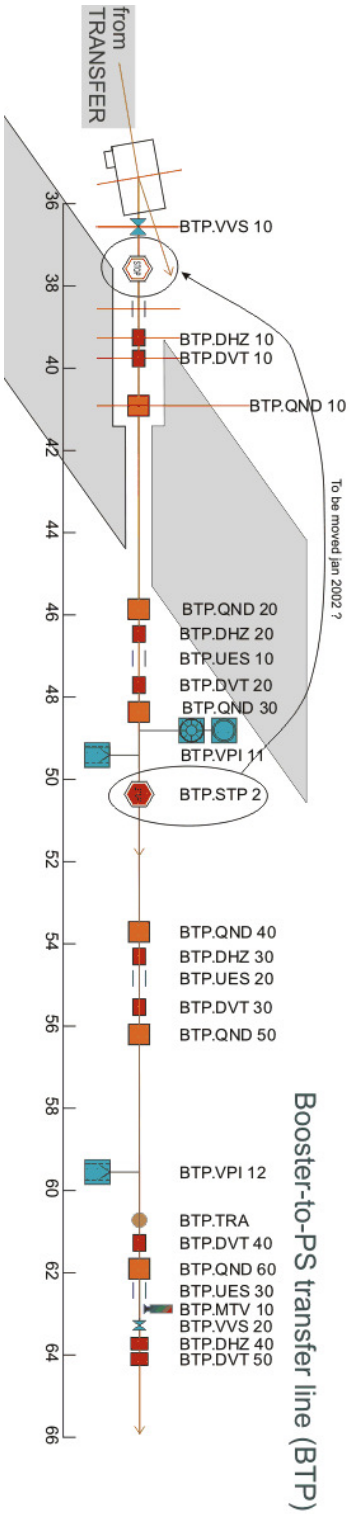

Figure 5.7: PSBooster extraction layout: BTP line (Booster To PS).Courtesy to S. De Man.

Closed Orbit Bump

Orbit bumps are used in accelerator for orbit correction and for the injection/extraction process. In this paragraph, two types of orbit bump are developed:

- the generation of a closed orbit bump with two dipole corrector magnets, the half-wavelength bump, or called also π-bump.

- the 4-magnets bump currently used in the CERN PS at injection.

Half-wavelength bump

A single dipole field perturbation at a fixe given location changes the angle $y'(s)$ of the particles and it can be seen from Eq 5.5. that the betatron oscillation provoked by the dipolar kick δ_1 can be compensated half a wavelength later or at any integer number of the half wavelength, once the excursion is again zero, by a similar dipolar kick δ_2. The excursion and the slope of the oscillation are given by Eq. 1.22,

$$y = a\sqrt{\beta}\cos(\mu + B) \quad \text{and} \quad y' = -a\frac{1}{\sqrt{\beta}}\left[\alpha\cos(\mu + B) + \sin(\mu + B)\right]$$

If the first kick $\delta_1 = y'_1$ is given at $\mu_1 = \pi/2$

$$\begin{aligned} \delta_1 &= -A\frac{1}{\sqrt{\beta}}\left[\alpha\cos(-\pi/2 + B) + \sin(-\pi/2 + B)\right] \\ &= -A\frac{1}{\sqrt{\beta}}\left[\alpha\sin B + \cos B\right] \end{aligned} \tag{5.5}$$

From the boundaries at the kick emplacement $y_1 = 0, y'_1 = \delta_1$, it can be deduced that $B = 0$ and $A = \delta_1\sqrt{\beta_1}$. Then, a second kick δ_2 is placed at $\mu_2 = \pi/2$ at a half-wavelength later where the excursion is again zero. At this point, the oscillation is cancelled by the second kick which equal and opposite to the trajectory slope at this point, i.e. $\delta_2 = -y'_2$ with the following conditions,

$$\begin{aligned} \mu_2 - \mu_1 &= \pi \\ \frac{\delta_1}{\sqrt{\beta_1}} &= \frac{\delta_2}{\sqrt{\beta_2}} \end{aligned} \tag{5.6}$$

The last equations may be generalized for extended bumps of n half wavelengths [4],

$$\mu_2 - \mu_1 = n\pi \quad \text{and} \quad \frac{\delta_1}{\sqrt{\beta_1}} = (-1)^{n+1}\frac{\delta_2}{\sqrt{\beta_2}}$$

The effect of the π-bump can be easily seen in the phase space (y, y') in Fig 5.8a. At a given position, a kick δ_1 is launched to a particle with the coordinates $(0,0) \rightarrow (0,\delta_1)$. After a phase advance π, the excursion goes back to zero and a second kick is applied to compensate the slope at this position. However, the generation of π-bumps requires a lattice phase advance that is an integer multiple of π and the closed orbit correction with this method is therefore very sensitive to optics imperfections and phase errors. Furthermore it is rare the magnets can be placed with a phase advance of exactly π and even if possible, the lattice becomes inflexible for future developments. In the case of the half-wavelength bump, only the amplitude at a certain position is controlled whereas the slope is left as free parameter. The π-bump is therefore limited only to special cases where the phase advance between the dipole corrector magnets is precisely known.

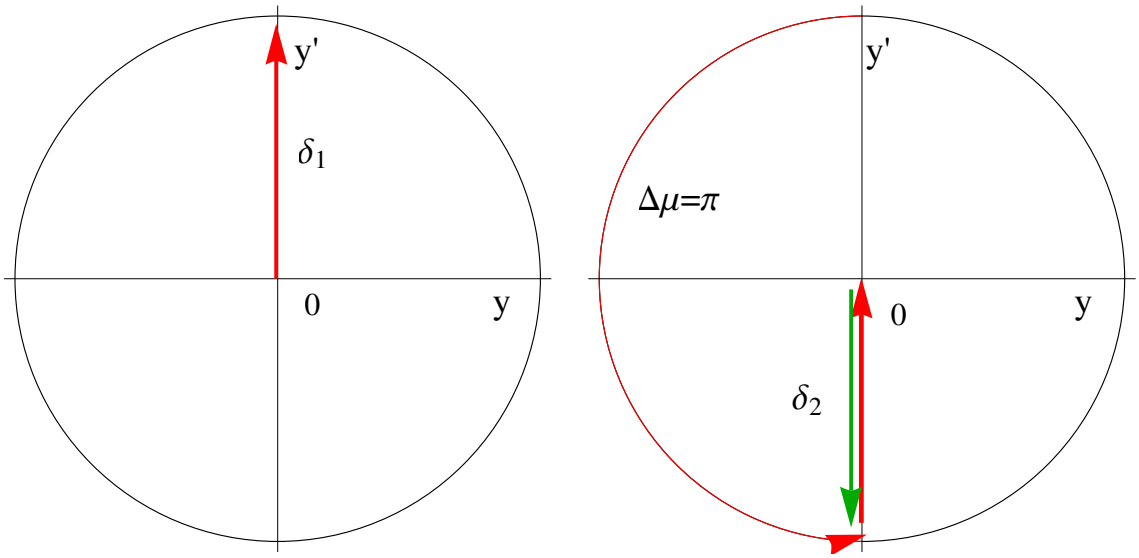

(a) Phase space representation of the π-bump performed with 2 magnets.

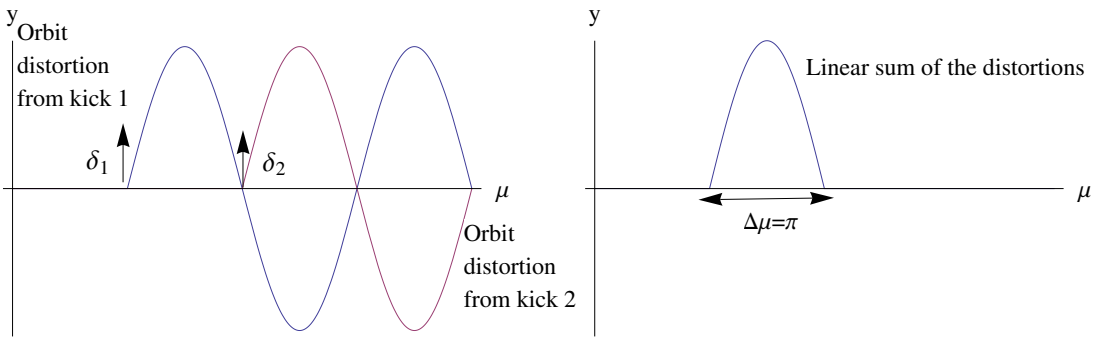

(b) 2-magnet closed orbit π-bump shows as the summation of the closed orbit distortions from the two kicks.

Figure 5.8: Half-wavelength orbit bump principle.

The CERN PS case: 4-magnets bump

In some cases, it is not only important to adjust the closed orbit but also the slope of the closed orbit in a certain location for a number of different optics configuration. Such an operation requires two upstream dipoles - as illustrated in Fig 5.3 - to match the required amplitude $x_s bump$ and the slope x'_s to zero at the last corrector magnet and then two downstream magnets for the adjustment of $x_s bump$ and x'_s at the desired position within the bump. To get the needed kicks for the four corrector bump closure, two conditions are used:

- the trajectory oscillation at the fourth corrector (BSM44 in the case of the PS) must be cancelled.
- the deflection angle at the fourth corrector magnet has the same magnitude but the opposite sign of the canonical momentum due to the first three dipole deflections.

One can derive the conditions for the four corrector bump closure. Denoting the location of the four corrector magnets with (s_1, s_2, s_3, s_4) and the target closed orbit amplitude x_s and slope x'_s at the position s_b and assuming that the position s_b lies in between the position of the second and third corrector magnet ($s_2 \leq s_b \leq s_3$), one can write the condition for closure as [87]

$$\delta_1 = \frac{1}{\sqrt{\beta_1 \beta_s}} \cdot \frac{\cos(\mu(s_b) - \mu(s_2)) - \alpha_s \sin(\mu(s_b) - \mu(s_2))}{\sin(\mu(s_2) - \mu(s_1))} \cdot x_s - \sqrt{\frac{\beta_s}{\beta_1}} \cdot \frac{\sin(\mu(s_b) - \mu(s_2))}{\sin(\mu(s_2) - \mu(s_1))} \cdot x'_s \tag{5.7}$$

$$\delta_2 = \frac{1}{\sqrt{\beta_2 \beta_s}} \cdot \frac{\cos(\mu(s_b) - \mu(s_1)) - \alpha_s \sin(\mu(s_b) - \mu(s_1))}{\sin(\mu(s_2) - \mu(s_1))} \cdot x_s - \sqrt{\frac{\beta_s}{\beta_2}} \cdot \frac{\sin(\mu(s_b) - \mu(s_1))}{\sin(\mu(s_2) - \mu(s_1))} \cdot x'_s \tag{5.8}$$

$$\delta_3 = \frac{1}{\sqrt{\beta_3 \beta_s}} \cdot \frac{\cos(\mu(s_4) - \mu(s_b)) - \alpha_s \sin(\mu(s_4) - \mu(s_b))}{\sin(\mu(s_4) - \mu(s_3))} \cdot x_s - \sqrt{\frac{\beta_s}{\beta_3}} \cdot \frac{\sin(\mu(s_4) - \mu(s_b))}{\sin(\mu(s_4) - \mu(s_3))} \cdot x'_s \tag{5.9}$$

$$\delta_4 = \frac{1}{\sqrt{\beta_4 \beta_s}} \cdot \frac{\cos(\mu(s_3) - \mu(s_b)) - \alpha_s \sin(\mu(s_3) - \mu(s_b))}{\sin(\mu(s_4) - \mu(s_3))} \cdot x_s - \sqrt{\frac{\beta_s}{\beta_4}} \cdot \frac{\sin(\mu(s_3) - \mu(s_b))}{\sin(\mu(s_4) - \mu(s_3))} \cdot x'_s \tag{5.10}$$

with $\beta_1, \beta_2, \beta_3, \beta_4$ and β_s the beta optics functions at the corrector magnets (BSM40, BSM42, BSM43, BSM44) and at the observation point s, here the injection point, α_s is the twiss optics function at the location s, μ the phase advance. The bare optics function of the CERN PS are presented in Fig. 5.9a and Fig. 5.9b.

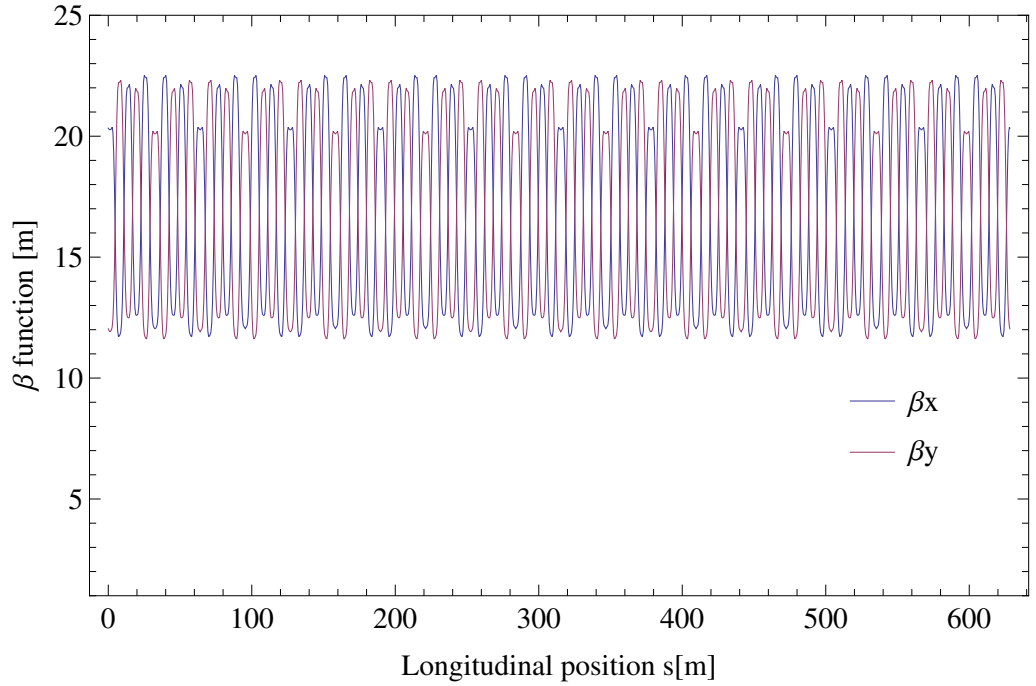

(a) Periodic β functions of the CERN PS.

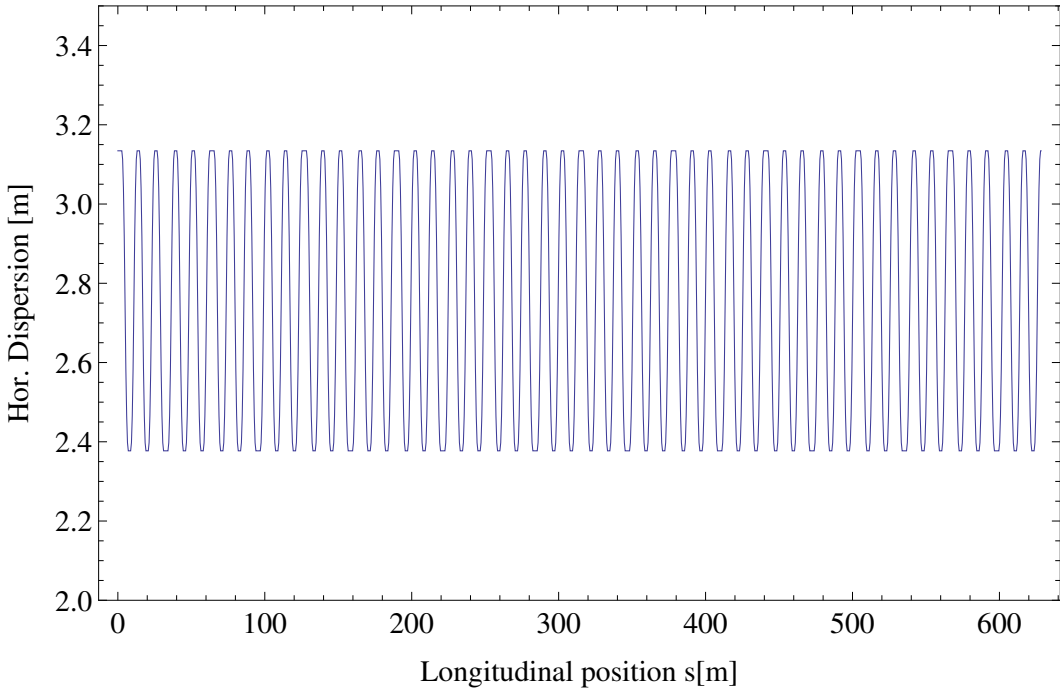

(b) Periodic dispersion function of the CERN PS.

Figure 5.9: Periodic optics functions of the CERN PS.

5.2 Loss Pattern Measurements

The first step in the understanding of the proton losses at the PS injection is their measurements with Beam Loss Monitors (BLMs) around the injection area. This experiment was also performed in the framework of the renovation and the upgrade of the beam loss detection system [88]. The improvement of the performances in speed to be able to monitor beam loss on a bunch-by-bunch basis and in long term stability to reduce or avoid the need for periodic calibration are aimed for. Two kinds of BLMs were available during the experiment, the so-called ACEM detectors which is the current system installed in the ring and LHC ionization chambers which is the beam loss monitor system used in LHC.

ACEM BLM

The ACEM active part is composed by a glass vacuum tube with a thin aluminum sheet as a cathode and, next to the cathode, a 10-stage electron photomultiplier (CsSb) [89]. Secondary particles produced by the beam loss interacts with the cathode, where electrons are produced and directed toward the first stage of the photomultiplier, to reach a maximum multiplication factor 10^6. The ACEM BLM has a fast time response and a high sensitivity, but its small size provide a small solid angle coverage of the beam loss particle shower and the detectors saturate with large losses.

LHC Ionization chamber or LHC BLM

LHC ionization chambers are currently in use in the LHC as part of the machine protection system [90]. The detectors are ionization chambers with parallel aluminium electrode plates, forming a very large volume of about 1.5 liter filled with nitrogen gas at 1100 mbar. These detectors have a slow time response, about 89 μs, due to the drift time of the ions in the gas which is about 300 μs, whereas the electron have a drift time of only about 100 ns. Their sensitive volume provides a very large solid angle coverage. They do not require regular calibration.

Proton Loss Experiment

The ACEM are the BLMs used in the PS and they are spread around the ring, installed in each straight section on the top of a main magnet unit. A LHC-type BLM was installed beside the injection septum and on the top of a main magnet and in straight section 43. The signals of the BLMs placed around the injection bump, i.e. the BLMs of the straight sections 42-43-44, noted BLM42, BLM43, BLM44, were directly connected to an oscilloscope in addition to the LHC-type BLM signal in SS42 and in SS43, noted LHC-BLM42 and LHC-BLM43. The signal of the ACEM BLM 45 standing close to the kicker was acquired as well. A trigger was set at the injection timing in order to record the BLM signals during several millisecond after the beam is injected into the ring. Fig. 5.10 shows the ACEM BLM42 signals for two high intensity beams

with the characteristics of Table 5.1, respectively in Fig. 5.10a for the single bunch beam ToF beam and in Fig. 5.10b for the multi bunch CNGS beam.

The acquisition is performed while the beam passes through the septum exactly at injection. The revolution period of the beam at 1.4 GeV is about 2.3 μs. A loss is observed in both case when the beam goes through the injection septum. A structure of 8 peaks in the loss signal is measured for the CNGS beam in Fig. 5.10b, presuming that the ACEM BLM is able to measure bunch-by-bunch losses. To confirm that the pattern corresponds to the loss of each of the 8 bunches, Fig. 5.11a for the ACEM BLM42 and Fig. 5.11b for the ACEM BLM43 compare the loss signal structure to the the longitudinal profile of the multi bunch beam. The same analysis is done for the single bunch beam in Fig. 5.11c and in Fig. 5.11d leading to the conclusion that the ACEM BLMs are able to distinguish the losses bunch-by-bunch. From Fig. 5.11, on can observe that beam losses are measured while the beam enters in the machine through the septum, i.e. where the orbit perturbation is close to the maximum, but also in SS43 which is the minimum of the injection bump, as shown in Fig. 5.5.

Beam id.	Nb. of bunches	Tot. Intensity 10^{10}	Bunch Length [ns]
ToF	1	850	≃234
CNGS	8	2300	≃173

Table 5.1: Summary of characteristics of the ToF and CNGS beams.

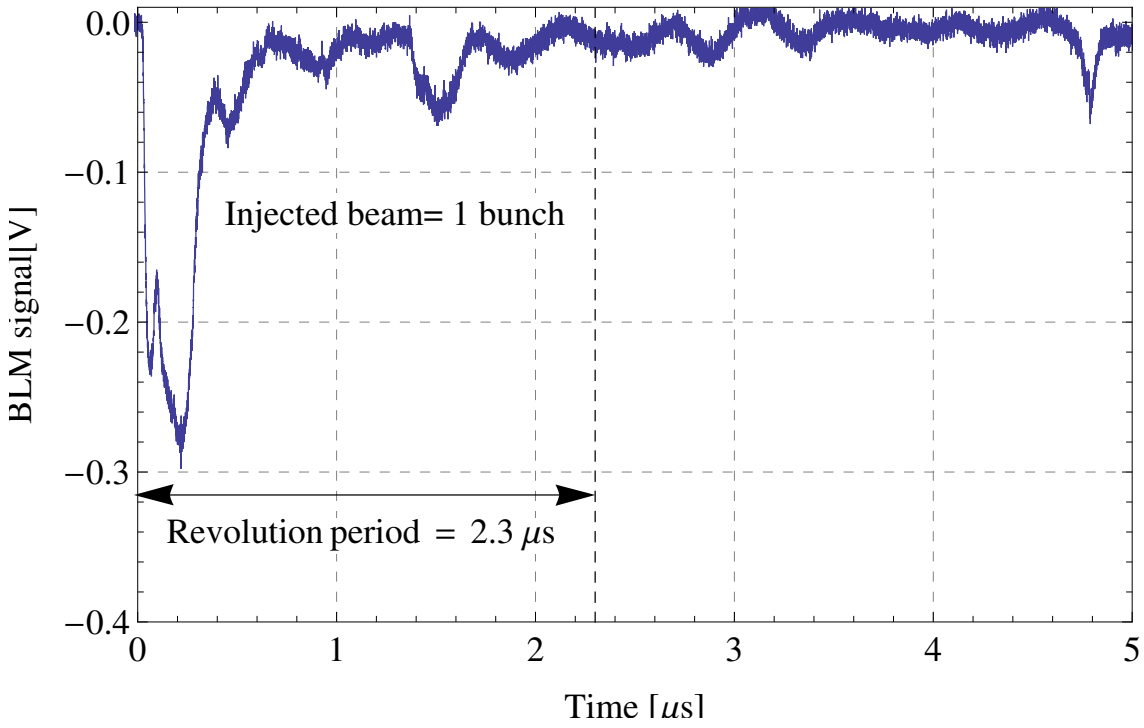

(a) ACEM BLM signal in SS42 for the single bunch beam ToF.

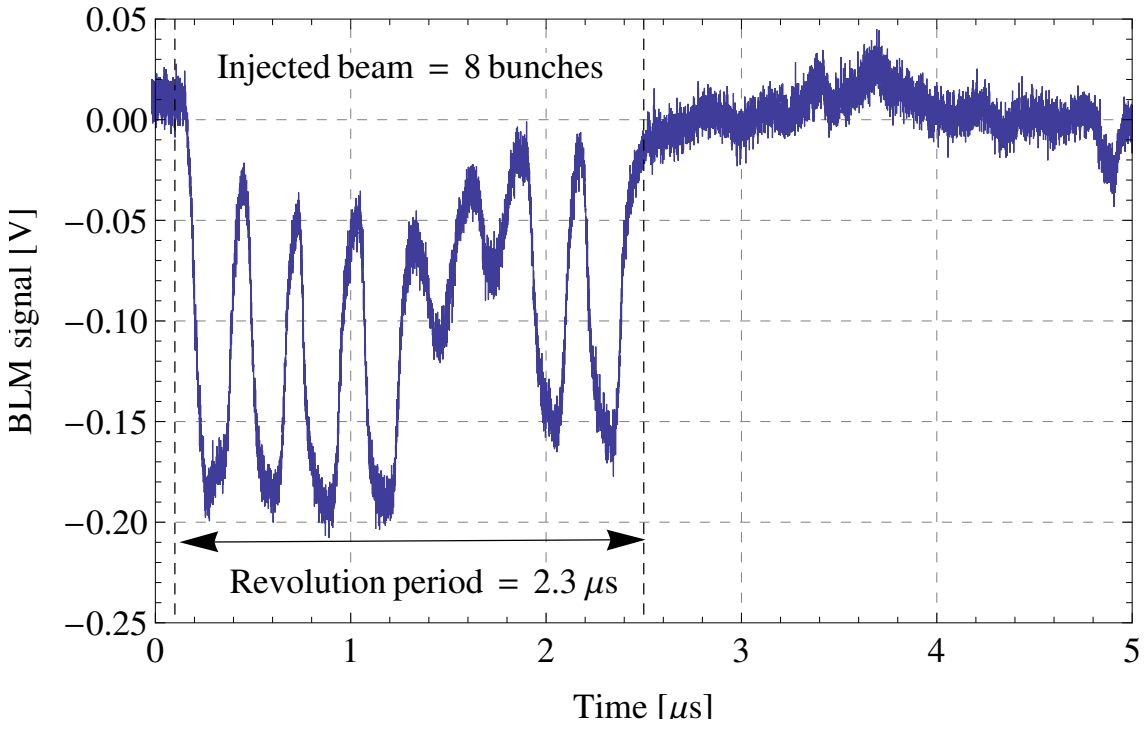

(b) ACEM BLM signal in SS42 for the multi bunch beam CNGS.

Figure 5.10: ACEM BLM42 signals close to the septum at injection for a single bunch and a multi bunch beam.

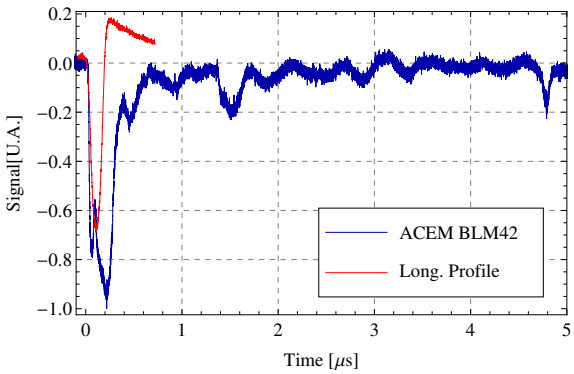

(a) ACEM BLM signal SS42 for ToF.

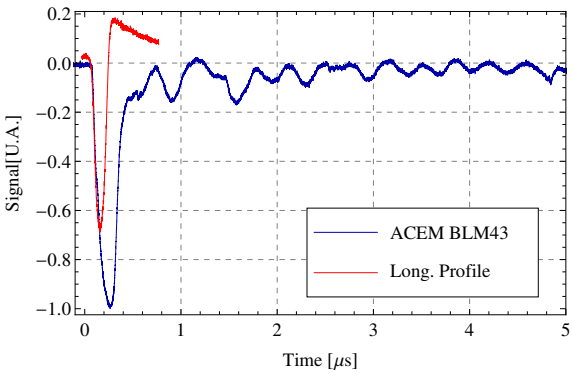

(b) ACEM BLM signal SS43 for ToF.

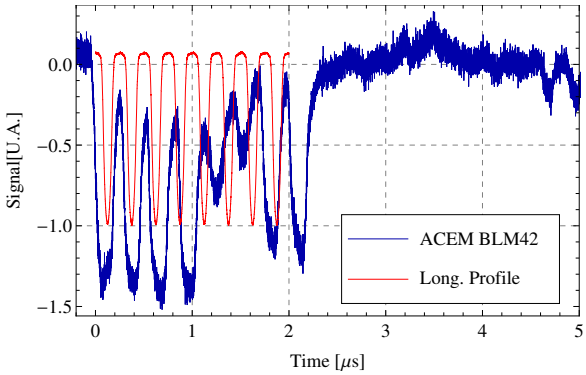

(c) ACEM BLM signal SS42 for CNGS.

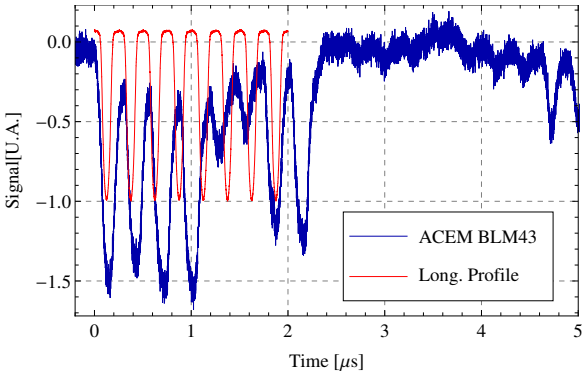

(d) ACEM BLM signal SS43 for CNGS.

Figure 5.11: ACEM BLM42 and BLM43 signals at injection for a single bunch and a multi bunch beam compared to their respective longitudinal profile.

The availability of two kind of detector allows to compare their signals in order to choose the most suitable BLM between the ACEM and the LHC-type. Fig. 5.12 compares the signal of the ACEM BLM42 to the signal of the LHC BLM42 during the first turn for the CNGS beam. The loss structure due to the 8 incoming bunches measured with the ACEM BLMs in Fig. 5.11c is hardly observed with the LHC-BLMs. In addition, the delivered signal is less sensitive than the signal acquired by the ACEM BLMs.

The next experiment requires to observe the beam losses over a longer acquisition time. Again the signals of the ACEM BLM42 is compared to the signal of the LHC-BLM42 during the 6th first turns after injection. Fig. 5.14a and Fig. 5.14b show that small losses are measured by the ACEM BLM42 turn by turn after injection whereas they are hardly detected by the LHC BLM. In conclusion, the LHC BLM does not seem to be the most suitable solution to replace the current ACEM BLM system of the CERN PS due to a lower sensibility to an equivalent loss and its inability to distinguish between bunches. Indeed, this is due to the drift time of the ions produced in the ionized gas of the detector, too long ($1/2 \times 300\ \mu s$ and $1/2 \times 100\ ns$) compared to the bunch spacing of about 170 ns in the case of the multi bunch beam CNGS.

The next experiment consisted of recording the ACEM BLM signals during the fall time of the injection bump for the two high intensity beams. The signal of the BLMs is not calibrated. The results are presented in Fig. 5.15a and in Fig. 5.15b respectively for the CNGS and the single bunch ToF beam. The losses are mainly observed turn by turn on the BLM 42 and 43 for the single bunch and on the BLM 43 for the multi bunch. This difference can come from the way how the beam is operated (steering at injection for instance). However, all the BLMs after the injection point record a signal either by a real loss at the location of the detector or due to a shower of secondary particles resulting of the interaction of beam with the vacuum chamber. The duration of the losses can be compared to the fall time of the orbit bump after injection of the beam presented in Fig. 5.13. It shows the signal with respect to time of the current powering the bumpers. The beam is injected at the maximum of the BSM current and their fall time is about 1 ms. A correlation can be seen between the duration of the losses and the fall time of the injection bump, meaning that the beam tail might be lost in the vacuum chamber due an aperture restriction. Once the injection bump collapses, the BLMs do not record such signal.

Since most of the losses of injection are observed in the straight section surrounding the orbit bump, in particular SS42 and SS43, the perturbation of the orbit presented in Fig. 5.5 might cause an aperture restriction and some part of the beams probably hit the vacuum chamber. If the tails of the transverse distribution are cut, according to the tune, i.e. the number of betatron oscillation performed in the phase space, the losses should stopped after few turns, 8 for the ToF beam with Qx about 6.11 and 6 turns for CNGS with Qx about 6.17. The Fig. 5.15a and in Fig. 5.15b show that the losses are slow and continue along the fall time of the orbit bump. Suppose that the particles are lost due an aperture restriction in the horizontal plane, the horizontal phase space is refill in few turns due to non-linearities inside the bunch which repopulate the transverse phase space. In particular, a periodic structure of about 10 turns

modulates the loss pattern of the ToF beam.

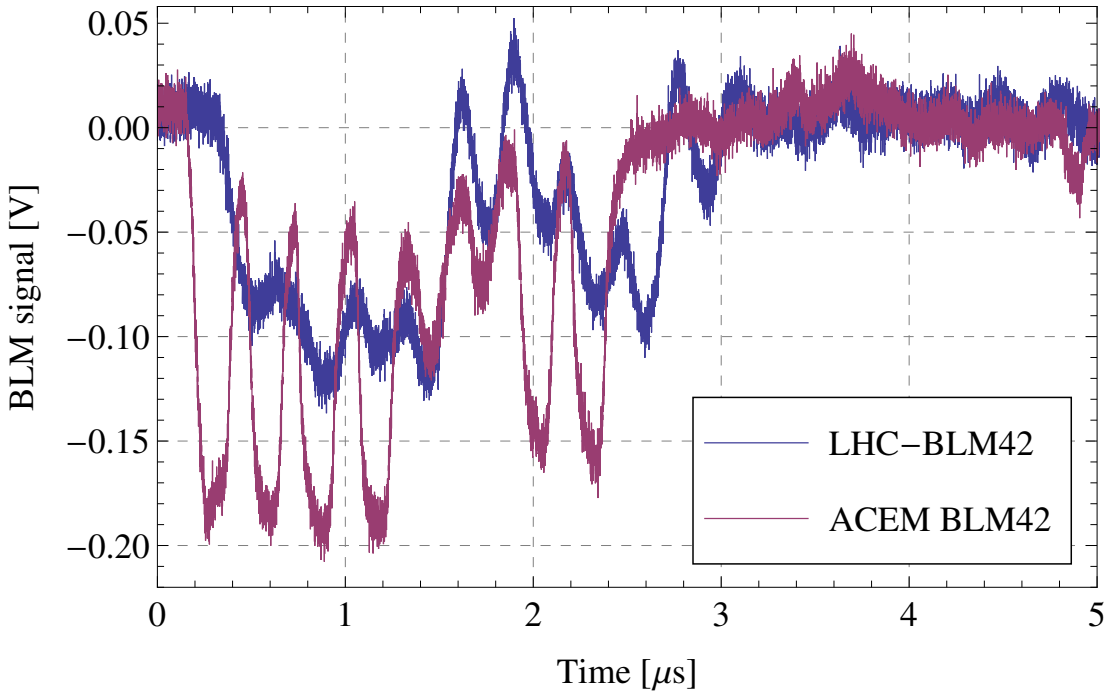

Figure 5.12: ACEM BLM42 signal compared to the signal of the LHC-BLM42 at injection.

Several hypothesis can be made in order to explain the injection losses:

- A mechanical aperture restriction might be the source of the first large beam loss observed in Fig. 5.12 while the beam passes through the septum.
- A particle beam going through a transfer line has to be injected with the same optics parameters β, α and dispersion as those of the ring. Otherwise, the phase space of the incoming beam is mismatched with the transverse phase space of the ring, provoking then emittance blow up, which might reduce the machine transverse acceptance. In addition, it is well know that the transfer line from the PSBooster to the PS - named BT-BTP line - operates with a mismatch in horizontal dispersion. Optics measurements are then needed at injection in order to establish the optical mismatch between the BT-BTP line with respect to the CERN PS.The next paragraph will be dedicated to optics measurements in the line and at injection of the PS.

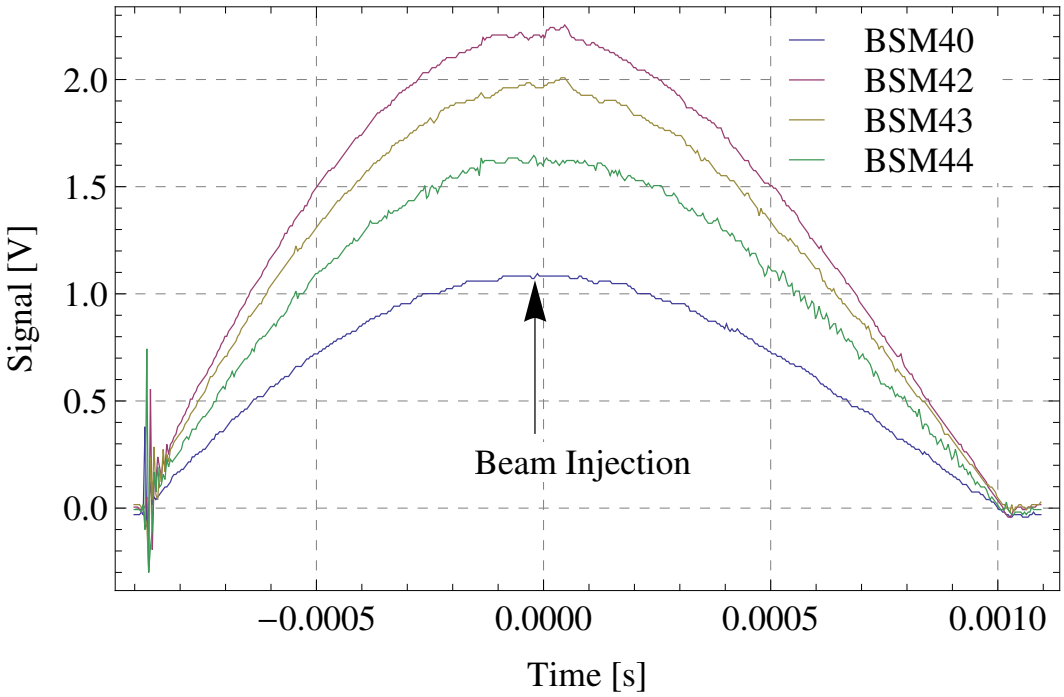

Figure 5.13: Signals of the bumpers BSM 40, BSM 42, BSM 43, BSM 44 as a function of time. The beam is injected at the maximum of the voltage.

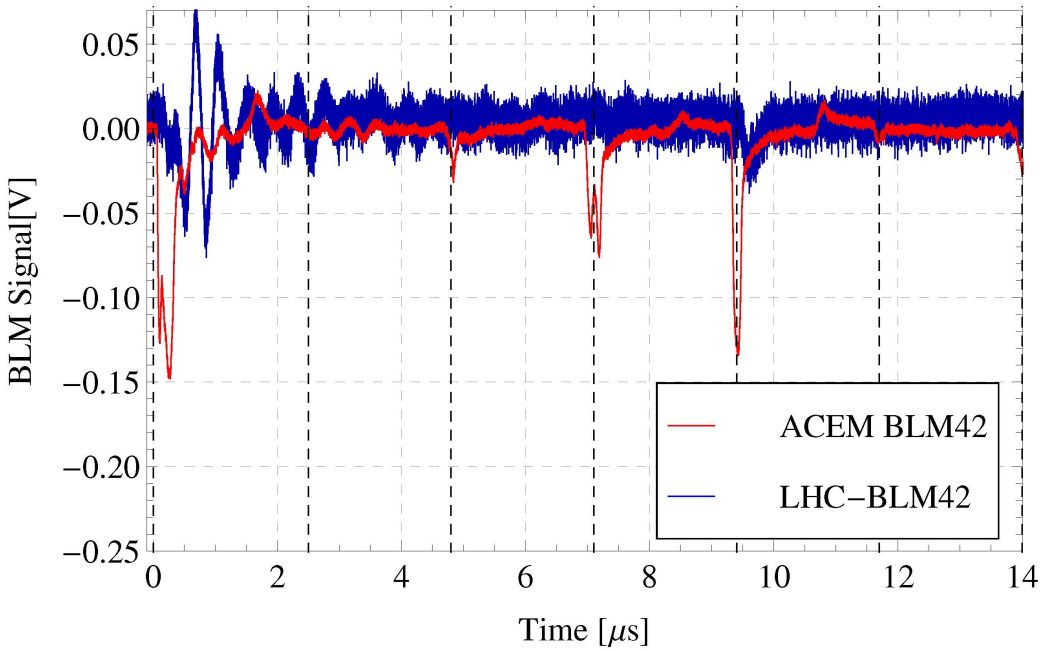

(a) Single bunch beam ToF.

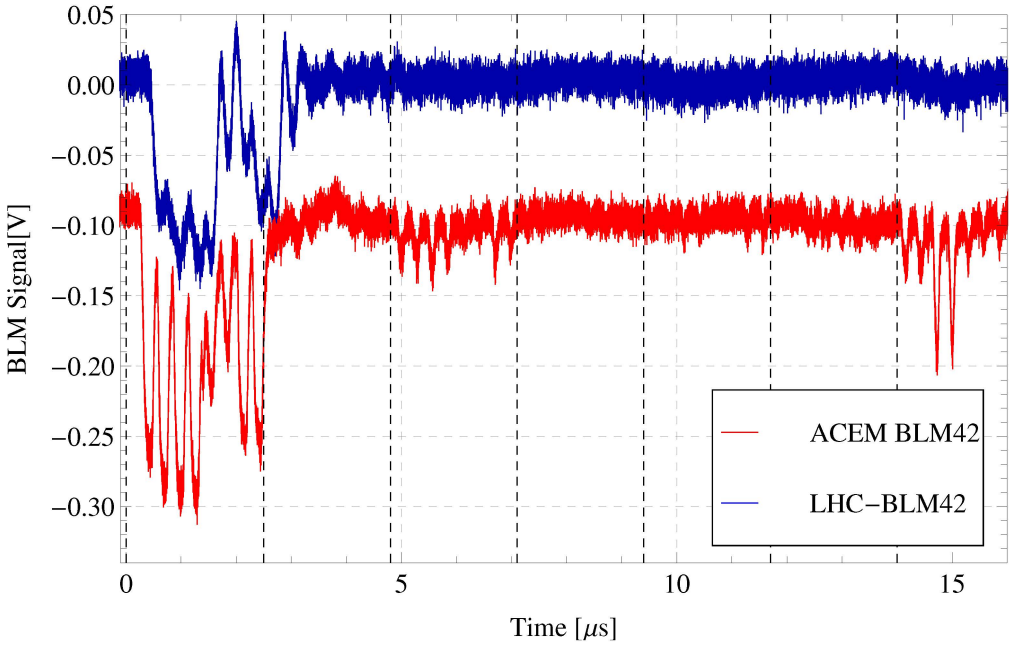

(b) Multi bunch beam CNGS.

Figure 5.14: ACEM BLM42 signals compared the signal of the LHC-BLM42 on the 6th first turns after injection for the single bunch beam and the multi bunch CNGS. Turn by turn losses are observed on the ACEM BLM in both cases where they are not detected by the LHC-BLM. The offset between the traces is an artificial offset to distinguish the signals.

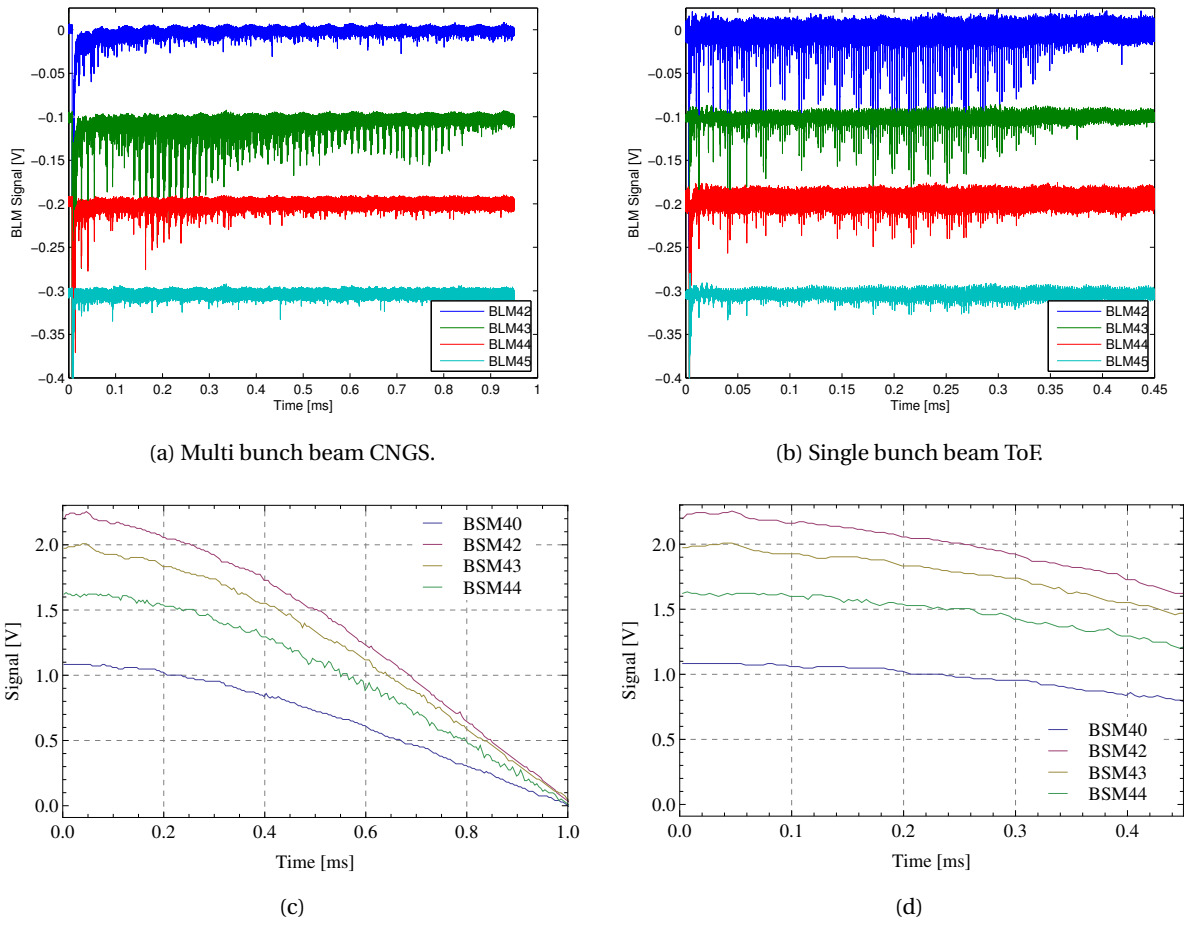

(a) Multi bunch beam CNGS.

(b) Single bunch beam ToF.

(c)

(d)

Figure 5.15: ACEM BLM signals measured during the injection bump for the single bunch beam and the multi bunch CNGS. Turn by turn losses are observed in both cases.

Conclusion of the experiment

Proton beam losses were measured with two different detectors, the ACEM BLM system, currently in use in the PS ring and ionization chambers in operation in the LHC. It appears that the ACEM are still the most convenient detectors. They have to be replaced since their signal is easily saturated for the beam losses occurring at extraction in the PS [65]. The experiment shows also that the losses at injection occur first while the proton beam passes through the septum and then turn by turn, in particular the larger losses are recorded at the BLM 42 and BLM 43. Fig. 5.5 shows that SS42 and SS43 are the sections in which the orbit perturbation due the injection bump is larger. The beam is therefore performing a large excursion and a reduction of the machine acceptance at these points is expected. The turn by turn losses could not be measured by acquiring only the LHC-BLM signals since they did not detect these losses. The next paragraph is devoted to optics measurements in the transfer line BT-BTP and at PS injection, aimed to measure the optics mismatch of the line with respect to the CERN PS and establish possible aperture restrictions due the orbit bump.

5.3 BT-BTP injection line matching

The tight emittance budget imposed to the LHC injector chain and the increasing request for high intensity beams for fixed-target physics requires a careful monitoring of the emittance and of the mismatch at injection during setting-up and normal operation. Optics mismatch between transfer lines and rings is a cause of transverse emittance blow up during the injection process. The phase space (x, x'),(y, y') at the end of the transfer line must be identical to the phase space of the ring at the injection point in order to avoid any blow up and respect the emittance budget, critical for LHC beams in particular. In the following paragraph, it will be explained the causes and the effects of an optics mismatch. Then measurements applied to the transfer line BT-BTP and the CERN PS are presented aiming to evaluate the emittance blow up due the injection process. This might reduce the acceptance of the machine and caused aperture restriction which could induced beam losses such as those measured on high intensity beams at injection, as described in the Sec. 5.2.

The periodicity of a circular machine imposed the same periodicity to the Twiss parameters α, β, γ and they are determined as unique. If the coordinates of a particle is sampled on successive turns the points will describe an ellipse in the phase space (x, x') and (y, y'). Only one set of triplet value α, β, γ will fit that ellipse and they derived from the matched single-turn transfer matrix. It is the periodicity of the machine which ensures that this ellipse is constant turn after turn and for this reason is called the *matched ellipse*. Let suppose now that a beam is injected with a distribution in phase space which does not have the same form as the matched ellipse and is defined with different Twiss parameters $\alpha_m, \beta_m, \gamma_m$. The circular machine will not faithfully return this ellipse after some turns. Instead the initial ellipse will turn round to get a larger ellipse than the matched one. In a linear system, the original ellipse defined by the distribution of the particles would turn round during an indefinite period inside the envelope of the matched ellipse and it would maintain its elliptical shape and area as if the circular accelerator would be a transfer line with an infinite length. However, in real lattice, non-linearities are always present which cause an amplitude frequency dependence and distort the ellipse by filamentation as illustrated in Fig. 5.16 [4]. After several turns, the beam is apparently uniformly distributed around the matched ellipse and the beam emittance has been increased. This is called dilution of the phase space by filamentation [91].

A transfer line does not have the constraints of periodicity. The beam passes only once and the shape of the phase space ellipse at its entrance determines the shape at the exit. The Twiss parameters then obtained depend on the input beam and on the lattice of the line itself and for a single particle, there will be an infinite set of α, β which could describe its motion in the line. Therefore the optics mismatch is a deviation of the optics, as seen by the beam, with respect to the model. Mismatch in the Twiss parameters α and β as well as in dispersion D and its derivative D' might occur. This can be represented in the normalised phase space

(x_n, x'_n) [11],

$$x_n = \frac{x}{\sqrt{\beta}} \tag{5.11}$$

$$x'_n = \frac{\alpha}{\sqrt{\beta}} x + \sqrt{\beta} x' \tag{5.12}$$

and for the dispersion

$$D_n = \frac{D}{\sqrt{\beta}} \tag{5.13}$$

$$D'_n = \frac{\alpha}{\sqrt{\beta}} D + \sqrt{\beta} D' \tag{5.14}$$

The phase space representation for a matched beam in normalized coordinates is a circle. Fig. 5.17 represents a mismatched beam with both betatron (or dispersion) and injection offset $(\Delta x_n, \Delta x'_n)$ mismatch [11]. A large part of this chapter is dedicated to optics measurements in the BT-BTP transfer line and in the PS ring.

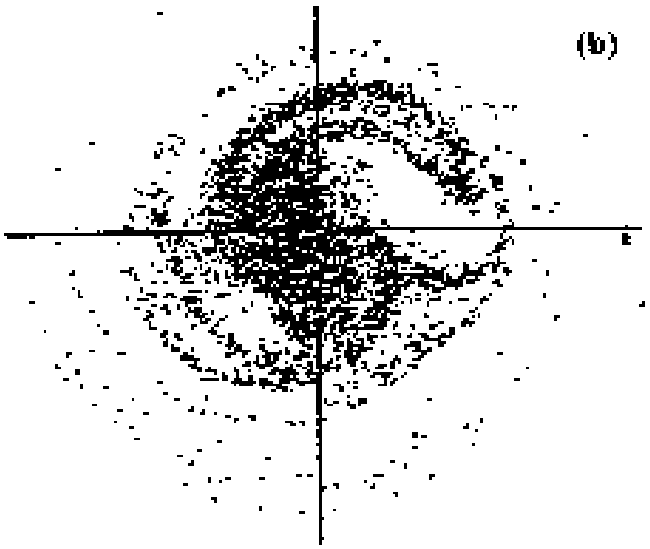

Figure 5.16: Filamentation of the transverse phase space for a unmatched beam. [4].

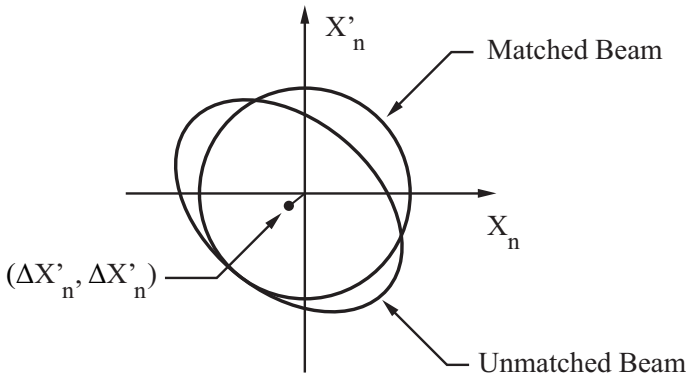

Figure 5.17: Representation of a matched and an unmatched beam (betatron or dispersion mismatch) with injection-offset in normalised phase space [11].

5.3.1 Dispersion Measurements

The momentum spread σ_p of a beam is not null. Particles with non-nominal momentum have different trajectories with respect to the reference particle having the nominal momentum as a result of different radii of curvature when passing through a dipole and the different focusing strength of quadrupoles. The dispersion function $D(s)$, with s the longitudinal position along the accelerator, is defined as [11]

$$\Delta x(s) = D(s)\Delta p/p + \frac{1}{2!}D^{(2)}(s)(\Delta p/p)^2 + \frac{1}{3!}D^{(3)}(s)(\Delta p/p)^3 + ... + \frac{1}{n!}D^{(n)}(s)(\Delta p/p)^n \quad (5.15)$$

with $\Delta p/p$ the relative momentum offset of an off-momentum particle, Δx its corresponding transverse displacement with respect to the reference particle at a given longitudinal position s. Δx can be developed in a Taylor series as a function of the relative momentum offset with $D^{(n)}$ is the n^{th} order of dispersion. Higher order of dispersion are non negligible if the accelerator is strongly non linear and, as it will be seen later, it is not the case for the CERN PS, therefore the expression is reduced to

$$\Delta x(s) = D(s)\Delta p/p \quad (5.16)$$

The optics measurements were performed in the transfer line from PSBooster to PS in order to evaluate a potential mismatch. The optics was measured on the BT3-BTP which is at the same vertical level as the PS and which does not see any vertical recombination and therefore any vertical dispersion. The measurements were also performed on the BT1-BTP line which goes through vertical dipoles along the recombination Fig. 5.6 and which can likely generate vertical dispersion. For each of the two series of measurements, the dispersion function has been also measured during the first turn after the injection into the PS. Here the ring is then considered as a line during the first revolution. The dispersion measurements will give horizontal and vertical dispersion values at several points of the transfer line and their derivative and in particular at the beginning of the line, i.e. at the PSBooster extraction. The

measurement consists in varying the momentum of the beam extracted from the PSBooster by slightly varying the reference revolution frequency since $\Delta p/p = \eta \Delta f/f$ and recording the beam transverse displacement $(\Delta x, \Delta y)$ at each available monitor in horizontal and vertical planes in the transfer line and in the PS. Six Beam Position Monitors (BPM) in the BT-BTP are available for each plane and 40 for the PS ring. When possible, a device so-called SEM-grid, were used as well. SEMs of the PS at injection are Secondary Electron Monitor [92] [93] composed each by an array of wires placed on the path of the beam. In the PS injection area, a SEM-grid is placed right after the septum in SS42 allowing to measure the transverse profile of the beam at this point and three other SEMs are standing in SS48-SS52-SS54. Under the impact of the beam particles on solid material, electrons are liberated from the surface, thus a flow of current is produced. Then, by measuring the secondary emission current from each wire, the transverse beam shape is obtained. The provision of a "clearing field" of a few 100 V/cm is essential to ensure that the liberated electrons are rapidly cleared away. Otherwise, an electron cloud may form over the foil surface and impede further emission. The measured horizontal and vertical beam distribution is, as example in x-plane for a Gaussian distribution

$$\rho_x(x) = \frac{\lambda}{\sqrt{2\pi}\sigma_x} e^{-\frac{x^2}{2\sigma_x^2}} \tag{5.17}$$

However, SEMs are very fragile beam diagnostics devices.To use them, a internal dump must be placed after them in the ring in order to avoid the beam to perform several revolutions. The optics is then measured only during the first turn after the beam is injected into the PS. One has to note that due the fragile instrumentation used during the measurements, only beams dedicated to the experiment are allowed to be injected into the machine and therefore SPS and other accelerators or experiments upstream the PS are stopped. For each change in revolution frequency, the relative momentum offset is calculated and the beam positions at the monitors measured several times and averaged. Then the beam displacement as a function of the momentum offset is obtained at each monitor position and first order fit is applied as shown Eq. 5.16 to get the linear coefficient which is the dispersion function at that position. Two protons beam were set for the measurements with the parameters of Table 5.2. Non-linear elements such as PFWs were not used and the low energy quadrupoles used to control the tunes were off.

Dispersion Measurements Results

The revolution frequency of PSBooster at extraction is 3492541.486536 Hz and has been changed by step of 500 Hz in the measurements in order to slightly modify the momentum of the beam. The transverse positions in the lines were acquired for the different Δf_{rev} and Fig. 5.18 presents the horizontal and the vertical trajectories in the lines while the revolution frequency is changed. The path of the beam in both transfer lines is modified and follows the dispersion function in particular in the horizontal in which the dispersion is expected to be the largest. As expected Fig. 5.18c show that the vertical trajectory of the transfer line BT3-BTP

Beam line	BT3-BTP	BT1-BTP
Nb. of bunches	1	2
Tot. Intensity 10^{10}	60	100
Physical Emittance $\epsilon_{x,y}$ (2 σ) [mm.mrad]	1.363/1.183	2.215/1.807
Bunch Length 4 σ (ns)	102.6	151
Momentum Spread (2 σ)	1.65×10^{-3}	2.35×10^{-3}
$Q_{x,y}$	6.22/6.27	6.22/6.27

Table 5.2: Beam parameters during the matching measurements.

almost does not change with the revolution frequency meaning that the vertical dispersion is very small since this line does not contain any vertical dipoles, at the opposite of the BT1-BTP line Fig. 5.18d in which more differences are observed while the frequency is changing. The resulting momentum change is obtained by,

$$\frac{\Delta p}{p} = \eta_{PSB} \frac{\Delta f_{rev}}{f_{rev}} \tag{5.18}$$

with $\frac{\Delta p}{p}$ is the relative momentum change, η_{PSB} is the momentum compaction factor of the PSBooster at extraction, $\frac{\Delta f_{rev}}{f_{rev}}$ is the relative revolution frequency change. Then the beam positions are extracted at each BPM of the line in the horizontal and the vertical plane and confronted to the relative momentum change. As example, Fig. 5.19 shows the horizontal and the vertical displacements at a monitor placed in BT1-BTP line as a function as $\Delta p/p$. The beam position change seems to behave in a linear way with the relative momentum change and a fit is then applied to the measurements to all the BPM, the slope giving the dispersion at the location of the monitor.

The dispersion D_0 and the dispersion derivative D'_0 at the PSBooster extraction point are

calculated by applying a fit to $D(s)$ with the help of the matrix Eq. 1.17,

$$D_{ifit} = C_i D_0 + S_i D'_0 + D_i \tag{5.19}$$

where C_i and S_i are the cos-like and the sin-like function of the transfer matrices at a location i, $\tilde{D}_i$ is the dispersion for $D_0 = D'_0 = 0$ at the beginning of the line. A calibration factor α is introduced as a fit parameter for the horizontal plane and introduced to take into account errors in the determination of the momentum offset due to possible scaling problem of the monitors. So the fitting function for the horizontal plane is

$$D_{ifit} = C_i D_0 + S_i D'_0 + \alpha \tilde{D}_i \tag{5.20}$$

The horizontal plane, in which the dispersion values are important, is used to calculate α. In the vertical plane, the dispersion is in principle very small, however since α represents an error in momentum, it is the same for the two planes. Once the fit is performed, the values of the measured horizontal dispersion and of the initial conditions are divided by the factor α. The function to be minimized with respect to $(\bar{D}_0, \bar{D}'_0, \alpha)$ is,

$$\chi^2 = \Sigma_{i=1}^{N} \left(\frac{D_i - C_i \bar{D}_0 + S_i \bar{D}'_0 + \alpha \tilde{D}_i}{\sigma_i} \right)^2 \tag{5.21}$$

with σ_i the error on the measurements. The coefficients cos-like and sin-like are given by MADX by extracting from the coefficients $(R_{11}, R_{12}, R_{33}, R_{34})$ of the response matrice. Fig. 5.20a and Fig. 5.20b present the resulting measured dispersion respectively in the horizontal and the vertical planes for the BT3-BTP and the BT1-BTP transfer lines helping to fit the parameters $(\bar{D}_0, \bar{D}'_0, \alpha)$. They are summarized respectively in Table 5.3 for the horizontal plane and in Table 5.4 for the vertical plane.

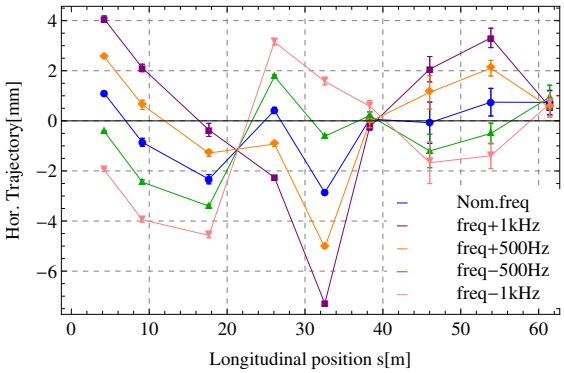

(a) Horizontal trajectories in the transfer line BT3-BTP.

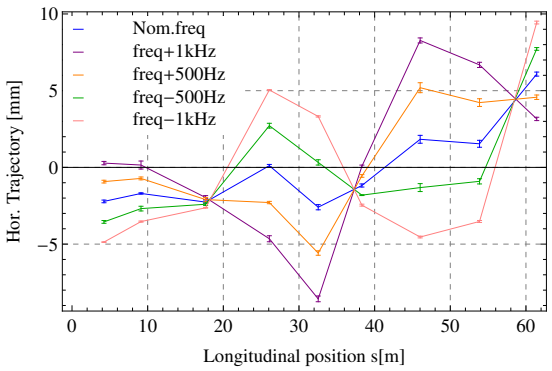

(b) Horizontal trajectories in the transfer line BT1-BTP.

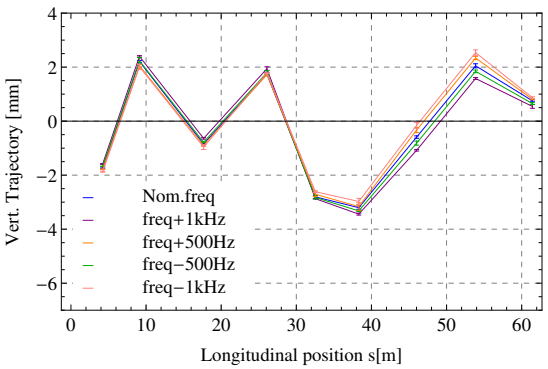

(c) Vertical trajectories in the transfer line BT3-BTP.

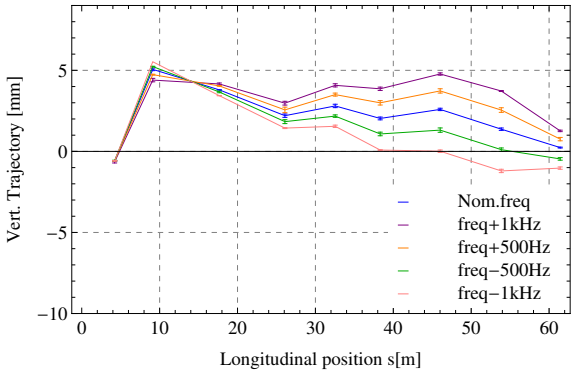

(d) Horizontal trajectories in the transfer line BT1-BTP.

Figure 5.18: Fig. 5.18a and Fig. 5.18c present respectively the horizontal and the vertical trajectories in the BT3-BTP line for different revolution frequencies in PSBooster, i.e. different momentum change. The same is presented in Fig. 5.18b and Fig. 5.18d for the BT1-BTP line.

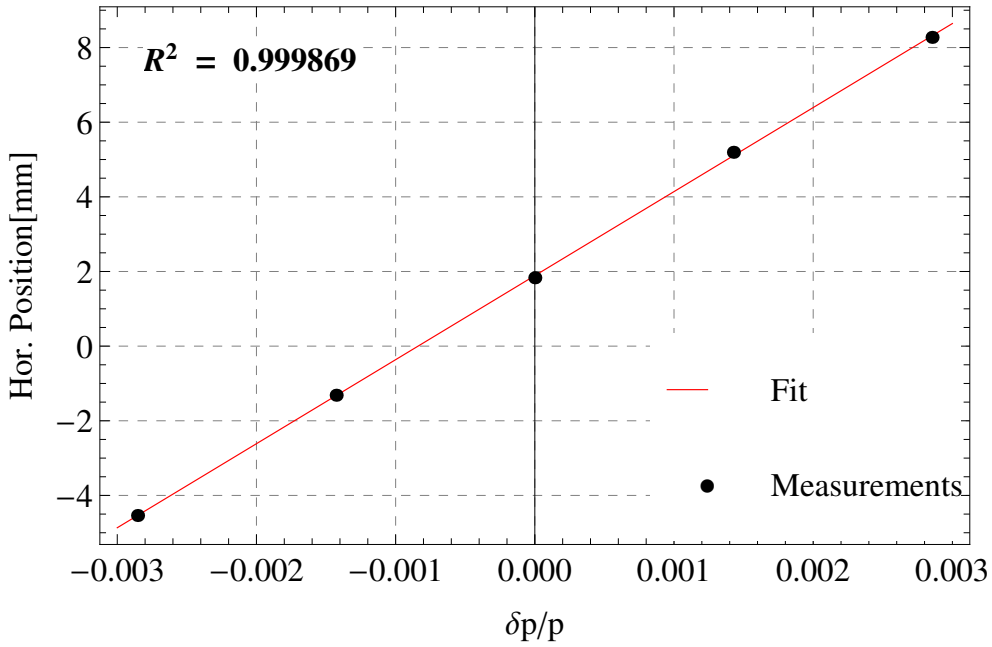

(a) Horizontal beam position.

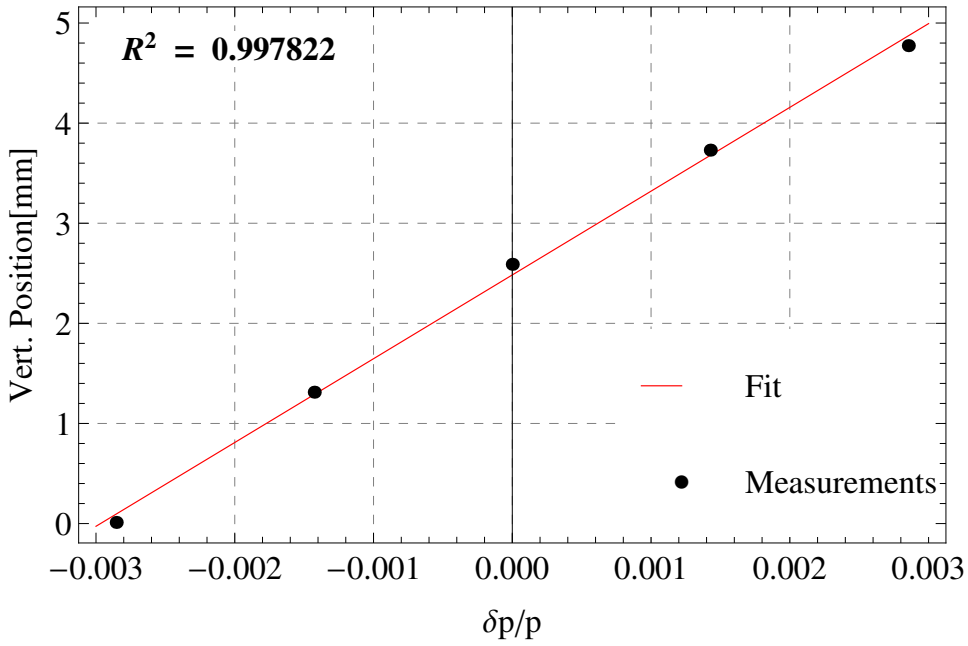

(b) Vertical beam position.

Figure 5.19: Fig. 5.19a and Fig. 5.19b present respectively the horizontal and the vertical beam position at a BPM location for in the BT1-BTP line as a function of the relative momentum change $\delta p/p$.

Beam line	BT1-BTP	BT3-BTP
Hor. D_0	1.166 m $\pm$ 0.244	0.953 m $\pm$ 0.010
Hor. D'_0	0.064 m $\pm$ 0.027	0.019 m $\pm$ 0.002
α	1.268 m $\pm$ 0.050	1.285 m $\pm$ 0.050
Not scaled to α	D_{x0} = 1.479 m, D'_{x0} = 0.082	D_{x0} = 1.224 m, D'_{x0} = 0.024

Table 5.3: Horizontal initial dispersion and its derivative deduced from the fit of the Eq.5.21.

Beam line	BT1-BTP	BT3-BTP
Vert. D_0	$-$0.049 m $\pm$ 0.093	0.007 m $\pm$ 0.019
Vert. D'_0	0.034 m $\pm$ 0.026	0.008 m $\pm$ 0.009
Not scaled to α	D_{y0} = 0.049 m, D'_{y0} = 0.044	D_{y0} = 0.008 m, D'_{y0} = 0.011

Table 5.4: Vertical initial dispersion and its derivative deduced from the fit of the Eq. 5.21.

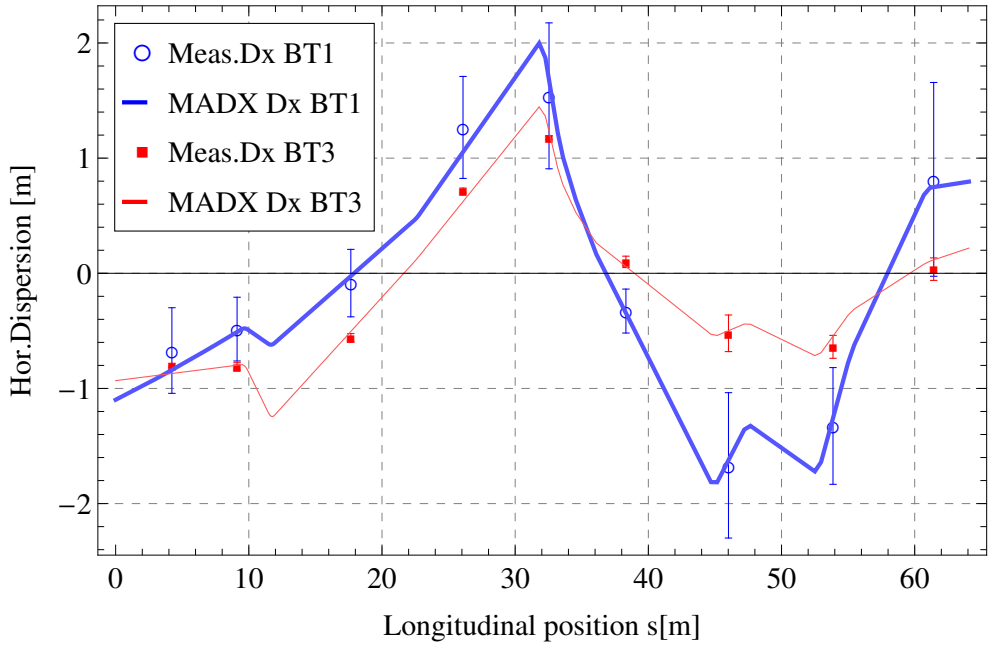

(a) Horizontal Dispersion.

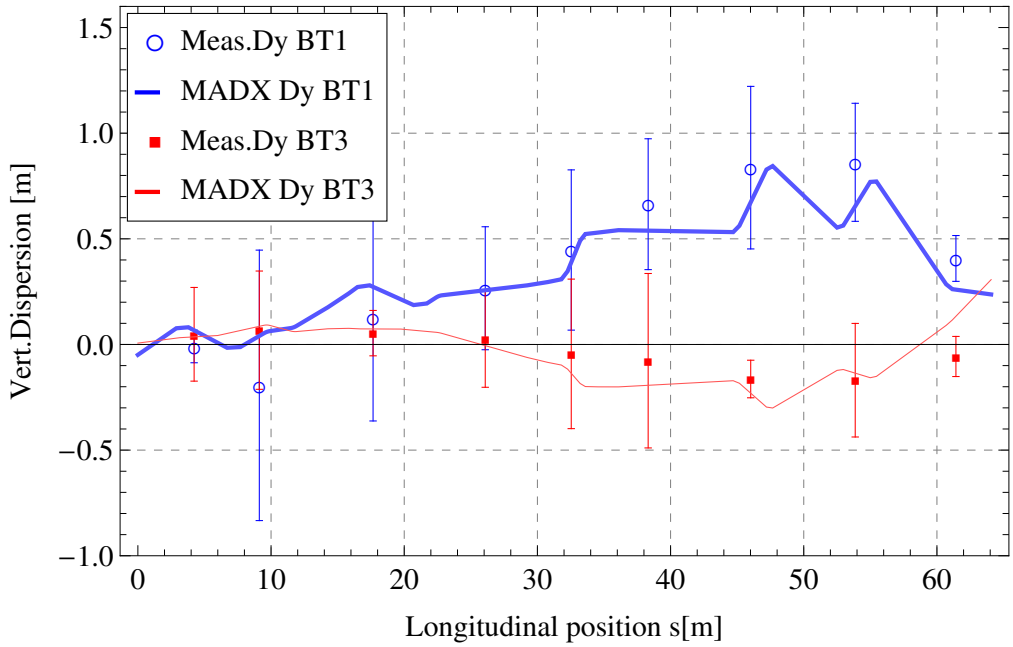

(b) Vertical Dispersion.

Figure 5.20: Fig. 5.20a and Fig. 5.20b present respectively the measured horizontal and the measured vertical dispersion at the BPM locations for in the BT1-BTP and the BT3-BTP lines.

Fig. 5.20a shows that the horizontal dispersion right after the PSBooster extraction is measured negative whereas in the PS the sign of the dispersion is positive. In all the accelerator at CERN, a horizontal positive displacement Δx is defined as a displacement which outward of the machine as illustrated in Fig. 5.21 A particle with a positive displacement in the PS means a negative offset in the PSB due to the fact that the beam circulates in Booster anti-clockwise and the sign of the dispersion in the PS and the PSB are opposite. Fig. 5.22 presents the theoretical horizontal dispersion at PSB extraction where it can be seen that MADX uses also the convention as in the PS. This means that the horizontal dispersion has to perform a large oscillation in the line from the PSB extraction to catch up the matched positive value of the dispersion at PS injection.

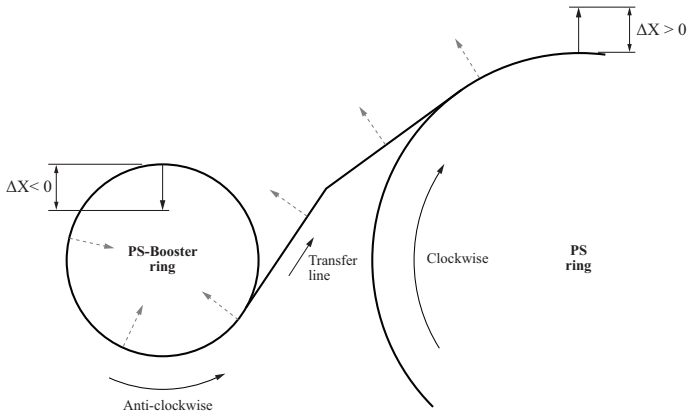

Figure 5.21: Convention difference between the PSB and the PS ring to illustrate the negative sign of the horizontal dispersion of the transfer line observed in the measurement.

Fig. 5.20a shows that the measured horizontal dispersion of the transfer lines from Ring 1 and Ring 3 are different, meaning that the bunches coming from different ring experience different optics. The initial dispersion D_{x0} and its derivative D'_{x0} computed from the measurements are indeed different between the BT1-BTP and the BT3-BTP lines, however the propagation of the initial conditions through the lattice of the lines with an optics code such as MADX allows to reproduce fairly well the measured horizontal and vertical dispersion in the two transfer line. The measured vertical dispersion in the BT3-BTP line is smaller than the dispersion in BT1-BTP as expected since the transfer line from Ring 1 experiences several vertical dipoles during the recombination and creating then vertical dispersion. However, their computed initial values at the PSB extraction are very small and D_{y0}, D'_{y0} can be considered negligible and close to zero.

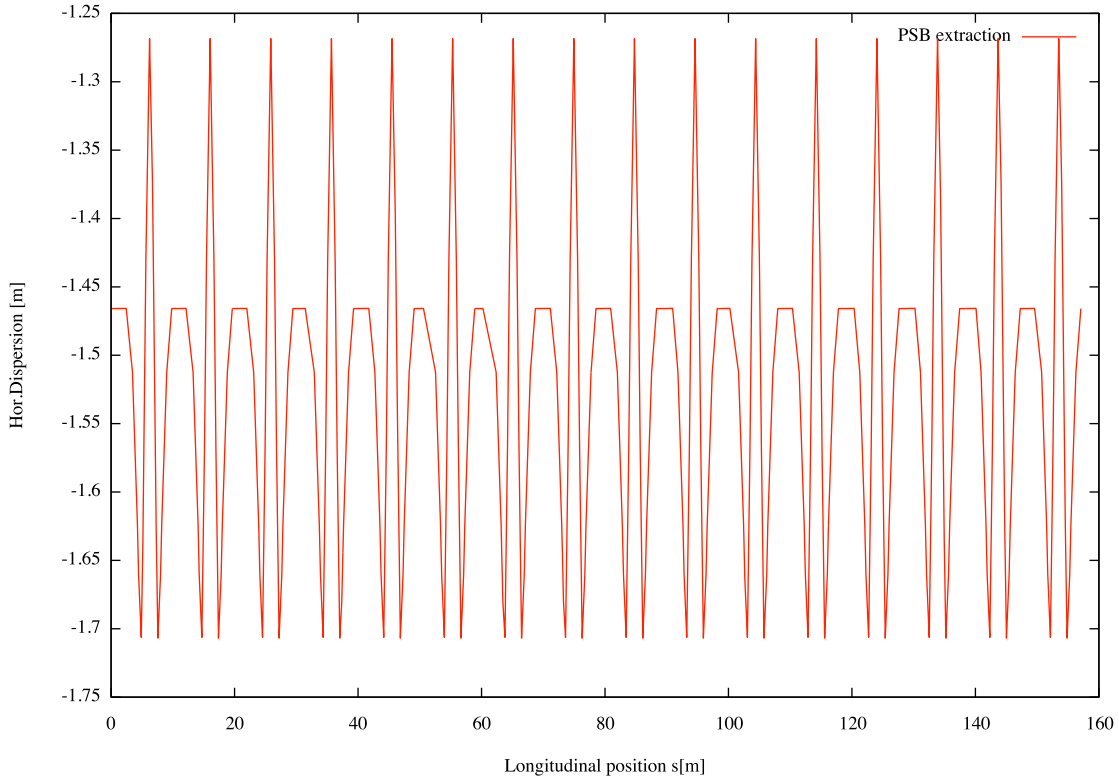

Figure 5.22: Theoritical horizontal dispersion at PSBooster extraction computed with MADX.

The same measurement was performed in the PS ring. The vertical dispersion was found too small to be measured with the current BPMs installed in the ring, because the BPM are not able to measure a vertical displacement due to small vertical dispersion. Fig. 5.23 presents the orbits measured during the first turn after injection into the PS for different momentum offset with respectively Fig. 5.23a for a beam coming from BT1-BTP line and Fig. 5.23b for the BT3-BTP. Using the BPMs of the PS, the same dispersion measurement method is applied and Fig. 5.24 shows the measured horizontal dispersion of the PS ring during the first turn for a beam either injected from BT1-BTP or from the BT3-BTP line. Here the PS ring is considered as a transfer line and not as a closed machine. As in the transfer line, the measured horizontal dispersion at the first turn seems to depend of the PSBooster where the beam comes from. There is therefore a dispersion mismatch depending on the transfer line used by the beam between the PSBooster and the PS.

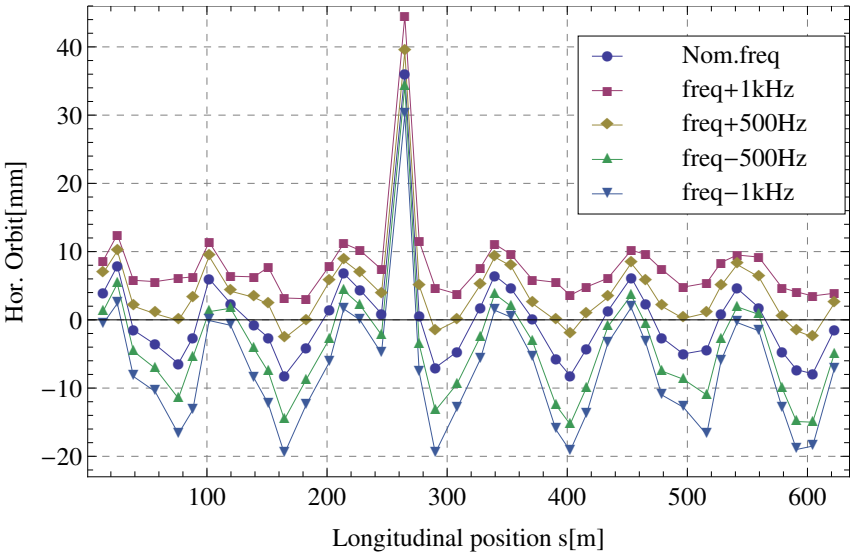

(a) Horizontal Orbit for a beam injected into the PS from the BT1-BTP line.

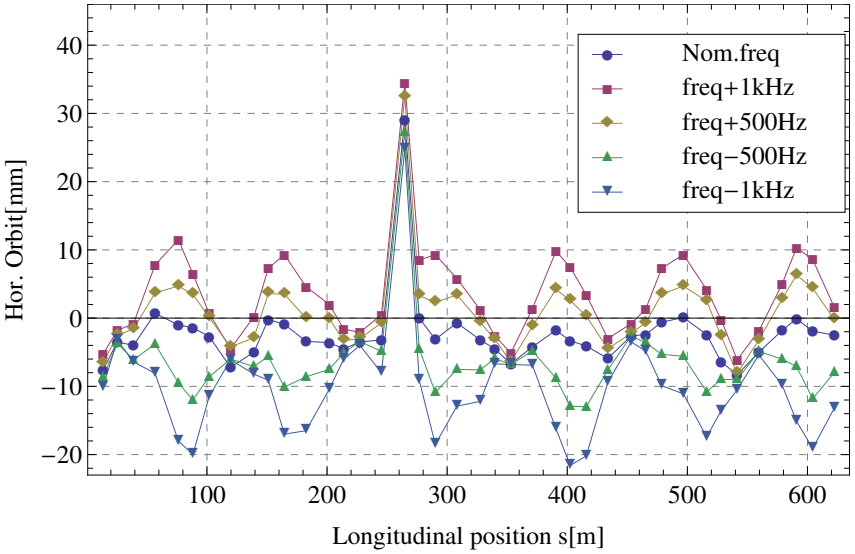

(b) Horizontal Orbit for a beam injected into the PS from the BT3-BTP line.

Figure 5.23: Fig. 5.23a and Fig. 5.23b present the horizontal orbit at the pickup locations during the first turn after injection in the PS for a beam coming from respectively the BT1-BTP and the BT3-BTP for different relative momentum change $\Delta p/p$.

The dispersion was also measured at a SEM-wire placed at the end of the injection septum (SEM 42) for a beam extracted either from the Ring 1 of the PSB or from Ring 3. An example of measurement is shown in Fig. 5.25: thanks to the signals of the wires, the transverse distribution of the beam, here horizontal, is observed. A Gaussian fit is applied to the distribution to deduce the mean position of the beam at the SEM 42. Fig. 5.26 presents the horizontal distribution at the SEM 42 for different $\Delta p/p$ in which we see that the bunch is displaced when the relative momentum changes.

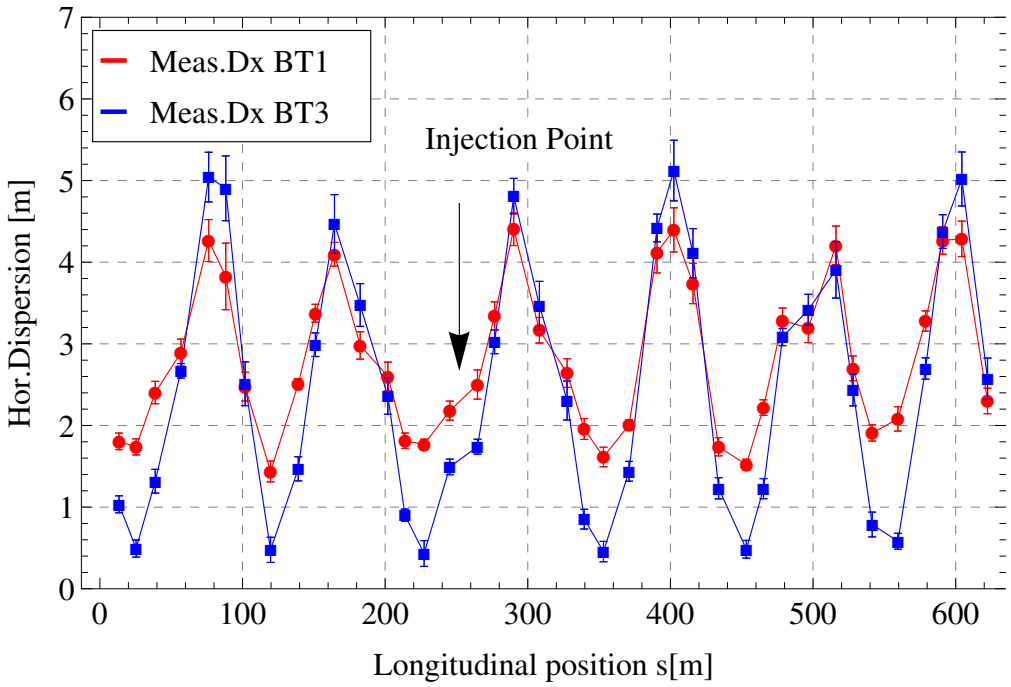

Figure 5.24: Measured horizontal dispersion during the first turn after injection for a beam coming either from the BT1-BTP or BT3-BTP line.

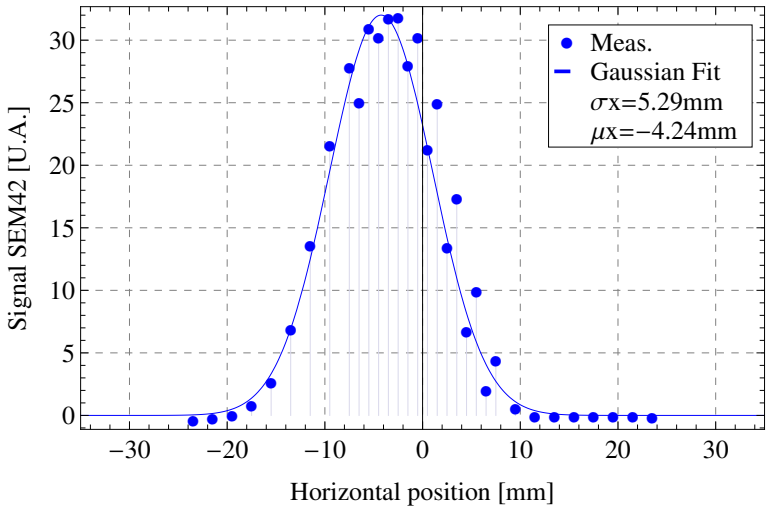

Figure 5.25: Example of SEM-wire 42 measurement of the beam horizontal distribution. A Gaussian fit is applied of the signals of the wires in order to deduce the mean position of the bunch at the SEM location as well as the σ RMS of the distribution which is nothing else than the beam size.

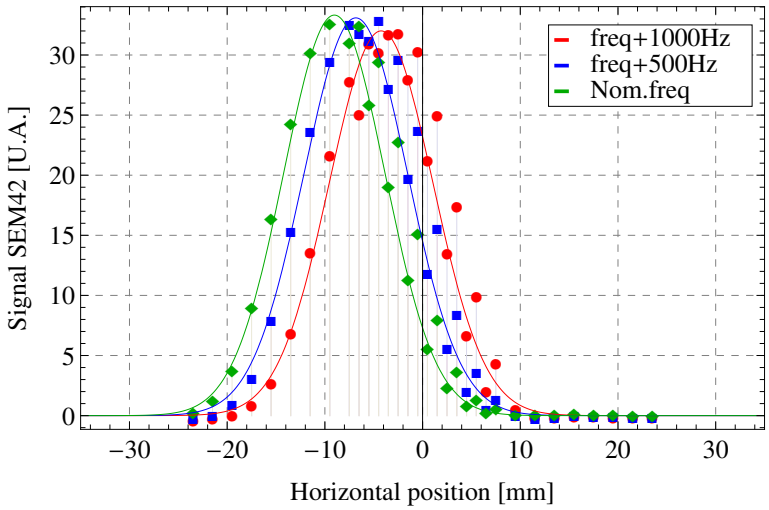

Figure 5.26: Example of SEM-wire 42 measurement of the beam horizontal distribution. A Gaussian fit is applied of the signals of the wires in order to deduce the mean position of the bunch at the SEM location as well as the σ rms of the distribution and for different relative momentum change.

The results of the measured horizontal dispersion are presented respectively in Fig. 5.27a for a beam coming from BT1-BTP and in Fig. 5.27b for a beam from BT3-BTP confirming a mismatch in dispersion between injection transfer line. The vertical dispersion D_y at this location can be also measured especially for the BT1-BTP Fig. 5.27c whereas the vertical dispersion from BT3-BTP very close to zero Fig. 5.27d.

Other three SEM-wires similar to the SEM 42 were used to measure the optics in the ring and they are located in SS48, SS52 and SS54 with the phase advance with respect to the injection point that we consider to be at the SEM 42. However, the dispersion at these monitors was measured only for the extraction line of Ring 1 and the results are presented in Fig. 5.28. They can be compared to the dispersion measurements performed in the PS ring Fig. 5.24 with a beam injected from BT1-BTP. The comparison is done in Fig. 5.29 and a good agreement is found, taking into account that two different measurements devices are used. In order to compute the dispersion mismatch, an optics model of the CERN PS at injection energy is needed. The next paragraph will be devoted to the MADX optics model of the PS and to the calculation of the optics mismatch between the BTP lines and the PS ring.

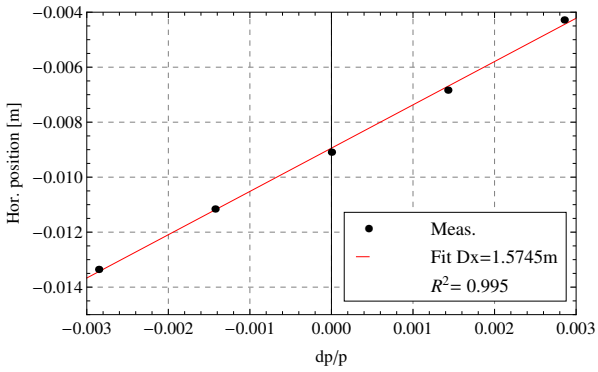

(a) Horizontal dispersion from the BT1-BTP line.

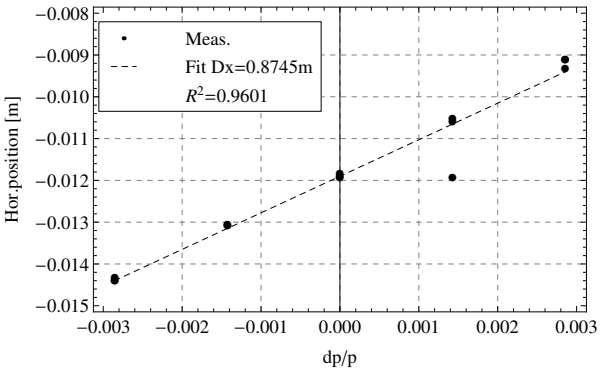

(b) Horizontal dispersion from the BT3-BTP line.

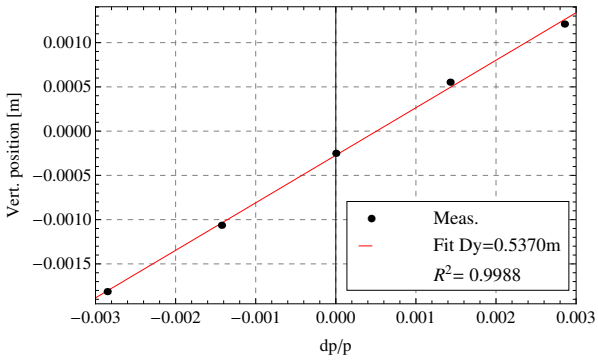

(c) Vertical dispersion from the BT1-BTP line.

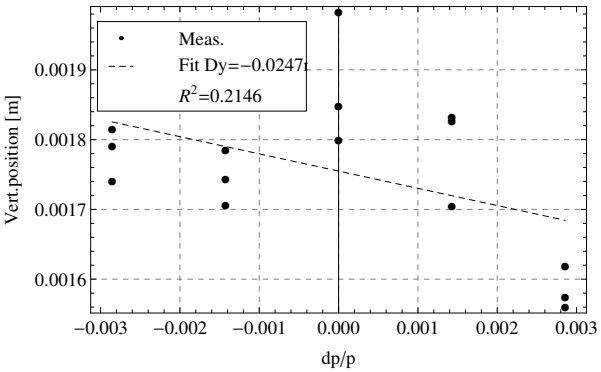

(d) Vertical dispersion from the BT3-BTP line.

Figure 5.27: Fig. 5.27a and Fig. 5.27b present the linear fit applied on the horizontal position of the beam at the SEM 42 placed right after the injection septum for different relative momentum change $\delta p/p$. Fig. 5.27c and Fig. 5.27d present the vertical position of the beam at the SEM 42 placed right after the injection septum for different relative momentum change $\delta p/p$.

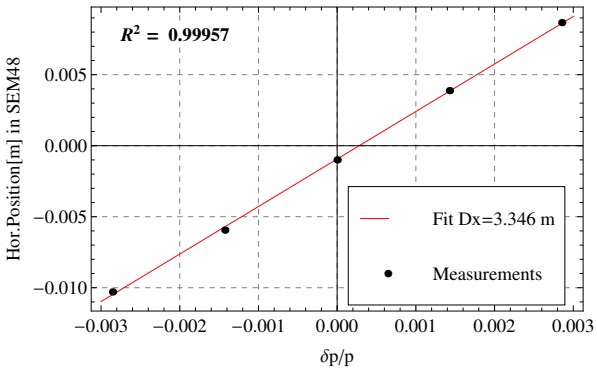

(a) Horizontal dispersion measured at the SEM 48 for a beam from the BT1-BTP line.

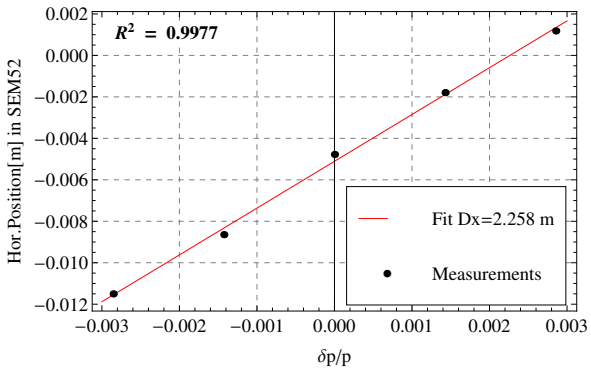

(b) Horizontal dispersion measured at the SEM 52 for a beam from the BT3-BTP line.

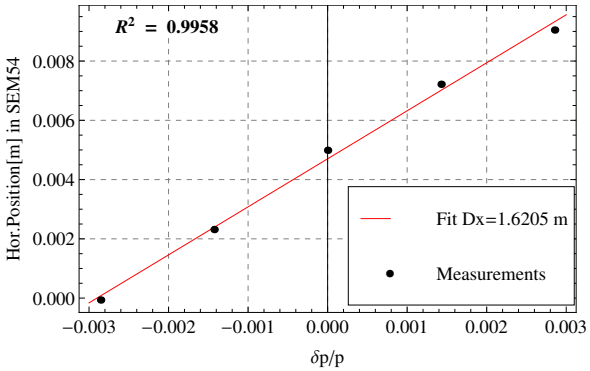

(c) Vertical dispersion measured at the SEM 54 for a beam from the BT1-BTP line.

Figure 5.28: Linear fit applied on the horizontal position of the beam at the SEM-grids 48, 52 and 54 placed later after the injection septum for different relative momentum change $\Delta p/p$.

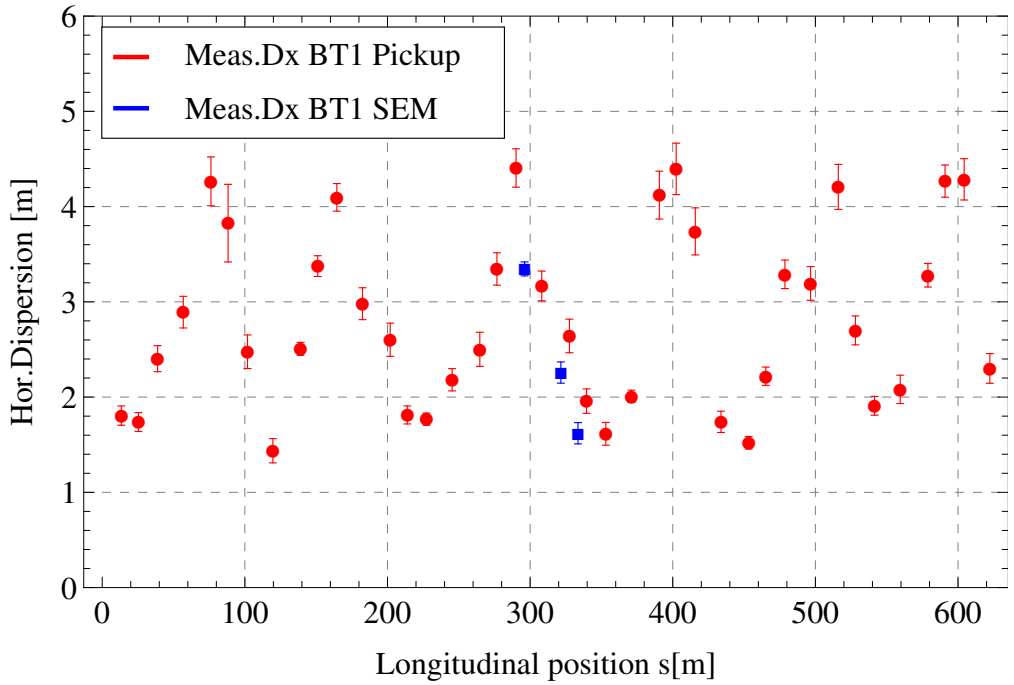

Figure 5.29: Horizontal dispersion measurements using SEM-grids after the injection area in SS48-SS52-SS54. The BT1-BTP line was used. They are compared to the horizontal dispersion measurements using the pickups of the PS and a good agreement is found.

5.3.2 Comparison of the optics measurements with the PS optics model

In order to compute the dispersion mismatch, the cos-like and sin-like ($C_i(s)$ and $S_i(s)$) functions at the positions of the pickups are needed and these parameters depend of the elements between the BPMs and the injection point. The nominal lattice of the PS starts in SS1 and if the Cos-like and Sin-like are extracted from the nominal lattice, they would describe the transfer matrix from the straight section SS1 to the pickups. However the path of the beam at injection starts in SS42, therefore the ($C_i(s)$ and $S_i(s)$) functions have to determined between the injection point and each pickup at which the dispersion was measured, by giving to MADX the constraint that the starting point is the end of the injection septum. The straight section 42 has a total length of 1 m and is composed by an injection bumper with a length of 0.1 m, the so-called BSM 42, and by the injection septum of a length of 0.8 m, noted SMH 42. In the nominal lattice, the injection septum does not act on the circulating beam and is therefore declared as a drift. In the MADX sequence of the PS, is introduced as a marker without any length right after the SMH 42. A marker in MADX is a non-physic element which does not perturb the optics and which is frequently used to record parameters at given locations.

The first step is to match the angles given by the bumpers in order to close as much as possible the injection bump and eliminate residual orbit oscillations outside the injection region. The given constraints aim to get the horizontal position x and the horizontal angle x' to zero outside the orbit bump and therefore only two variables, here the currents BSM 43 and BSM 44, are needed to match the two constraints. The so-called algorithm *Jacobian* [94] was used to find the suitable bumpers strengths to close the orbit injection bump. The initial currents given to MADX are shown in Table 5.5 and compared to the final values found by the Jacobian algorithm after matching as well as the resulting closed orbit in Fig 5.30.

Bumper Currents	Operational values (CNGS)	After Matching
BSM 40 (A)	905	905
BSM 42 (A)	3632	3632
BSM 43 (A)	3290	3272.739507
BSM 44 (A)	1530	1504.164977

Table 5.5: Currents of the bumpers at injection from the CNGS beam matched before and after matching in MADX.

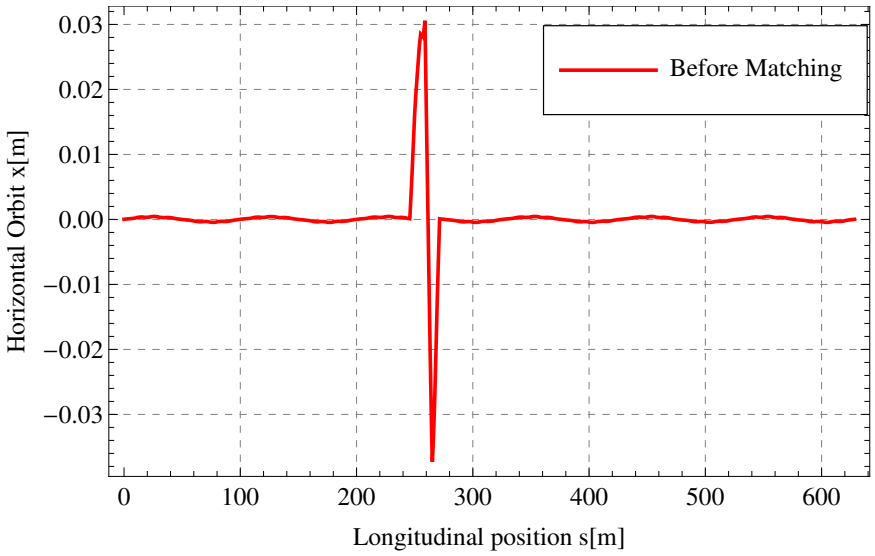

(a) Horizontal Orbit for a beam injected into the PS from the BT1-BTP line.

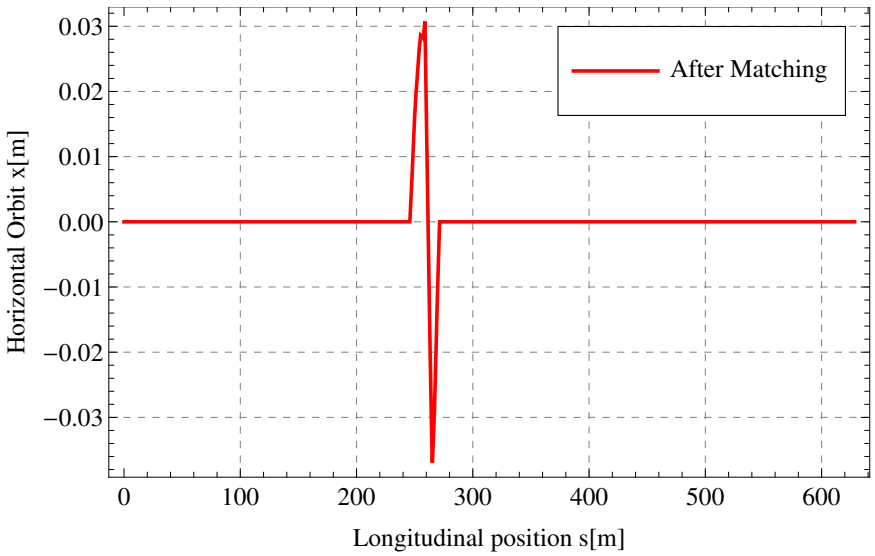

(b) Horizontal Orbit for a beam injected into the PS from the BT3-BTP line.

Figure 5.30: Fig. 5.30a presents the closed orbit computed by MADX with some initial values of currents powering the injection bumpers and Fig. 5.30b shows the resulting closed orbit after a matching performed with MADX aimed to alleviate residual orbit oscillation outside the injection orbit bump.

The lattice is then cycled at the marker situated at the same emplacement as the SEM-grid mounted after the injection septum. The resulting orbit is shown in Fig 5.31. The PS lattice starts then in the middle of the injection bump and the response matrix can be then computed in MADX from the marker and the respective longitudinal location of the pickups. The initial conditions in dispersion and its derivative for beams injected from BT1-BTP and BT3-BTP are then deduced using Eq. 5.21 and in a similar way as done for the injection line, the results are presented in Table 5.6.

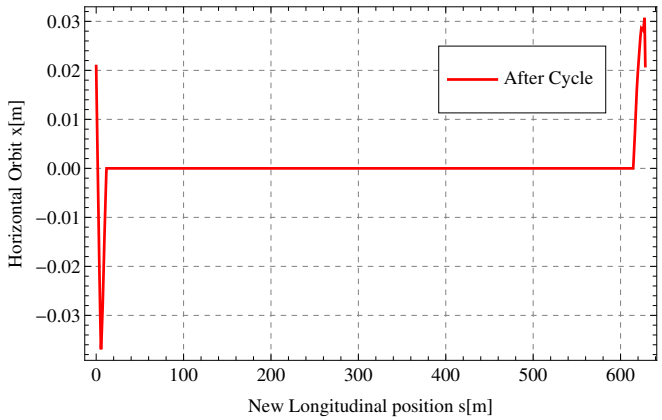

Figure 5.31: Horizontal Orbit od the CERN PS after having cycled the lattice at the injection point. One has to figure out that $s = 0$ in this figure, $s = 0$ corresponding to the injection point, corresponds to $s = 269$ m in the nominal lattice, the longitudinal positions of all element of the machine were shifted with the cycling.

The initial conditions of Table 5.6 are then tracked through the PS lattice using MADX and the resulting horizontal dispersion is compared to the measured one and a very good agreement is found in Fig 5.32a and in Fig. 5.32b. They are then compared to the periodic dispersion in Fig. 5.32c and in Fig. 5.32d showing a dispersion mismatch at injection which will be computed in the next paragraph. The PS lattice is used as a transfer line in MADX by giving an ensemble of initial conditions to compute the optical functions.

In a similar way, initial conditions in dispersion are deduced from the dispersion found at the SEM-grids. They are then tracked through the lattice with MADX (in blue line in Fig. 5.33) and compared to the computed dispersion found from the BPM (in green line in Fig. 5.33), showing a very good agreement and corroborate the mismatch in dispersion found with BPMs measurement method. The results are presented in Fig. 5.33.

Transfer line	PR.MARK 42 from Ring 1	PR.MARK 42 from Ring 3
Hor.D_0	1.569 m $\pm$ 0.0215	0.783 m $\pm$ 0.0262
Hor.D'_0	0.051 $\pm$ 0.002	0.084 $\pm$ 0.002
α	0.993	0.888
Not scaled to α	D_{x0} = 1.527 m, D'_{x0} = 0.0568	D_{x0} = 0.706 m, D'_{x0} = 0.0753

Table 5.6: Initial dispersion conditions D_0 and its derivative found from the dispersion measurement method using the pickup of the PS ring for the beam injection lines BT1-BTP and BT3-BTP.

The results of the dispersion measurements in the horizontal and vertical planes at the injection point in the PS are summarized in Table 5.6 in which different methods are compared. Beside the fact that the values of the initial conditions in dispersion are cross check by the BPMs and the SEM-grids methods, the results show a measurable mismatch with respect to the periodic dispersion at injection.

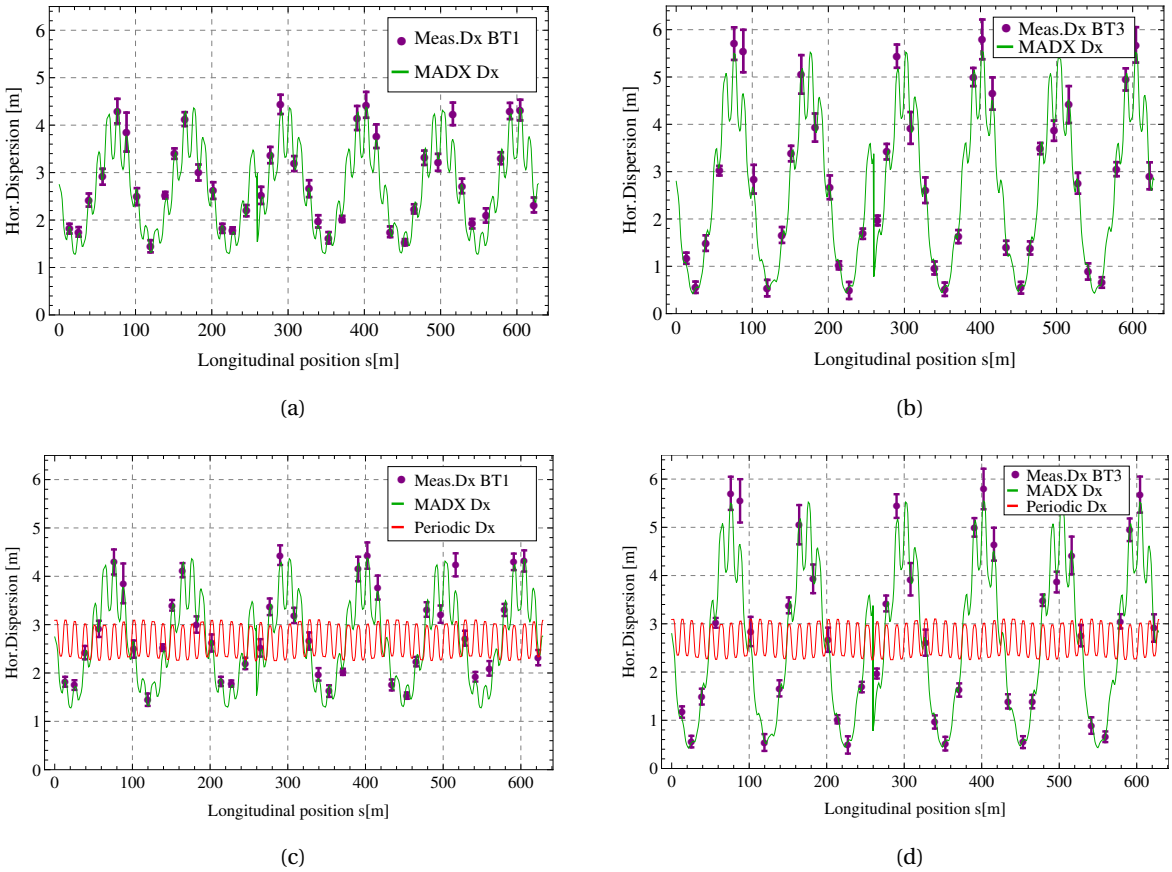

Figure 5.32: Fig. 5.32a and Fig. 5.32b present the measured horizontal dispersion compared to the dispersion tracked by MADX in PS lattice using the initial dispersion deduced in Table 5.6 for a beam respectively from the BT1-BTP and from the BT3-BTP transfer line. Fig. 5.32c and Fig. 5.32d compare the measured and the MADX dispersion to the periodic one.

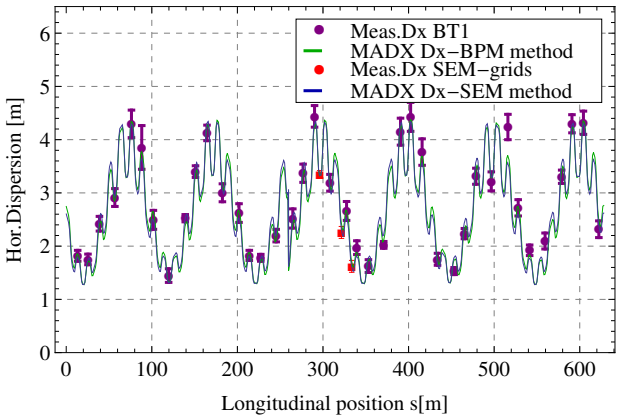

Figure 5.33: The horizontal dispersion found at the SEM-grids SEM 48, SEM 52 and SEM 54 allow to compute in the same way as done for the BPMs method, initial conditions for the dispersion and its derivative at the injection point. They are then propagated through the PS lattice and the resulting dispersion function, in blue, is compared to the dispersion calculated by MADX of Fig. 5.32a, here in green.

5.3.3 Dispersion mismatch

Each beam particle is characterised by the coordinates (x_n, x'_n, δ) and in the case of a dispersion mismatch, it introduces an offset in the transverse phase space by

$$x_n \rightarrow x_n + \Delta D_n \delta \tag{5.22}$$
$$x'_n \rightarrow x'_n + \Delta D'_n \delta \tag{5.23}$$

The mismatched beam at injection has an elliptical equi-density line with a minor axis of the ellipse being $\sqrt{\epsilon}$ and the major axis $\lambda_D\sqrt{\epsilon}$ with

$$\lambda_D = \sqrt{1 + \frac{(\Delta D_n^2 + \Delta D_n'^2)}{\epsilon}\delta_{rms}^2} \tag{5.24}$$

with ϵ the transverse r.m.s. emittance, δ the r.m.s. momentum spread, ΔD_n is the difference between the periodic and the measured dispersion normalized to the periodic β at the injection point, $\Delta D'_n$ is the normalized difference between the periodic and the measured dispersion derivative. The emittance of the mismatched beam is given by $\epsilon\lambda_D$ and is larger than the emittance of the matched beam already before filamentation. The geometrical blow-up G_D and the total blow-up after filamentation J_D are given by [11]

$$G_D = \lambda_D^2 \tag{5.25}$$
$$= 2J_D - 1$$
$$J_D = 1 + \frac{(\Delta D_n^2 + \Delta D_n'^2)}{2\epsilon}\delta_{rms}^2$$
$$= \frac{1 + \lambda_D^2}{2} \tag{5.26}$$

Then using Eq. 5.14

$$J_D = 1 + \frac{\Delta D^2 + (\Delta D'\beta_0 + \Delta D\alpha_0)^2}{2\epsilon\beta_0}\left(\delta^2\right) \tag{5.27}$$

with α_0, β_0 the Twiss parameters at the injection point, ϵ the transverse r.m.s. physical emittance. Considering that $\beta_0 = 11.856$ m, $\alpha_0 = -0.095$ and the horizontal periodic dispersion $D_{x0} = 2.261$ m and its derivative $D'_{x0} = 0.0014$ at the injection point, the total blow-up after filamentation is calculated for beams injected either from Ring 1 or Ring 3 in Table. 5.7 with the transverse emittances of Table 5.2

Transfer line	PR.MARK 42 from Ring 1	PR.MARK 42 from Ring 3
Hor.D_0	1.569 m $\pm$ 0.0215	0.783 m $\pm$ 0.0262
Hor.D'_0	0.051 $\pm$ 0.002	0.084 $\pm$ 0.002
J_D	1.032	1.069
G_D	1.064	1.139

Table 5.7: Dispersion mismatch measured for a beam coming from BT1-BTP and BT3-BTP lines.

5.3.4 Betatron Mismatch Measurements

Transverse emittance blow up are also provoked by betatron mismatch due to the twiss beta function β and its derivative α. In a similar way as the dispersion, the betatron mismatch is caused by the difference in betatron function with respect to the periodic twiss parameters. This is why the β, α optics parameters were measured at the injection point, i.e. right after the injection septum, using the standard 3-monitors method, explained in Ref [11] [2]. This method consists of measuring the beam transverse profile at 3 monitors as in Fig. 5.25 in order to get the beam size at 3 different locations and using the transfer matrices, the twiss parameters at injection is then deduced. In the experiment, the SEM-grids SEM 48, SEM 52, SEM 54 were used and the data of the SEM 42 were measured for cross check.

The transverse beam profile is measured at 3 SEM-grids in order to get the r.m.s. beam size in both plane from a Gaussian fit as done in Fig. 5.25. The r.m.s. beam size measured at the i-th monitor is

$$\sigma^2_{meas,i} = \sigma^2_{\beta,i} + D_i^2 \left(\frac{dp}{p}\right)^2 \tag{5.28}$$

with $\sigma^2_{meas,i}$ the r.m.s. beam size, D_i is the dispersion at the location i, dp/p the momentum spread,$\sigma^2_{\beta,i}$ the r.m.s. betatron contribution to the beam size which is $\sigma^2_{\beta,i} = \sqrt{\beta_i}\epsilon$, β_i is the beta function at the location i and ϵ the r.m.s. transverse emittance. Eq. 5.28 is then composed by a dispersive contribution, the second part of the equation, and a betatron contribution. The latter can be also be written in terms of cos-like and sin-like functions defined in Eq. 1.20 and of the Twiss parameters at the injection point

$$\sigma^2_{\beta,i} = \epsilon\beta_i = \epsilon\left(C_i^2\beta_0 - 2C_iS_i\alpha_0 + S_i^2\gamma_0\right) \tag{5.29}$$

therefore with the knowledge of of the beam size at the three monitors, it leads to the following system [95]

$$\begin{bmatrix} \sigma^2_{\beta,1} \\ \sigma^2_{\beta,2} \\ \sigma^2_{\beta,3} \end{bmatrix} = \begin{bmatrix} C_1^2 & -2C_1S_1 & S_1^2 \\ C_2^2 & -2C_2S_2 & S_2^2 \\ C_3^2 & -2C_3S_3 & S_3^2 \end{bmatrix} \begin{bmatrix} \epsilon\beta_0 \\ \epsilon\alpha \\ \epsilon\gamma_0 \end{bmatrix}. \tag{5.30}$$

From the system, the triplet ($\epsilon\beta_0$,$\epsilon\alpha_0$,$\epsilon\gamma_0$) is obtained and the transverse emittance is deduced using the relation $\beta\gamma - \alpha^2 = 1$ used in Eq. 1.22 of Section 1.1.3

$$\epsilon = \sqrt{(\epsilon\beta_0)(\epsilon\alpha_0) - (\epsilon\gamma_0)^2} \tag{5.31}$$

and the values of the Twiss parameters $\beta_0, \alpha_0, \gamma_0$ at the injection point are then calculated. The transverse beam emittance is also measured several millisecond after injection with

the so-called Fast Wire Scanner (FWS). It consists of a wire stretched between the tips of the lightweight arms going through the circulating beam. Like the SEM, the phenomena of secondary emission current is used. An example of emittance measurements is presented in Fig. 5.34, from which, in a similar way as the SEM, a Gaussian fit is applied to determine the beam size and then the transverse emittance by knowing the optics functions at the location of FWS. The main difference between the two systems is that the FWS goes through the beam during several consecutive turns whereas the SEM is a single turn device.

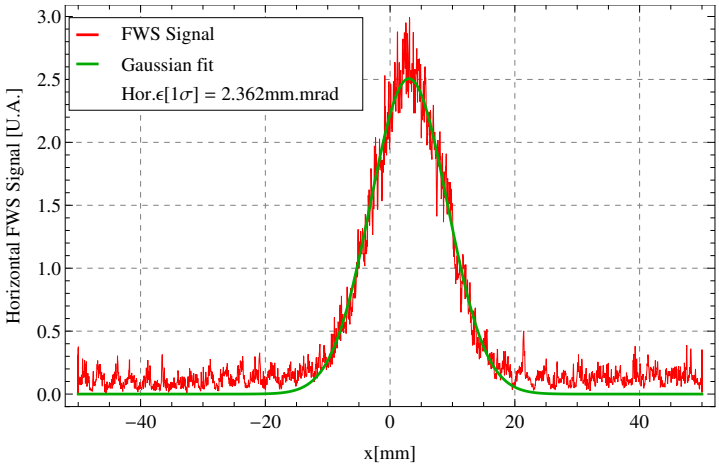

Figure 5.34: Horizontal Fast Wire Scanner signal measurement on which a Gaussian fit is applied aimed to find the physical emittance.

The 3-monitor method was used during the optics matching measurements and by applying the system of equations 5.30, the initial conditions in Twiss parameters and the blow-up after filamentation H were computed for beam coming from the BT1-BTP or the BT3-BTP line, with H,

$$H = \frac{1}{2}\left[\frac{\beta_0}{\beta_m} + \frac{\beta_m}{\beta_0} + \left(\alpha_0\sqrt{\frac{\beta_m}{\beta_0}} - \alpha_m\sqrt{\frac{\beta_0}{\beta_m}}\right)^2\right[\tag{5.32}$$

The results are presented in Table 5.8. The periodic Twiss parameters at the injection point are also needed

- In horizontal plane: $\beta_{x0} = 11.856$ m, $\alpha_{x0} = -0.095, \gamma_{x0} = 0.084$
- In vertical plane: $\beta_{y0} = 22.3314$ m, $\alpha_{y0} = -0.0511587, \gamma_{y0} = 0.0448972$

Betatron and dispersion mismatches were measured for a beam produced by either Ring 1 or Ring 3. The largest mismatch is measured for the transfer line BT1-BTP in the horizontal plane

Transfer line	Marker 42 from Ring 1	Marker 42 from Ring 3
Hor.$\beta_0, \alpha_0, \gamma_0$ Hor.$\epsilon(1\ \sigma)$[mm.mrad]	8.926 m, 0.262, 0.120 2.102	11.488 m, −0.159, 0.089 1.192
Hor. H mismatch	1.117	1.0028
Vert.$\beta_0, \alpha_0, \gamma_0$ Vert.$\epsilon(1\ \sigma)$[mm.mrad]	26.778 m, −0.238, 0.039 1.290	27.427, −0.210, 0.038 0.657
Vert. H	1.0296	1.030

Table 5.8: Measured betatron mismatches in the horizontal and vertical planes for a beam coming from BT1-BTP and from BT3-BTP.

and it concerns the betatron part (11%), whereas Ring 3 is more concerned by the dispersion mismatch (6%). In addition, an emittance blow up of about 10% is the minimum value that the emittance system measurement can detect and no significant emittance blow up has been measured between the PSBooster and the PS since these last few years [96, 97].

5.4 Aperture available in the Transfer Line

In this section, the available aperture for the beam is computed in both transverse plane in the transfer line and at the septum. Using the MADX optics model of the BT-BTP line and the optics measurements of the previous section, it is possible to identify in term of RMS beam size at 3 σ the possible aperture restrictions in the line. The two following quantities are defined:

$$\text{Hor.,Ver. RMS Available Aperture} = \frac{Aperture}{\sigma_{x,y}} \tag{5.33}$$

where the transverse available aperture in the line is defined as the ratio between the aperture and the rms beam size. The same can done at 3σ beam size

$$\text{Hor.,Ver. Available Aperture}3\sigma = \frac{Aperture}{3\sigma_{x,y}} \tag{5.34}$$

the results as a function of the longitudinal position along the line are presented in Fig. 5.35a for the horizontal plane and in Fig. 5.35b for the vertical plane for the the BT1-BTP line, since it is the most concerned by optics mismatch. The RMS normalized transverse emittance used to compute the beam size are those of typical high intensity beam: RMS ϵ_x = 12.85 mm·mrad and RMS ϵ_y = 10.56 mm·mrad [12]

From Fig. 5.35, the ratio between the line aperture and the transverse beam size in both planes are about 1 at the end of the line, which is the position of the injection septum namely SMH 42. This implies that the tails of the beam, that is assumed Gaussian, are cut at 3 σ in the horizontal and the vertical plane. This is the ideal case if the beam is well centred in the septum. However, it is not true. Indeed, as explained in Sec. 5.1, in order to minimize the needed angle the injection kicker has to provide, the offset between the position of the beam at the exit of the septum and the closed orbit has to be reduced. This is exactly the current situation of the PS. The injection kicker is operating at its limit and therefore the beam is pushed very close to septum blade [98] and the goodness of the injection process for the operation of the machine is a compromise between the losses produced in the septum blade, residual orbit oscillations due to an injection error in position and the strength of the kicker. Using then the horizontal beam profile measurements of Fig.5.36 as example, the beam size for a high intensity beam at the exit of the septum can be reconstructed using the measured optics and considering the same position as the beam used during the measurements. This beam size is compared to the horizontal aperture of the septum and if the beam is not centred in the vacuum chamber, up to 3% of the beam can be lost, as illustrated in Fig. 5.36. This figure represents the horizontal beam profile at exit of the septum for a high intensity beam and the beam used during the matching measurements. The aperture of the septum is added with a measured and realistic horizontal position extracted from the optics measurements at the SEM-fil 42 and the result is that the tail which represent 3% of the beam is cut for the high intensity beam whereas 1% for the medium one.

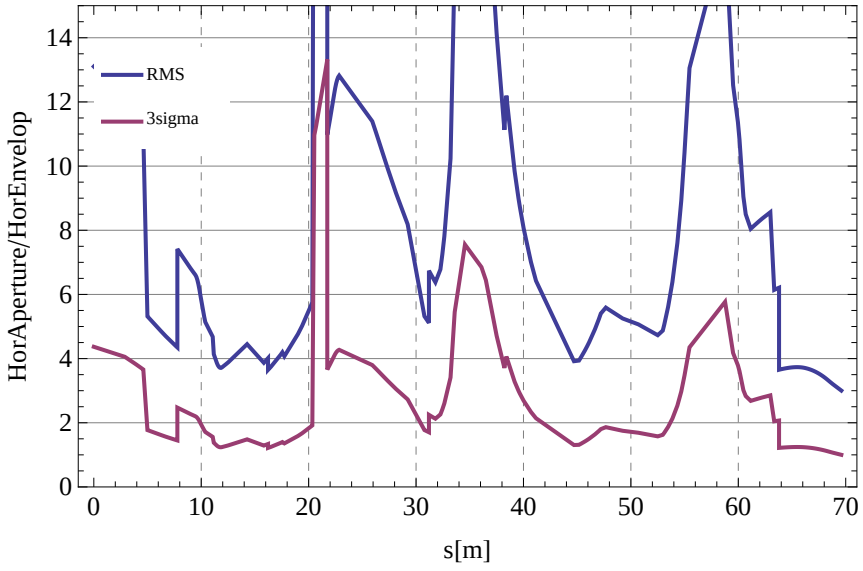

(a)

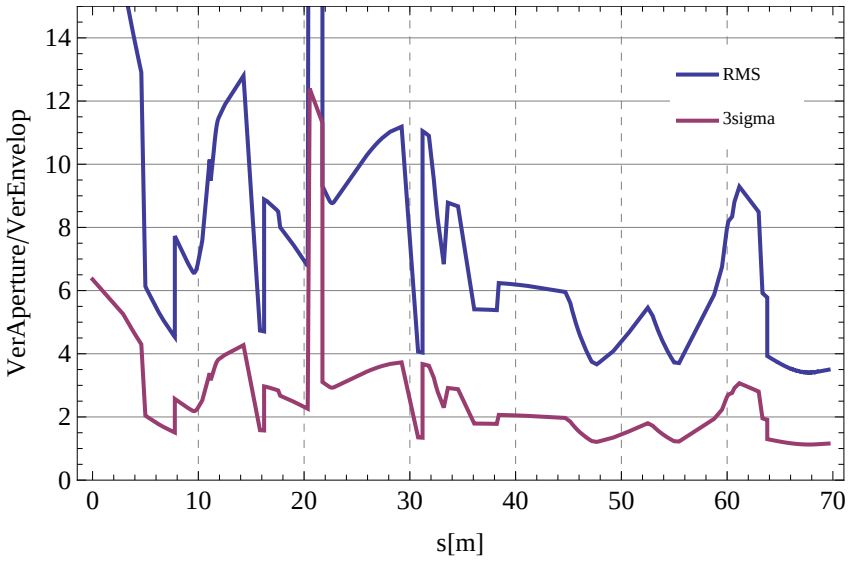

(b)

Figure 5.35: Fig. 5.35a and Fig. 5.35b show the available aperture in the BT1-BTP line as a function of the longitudinal position along the line. They are computed from the current optics and for a beam RMS and at 3 σ

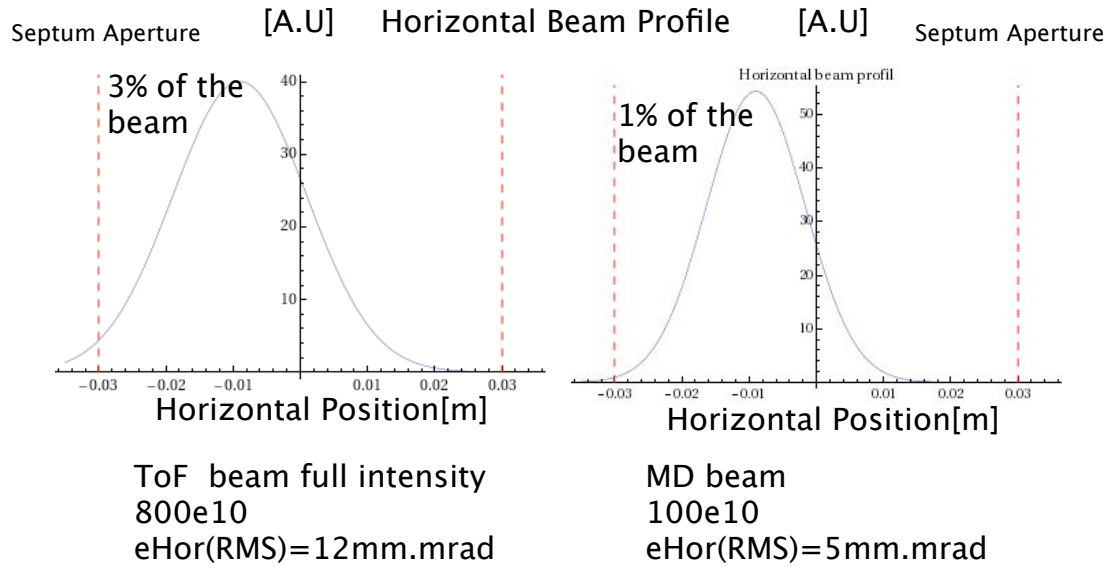

Figure 5.36: Horizontal beam profiles reconstructed from the optics measurements for a high and medium intensity beam. The beam size is compared to the septum aperture which shows that if the beam is not centred in the vacuum chamber, up to 3% of the beam can be lost.

The first bottleneck in aperture for high intensity beams is the large beam size at the injection septum in both horizontal and vertical plane. Due to the limitation of the kicker, the beam is also pushed as close as possible of the septum blade and some tails of the beam are then cut. This explains at least 1% of the total losses at injection. However, as described in Sec 5.2, the loss process is not only due to the aperture restriction at the septum. The proton losses continue turn by turn while the beam is circulating in the machine, while the injection bump is decreasing. This is the subject of the next section.

5.5 Losses during the Injection Bump

While the beam is going through the septum, about 1% of the beam can be lost at the blade. The beam is injected while the bump is the maximum. However the losses occur turn by turn while the injection bump is collapsing. The mechanisms of such losses are not yet understood but possible explanations are briefly discussed here.

The two possible apertures restrictions are at maximum and the minimum of the bump, i.e. in SS42 and at the bumper BSM 43, as illustrated in Fig. 5.37a and in Fig. 5.37b which represent the beam size along the machine and in particular at region of the bump compared to the physical aperture of the machine. The beam envelop is computed from the periodic optics of the PS with MADX.

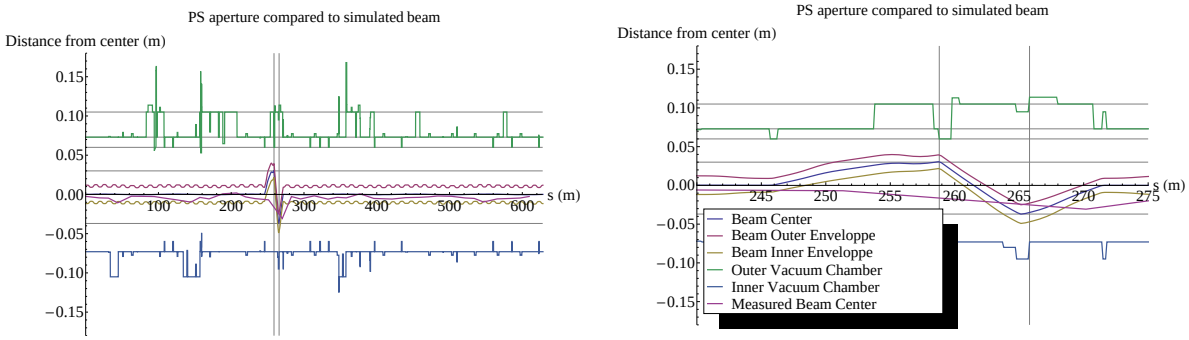

(a) Entire PS

(b) Bump region

Figure 5.37: 1 σ Horizontal envelop calculation with bump, compared to aperture for a RMS horizontal emittance $\epsilon_x = 12.85$ mm·mrad and a RMS $\frac{\Delta p}{p} = 1.6 \cdot 10^{-3}$

The aperture available at the SS42 in terms of beam size is 3.37 whereas it is 3.15 at the beginning of the main magnet 43 at the longitudinal position s in the ring $s = 265.8$ m, therefore the most critical aperture restriction is at the minimum of the bump. Its intensity follows the law $I = I_0 cos(\omega t)$ with $\omega = \pi 10^{-3}/2$. Every 0.1 ms the closed orbit solution is recalculated with the new bump intensity. In Fig. 5.38, the available aperture is presented as a function time, which represents the time in which the injection bump collapses. When the beam is injected, the available aperture in term of σ is 3.15 and it increases then up 5.5. However, these losses would occur during 150 μs while the turn by turn BLMs signal in Sec. 5.2 are recording a signal during at least between 300-800 μs.

Another possible source of losses is the elliptical shape of the PS vacuum chamber. If the beam is horizontally off-center, as it is the case during the bump, some particles can be lost in the vertical plane, where the vertical aperture is decreasing. Let consider the available space with respect to the real geometry of the problem. The vacuum chamber has an elliptical shape. So the distance between the beam center $(x_{bc}, 0)$ and the wall can be expressed as function of an

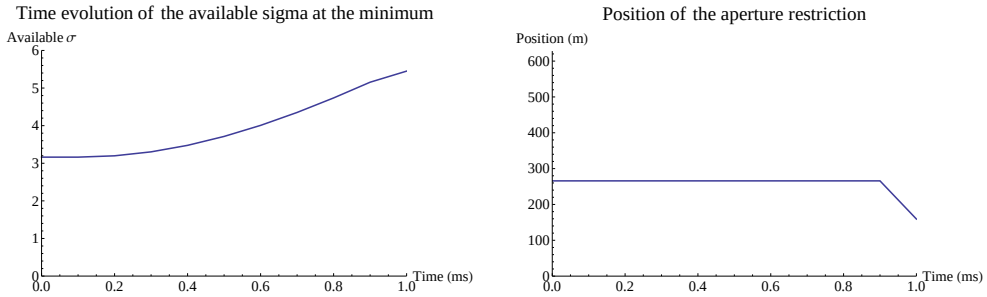

(a) Minimum available sigma as function of time (b) Position of the minimal available space

Figure 5.38: Time evolution of the aperture restriction in SS43

angular parameter θ, and we would like to identify the minimal distance

$$x(\theta) = x_0 cos(\theta) \qquad y(\theta) = y_0 sin(\theta) \qquad x_0 = 2 \cdot y_0 = 73\ mm \tag{5.35}$$

$$d(\theta)^2 = (x_0 cos(\theta) - x_{bc})^2 + y_0^2 sin^2(\theta) \tag{5.36}$$

$$d(\theta)' d(\theta) = sin(\theta)(-x_0(x_0 cos(\theta) - x_{bc}) + y_0^2 cos(\theta)) \tag{5.37}$$

$$-x_0(x_0 cos(\theta) - x_{bc}) + y_0^2 cos(\theta) = 0 \qquad cos(\theta) = \frac{x_0 x_{bc}}{x_0^2 - y_0^2} \tag{5.38}$$

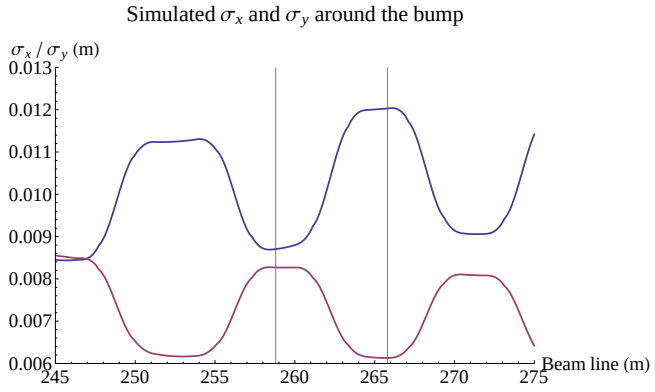

Figure 5.39: σ_x and σ_y around the bump

In our case the beam at the minimum of the bump is at $x_{bc} = 4.0\ cm$, yielding to $d = 27.5\ mm$. The vertical emittance of the beam is different from the horizontal one and the beta functions

in the two planes have opposite phases

$$\epsilon_y^* = 7 \cdot 10^{-3}\ mm \cdot mrad \qquad \epsilon_y = \epsilon_y^* / \gamma\beta = 3.10\ \mu m \tag{5.39}$$

Using the values for $\beta_{x/y}$ and $D_{x/y}$ given by Mad-X the sigma function is plotted in both direction along the beam line. The sigma value at the minimum of the bump into the direction where the minimum available space appears is calculated as follows.

$$\sigma_\theta^2 = (\sigma_x cos(\theta))^2 + (\sigma_y sin(\theta))^2 \qquad \sigma_\theta \approx 9.5\ mm \tag{5.40}$$

The available space was $d = 27.5\ mm$, thus we get a cut at $27.5/9.5 \approx 2.9\sigma$ around the magnet in section 43. This would already be sufficient to explain the beam losses.

With only aperture restriction at the septum and at the minimum of the bump in the the horizontal and the vertical planes, it is possible to explain 3% of losses but only during a few turns which depends on the tune. When the different tails are lost in the aperture, in less than 10 turns if the transverse tunes are about $Q_{x,y} = 6.11, 6.28$ should stopped due to the fact that the beam is at its initial position in the transverse phase space without all the tails, cut by aperture restrictions. However, the losses continue up to 800 μs while the bump is decreasing, depending of the type of beam as shown in Fig. 5.14a and Fig. 5.14b. In addition, there is periodic pattern of about 8 turns, meaning that after this period, the phase space is refilled either by slow emittance blow-up or by resonance crossing and possible sources will be discussed later in Sec. 5.7.

One the main goal of the this study was reproduced by Monte Carlo simulations the pattern of losses and the radiation detected by the BLMs while the beam in injected in the ring. This is the subject of the next section.

5.6 FLUKA simulations of beam losses at injection

As explained earlier in Sec. 5.2, beam losses are observed when the beam is injected in the machine. In order to verify that the high radiation levels observed at Rue Goward, which are correlated with the PS BLMs, are related directly to the injection losses, a shower simulation with the code FLUKA [68, 69, 99] has been performed.

FLUKA is a Monte Carlo code that tracks a given distribution of source particles, called primary, through a geometry programmed by the user. Interactions between the primary particles and the different materials in the geometry are sampled and all secondary particles are tracked. Both the hadronic and the electromagnetic showers are simulated. The simulation outputs are different quantities specified by the user, for example the energy deposition. in given parts of the geometry or a full record of all particle tracks and interactions.

A geometry of the region around the injection septum has already been implemented in FLUKA [100]. The existing input file has been adapted for this particular study through the addition of BLMs. The FLUKA geometry is shown in Fig. 5.40. The BLMs, of the type ACEM, are described in detail in Sec. 5.2

The primary particles are started at the surface of the inside of the beam pipe at the longitudinal locations with the smallest normalized aperture as calculated with MAD-X. These locations correspond approximately to the maximum and minimum of the PS injection bump and they are shown in Fig. 5.40. Several simulations were performed, and the relative weights of the locations of the source particles were empirically adjusted in order to fit with the measurements. This was done to see if the loss locations are compatible with the aperture restrictions. The different positions with their relative weights are also described in Table 5.9. The particles are assumed to be at their maximum amplitude and therefore have a zero angle towards the longitudinal beam axis. An example of a starting distribution in the transverse plane is shown in Fig. 5.41.

Injection	30%	At Septum 42, an electrostatic dipole in the straight section 42 to deflect the incoming beam form the PSB into the PS. The tail of the beam is hitting on the inside at the end of the septum
Maximum of the bump	10%	At the beginning on the outside of Septum 42, the tail of the beam is cut at the blade
Minimum of the bump	60%	On the inside on the first metre of Magnet 43. Spread on three equally spaced spots (30%,20%,10%)

Table 5.9: Location of the different sources in FLUKA

In order to gain in CPU time, 33 simulations were launched in parallel on a cluster and the

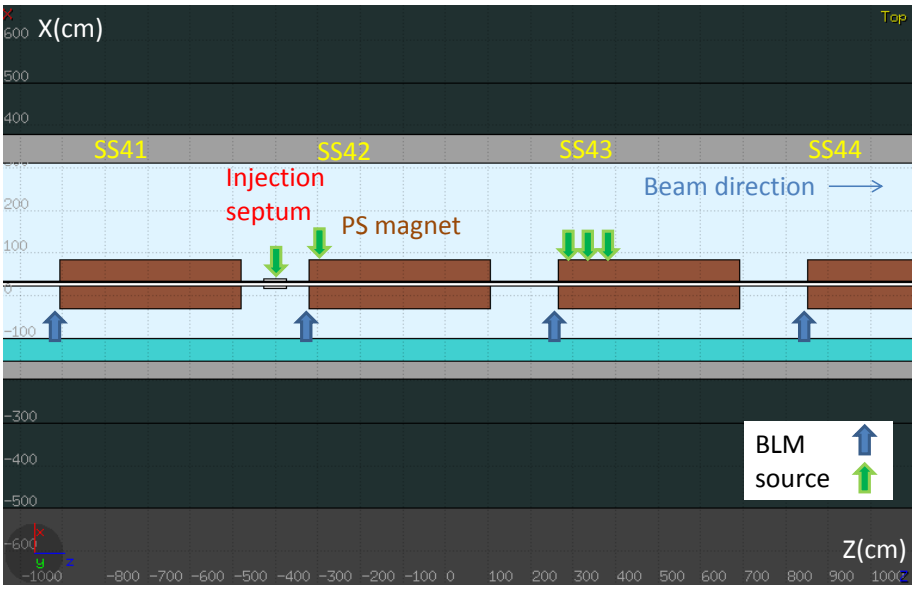

Figure 5.40: A cross-section through the FLUKA geometry in the horizontal-longitudinal plane around the injection septum. The longitudinal locations of the source particles, representing the losses, as well as the added BLMs, are shown.

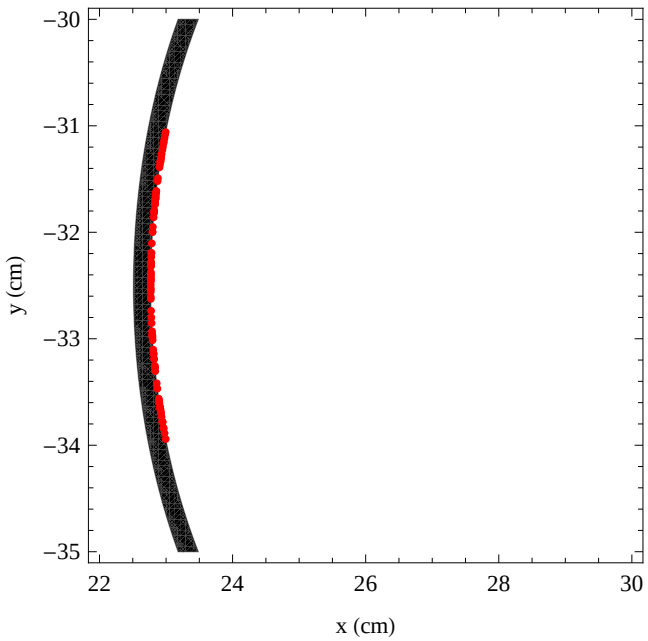

Figure 5.41: Some starting coordinates of primary particles in the FLUKA simulation in the transverse plane (represented as red dots). The particles are hitting the inside of the vacuum pipe (shown in black).

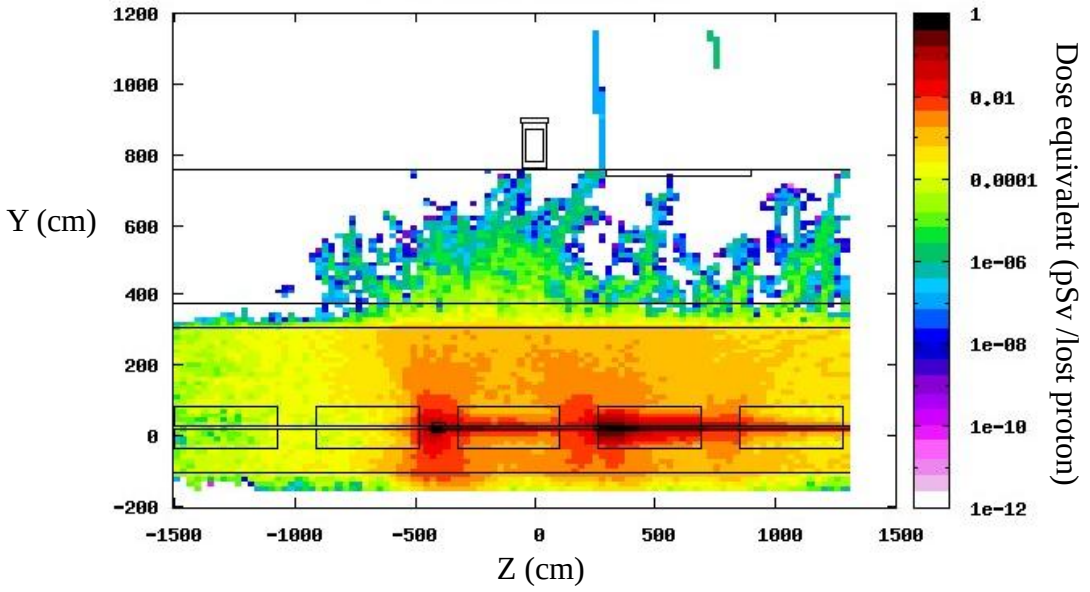

Figure 5.42: The simulated dose from FLUKA in a vertical cross section through the geometry.

results combined in the end. In each simulation, 1×10^6 primary particles were launched, meaning a total statistics of 33×10^6. Furthermore, an energy cut-off of 0.1 MeV was applied to speed up the simulations, as well as a region-based importance biasing. This means that in less important parts of the geometry, only a fraction of the total shower particles are tracked, but attributed a higher statistical weight. Once in an important region, particles are instead split in several identical particles in order to increase the number of tracked histories.

The resulting simulated equivalent dose in different parts of the geometry is shown in Fig. 5.42. As expected, the highest dose is obtained close to the septum and in the beginning of Section 43. In the top part of the plot the radiation monitor at Rue Goward can be seen. Later work [100] has shown that a simulation with significantly higher statistics reproduces well the observed radiation levels on the road. The resulting profile of the BLM signals is shown in Fig. 5.43. Both the simulation and the measurements have been normalized to the highest peak. As can be seen, the profiles match rather well.

In conclusion, the FLUKA simulations have shown that the observed BLM signals during injection are qualitatively compatible with the presumed loss locations and provided a first step towards a quantitative understanding of the radiation levels at Rue Goward. A more detailed study, including the quantitative normalization to the real flux of protons has later been done by others [100], with good agreement.

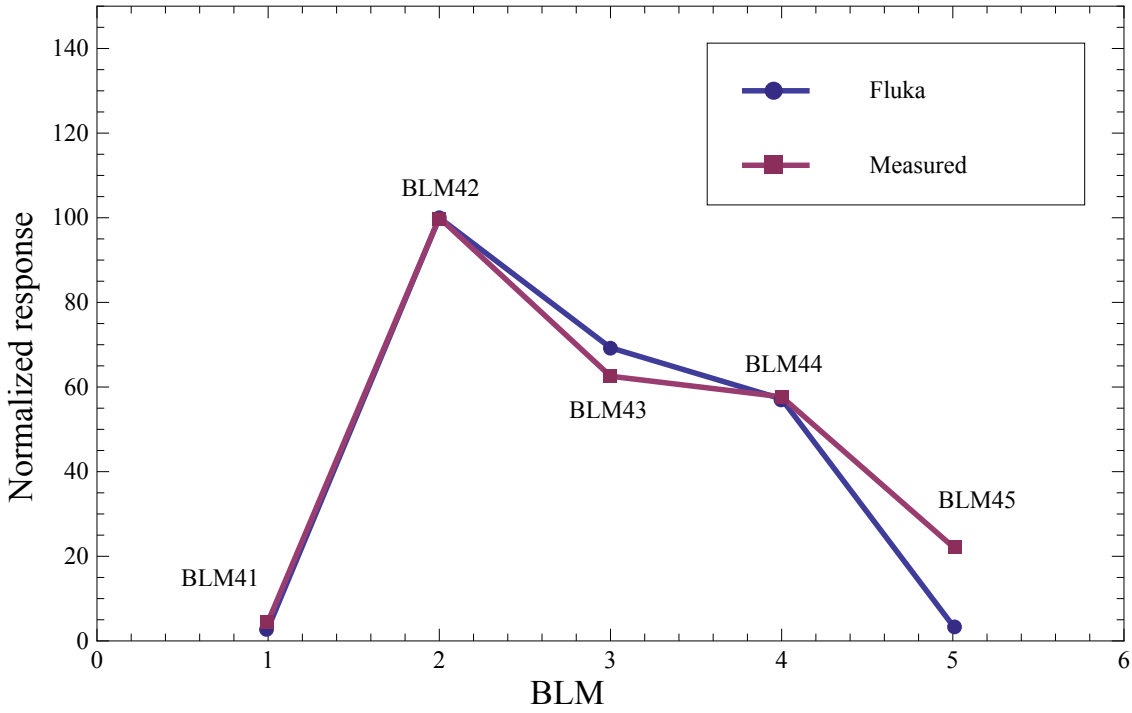

Figure 5.43: The loss patterns from measurements and from FLUKA simulations. Both results have been normalized to the highest peak in the measurements, set at 100%. Therefore, the second point in the two curves agree exactly.

5.7 Proposal - Discussions

In this chapter, the results of proton beam losses were presented. The optics mismatch between the transfer line and the injection of the PS was evaluated and aperture restrictions were identified thanks to these experiments. In particular, the beam size of the high intensity beams are now large and they reach the aperture of the septum. Maximum and minimum of the injection bump were also identified as aperture restriction, however, it is rather difficult to conclude that they are the only mechanism of the observed losses. Only a complete tracking of the trajectory from the Booster over 500 hundred turns after injection into the PS could confirm the bottleneck identified in this study.

Several propositions were done in order to alleviate beam losses at injection. First, a new optics in the transfer line is needed, not necessary to get a perfect mismatch but only gain in flexibility. Several attempts were tried to match the horizontal dispersion and the betatron function by keeping the vertical residual dispersion at a reasonable value. By keeping the line as the current one, it is rather difficult, therefore the idea is to add one quadrupole to gain in flexibility.

The problem of the high intensity beams is not the mismatch but aperture restriction at the septum and in the ring. Smaller beam size in both planes at the septum would be an asset. It appears that increasing the aperture in the septum would reduce the quality of the field [101], therefore the only way to reduce the losses is to make a small beam size at the bottleneck, with a collimation system downstream the septum to remove unwanted tails. This method will mean that the PS optics should be adapted the new optics in the transfer line, which mean another risk of mismatch. Since LHC beams are not so concerned by beam losses at injection, except at the septum, two different optics could take place in the BT-BTP line. The current optics could be kept for the LHC beams and another optics would be implemented for high intensity beams. The gradients of the quadrupoles should then change from shot to shot depending of the type of beam crossing the transfer line. Several magnets should be then changed. This is the reason why it would be an asset to gain in flexibility with the possibility to change the optics in the line.

The PS optics at injection should be adapted for this new optics. Small beam size in the transverse plane implies small beta-functions, which would help the kicker strength, see Sec.5.1, Eq. 5.4.

The turn by turn losses are rather slow and they occur up to 800 μs for the CNGS beam for instance, while the injection bump is decreasing, meaning that the available aperture is going to large values. Every 8 turns, a local maximum in losses is reached as shown in Fig. 5.14a and Fig. 5.14b. Even with an larger aperture, particles are lost in SS42 and SS43. The transverse phase space is then refilled in 8 turns, a betatron period, which is the time for a single particle to describe the phase space. Some non-linear forces are then acting on the particles to fill the phase space. The PS is a medium energy machine and it is well know that direct space charge is present at injection [102]. In order to repopulate the transverse phase space, space charge

combined to resonance crossing are good candidates.

Several possibilities were considered to change the PS optics at injection using already existing quadrupoles in the ring, and the so-called QKE quadrupoles. They are magnets used in order to perturb the periodic optics at extraction [7]. The aim is to check how the beta function in the horizontal plane evolve if the quadrupoles are pulsing and it shown in Fig. 5.45 for two values of currents in the QKE, the blue curve is the unperturbed case. Fig. 5.44 shows the horizontal beta function along the PS. A perturbation is opened for $s > 150$ m while before the machine is unperturbed. It is rather the same for the vertical plane. Fig. 5.44 present the β_x function evolution while the current in the QKE quadrupoles is increasing. The optics is computed in the injection straight section 42, SS 43 and at the injection kicker. The beta function in the horizontal plane is decreasing at the SS 42 and SS 43 which would help to reduce the beam size at the maximum and at the minimum of the bump. However the vertical beam size will increase and the beta function is going up at the injection kicker KFA 45, which would not help the strength of the magnet. Studies are still ongoing to find a better optics.

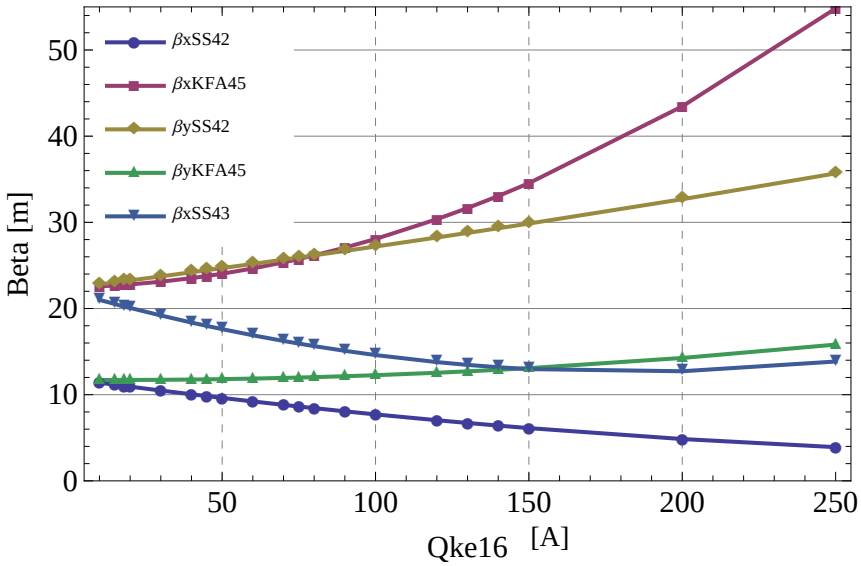

Figure 5.44: Horizontal β-function at different important location of the ring close to th einjection area when the current of the QKE quadrupoles are increased.

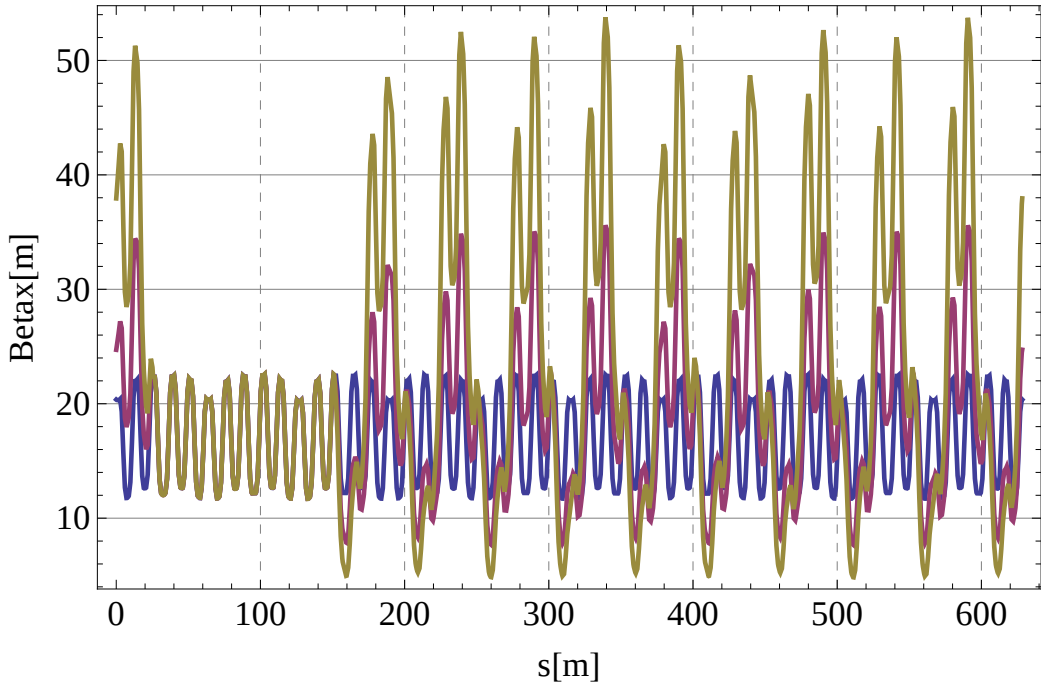

(a) Horizontal beta-function

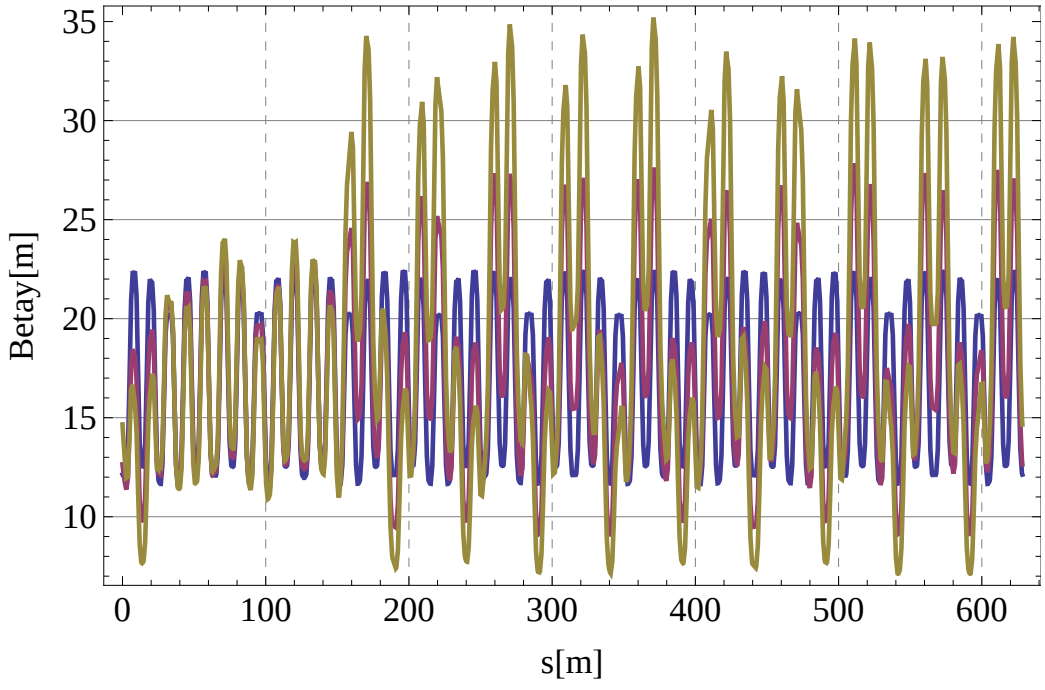

(b) Vertical beta-function

Figure 5.45: Horizontal and vertical beta function along the ring for different value of the current in the QKE. The blue curve is for the unperturbed case.

Let assume a high intensity beam injected into the PS. Due the number of protons, direct space charge is present and provoke a tune spread in the bunch. Each particle then has different tune and the total tune spread depends on the distribution as [24],

$$\Delta Q = \frac{r_p N_b}{(2\pi)^{2/3}\gamma^2\beta\sigma_z}\oint \frac{\beta_{x,y}(s)ds}{\sqrt{\epsilon_{x,y}\beta_{x,y}(s)}(\sqrt{\epsilon_x\beta_x(s)}+\sqrt{\epsilon_y\beta_y(s)})} \tag{5.41}$$

and for instance $\Delta Q_y = -0.31$ for the ToF beam and $\Delta Q_y = -0.26$ for the LHC-50 ns ultimate beam. Typical operational transverse tunes in the PS are situated between 6.11 and 6.30. With such tune spread, particles might cross some dangerous resonances, making then the particles oscillating at high amplitude and provoking transverse emittance blow-up. Some macro particle codes exist such as ORBIT, which is a code to simulating space charge. Developments are ongoing at CERN to use ORBIT with the optics code MADX-PTC and therefore consider the optics of the machine with space charge simulation. This would be very convenient for the case of the PS to simulate the decrease of the bump and compute all around the ring the effect of space charge on the transverse emittance while the particles are lost in the aperture. An example has been performed for the ToF beam in order to evaluate the effect of the space charge on the tune spread. The beam parameter of the the ToF beam were given to ORBIT which defines some space charge nodes along the ring. PTC-MADX is doing the tracking of the particles between these nodes. It is then very convenient, in particular if change in optics occur, such beta-function for instance. Due the high CPU time, a try of 100 turns was performed. Fig. 5.46 presents the tune diagram (Q_x, Q_y) after 20 turns for a beam of 700×10^{10} protons in a single bunch for a full bunch length of 200 ns. 1000 macro particles were launched. Fig. 5.46 shows that some particles can cross the integer resonance, particularly destructive. An hypothesis is the following: due to direct space charge, protons are crossing resonances and start to oscillate. They can be lost in the aperture or not, since their position in the necktie depends on their position in the longitudinal distribution. Due to synchrotron motion, the particles exchange also their positions in the necktie. Therefore even if they are lost, other particles in the distribution will cross resonances until the beam losses are such that the direct space charge decreases or the bump has collapsed. This idea has been proposed in Ref. [103] and space charge studies by resonance crossing started in the PS [104].

A way to decrease the space charge effect in the PS at injection is to injected at higher energy. This is studied in the current PS Upgrade project which belongs to the LIU project, the LHC Injector Upgrade. The aim of the project is to identify the different limitations for the production of the High Luminosity LHC beam. Increasing the injection energy from 1.4 GeV kinetic to 2 GeV would be a gain of 63% concerning the transverse space charge effect. There is also a natural gain in beam size due to smaller transverse emittance, which then makes easier the production of small beam size. On the other hand, the kicker strength has to increase due to the change in magnetic rigidity $B\rho$. In the new injection system, it has been studied to install an additional kicker to correct the leakage in trajectory that the current kicker would not be able to correct: the current kicker is at the limit of its strength, which means that, if the injection energy is increasing, the maximum angle it can provide would not be enough

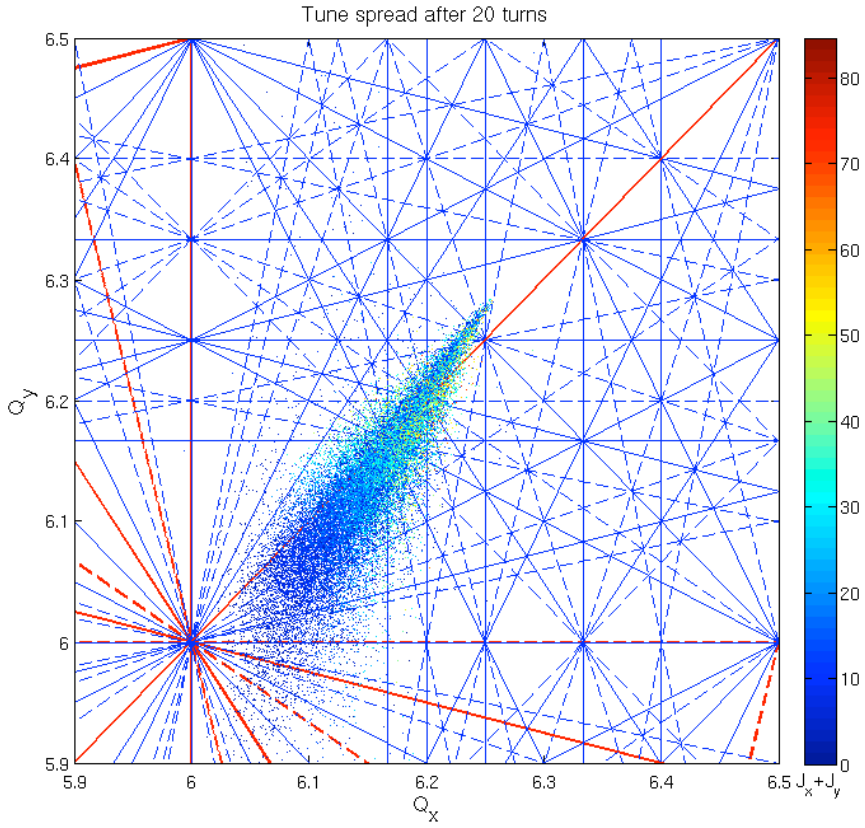

Figure 5.46: Tune diagram computed by ORBIT after 20 turns for a ToF beam.

to kick the beam on the closed orbit. Therefore the beam will continue to oscillate until a second kicker compensate the leakage that the first kicker could not provide. The possibility to implement two different optics in the transfer line between the PSBooster and the PS is currently studied in the framework of the PS Upgrade, as well as the effect of space charge and resonance crossing [104]. Impedance studies are also on going.

In this context, the measurements of the tune shift with the beam intensity was evaluated. The first aim was to evaluate the effective imaginary impedance: the beam interaction with the imaginary part of the impedance produces a real tune shift, whereas, as studied in Chapter 3, the beam interaction with the real part of the impedance produces an imaginary tune shift, therefore a growth rate. Coherent tune shift give important informations about impedance. The aim is also to evaluate from those measurements the part of the tune shift due to space charge.

5.8 Transverse Impedance Measurements with Betatron Frequency Shift

5.8.1 Tune Shift Measurements at Injection Energy

Experimental Beam Conditions

A single bunch proton beam was set up with the parameters of the Table 5.10 for the measurements with a long flat bottom magnetic cycle shown in Fig. 5.47a. The duration of the energy plateau is about 630 ms and then the beam accelerated and extracted at 3.5 GeV/c. The transverse tunes $Q_{x,y}$ were set up with the low energy quadrupoles at the values of Table 5.10. The voltage of 10 MHz RF cavities which determine the height of the bucket were adjusted as in Fig. 5.47b. This setting was chosen in such a way to minimize longitudinal dipolar and quadrupolar oscillations of the bunch length after injection due to a longitudinal mismatch. The transverse tunes $Q_{x,y}$ are acquired while the number of proton N in the bunch is varied in a such a way to establish a function $\Delta Q_{x,y} = f(N_b)$. For each set of data, the longitudinal emittance is measured and the horizontal and the vertical tune are acquired for different beam intensities with a beam position monitor which belongs to the "diode based-band tune" system [77] so-called BBQ.

Kinetic energy	1.4 GeV
Lorentz factor γ_{rel}	2.47
Momentum compaction factor η	-0.137
Transverse programmed tunes $Q_{x,y}$	6.210, 6.245
Chromaticities (natural) $\xi_{x,y}$	$-0.8, -1$
Total RF Voltage 10MHz cavities	60 kV
RF Harmonic h	8
Full bunch length 4 σ_t	180 ns
Longitudinal emittance ϵ_l (2 σ)	$\simeq$ 2 eVs
Synchrotron Tune Q_s	0.0023

Table 5.10: Injection beam parameters.

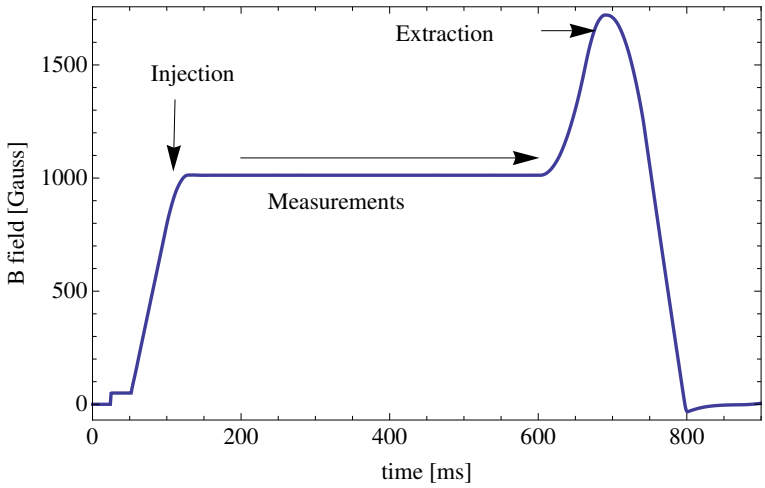

(a) Magnetic field cycle used during the measurements.

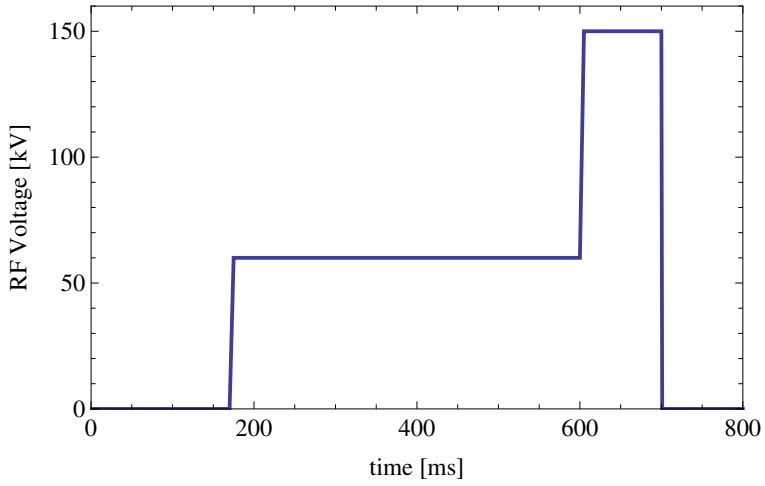

(b) Voltage applied on the RF 10 MHz cavities.

Figure 5.47: Magnetic field applied on all along the flat bottom cycle used during the measurements presented in the Fig. (a) and the voltage applied to the RF 10 MHz cavities in the Fig. (b)

Experimental Observations

The transverse tune Q is the number of beam oscillation over a machine revolution and Q is given by the the ratio of the betatron frequency ω_β by the revolution frequency ω_0

$$Q = \frac{\omega_\beta}{\omega_0} \tag{5.42}$$

In general, the beam is transversally kicked, i.e. a dipole magnet called kicker gives an angle x' ou y' to the particles and then the beam will perform betatron oscillation. In the case of the PS, a electromagnetic wave, called a chirp, that the frequency is closed to the tune, is emitted to excite the beam which performs then betatron oscillation around the machine. The BBQ is

composed by a beam position monitor (BPM) which acquires the transverse position of the bunch particle turn by turn and the tune is obtained by applying a Fast Fourier Transform (FFT) on the motion of the transverse beam centroid [77]

The measured horizontal tune spectrum revealed three peaks in frequency domain are shown in Fig. 5.48. The main peak corresponds to the horizontal tune Q_x, the second peak is the vertical tune visible due to the linear coupling of the machine. Another peak appears at 0.2017. Chromaticity corrections with sextupoles at injection shows that the third peak can disappear, therefore it might either to the synchrotron side band or a headtail mode if the beam is unstable by headtail instability.

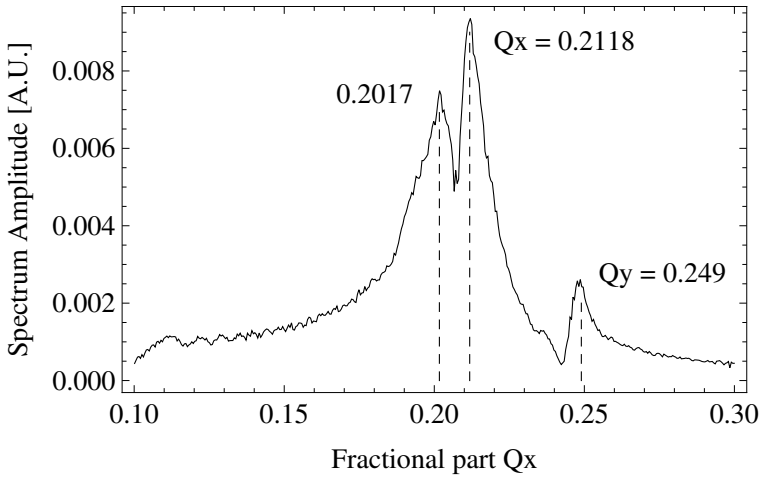

Figure 5.48: Horizontal tune spectrum for a beam intensity of 100×10^{10} protons. The horizontal tune frequency is the peak at $Qx = 0.2118$, the vertical tune at $Qy = 0.249$ and the third frequency at $Q = 0.2017$.

Tune Shift Data at Injection Energy

The measured horizontal and vertical tune shifts $\Delta Q_{x,y}$ have been analysed and correlated to the beam intensity in Fig. 5.49. The space charge force is a defocusing force - see Sec. 1.4.2 about space charge - therefore it is not surprising that the tune in both planes is decreasing while the beam intensity is increasing in the bunch. At this low energy, space charge is expected to be provoke a tune shift. In fact, a tune shift due impedance is also expected, the total tune shift is then the sum of the tune shift due to space charge and due to transverse impedance. In this experiment, the coherent motion of the beam is measured. The betatron oscillation of the beam as a whole represents a coherent motion, which has a little effect on the direct space charge effects, determined by internal forces inside the beam. The images charges and currents - indirect space charge - induced in the wall are modulated by the coherent beam oscillation. This leads to coherent tune shift different from incoherent ones. Here the tune shift ΔQ_y in the vertical plan is more important than the horizontal tune shift ΔQ_x due to the

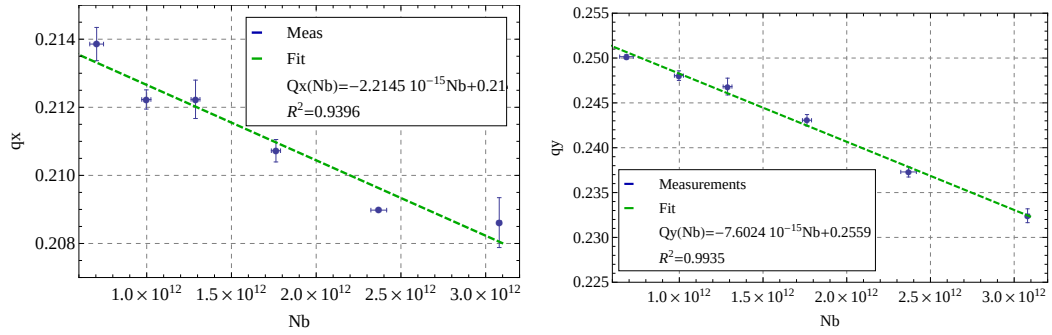

(a) Horizontal tune shift

(b) Vertical tune shift

Figure 5.49: Transverse tune shift $\Delta Q_{x,y}$ measurements as a function of the beam intensity at injection energy.

elliptical shape [64] of the PS vacuum chamber. ΔQ due to the indirect space charge coherent is estimated as following with the Laslett coefficients [6]

$$\Delta Q_{coh} = -\frac{N_b R r_0}{\pi Q \gamma \beta^2}\left(\frac{\epsilon_1}{h^2}+\frac{\epsilon_2}{g^2}+\frac{\xi_1}{h^2}\frac{1-\beta^2}{B^2}\right) \tag{5.43}$$

with N_b the total number of particles in the bunch, R the machine radius, r_0 the classical proton radius, Q the unperturbed tune (Q_x/Q_y), γ,β the relativistic Lorentz factors, B the bunching factor given by the longitudinal emittance measurement system - the tomoscope - h half inside height of the vacuum chamber (h=35 mm for the PS), g is the half magnet gap and $\epsilon_{1,2},\xi_1$ the Laslett coefficients. The bunching factor is given by the tomoscope in Fig. 5.50, while the longitudinal emittance is acquired. From the Eq. 5.43, it can be see easily that the coherent tune shift will be more important in the vertical plane due to the $1/h^2$ term. A linear fit is applied on the measured tune shifts and the equations are written as $Q_{x,y} = a \cdot Nb + b$

$$Q_x(N_b) = (-2.2145 \pm 0.2873)10^{-15} \times N_b + (0.2149 \pm 0.0005) \tag{5.44}$$

$$Q_y(N_b) = (-7.6024 \pm 0.3083)10^{-15} \times N_b + (0.2559 \pm 0.0005) \tag{5.45}$$

The errors on the slope and on the coefficient at the origin were deduced from the error made on the linear regression. The error on the slope for a linear fit $y_i = ax_i + b$ is

$$\begin{aligned}\sigma_a &= \sqrt{\frac{\frac{1}{n-2}\sum_{i=1}^{n}(y_i-\hat{y}_i)^2}{\sum_{i=1}^{n}(x_i-\overline{x})^2}} \\ \sigma_b &= \sqrt{\frac{1}{n-2}\sum_{i=1}^{n}(y_i-\hat{y}_i)^2}\sqrt{\frac{1}{n}+\frac{\bar{x}^2}{\sum_{i=1}^{n}(x_i-\overline{x})^2}}\end{aligned} \tag{5.46}$$

where n is the number of measurements, (x_i, y_i) are the ith values of the variables in the measurement, $\overline{x}$ are the average values of the variable x, $\hat{y}$ is the predicted value of the variable

y by the model. The goodness of the linear fit is defined by the coefficient R^2

$$
\begin{aligned}
R^2 &= 1 - \frac{SS_{err}}{SS_{tot}} \\
SS_{err} &= \sum_{i=1}^{n} (y_i - \hat{y}_i)^2 \\
SS_{tot} &= \sum_{i=1}^{n} (y_i - \overline{y})^2 \\
\overline{y} &= \frac{1}{n} \sum_{i=1}^{n} y_i
\end{aligned}
$$

For each linear fit, the coefficient R^2 is shown in Fig. 5.49a and in Fig. 5.49b and a very good agreement with linear tendance of the tune shift with respect to beam intensity is found. The tune shift from the origin are about

$$
\begin{aligned}
\Delta Q_x &= Q_x(Nb = 308 \times 10^{10}) - Q_x(Nb = 0) = -0.0063 \\
\Delta Q_y &= Q_y(Nb = 308 \times 10^{10}) - Q_y(Nb = 0) = -0.023
\end{aligned}
$$

The measured tune shifts at injection are composed by the tune shifts due to space charge forces and due to the beam interaction with the impedance. The next section will be devoted by the measurements performed at extraction energy of LHC beam. At such energy, space charge forces become negligible and the measured tune shifts are mainly due to the impedance.

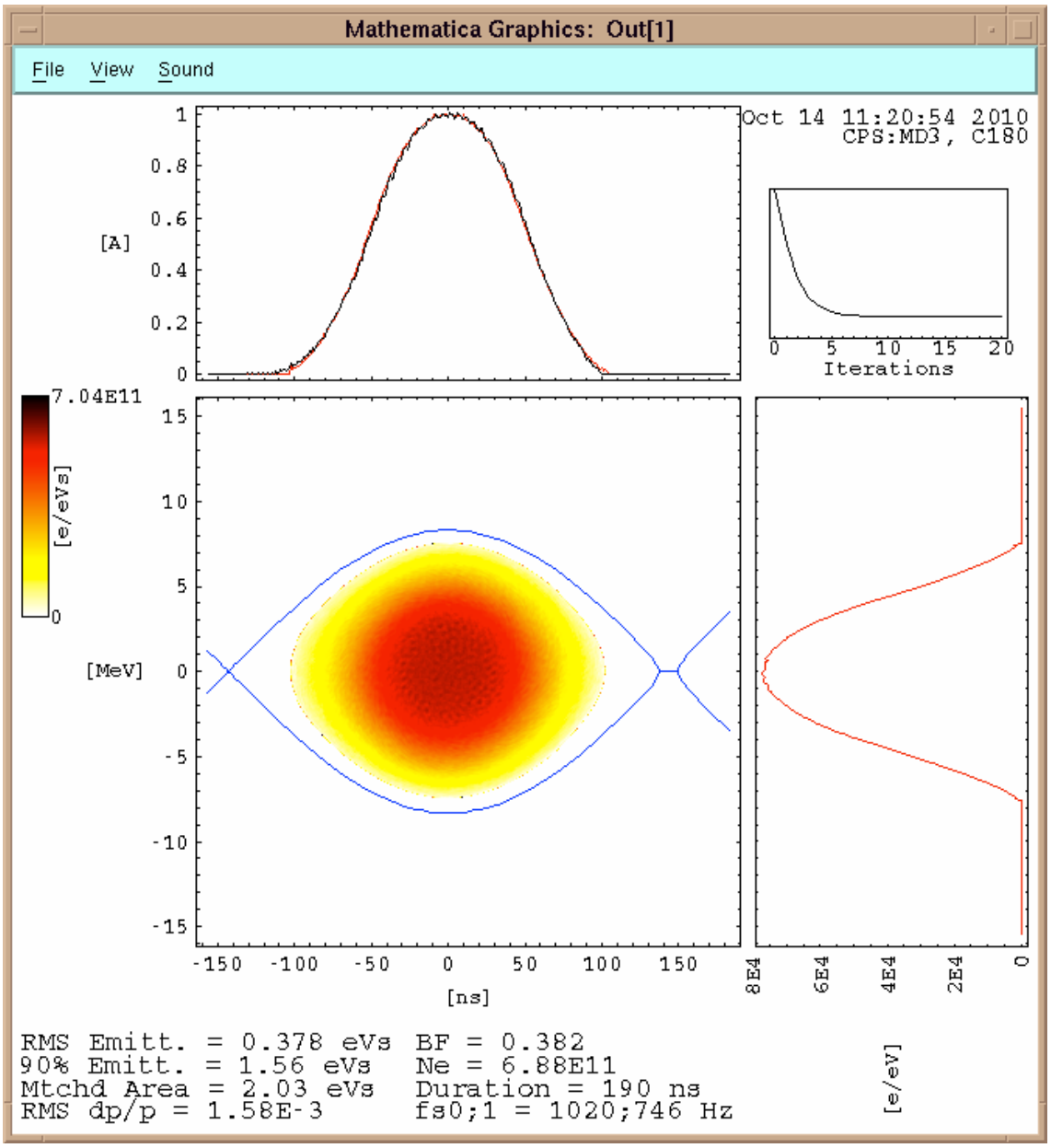

Figure 5.50: Example of longitudinal emittance measurements with the tomoscope [3]. The bunch length and the bunching factor are also computed.

5.8.2 Tune Shift Measurements at LHC extraction Energy

Experimental Beam Conditions

Tune shift measurements were performed at 25 GeV which corresponds to the ejection kinetic energy of LHC beams. The LHC magnetic fields have a long flat top energy plateau to perform the measurements. Again, a single bunch beam was set up with a LHC-like magnetic field presented in Fig. 5.51. The beam parameters are presented in the Table. 5.11. The measurements and the analysis were performed in the same way as the data tune shift at injection.

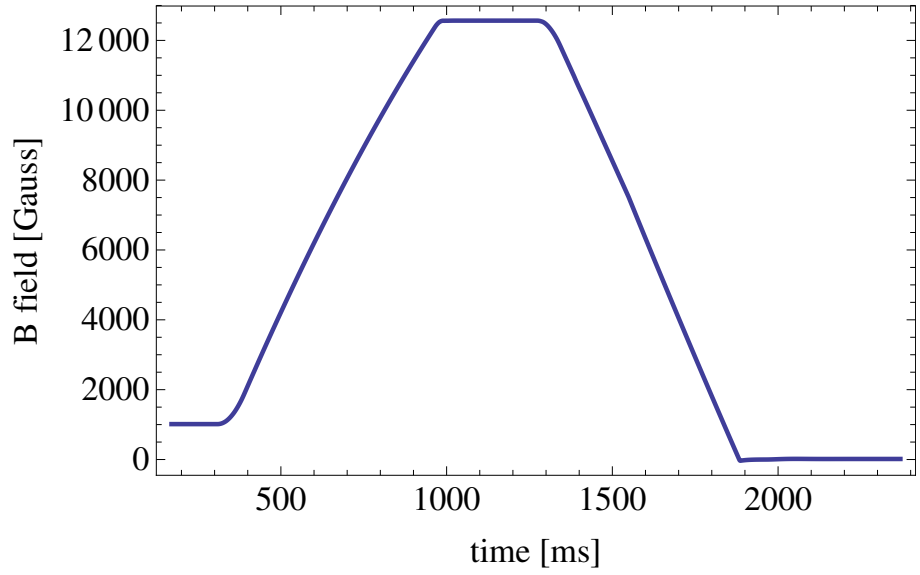

Figure 5.51: LHC magnetic field cycle used for the measurements at extraction energy.

Tune Shift at Extraction Energy

The analysis of the horizontal tune shift revealed the change in Q_x with the beam intensity is very small. In addition the horizontal tune appeared to be drifting with time on the flat top as shown in Fig. 5.52, whereas the optics is not changing. More detailed tune measurements [105] on a long plateau at different beam energy show that both betatron frequencies $Q_{x,y}$ can be affected. Recent studies have shown that this defocalisation of the beam would be due to the bare machine. Eddy currents at the edge of the main PS magnets might be a possible source of this effect [106]. In the experiment, the defocalisation of the beam is mainly visible on the horizontal tune. Therefore the Fast Fourier Transform cannot be applied all along the flat top at least in the horizontal plane.

Kinetic energy	25 GeV
Lorentz factor γ_{rel}	27.7
Momentum compaction factor η	0.0254615
Transverse programmed tunes $Q_{x,y}$	6.24, 6.26
Chromaticities (corrected) $\xi_{x,y}$	0.2, 0.2
Total RF Voltage 10 MHz cavities	200 kV
RF Harmonic h	8
Full bunch length 4 σ_t	50 ns
Longitudinal emittance ϵ_l (2 σ)	≃2.7 eVs
Synchrotron Tune Q_s	0.0005

Table 5.11: Extraction beam parameters.

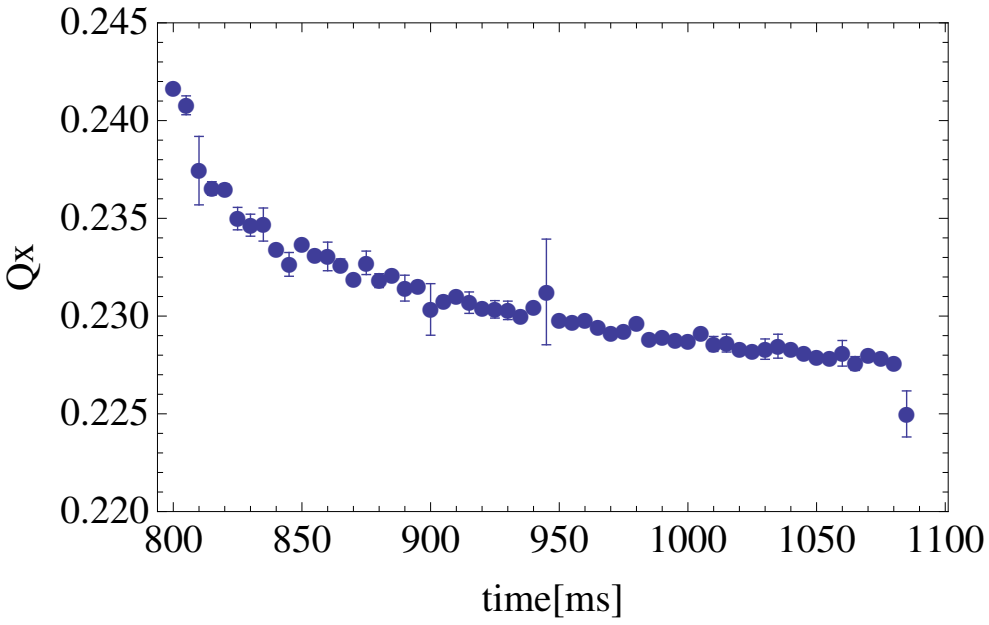

Figure 5.52: Measured horizontal tune at flat top energy 25 GeV as a function of time.

$$Q_x(Nb) = (-0.1164 \pm 0.03) \times 10^{-15} \times Nb + (0.229 \pm 0.0001) \tag{5.47}$$

$$Q_y(Nb) = (-1.0545 \pm 0.1045) \times 10^{-15} \times Nb + (0.2674 \pm 0.0003) \tag{5.48}$$

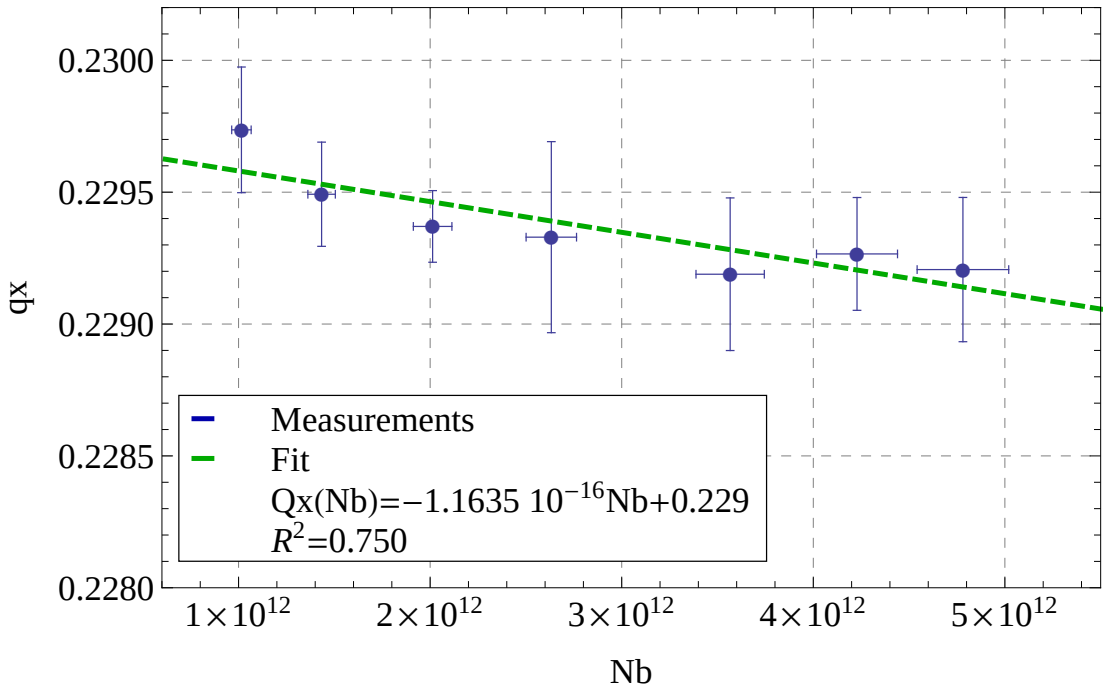

(a) Horizontal tune measurements

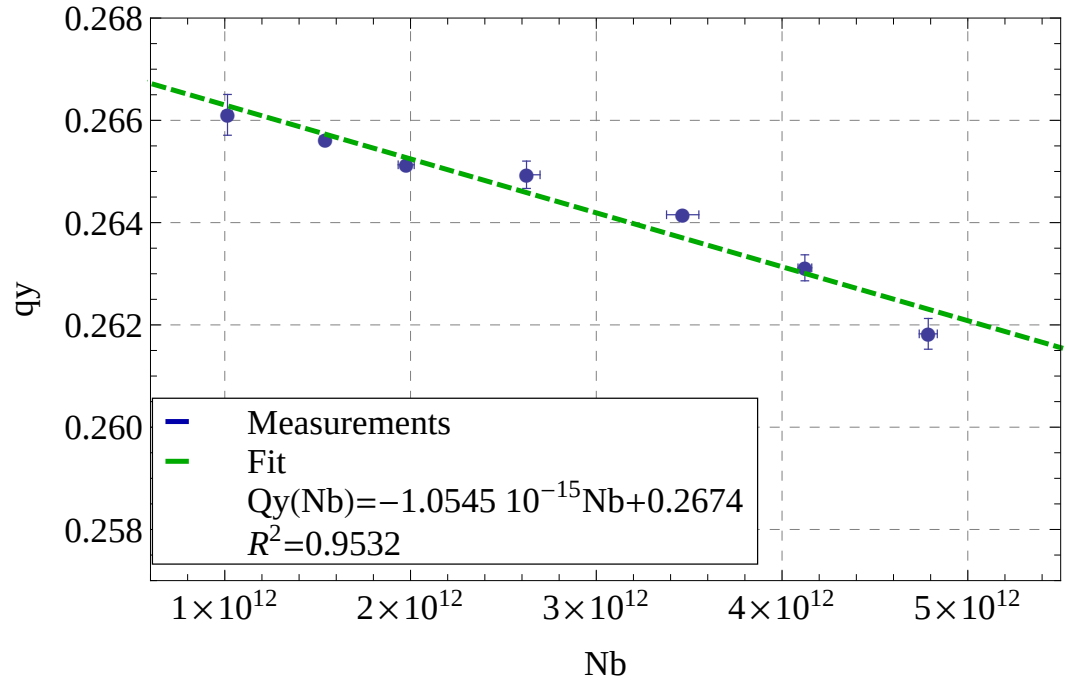

(b) Vertical tune shift measurements at 26 GeV/c.

Figure 5.53: Transverse tune measurements at extraction energy.

5.8.3 Effective generalized inductive impedance estimation

The detailed of the theory of transverse bunched beam instabilities and the beam-impedance interaction developed by Sacherer can be found in Ref. [31, 107].

The beam-impedance interaction generates a complex tune shift $\Delta\omega$ of the betatron frequency. The real part of $\Delta\omega$ measured at injection and extraction energy corresponds to the interaction of the beam with the imaginary part of the transverse impedance $Z_\perp$ that is supposed broadband. Chap. 4 has shown that the measurements of the fast transverse instability rise times can be compared to *HEADTAIL* simulations assuming a broadband impedance. Growth rates are the interaction of the beam with the real part of the impedance, so at transition, we have measured $Re(Z_\perp)$ of the broadband impedance. With tune shift measurements, $Im(Z_\perp)$ is evaluated and as it will be seen this paragraph, this value is not absolute. This is why we defined Z_{eff}, the effective impedance, i.e. the impedance weighted by the transverse bunch spectrum $h(\omega)$ centred at the chromatic frequency ω_ξ as shown in Fig. 5.54,

$$Z_{eff} = \frac{\sum_{p=-\infty}^{\infty} Z_\perp(\omega')h(\omega'-\omega_\xi)}{\sum_{p=-\infty}^{\infty} h(\omega'-\omega\xi)} \begin{cases} \omega' & = \omega_0 p + \omega_\beta \\ \omega_\xi & = \xi\omega_\beta/\eta \\ h(\omega) & = e^{-\omega^2\sigma^2/c^2} \end{cases} \tag{5.49}$$

with ω_0 the angular revolution frequency, ξ the chromaticity, ω_β the betatron frequency, η the momentum compaction factor, $h(\omega)$ the bunch spectrum, which a line spectrum within the envelope $h(\omega'-\omega_\xi)$ and then for a single bunch $\omega' = (p+Q)\omega$, with p is an integer $-\infty < p < \infty$. Since the beam is assumed Gaussian, $h(\omega')$ is also a Gaussian spectrum. $Im(Z_\perp)$ is assumed constant all over the spectrum of the oscillation mode at least for the lowest mode considered herein (m=0). Such simplification is generally valid for long proton bunches. The real tune shift is related to the effective generalized impedance developed by the Sacherer for a bunched beam [107]

$$\Delta Q_m = -\frac{1}{1+m}\frac{j}{2Q_0\omega_0^2}\frac{e\beta I}{\gamma m_0 \tau_b} Im\left(Z_{eff}\right) \tag{5.50}$$

with m the oscillation mode, here $m = 0$ since we are interested by the rigid mode, Q_0 the transverse tune, I the intensity in A and τ_b the full bunch length in meter. The computation gives an effective generalized transverse impedance. Effective since its value is not absolute and might change according the energy and the length of the beam.

For asymmetric structures as in the PS and as explained in Ref [34] and briefly in Sec. 1.4.1, the impedance can be expanded in the offset of the trailing particles and of a source particle. Usually the higher orders are neglected, therefore only the dipolar Z^{dip} and the quadrupolar part Z^{quad} of the effective generalized transverse impedance are kept: the transverse wake potential can be separated into superposition of dipolar components, which are proportional to the offset of the bunch offset, and of quadrupolar components, proportional to the offset of the trailing particles. This superposition is fundamental for impedance in asymmetric

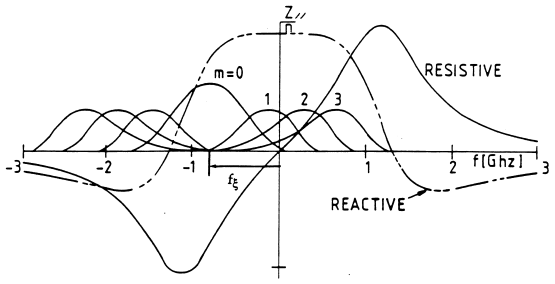

Figure 5.54: Impedance spectrum.

chambers. For any beam energy

$$Z_{x,y} = Z_{x,y}^{dip} + Z_{x,y}^{quad} \tag{5.51}$$

Hence the measured coherent tune shift for asymmetrical vacuum chamber is composed by the contribution of the dipolar impedance ΔQ_{dip}^{Z} and the quadrupolar part ΔQ_{quad}^{Z} (or incoherent tune shift)[24]

$$\Delta Q_{coh} = \Delta Q_{dip}^{Z} + \Delta Q_{incoh}^{Z} \tag{5.52}$$

From the Eq. (5.50) and the slopes of the fitted Eq. 5.48 and Eq. 5.47, an effective generalized impedance can be estimated at at injection and extraction energies with the beam parameters of Table 5.10 and Table 5.11. The results are summarized in the Table 5.12. The second part of this table is dedicated to the results of previous measurements done in 1989 [80] and 2000 [81].

Kinetic energy (GeV)	1.4	25
Hor. $Im(Zeff)$ (MOhm/m)	3.5	< 1
Vert. $Im(Zeff)$ (MOhm/m)	12.5	6.1
Previous measurements [80, 81]		
Kinetic energy (GeV)	25	
Hor./Vert. $Im(Zeff)$ (MOhm/m)	3-13 / 3-7.9	

Table 5.12: Effective generalized impedance results compared also to previous measurements.

Tune measurements were performed in the past Ref [80] in 1989 at 1 GeV and 26 GeV/c and

also in Ref [81] earlier in 2000/2001 at 1.4 GeV and 26 GeV/c.

The vertical tune shift is about 4 times bigger in the measurements presented in Ref. [80] (Fig. 5.55a and Fig. 5.55b) due the lower PS injection kinetic energy of about 1 GeV in 1989 and therefore the space charge forces were more important than in the current 1.4 GeV injection energy. At 26 GeV/c, ΔQ_v measured in the experiment is twice larger than in 1989. In order to avoid the effect of the bunch length on the effective impedance, the measured beam intensities are divided by σ_z. $Im(Z_{eff})$ in the y-plane appears to have increased over the years (Fig. 5.55a and Fig. 5.55c). In the horizontal plane, no significant change is measured. The measurements

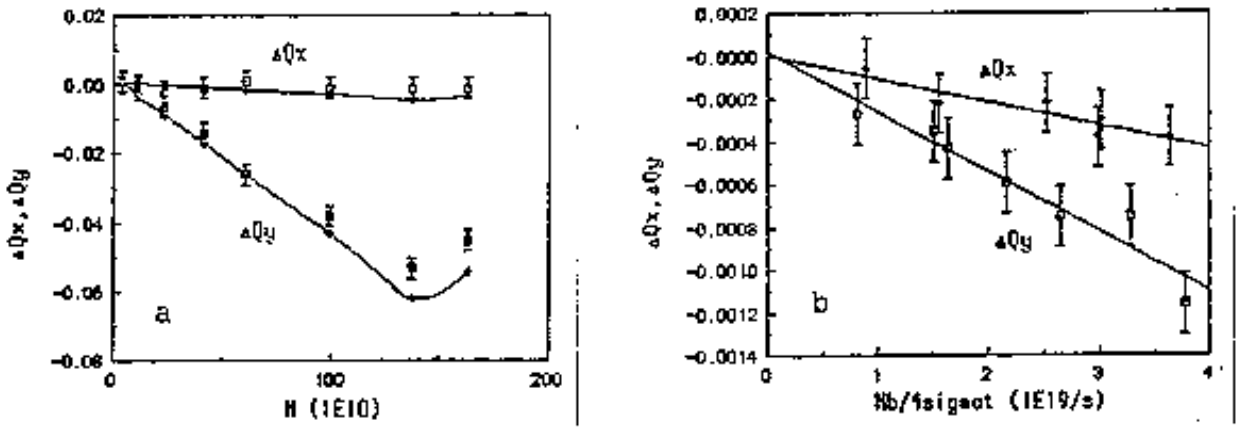

(a) 1989 measurements [80].

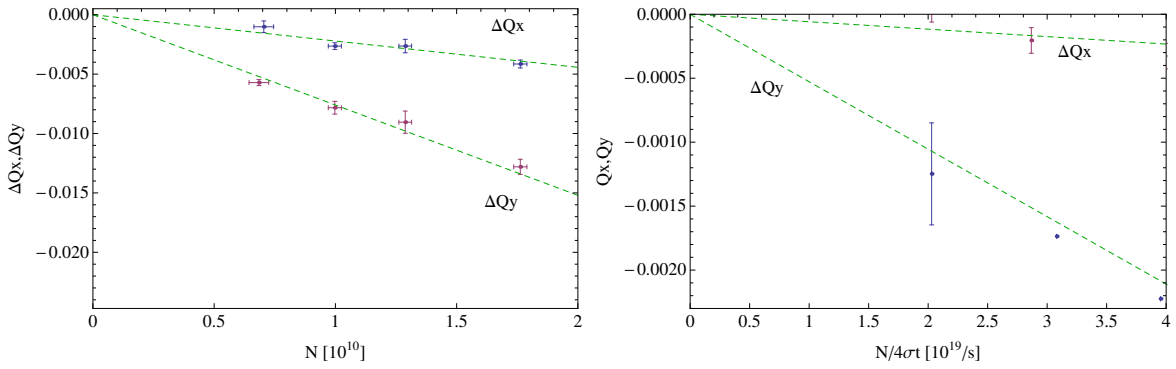

(b) injection.

(c) extraction.

Figure 5.55: Tune shift measurements at injection kinetic energy 1 GeV and extraction momentum 26 GeV/c in 1989 in the Fig. (a) versus our measurements in Fig. (b) and Fig. (c).

of 2000-2001 were performed with positron beams at 3.5 GeV/c and the results show large discrepancies from a year to another [81]. These differences were not understood. However the impedance found for the vertical plane in 2001 seems to agree with the current values. Table 5.13 summarizes the generalized effective inductive impedance.

Effective $Im(Z_{\perp})$	1989	2000/2001	Current
Hor. $Im(Zeff)$ (MOhm/m)	1.1	3.2/13.5	1
Vert. $Im(Zeff)$ (MOhm/m)	2.8	2.9/7.6	6.1

Table 5.13: Effective generalized impedance

5.8.4 Estimation of the Tune Shift due to Space charge

The measured tune shift at injection and extraction energy is the sum of the contribution from space charge ΔQ_{sc} and from the impedance ΔQ_z. Let us consider the vertical effective impedance at the two energies. If the coherent tune shift due to space charge is assumed negligible at 26 GeV, it does not mean that the value of the imaginary part of the broadband impedance is the difference between $Z_y^{eff}(26\ GeV) - Z_y^{eff}(1.4\ GeV) = 12.5 - 6.1 = 6.9$ MΩ/m, since the bunch length at the two energies were different.

Very small coherent tune shift at 26 GeV were measured, assuming that the contribution from the space charge is negligible,

$$\Delta Q_{coh}^{x} \simeq 0 \tag{5.53}$$

It does not mean that Z_x^{eff}, the horizontal impedance is zero. As explained previously, the tune shift is the sum of the dipolar part and an incoherent part

$$\Delta Q_{coh}^{x} = \Delta Q_{dip}^{x} + \Delta Q_{quad}^{x}$$

in term of impedance,

$$\Delta Q_{coh}^{x} \simeq 0 \rightarrow Z_{dip}^{x} + Z_{quad}^{x} = 0$$

therefore the dipolar part compensates the quadrupolar part of the impedance in the horizontal plane. In the case of a vacuum chamber assume to be like two parallel conductive infinite plates, the wake force seen by a trailing particle behind a source particle will not depend neither on the position of the source nor the position of the test particle. The vacuum chamber of the PS is elliptical with the half width being twice the half height. With such dimensions, the results of the two parallel conductive plates is found for the PS. The different contributions of the dipolar and quadrupolar parts of the impedance in the PS are not known. 2-wire technique is required to obtain the dipolar part of the impedance [34, 108].

$$Z_{dip}^{x} = -Z_{quad}^{x} \tag{5.54}$$

Concerning the vertical plane, the space charge has be taken into account

$$\Delta Q_{coh}^{y} = \Delta Q_{coh}^{sc} + (\Delta Q_{dip}^{Z_y} + \Delta Q_{quad}^{Z_y}) \tag{5.55}$$

The coherent tune shift due to space charge depends on the magnetic and electric contribution with the environment, here the wall. It can be evaluated thanks to the Laslett coefficients of Eq. 5.43, with ϵ_1^y and ϵ_2^y the Laslett coefficients which define the contribution from the magnetic images in the magnet poles and from the transverse motion, ξ_1^y the Laslett coefficient which defines the contribution of the electric images. The formula allows to evaluate the coherent tune shift due to image charges, i.e. indirect space charge, and it is found that it contribute for 1/4 of the total coherent tune shift measured at injection in the vertical plane as

shown in Fig. 5.56. The same analysis can be made for the tune shift at 26 GeV in Fig. 5.57 for

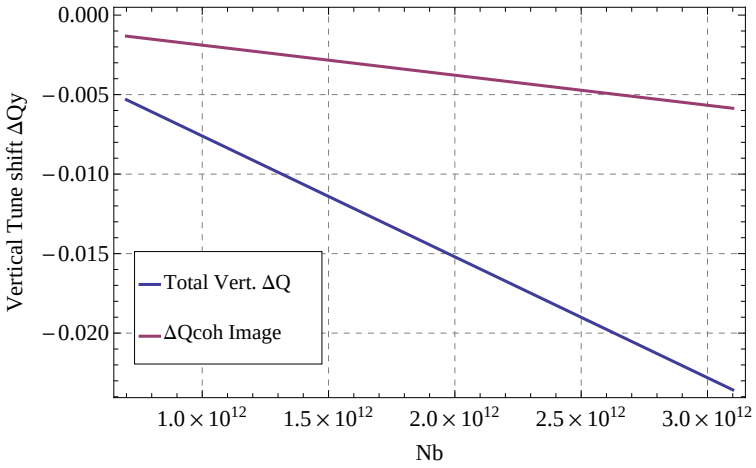

Figure 5.56: Coherent tune shift from indirect space charge computed from Eq. 5.43 and compared to the total vertical tune shift measured at injection energy.

the vertical plane and as expected, the contribution of space charge is negligible.

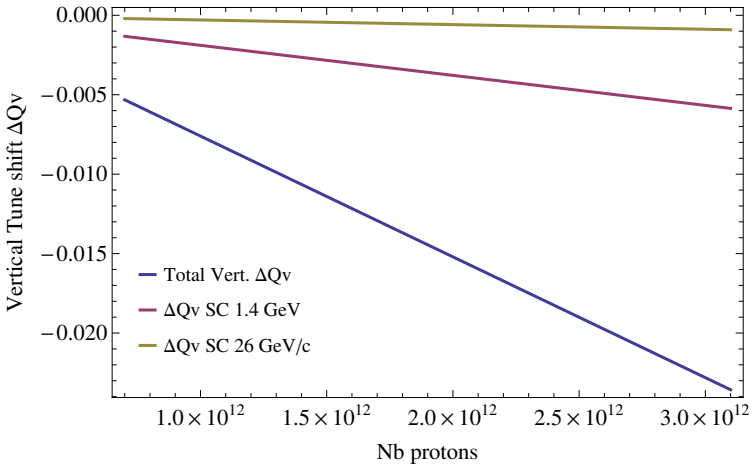

Figure 5.57: Coherent tune shift from indirect space charge computed from Eq. 5.43 at 1.4 GeV and at 26 GeV and compared to the total vertical tune shift measured at injection energy.

5.9 Conclusions

The important issue concerning the injection study was the understanding of the high radiation measured outside the ring due to proton beam losses at injection. Extensive measurements using the PS BLM system were performed in order to identify the loss process. Optics mismatch measurements were also done to see if it is a strong limitation. From these experiments, an aperture restriction was identified at septum blade. The beam sizes are rather large in the transverse plane and in horizontal the beam is pushed close to the septum blade to save strength of the kicker . Some tails of the beam are then cut.

Turn by turn losses are very difficult to explain, however they are mostly measured in the straight section of the injection system, i.e. at the maximum of the bump, and at the beginning of the main magnet of the straight section 43, i.e. at the minimum of the bump. They are due to large beam size and the shape of the injection bump. The reason of the their mechanism can be understood if the beam crosses resonances due to a transverse space charge tune spread.

Several cure were proposed and they are now studied in the framework of the PS Upgrade project, which is planning a complete review of the injection system by increasing the injection energy from 1.4 GeV to 2 GeV. This will help to decrease by 63% space charge forces and it will produce smaller beam sizes.

The beam sizes at the septum have to be reduced for high intensity beams, on top of the reduction of the physical emittance due to higher injection energy. Therefore a new optics is under study to propose two different settings for LHC and High intensity beams. A collimation system could be also installed in order to reduce the losses in the injection region. The PS optics has to be then adapted to the line, therefore a new optics has to be computed by using for example the QKE quadrupoles. Working point studies to identify dangerous resonances at injection are also part of the project with and without space charge. In order to evaluate the space charge contribution on the tune at injection, tune shift measurements were performed at injection and extraction energy and the results allow to define effective impedance for space charge and for the impedance.

Conclusions

This thesis aimed to study high intensity beam issues at transition energy and at injection. In both cases, extensive beam based measurements were performed, in order to understand the mechanisms of the limiting the maximum intensity.

Chapter 4 was dedicated to the study of the dynamics of a fast vertical instability developing near transition energy. A large campaign of measurements and macro particle simulations were performed first without a gamma transition jump. Using a simple impedance model in HEADTAIL, the simulations reproduced well the observed travelling wave along the Δ_y profile, with broadband resonator frequency $f_r = 1$ GHz, a quality factor $Q = 1$ and shunt impedance $R_s = 0.7$ MΩ/m. The wake force responsible of the turbulence is short range wake field and particles near the peak density are unstable. The rise times as a function of the beam intensity were measured and compared to HEADTAIL simulations and a fair good agreement is found and the threshold in intensity is found within less than 50% error. This is a good result for the use of such simple impedance model.

Momentum compaction factor thresholds were also deduced from the experiment. This parameter is very important since it allows to identify when the beam is going into the non-adiabatic regime, i.e. when the synchrotron motion is almost frozen. η_{th} is linearly proportional to the beam intensity and chromaticity is a way to increase η_{th}, i.e. with betatron frequency spread, it is possible to cross transition with more particle with the same η. It was confirmed by simulation and by few formula using the coasting beam formalism. However the slope of the linear function of η_{th} as a function the beam intensity are not well reproduced by HEADTAIL, this can come from the difference in impedance model between the real machine and the simple broadband resonator. It was measured that the working point can increase the threshold in intensity however this was not reproduced by simulation and this could be due to the limit of the impedance model used in HEADTAIL. High order component of the magnetic field can be also a cause of spread in the measurements since the PFWs induce octupolar component and non-linear coupling, even if the measured Q'' was very small. However, $Q'' = -50$ already introduces higher rise time. Further investigation on the fields generated by the PFWs are needed to check their influence on intensity threshold.

The introduction of a gamma transition jump in the simulation and in the measurements increases by a factor 6 the threshold in intensity. Therefore η-jump and an adequate working

point (such chromaticity-jump) are two ways to increase the limit in intensity of the instability, instead of compromising the the longitudinal density. This study brought new physics result in a region in which the measurements are very complex to perform. These results can be used in the future to validate the complete impedance model, which is ongoing. Already with measurements, the real part of the impedance has been evaluated to $Re(Z_y^{\perp}) = 0.7$ MΩ/m and the imaginary part $Im(Z_y^{\perp}) = 6$ MΩ/m with tune shift measurements.

In Chapter 5, the results of the beam losses studies was presented. Thanks to experiments done with BLM and matching measurements, it was identified that the beam loses particles on the septum blade and then turn-by-turn during up to 800 μs. The mismatch between the injection line and the PS has been estimated at 10%, which is reasonable for the requirement of LHC beams. With the PS Upgrade project, several solutions were proposed and they are under studies in the framework of the 2 GeV injection upgrade. Space charge and resonance crossing might explain the slow losses at the minimum and maximum of the bump, this is the reason why tune shift measurements were performed at injection and extraction energy, in order to evaluate the contribution of space charge but also the effect of impedance. With an injection at 2 GeV, a gain of 63% on space charge is expected and a higher energy will naturally decrease transverse emittance and therefore the beam size, which an advantage for the losses at the septum.

Many more studies were proposed in this thesis. Transverse space charge effects on the instability at transition and on the mechanism at injection can bring to interesting results and push forward the limitations in intensity of the CERN PS.

Bibliography

[1] M. Martini. *Introduction to Transverse Beam Dynamics in Accelerators.* 1996. CERN/PS-96-11(PA).

[2] H. Wiedemann. *Particle Accelerator Physics; 3rd ed.* Springer, Berlin, 2007.

[3] S. Hancock, M. Lindroos, E. McIntosh, and M. Metcalf. *Tomographic Measurements of Longitudinal Phase Space Density.* Technical Report CERN-PS-99-002-OP, CERN, Geneva, January 1999.

[4] P.J. Bryant and K. Johnsen. *The Principles of Circular Accelerators and Storage Rings.* Cambridge University Press, 1993.

[5] S. Aumon, B. Salvant, W. Bartmann, S. Gilardoni, E. Métral, G. Rumolo, and R. Steerenberg. *Beam Instabilities studies at transition crossing in the CERN Proton Synchrotron.* Technical Report CERN-ATS-2009-024, CERN, Geneva, May 2009.

[6] K. Schindl. *Space charge.* 2006.

[7] S. Gilardoni and D. Manglunki, editors. *Fifty years of the CERN Proton Synchrotron,* volume I, 2011. (CERN-2011-004).

[8] M. Juchno. *Electromagnetic FEM analysis of the CERN Proton Synchrotron main magnetic unit.* Master's thesis, Cracow, Poland, Cracow University of Technology, 2009.

[9] G.C. Schneider. *A 1.5 GHz wide-band beam-position and intensity monitor for the electron-positron accumulator.* (CERN-PS-87-44-BT), 1987.

[10] J. Gareyte and F.J. Sacherer. *Head-tail type Instabilities in the CERN PS and Booster.* (CERN-MPS-DL-74-4):5 p, 1974. Ninth International Conference on High Energy Accelerators, Stanford, 2-7 May 1974.

[11] P. Raimondi G. Arduini. *Transverse emittance blow-up due to injection errors.* Technical Report SL-Note-99-022-SLI, CERN, Geneva, Mar 1999.

[12] http://op-webtools.web.cern.ch/op-webtools/dokuwiki/doku.php PS Beam documentation.

[13] H. Damerau. Multi-bunch beam for LHC in the PS, BE/OP Shutdown Courses, 2011.

[14] M. Sands. *The Physics of electron storage rings: an Introduction.* November 1970. SLAC-R-121.

[15] S. Y. Lee. *Accelereto Physics.* World Scientific, 1999.

[16] Frenet–Serret formulas. http://en.wikipedia.org/wiki/frenet

[17] R. Bruce. *Beam loss mechanisms in relativistic heavy-ion colliders.* PhD thesis, Lund U., Lund, 2009. Presented on 18 Sep 2009.

[18] J. Thomashausen F. Ruggiero, editor. *CAS - CERN Accelerator School : Basic Course on General Accelerator Physics, 2 - 13 Oct 2000, Loutraki, Greece*, Geneva, 2005. CERN, CERN.

[19] H. Blewett. *A night to remember. CERN Courier, A golden anniversary for the PS*, pages 479–482, November, 2009.

[20] H. Bartosik. *PhD Thesis.* PhD thesis, 2012.

[21] H. Bartosik, T. Argyropoulos, T. Bohl, S. Cettour Cave, J. E. Muller, K. Cornelis, Y. Papaphilippou, G. Rumolo, B. Salvant, E. Shaposhnikova, and J. Wenninger. *Experimental studies with low transition energy optics in the SPS.* Technical Report CERN-ATS-2011-086, CERN, Geneva, 2011.

[22] H. Wiedemann. *Particle Accelerator Physics.* Springer, 2007.

[23] K.Y. Ng. *Transition and Space-charge Mismatch*, chapter 16. US Particle Accelerator School, 2002.

[24] E. Metral and G. Rumolo. Collective effects. In *US Particle Accelerator School 2009.*

[25] D. Möhl. *Compensation of space charge effects at transition by an asymmetric Q-Jump: a theoretical study. CERN-ISR/300/GS/69-62.*

[26] A. Sørenssen. *Crossing the phase transition in strong-focusing Proton Synchrotrons.* In *CERN/MPS/DL 73-9/Rev.*

[27] A. Sørenssen. *How to pass Transition in the CPS at high intensity ? CERN/MPS/DL 71-6.*

[28] T. Risselada. *Gamma transition jump schemes.* 1993.

[29] M. Martini. *PS gamma transition jump scheme.* December 2005.

[30] M. Martini S. Aumon, S. Gilardoni. *Study of Beam Losses at Transition Crossing at the CERN PS.* (CERN-AB-2008-015):4 p, Aug 2008.

[31] A.W. Chao. *Physics of Collective Beam Instabilities in High Energy Accelerator.* John Wiley and Sons.

[32] K.Y. Ng. *Physics of Intensity Dependent Beam Instabilities*. World Scientific, 2006.

[33] K.Y. Ng. *Wake and Impedances*, USPAS02. 2002.

[34] S. Heifets et al., SLAC-AP-110, 1998.

[35] A. Hofmann. *Tune Shifts from Self-Fields and Images, CERN Accelerator School CAS*.

[36] B. Salvant. *Impedance model of the CERN SPS and Aspects of LHC Single-Bunch Stability*. (CERN-THESIS-2010-087), Mars 2010.

[37] K. Yokoya. Cumulative beam breakup in large-scale linacs. Technical Report DESY-86-084, DESY, Hamburg, August 1986.

[38] K.Y. Ng. *Beam Breakup*. US Particle Accelerator School, 2002.

[39] R. Cappi, E. Métral, and G. Métral. *Beam Break-up Instability in the CERN PS near Transition*. (CERN-PS-2000-017-AE), 2000.

[40] D. Brandt and J. Gareyte. *Fast instability of positron bunches in the CERN SPS*. (CERN-SPS-88-17-AMS), June 1988.

[41] *The CERN Proton Synchrotron*, 1959. 3 volumes, CERN 59-29 (1959), 60-26 (1960), 62-03 (1962).

[42] F. Blas, P. Bossard, R. Cappi, G. Cyvoct, R. Garoby, G. Gelato, H. Haseroth, E. Jensen, D. Manglunki, K. D. Metzmacher, F. Pedersen, N. Rasmussen, K. Schindl, G. C. Schneider, H. O. Schönauer, L. Sermeus, M. Thivent, M. Van Rooij, F. V. Völker, and E. Wildner. *Acceleration of lead ions in the CERN PS Booster and the CERN PS*. (CERN-PS-95-027 HI):3 p, Jun 1995.

[43] D. Manglunki, A. Beuret, J. Borburgh, C. Carli, M. Chanel, L. Dumas, T. Fowler, M. Gourber-Pace, S. Hancock, M. Hourican, J. Jowett, D. Küchler, E. Mahner, M. Martini, S. Maury, S. Pasinelli, U. Raich, A. Rey, J-P Royer, R. Scrivens, L. Sermeus, G. Tranquille, J L Vallet, and B. Vandorpe. *IONS FOR LHC: STATUS OF THE INJECTOR CHAIN*. Technical Report CERN-AB-2007-012, CERN, Geneva, January 2007.

[44] P. Asboe-Hansen, O. Barbalat, D. Boussard, M. Bouthéon, J. Gareyte, H. Haseroth, J. Jamsek, and S. Myers. *Acceleration and stacking of deuterons in the CERN PS and ISR. IEEE Trans. Nucl. Sci.*, 24(CERN-ISR-OP-77-14):1557–1560, 1977.

[45] *n-ToF Technical Design Report on Experimental Area*. Technical Report CERN-INTC-2000-018, CERN, Geneva, November 2000.

[46] T. Erikson, S. Maury, and D. Möhl. *Status Report on the Antiproton Decelerator (AD)*. *Nucl. Phys. A*, 692(CERN-PS-2000-072-AE. 1-2):187–192. 3 p, Nov 2000.

[47] J. Schacher. *The DIRAC Experiment at CERN*. (DIRAC-CONF-1999-04), 1999.

[48] http://cloud.web.cern.ch/cloud/.

[49] *Search for $\nu_\mu \rightarrow \nu_\tau$ oscillation with the OPERA experiment in the CNGS beam.* Technical Report CERN-PH-EP-2011-116, CERN, Geneva, July 2011. Submitted to Physics Letters B.

[50] R. Cappi, R. Garoby, S. Hancock, M. Martini, N. Rasmussen, T. Risselada, J. P. Riunaud, K. Schindl, H. O. Schönauer, and Edmund J. N. Wilson. *The PS complex as part of the LHC injector chain.* Technical Report CERN-PS-91-07-PA. LHC-NOTE-144. CERN-LHC-Note-144, CERN, Geneva, Apr 1991.

[51] M. Benedikt, R. Cappi, M. Chanel, R. Garoby, M. Giovannozzi, S. Hancock, M. Martini, E. Métral, G. Métral, K. Schindl, and J. L. Vallet. *Performance of the LHC Pre-Injectors.* Technical Report CERN-PS-2001-011-DR, CERN, Geneva, Apr 2001.

[52] M. Scholz. *Simulations of the H^- Charge Exchange Injection into the CERN Proton Synchrotron Booster with Linac4.* (CERN-THESIS-2010-201).

[53] A. Findlay H. Damerau. *LHC 50 and 75 ns single batch beams in Booster and PS.*

[54] *The CERN Proton Synchrotron.* CERN Yellow Report 59-29, 1959.

[55] R. Gouiran P. Lefèvre. *Projet de nouveaux enroulements polaires pour le CPS. MP-S/DL/Note 74-11, June 1974.*

[56] *Specification for pole face windings. CERN MPS/Int. MA 67-15 (1967).*

[57] J. P. Burnet, M. Giovannozzi, E. Métral, O. Michels, R. Steerenberg, and B. Vandorpe. *CERN Proton Synchrotron working point control using an improved version of the pole-face-windings and figure-of-eight loop powering.* (CERN-AB-2006-065):4 p, Jul 2006.

[58] P. Freyermuth, D. Cotte, M. Delrieux, H. Genoud, S. Gilardoni, K. Hanke, O. Hans, S. Mataguez, G. Metral, F. Peters, R. Steerenberg, and B. Vandorpe. CERN Proton Synchrotron working point matrix for extended pole face winding powering scheme. *Proceeding of IPAC10, Kyoto, Japan, CERN-ATS-2010-180*, 2010.

[59] M. Martini E. Metral G. Metral R. Steerenberg CERN Geneva R. Cappi, M. Giovannozzi and Forschungszentrum Karlsruhe Germany A.S. Müller, ISS. *CERN-AB-2003-017 ABP, Particle Accelerator Conference 2003, Portland, Oregon, USA.*

[60] O. Michels J.-P. Burnet. *Projet de Consolidation des Convertisseurs PFW. Note Technique AB-PO N10,(EDMS585302).*

[61] R. Gouiran. *Projet d'un nouveau système d'enroulements polaire à cinq courants. CERN MPS/SM/Note 75-21, 1975.*

[62] C. Steinbach, H. Stucki, and M. Thivent. *The new slow extraction system of the CERN PS.* (CERN-PS-93-28-OP):4 p, Jun 1993.

[63] M. Giovannozzi, E. Métral, and R. Steerenberg. *PS 4-turn Continuous Transfer Extraction Test.* Technical Report AB-Note-2005-006. CERN-AB-Note-2005-006, CERN, Geneva, Feb 2005.

[64] M. Giovannozzi, M. J. Barnes, O. Berrig, A. Beuret, J. Borburgh, P. Bourquin, R. Brown, J.P. Burnet, F. Caspers, J. M. Cravero, T. Dobers, T. Fowler, S. Gilardoni, M. Hourican, W. Kalbreier, T. Kroyer, F. Di Maio, M. Martini, V. Mertens, E. Métral, K. D. Metzmacher, C. Rossi, J. P. Royer, L. Sermeus, R. Steerenberg, G. Villiger, and T. Zickler. *The CERN PS multi-turn extraction based on beam splittting in stable islands of transverse phase space: Design Report.* CERN, Geneva, 2006.

[65] J. Barranco and S. Gilardoni. *Study of losses during continuous transfer extraction at CERN Proton Synchrotron.* (CERN-AB-2008-021):4 p, Aug 2008.

[66] http://mad.web.cern.ch/mad/.

[67] W. Herr and F Schmidt. A MAD-X Primer. (CERN-AB-2004-027-ABP):32 p, June 2004.

[68] A. Fasso, A. Ferrari, J. Ranft, and P. R. Sala. *FLUKA: a multi-particle transport code. CERN Report CERN-2005-10*, 2005.

[69] G. Battistoni, S. Muraro, P. R. Sala, F. Cerutti, A. Ferrari, S. Roesler, A. Fasso, and J. Ranft. The fluka code: Description and benchmarking. *Hadronic Shower Simulation Workshop 2006, Fermilab 6–8 September 2006, AIP Conference Proceeding*, 896:31–49, 2007.

[70] http://www.fluka.org/fluka.php.

[71] Headtail Working Group.

[72] F. Zimmermann G. Rumolo. Practical User Guide for HEADTAIL. (CERN-SL-Note-2002-36 AP), November 2002.

[73] S. Aumon, H. Damerau, and S. Gilardoni. *Optimization of the position of the Radial Loop Pickups in the CERN PS.* (CERN-ATS-2010-031), June 2010.

[74] E. Métral. *Effect of bunch length, chromaticity, and linear coupling on the transverse mode-coupling instability due to the electron cloud.* (CERN-PS-2002-009-AE):9 p, Apr 2002.

[75] *Beam Measurements, Proceedings of the Joint US-CERN-Japan-Russia School on Particle Accelerators, Montreux, and CERN, Switzerland, 11-20 May, 1998.* S. I. Kurokaw, 1999.

[76] T. Nakamura et al. *Suppression of transverse instabilities by chromaticity modulation. Proceeding of IPAC10, Kyoto, Japan*, 2010.

[77] M. Gasior and R. Jones. *The principle and first results of betatron tune measurement by direct diode detection.* Technical Report LHC-Project-Report-853. CERN-LHC-Project-Report-853, CERN, Geneva, Aug 2005.

[78] H. Damerau. Private communication, 2010.

[79] E. Métral. *Fast High-Intensity Single-Bunch Transverse Coherent Instability in Synchrotrons due to a Broad-Band Resonator Impedance.* Technical Report CERN-PS-2001-035-AE, CERN, Geneva, Jul 2001.

[80] R. Cappi, M. , T. , J. P Riunaud, and D. Trione. *Recent studies on transverse beam behaviour at the CERN PS. Part. Accel.*, 27(CERN-PS-89-39-PA):197–202. 7 p, Jul 1989.

[81] E. Metral G. Metral R. Steerenberg J. Bento R. Gabory S. Hancock J.L. Vallet R. Cappi, M. Giovannozzi. *Measurements of the PS low frequency inductive broad band impedance*, PPC meeting, 14th of December 2001.

[82] N. Mounet. *The LHC Transverse Coupled Bunch Instability.* (CERN-THESIS-2012), January 2012.

[83] A. Burov. private discussions. 2012.

[84] A. Burov. *Suppression of bunch transverse instabilities by the chamber asymmetry.* Technical Report FERMILAB-TM-2050, FERMILAB, Batavia, IL, Jul 1998.

[85] V. Kapin V. Kornilov, O. Boine-Frankenheim. Coherent instability thresholds and dynamics aperture with octupoles and non-linear space charge in sis100 synchrotron. In *Proceedings of IPAC10, Kyoto, Japan.*

[86] M. Juchno. PhD thesis, 2012.

[87] *Linear Imperfection, CERN Accelerator School CAS.*

[88] E. Effinger J. Gil-Flores S. Gilardoni, S. Aumon. *Beam Loss Monitors Comparison at the CERN Proton Synchrotron.* (CERN-ATS-2011-131):4 p.

[89] V. Agoritsas, F. Beck, G. P. Benincasa, and J.P. Bovigny. *A microprocessor-based system for continuous monitoring of radiation levels around the CERN PS and PSB accelerators. Nucl. Instrum. Methods Phys. Res., A*, 247(CERN-PS-85-60-CO):44–49. 22 p, Oct 1985.

[90] E. B. Holzer et al. *Commissioning and optimization of the LHC BLM System.* (CERN-BE-2010-031):5 p, Sep 2010.

[91] *CAS - CERN Accelerator School: General Accelerator Physics, v.2*, Geneva, 1985.

[92] H. Koziol. *Beam Diagnostics for Accelerators.* Technical Report CERN/PS 2001-012 (DR), CERN, Geneva, 2001.

[93] C. Dutriat. Technical report, Private conversation, 2008.

[94] R. De Maria. *LHC Interaction region upgrade.* PhD thesis, Ecole Polytechnique, Lausanne, Lausanne, 2008. Presented on 14 Apr 2008.

[95] E. Benedetto. *Optics Measurements and Matching of TT2-TT10 line for Injection of the LHC Beam in the SPS.* Technical Report CERN-AB-Note-2008-055, CERN, Geneva, Nov 2008.

[96] S. Gilardoni. private conversation, 2012.

[97] G. Arduini. *Beam Quality Preservation in the CERN PS-SPS Complex.* (CERN-AB-2004-047), 2004.

[98] R. Steerenberg. private conversation, 2010.

[99] A. Fasso *et al. The physics models of FLUKA: status and recent developments. Proc. of the Computing in High Energy and Nuclear Physics 2003 Conf., La Jolla*, 2003.

[100] S. Damjanovic. *Shielding studies for the Route Goward /PS Crossing.* (CERN-DGS-2011-065-RP-TN), 2011.

[101] J. Borburgh, S. Aumon, W. Bartmann, S. Gilardoni, B. Goddard, L. Sermeus, and R. Steerenberg. *Feasibility Study of a CERN PS Injection at 2 GeV.* Technical Report CERN-ATS-2011-271, CERN, Geneva, Dec 2011.

[102] E. Metral et al. *Space Charge Experiments at the CERN PS. CERN-AB-2005-019*, 2005.

[103] G. Franchetti, B. Franczak, and P. Schutt. *Benchmarking experiment in SIS for dynamic aperture induced beam loss.* Technical Report GSI-Acc-Note-2004-05-001, GSI, 2004.

[104] S. Gilardoni, S. Aumon, J. Brenas, P. Freyermuth, A. Huschauer, R. Maillet, E. Matli, R. Steerenberg, B. Vandorpe, and E. Benedetto. *Tune and space charge studies for high-brightness and high-intensity beams at CERN PS.* Technical Report CERN-ATS-2011-090, CERN, Geneva, Sep 2011.

[105] private communication, 2009.

[106] M. Buzio. Mini-Workshop about the PS magnets, 24 February 2012.

[107] F.J. Sacherer. *Transverse Bunched Beam Instabilities. CERN/PS/BR 76-21 (1976).*

[108] H. Tsutsui. One single wire technique for transverse coupling impedance measurement, SL-NOTE-2002-034.